Doctoral Dissertation
Doctoral Program in Energy Engineering (38^{th}cycle)

Triply Periodic Minimal Surfaces as structured porous media cooling systems for the removal of high heat fluxes

By

Eleonora Gajetti

******

Supervisor(s):
Prof. L. Savoldi, Politecnico di Torino
Prof. G. Boccardo, Politecnico di Torino
Prof. A. Buffo, Politecnico di Torino
Prof. L. Marocco, Politecnido di Milano

Politecnico di Torino
2026

Declaration

I hereby declare that, the contents and organization of this dissertation constitute my own original work and does not compromise in any way the rights of third parties, including those relating to the security of personal data.

Eleonora Gajetti
2026

* This dissertation is presented in partial fulfillment of the requirements for **Ph.D. degree** in the Graduate School of Politecnico di Torino (ScuDo).

Abstract

Many engineering applications in energy and non-energy sectors require advanced thermal management systems for proper operation. The development of innovative enhanced heat removal systems is therefore essential. The rise of Additive Manufacturing (AM) in recent years has enabled the exploration of structures that were previously impossible to achieve with traditional manufacturing methods, including cellular lattice structures, among which Triply Periodic Minimal Surfaces (TPMS) stand out. TPMS are periodic, non-intersecting and highly interconnected surfaces, with no sharp angles and large specific surface area, arising in many fields for thermal, structural, biomedical, or chemical applications. Discovered in the late 1800s as mathematical combinations of trigonometric functions in 3D space, they are now extensively studied due to their recent manufacturability. Many researchers have attempted to develop TPMS-based systems, for example for heat-exchangers or heat sinks applications, and compare them with more traditional devices. Studies aiming at modeling TPMS in order to analyze their thermal and hydraulic performance are present in the literature, too. Notwithstanding the enormous amount of work on TPMS, most current literature lacks generalizability or repeatability, frequently based on questionable assumptions or providing insufficient detail in the descriptions or inconsistent definitions of descriptive parameters.

The objective of the present thesis is thus to provide a solid basis on the hydraulic and thermal characterization of TPMS at low Reynolds numbers, by starting from simple and generalizable models (such as the porous medium framework) that can be employed in other problems, and investigating a significant range of geometric parameters, such as porosity and different topologies. At the same time, this work does not only intend to study TPMS from a theoretical point of view, but also aims to exploit their analysis for real-use purposes, specifically in a solar application as volumetric solar receivers for Concentrated Solar Power (CSP), and, for the first time, in a nuclear fusion application as cooling system for mirrors reflecting high-frequency electromagnetic beams.

For the hydraulic characterization of Triply Periodic Minimal Surfaces, the Darcy-Forchheimer equation was approached, and other common frameworks such as the Ergun equation, considering TPMS as a structured porous medium. The developed models correlated the hydraulic impedance of diverse topologies to their porosity and tortuosity, proving successfully also in different geometries than those used for the development. The hydraulic phenomena were related to the energy transport within TPMS, enabling the building of correlations between the thermal and hydraulic variables. Concerning the use of TPMS for heat removal, problem-specific devices were designed, compliant with the working conditions, investigated from a numerical point of view, manufactured with AM and tested, both thermally and hydraulically. The performance assessment of these TPMS-based devices was successful, as the volumetric receivers filled with TPMS proved outstanding compared to other traditional receivers in terms of thermal efficiency, and the mirror cooled by TPMS structures was thermally superior to other proposed cooling options. The comparison between simulation and experimental results highlighted the reliability of numerical models for large structures printed in polymeric materials, but significant discrepancies occurred with metal samples, probably due to the residual roughness of the prototypes. Furthermore, these differences increased as the characteristic hydraulic size of the TPMS decreased, thereby making any porosity or printing defects more significant. In theory, the large roughness of the samples should also raise heat exchange, by increasing the effective heat exchange surface area. However, thermal tests on the mirror filled with TPMS failed to detect this phenomenon, probably due to the inadequacy of the experimental setup - an issue that could be resolved by testing the prototype in a facility more suitable for delivering high heat fluxes, such as the solar simulator used for the receivers.

Contents

List of Figures viii

List of Tables xix

Nomenclature xxi

1 Introduction 1

1.1 Triply Periodic Minimal Surfaces (TPMS) 2

1.2 State of the art on TPMS-based cooling systems and research gap . . 7

1.3 Concentrated Solar Power plants 13

1.4 Nuclear fusion and heating of plasma 14

1.5 Aim of the thesis 16

2 Numerical characterization of TPMS 18

2.1 Fundamental equations 19

2.2 Geometric parameters 21

2.3 Hydraulic behavior 24

2.3.1 Computational methodology 26

2.3.2 Results and discussion 31

2.4 Thermal behavior 51

2.4.1 Reynolds analogy 51

2.4.2 Computational methodology 54
2.4.3 Results and discussion 57
2.5 Chapter summary 76

3 TPMS for Concentrated Solar Power 78
3.1 Design and manufacture of the receivers 79
3.2 Test of thermal performance in air 81
3.2.1 Experimental setup 81
3.2.2 Data reduction and uncertainty evaluation 83
3.2.3 Results and discussion 87
3.3 Experimental analysis in water: hydraulic performance 91
3.3.1 Experimental setup 91
3.3.2 Data reduction and uncertainty evaluation 92
3.3.3 Results and discussion 95
3.4 Comparison to expectations from simulated results 97
3.4.1 Computational methodology 98
3.4.2 Turbulence models 101
3.4.3 Results and discussion 103
3.5 Chapter summary 107

4 TPMS for fusion applications 109
4.1 DTT Electron Cyclotron Heating system 110
4.2 Design and simulations of the TPMS-based cooling systems 114
4.2.1 Computational methodology 114
4.2.2 Splitter mirror: a parametric study on TPMS thermal performance 116
4.2.3 Polarizer mirror 127
4.2.4 Launcher mirror M2 131

- 4.3 Design, manufacture and test of a prototype mirror equipped with TPMS . . . 140
  - 4.3.1 Mirror design . . . 140
  - 4.3.2 Numerical nominal performance . . . 142
  - 4.3.3 Manufacturing . . . 144
  - 4.3.4 Experimental analysis . . . 145
- 4.4 Chapter summary . . . 159

5 Conclusions and future perspectives 161

References 164

Appendix A Automatic TPMS generation 183

Appendix B Thermal periodic boundary condition in OpenFOAM 187

Appendix C Machine learning for TPMS 191

- C.1 Neural network . . . 191
- C.2 Dataset creation . . . 194
  - C.2.1 Dataset inputs . . . 196
  - C.2.2 TPMS geometry and meshing . . . 196
  - C.2.3 Thermal-hydraulic simulations . . . 197
- C.3 Neural network training and testing . . . 197
  - C.3.1 Hyperparameters tuning . . . 198
  - C.3.2 Predictive ability of the NN . . . 200

Appendix D A correlation between “solid” and “sheet” structures 203

- D.1 Viscous regime . . . 204
- D.2 Inertial regime . . . 205

List of Figures

1.1 Example of periodic cellular lattices. (a) Beam-based, (b) plate-based and (c) TPMS. 2

1.2 Solid-Gyroid: (a) both subvolumes together, (b) and (c) view of the two subvolumes separately. 6

1.3 Sheet-Gyroid: (a) the three subvolumes together, (b) the two subvolumes equal to a solid-Gyroid and (c) wall. 6

1.4 Example of a cylindrical Gyroid. 7

2.1 Analyzed TPMS geometries at 30, 40, 50, 60 and 70% porosities. a) Gyroid, b) Diamond, c) SplitP 1, d) SplitP 2. Fluid and solid domain (not simulated) are indicated by arrows. 19

2.2 Geometric parameters: (a) c value, (b) A_{wet}, (c) D_h and (d) ζ. . . . 22

2.3 Fully developed periodic boundary conditions for the inlet/outlet section. 27

2.4 Normalized velocities vs normalized average cell size. 28

2.5 Surface mesh views: (a) Gyroid, (b) Diamond, (c) SplitP1 and (d) SplitP2. 29

2.6 Normalized velocity in the flow direction for 50% porosity. (a), (c), (e), (g) $Re_{D_h} \approx 0.3$, (b), (d), (f), (h) $Re_{D_h} \approx 100$ for the Gyroid (a),(b), Diamond (c),(d), SplitP1 (e),(f) and SplitP2 (g),(h), respectively. 33

2.7 Line convolution integral of the normalized vorticity for 50% porosity. (a), (c), (e), (g) $Re_{D_h} \approx 0.3$, (b), (d), (f), (h) $Re_{D_h} \approx 100$ for the Gyroid (a),(b), Diamond (c),(d), SplitP1 (e),(f) and SplitP2 (g),(h), respectively. 34

2.8 Probability density function (PDF) of the helicity in the fluid domain. (a) Gyroid, (b) Diamond, (c) SplitP1 and (d) SplitP2. 35

2.9 Linear pressure drop vs superficial velocity. (a) Gyroid, (b) Diamond, (c) SplitP1 and (d) SplitP2. The continuous black lines refer to isolines of constant Reynolds number. 36

2.10 Comparison of TPMS results with the Ergun equation at different porosities with zooms in the inertial region: (a) 30% and (b) 60%. The relative errors for SplitP2 in (a) exceed the maximum value of the axis and are well beyond 100% for the highest Re^* value. 39

2.11 Comparison of CFD results with modified Ergun equations by Hawken et al. and Cheng et al. (a) Gyroid, (b) Diamond. 40

2.12 Normalized permeability (a) and inertial drag coefficient (b) as function of porosity, for the four TPMS topologies, using Eqs. (2.33) and (2.34). The symbols are the computed results, the line the power law fitting. 41

2.13 Comparison between the two SplitP structures at 50% porosity and $Re_{D_h} = 100$: (a) normalized cross sectional area, (b) normalized velocity in the flow direction and (c) square of the normalized velocity in the flow direction. 42

2.14 Comparison in terms of relative permeability between results from literature and present work. a) Gyroid, b) Diamond. 43

2.15 C_K (a) and S_V^2 (b) vs porosity φ for the different TPMS unit cells investigated here. 44

2.16 Relative permeability as function of porosity φ and tortuosity ζ, using Eq. (2.36). 46

2.17 Relative permeability as function of porosity φ and tortuosity ζ, using Eq. (2.37). 46

2.18 Comparison of predicted pressure drop for the unit cell with 55% porosity using the developed models and CFD results. (a) $Re_{D_h} \approx 5$, (b) $Re_{D_h} \approx 100$. 47

2.19 Geometry and boundary conditions of the pipes D = 40 mm diameter (and L = 50 mm). a) Gyroid, b) Diamond, c) SplitP1 and d) SplitP2. 49

2.20 Comparison of predicted linear pressure drops of water in the pipes at (a) $Re_{D_h} \approx 5$ and (b) $Re_{D_h} \approx 100$, using the developed models and CFD results. φ and $\varphi - \zeta$ in the legend refer to the developed power laws for the permeability, one depending only on porosity, and the other on porosity and tortuosity. KC refers to the Kozeny-Carman equation. The horizontal lines refer to the models predictions. . . . 50

2.21 Thermal-hydraulic boundary conditions. 55

2.22 Numerical grid employed for the thermal-hydraulic simulations. (a) Gyroid, (b) Diamond, (c) SplitP1, (d) SplitP2. 57

2.23 Grid convergence results for the computational mesh used in the thermal-hydraulic simulations. 59

2.24 Normalized temperature in Gyroid, 50% porosity, computed on two cut sections (parallel and normal to the flow direction, respectively). (a) $Re_{D_h} = 20$ and (b) $Re_{D_h} = 100$. 60

2.25 Normalized velocity magnitude in Gyroid, 50% porosity, computed on two cut sections (parallel and normal to the flow direction, respectively). (a) $Re_{D_h} = 20$ and (b) $Re_{D_h} = 100$. 60

2.26 Average wall shear stress on the four TPMS and porosities. (a) Gyroid, (b) Diamond, (c) SplitP1 and (d) SplitP2. 61

2.27 Linear pressure loss on the four TPMS and porosities. (a) Gyroid, (b) Diamond, (c) SplitP1 and (d) SplitP2. 62

2.28 Average wall heat flux on the four TPMS and porosities. (a) Gyroid, (b) Diamond, (c) SplitP1 and (d) SplitP2. 63

2.29 Friction coefficient of the four TPMS and porosities. (a) Gyroid, (b) Diamond, (c) SplitP1 and (d) SplitP2. 64

2.30 Friction factor of the four TPMS and porosities. (a) Gyroid, (b) Diamond, (c) SplitP1 and (d) SplitP2. 65

2.31 Comparison of the friction factor computed within the purely hydrodynamic analysis of Section 2.3 and the present section study.(a) Gyroid, (b) Diamond, (c) SplitP1 and (d) SplitP2. 67

2.32 Nusselt number of the four TPMS and porosities. (a) Gyroid, (b) Diamond, (c) SplitP1 and (d) SplitP2. T_w and q_w refer to the imposed constant T_w and q_w, respectively. 68

2.33 Stanton number of the four TPMS and porosities. (a) Gyroid, (b) Diamond, (c) SplitP1 and (d) SplitP2. T_w and q_w refer to the imposed constant T_w and q_w, respectively. 69

2.34 Reynolds analogy considering C_f (a)-(b) and f (c)-(d) for the Gyroid. (a) and (c) imposing T_w and (b) and (d) imposing q_w. 70

2.35 Reynolds analogy considering C_f (a)-(b) and f (c)-(d) for the Diamond. (a) and (c) imposing T_w and (b) and (d) imposing q_w. 70

2.36 Reynolds analogy considering C_f (a)-(b) and f (c)-(d) for the SplitP1. (a) and (c) imposing T_w and (b) and (d) imposing q_w. 71

2.37 Reynolds analogy considering C_f (a)-(b) and f (c)-(d) for the SplitP2. (a) and (c) imposing T_w and (b) and (d) imposing q_w. 71

2.38 Modified Reynolds analogy of Eq. (2.64) for Gyroid. (a) With computed f and (b) using the f correlation. 73

2.39 Modified Reynolds analogy of Eq. (2.66) for Diamond. (a) With computed f and (b) using the f correlation. 73

2.40 Modified Reynolds analogy of Eq. (2.64) for SplitP1. (a) With computed f and (b) using the f correlation. 74

2.41 Modified Reynolds analogy of Eq. (2.64) for SplitP2. (a) With computed f and (b) using the f correlation. 74

3.1 Samples geometry. (a)-(c) Drawing of the envelope and transversal cross-section views, longitudinal cross-section view with (d) the Diamond and (e) the SplitP lattice and (f) the external envelope geometry. Dimensions are in millimeters. 79

3.2 Geometric parameters: (a) c value, (b) A_{wet}, (c) D_h and (d) τ. . . . 80

3.3 The test table with the Xenon lamps. 82

3.4 Sketch of the experimental air circuit at IMDEA. (a) Positions of the thermocouples on the samples on the back and lateral side and (b) front side of mounted sample. 83

3.5 Heat flux field as in Eq. (3.1), and the position of the sample for a nominal heat flux of (a) 100 kW/m^2 and (b) 325 kW/m^2. 84

3.6 Example of the acquired data at the mass flow rate of 0.5 g/s for the sample filled with (a) Diamond and (b) SplitP. The temperature increase is referred to the inlet temperature. 88

3.7 Temperature rise with respect to room temperature in TC3 (a,b) and at the outlet (c,d) for Diamond (a,c) and SplitP (b,d). 89

3.8 Heat absorbed for different incident heat for (a) Diamond and (b) SplitP samples. 90

3.9 Thermal efficiency for (a) Diamond and (b) SplitP samples 90

3.10 Hydraulic circuit used for the tests of AISI samples: (a) photo, (b) sketch 91

3.11 Hydraulic circuit used for the tests of polymeric samples (a) and short-circuited section (b). 93

3.12 Pressure losses in the polymeric circuit and short-circuited section. . 95

3.13 Hydraulic impedance of metallic samples in dimensional form U_s vs Δp (a) and dimensionless form f vs Re_{D_h} (b). 96

3.14 Hydraulic characteristic for the Diamond (a) and the SplitP (b) sample, respectively. 97

3.15 Numerical domain of the Diamond sample, with inlet and outlet conditions highlighted (a) and mesh detail (b). 98

3.16 Grid convergence results on the normalized pressure drop within the samples: (a) Diamond and (b) SplitP. 100

3.17 Grid convergence results on the normalized pressure drop within the samples, with the addition of the coarser grid for the verification of the asymptotic range attaining: (a) Diamond and (b) SplitP. 100

3.18 CFD tools comparison on the Diamond hydraulic impedance. 104

3.19 Pressure drop vs superficial velocity in the Diamond (a) and SplitP (b) samples - comparison of experimental and numerical results. . . 105

3.20 Linear pressure drop vs superficial velocity in the Diamond (a) and SplitP (b) samples - comparison of CFD results and predictive values for the correlation of the Darcy-Forchheimer parameters (Chapter 2). 106

4.1 Schematics of a gyrotron cluster and SBTL. 110

4.2 Heat flux on the mirrors surfaces. (a) Splitter, (b) combiner, (c) polarizer, (d) M2 and (e) prototype. The colorbars refer to the heat flux values. 113

4.3 Example of the splitter mirror cut in a quarter with imposed symmetry. (a) Heat load on the reflective surface and (b) inlet and outlets locations. 115

4.4 Grid convergence analysis for the mirror models. (a) Maximum temperature increase and (b) pressure drop. 116

4.5 Sketch of the splitter with dimensions of the inlet/outlets, pivots and reflective layer. 117

4.6 Splitter mirror filled with TPMS. 118

4.7 Surface-to-fluid volume ratio versus porosity (a) and porosity times cell size (b) for the TPMS adopted. Different colors correspond to different values of L_C. Splitter mirror. 119

4.8 Computational grid for the thermal-hydraulic simulations of the splitter. Configuration GY6. 120

4.9 Mechanical constraints of the splitter mirror. 121

4.10 Computational grid for the thermo-mechanical simulations of the splitter. 121

4.11 Streamlines computed for the mirror equipped with the cooling structures (a) GX1, (b) GY2, and (c) SX1 colored by velocity. Splitter mirror. 122

4.12 Temperature field on the reflective layer of (a) GX1, (b) GY2 and (c) SY1. Splitter mirror. 123

4.13 Temperature field of the solid and fluid domain of (a) GX1, (b) GY2 and (c) SY1. Splitter mirror. 123

4.14 Maximum temperature increase on the reflective surface, computed as a function of S_V and $L_c\varphi$. Splitter mirror. 124

4.15 Thermal-hydraulic performance: (a) ΔT_{max} vs Δp plot and large localized pressure losses at inlet location for GY6. Splitter mirror. . 125

4.16 Maximum displacement versus central temperature increase for the Gyroid structures. The visual deformation is greater than the actual value for graphic purposes. Splitter mirror. 126

4.17 Polarizer geometry filled with cartesian TPMS: (a) top view of the fluid domain, (b) bottom view of the fluid domain and (c) zoom detail. Polarizer mirror. 128

4.18 Polarizer mirror. Temperature field of the cartesian lattice: (a) reflective surface and (b) solid-fluid interface. 129

4.19 Polarizer geometry filled with cylindrical TPMS: (a) fluid domain, (b) section cut and (c) zoom of the cut section. The white dotted line highlights the transition between the two cylindrical TPMS geometries.130

4.20 Temperature field of the cylindrical lattice: (a) reflective surface and (b) solid-fluid interface. Polarizer mirror. 131

4.21 Computational domain with inlet/outlet boundary conditions (a) and zoom on the inlet region (b) - single outlet configuration. The reflective layer has been removed to appreciate the internal structure. M2 mirror. 133

4.22 Velocity magnitude at 2 mm below the reflective layer, single outlet configuration: whole domain (a) and zoom in the central part (b). M2 mirror. 133

4.23 Temperature results of the single outlet configuration: (a) solid temperature and (b) fluid temperature. M2 mirror. 134

4.24 Computational domain with inlet/outlet boundary conditions (a) and zoom on the inlet region (b) - two outlets configuration. The reflective layer has been removed to appreciate the internal structure. M2 mirror. 134

4.25 Velocity magnitude at 2 mm below the reflective layer, two outlets configuration: whole domain (a) and zoom in the central part (b). M2 mirror. 135

4.26 Temperature results of the two outlets configuration: (a) solid temperature and (b) fluid temperature. M2 mirror. 135

4.27 Allio et al. proposal [147] of the M2 mirror made of only AISI 316L. (a) Geometry and (b) temperature on the reflective layer. 136

4.28 Temperature results of the two outlets configuration with Inconel 718: (a) solid temperature and (b) fluid temperature. M2 mirror. . . 136

4.29 Mechanical boundary conditions on the M2. (a) Whole mirror with the two pivots on the minor axis and (b) a mirror quarter, with the permitted displacement highlighted. 137

4.30 Von Mises stress field on the M2 mirror. (a) AISI 316L and (b) Inconel 718. 138

4.31 Deformation field normal to the reflective surface on the M2 mirror. (a) AISI 316L and (b) Inconel 718. 138

4.32 Von Mises stress distribution on TPMS-based cooling system within the M2 mirror. (a) AISI 316L and (b) Inconel 718. 139

4.33 Prototype geometry. (a) Solid domain with inlet/outlet boundary conditions, (b) cut section highlighting the varying TPMS and (c) zoom of the cut section. 141

4.34 Velocity magnitude, in a cut section 1.5 mm below the concave surface (a) and zoom in the central zone (b) – prototype mirror. . . . 143

4.35 Velocity magnitude, in a cut section normal to the minor axis (a) and zoom in the central zone (b) – prototype mirror. 143

4.36 Temperature map of (a) the solid domain and (b) the fluid domains, simulated in the nominal operating conditions at FALCON – prototype mirror. 144

4.37 3D printed prototype mirror after manufacturing and depowdering. . 145

4.38 Experimental circuit at *Frigorifero* Laboratory, in the Department of Energy of the Politecnico di Milano, used for the experimental tests of the miror prototype. (a) Picture of the hydraulic circuit connected to the sample and (b) Sketch of the equivalent circuit of the experimental setup, with also the thermal components. 146

4.39 Thermal test preparation: (a) thermocouples, (b) copper tape and (c) silicon thermal paste on the mirror surface. 147

4.40 Thermal test setup: (a) PTC resistors with highlight of the resistors ends and (b) the resistors blocked with a wood plate and inserted into a box filled with rock wool. 148

4.41 Constant heat flux imposed in the simulations reproducing the experimental tests on the prototype mirror. The red area is where the thermal load is imposed, blue where the surface is considered adiabatic. 150

4.42 Mirror surface divided into sectors for T_{HL} computation – prototype mirror. 151

4.43 Comparison of experimental and numerical results: (a) pressure losses, and Gyroid unit cells at different posorities: (b) nominal 48%, (c) 34 % and (d) 27 % – prototype mirror. 152

4.44 Measured temperature increases at the nominal voltage of 84 V. Nominal flow rates of (a) 1.7 l/min and 84 V, (b) 2.5 l/min, (c) 3.3 l/min, (d) 4.2 l/min and (e) 5 l/min – prototype mirror. 154

4.45 Measured temperature increases at the nominal voltage of 94 V. Nominal flow rates of (a) 1.7 l/min and 84 V, (b) 2.5 l/min, (c) 3.3 l/min, (d) 4.2 l/min and (e) 5 l/min – prototype mirror. 155

4.46 Measured temperature increase as function of the flow rate, at approximately the same power of 670 W. (a) *TC1-5* and (b) *TC6-10* – prototype mirror. 156

4.47 Comparison of thermal performance of the experimental and numerical results through the heat transfer coefficient. (a) $\Delta V = 84\,V$ and (b) $\Delta V = 94\,V$. The x label refers to the nominal values of flow rates – prototype mirror. 157

4.48 Comparison between simulations and experiments: measured temperature increase at 1.77 l/min and 460 - 580 W – prototype mirror. 158

4.49 Effect of the thermal conductivity on the numerical results – prototype mirror. 158

A.1 Directory tree layout of the TPMSproject showing main folders and files. 185

A.2 Comparison of time performance of the TPMSproject and MATLAB code of Gunther et al. 186

A.3 Comparison of a Gyroid cell generated with (a) MATLAB code of Gunther et al. and (b) TPMSproject. 186

B.1 Example of θ at inlet and outlet computed on the Gyroid at 50% and $Re_{D_h} = 50$. 190

C.1 Sketch of a simple neural network with 2 input neurons, one neuron in a single hidden layer and single output. 192

C.2 Automatic workflow for dataset creation 195

C.3 Example of non contiguous regions belonging to the same unit cell. Gyroid at 70% porosity. 197

C.4 TPMS dataset. (a) Reynolds number vs porosity, (b) friction factor versus Reynolds number and (c) Nusselt number vs Reynolds number. 198

C.5 Neural network sketch. φ and Re as input neurons, f and Nu as output. 199

C.6 Loss function evaluation during the training process. (a) Losses computed on the training dataset and (b) losses computed on the testing dataset. 199

C.7 Hyperparameters investigation: (a) and (c) mean error on f prediction, (b) and (d) mean error on Nu prediction. (a) and (b) batch size = 30, (c) and (d) batch size = 40. 200

C.8 Predictive ability of the neural network trained and tested on the sole Gyroid data. 201

C.9 Predictive ability of the neural network trained and tested on the dataset containing the three TPMS topologies. (a) Prediction of f and (b) prediction of Nu. 201

D.1 Comparison sheet-solid Gyroid: (a) the two subvolumes of the sheet type, (b) and (c) the two solid subvolumes. 204

D.2 Comparison sheet-solid SplitP: (a) the two subvolumes of the sheet type, (b) SplitP1 and (c) SplitP2 solid subvolumes. 206

List of Tables

2.1 Number of polyhedral cells in the 30% porosity TPMS. 28

2.2 Volume-average velocity magnitudes flowing through the 30% porosity TPMS (in cm/s) with their numerical uncertainties 31

2.3 Computed order of convergence γ for the flow within the four TPMS topologies. 31

2.4 Power law fitting parameter - K and C_F, for all TPMS and porosities 37

2.5 Power law fitting parameter - K_{rel} and C_F 40

2.6 C_K quadratic fitting coefficients 44

2.7 Fitting coefficients for $K_{rel} - \varphi - \zeta$ and $C_F - \varphi - \zeta$ relationships . . . 45

2.8 Number of hexahedral cells in the 30% porosity TPMS. 56

2.9 Relative numerical uncertainties of the considered quantities. 58

2.10 Computed orders of convergence γ for the considered quantities. . . 58

2.11 Parameters of the fitting correlations for the modified Reynolds analogy of Eqs. (2.64-2.69). 75

3.1 Design data of the planar receivers. 81

3.2 Instrumentation data for the thermal tests of the planar receivers. . . 83

3.3 Vertical positions of the testbed y_{TB} (origin at x = 0 and y = 0) associated to each nominal heat flux level q and the incident power Q_{inc} from Eq. (3.1) 85

3.4 Tests information containing the mass flow rates and heat flux levels for Diamond and SplitP samples. 86

3.5 Measuring instruments for the hydraulic circuit of laboratory *Frigorifero* at Politecnico di Milano. 92

3.6 Tested mass flow rates and corresponding superficial velocities for the metallic and polymeric Diamond samples. 93

3.7 Tested mass flow rates and corresponding superficial velocities for the metallic and polymeric SplitP samples. 94

3.8 Number of polyhedral cells in the receiver grids. 99

3.9 Numerical uncertainty due to discretization in the receiver models. . 101

3.10 Computed order of convergence γ for the different turbulent models. 101

4.1 Parameters of the microwave heat flux. 112

4.2 Mesh parameters for the grid convergence evaluation of the mirror model. 116

4.3 Geometrical parameters of the TPMS lattices adopted in the parametric study on the splitter mirror. 119

4.4 Geometrical parameters of the TPMS lattices adopted in the parametric study on the splitter mirror. 126

4.5 Measuring instruments 146

4.6 Tested conditions in the thermal experiments. 149

Nomenclature

Roman letters

a	Coefficient	
ac	Accuracy	
A	Area	(m^2)
$\mathcal{A}$	Absorption	
b	Coefficient	
B	Coefficient	
c	Coefficient	
c_p	Specific heat capacity at constant pressure	(J/(kg K))
C	Coefficient	
C_F	Inertial drag factor	
C_K	Kozeny coefficient	
D	Diameter	(m)
$\mathcal{D}$	Destruction term	
e	Eccentricity	
er	Error	
g	Coefficient	

$\mathcal{G}$	Gyrotron	
H	Heat transfer coefficient	(W/(m^{2}K))
$\mathcal{H}$	Mean curvature	
I	Electric current	(A)
$\mathscr{I}$	Beam intensity	(W/m^2)
$\mathcal{I}$	Identity tensor	
k	Turbulent kinetic energy	(m^2/s^2)
K	Permeability	(m^2)
$\mathcal{K}$	Gaussian curvature	
l	Coefficient	
L_c	TPMS cell size	(m)
$\dot{m}$	Mass flow rate	(kg/s)
$\mathcal{M}$	Surface	
n	Coefficient	
$\boldsymbol{n}$	Wall normal vector	
p	Pressure	(Pa)
$\mathcal{P}$	Production term	
q	Heat flux	(W/m^2)
Q	Power	(W)
r	Ratio	
R^2	Coefficient of determination	
$\mathcal{R}$	Shear stress tensor	(Pa)
$stdev$	Standerd deviation	

S_V	Surface to volume ratio	(m^{-1})
$\mathcal{S}$	Strain rate tensor	(1/s)
$\boldsymbol{u}$	Velocity	(m/s)
un	Uncertainty	
U	Velocity magnitude	(m/s)
$\boldsymbol{v}$	Generic vector	
$\dot{V}$	Volumetric flow rate	$(\mathrm{m}^3/\mathrm{s})$
Vol	Volume	(m^3)
$\mathcal{V}$	Average part of the velocity vector	(m/s)
w	Wave waist size	(m)
X	Modified x coordinate	(m)
Y	Modified y coordinate	(m)
Z	Modified z coordinate	(m)
x	x coordinate	(m)
y	y coordinate	(m)
z	z coordinate	(m)

Greek letters

α	Coefficient	
β	Polar angle	
γ	Computed order of convergence	
Γ	Generic variable	
δ_{ij}	Kronecker Delta	
Δh	Average mesh cell size	(m)

ΔV	Electric potential difference	(V)
ϵ	Deformation	
ε	Turbulence dissipation rate	(m^2/s^3)
ζ	Tortuosity	
η	Efficiency	
θ	Normalized temperature	
Θ	Helicity	
κ	Curvature	
λ	Thermal conductivity	(W/(mK))
μ	Dynamic viscosity	($Pa \cdot s$)
ν	Kinematic viscosity	(m^2/s)
ξ	Radius	(m)
ϖ	Vorticity	(1/s)
ρ	Density	(kg/m^3)
σ	Stress	(Pa)
ς	Turbulent coefficient	
τ_w	Wall shear stress vector	(Pa)
ϕ	Lag parameter	
φ	Porosity	
ω	Specific turbulence dissipation rate	(1/s)

Non-dimensional numbers

C_f	Friction coefficient
f	Friction factor

Nu	Nusselt number
Re	Reynolds number
St	Stanton number

Operators

$\langle\cdot\rangle_V$	Average over volume
$\langle\cdot\rangle_{A_{wet}}$	Average over wet area
$\langle\cdot\rangle_{L_c}$	Average over L_c
$\mathscr{L}(\cdot)$	Least-square function
$\mathscr{S}(\cdot)$	Shape operator
$tr(\cdot)$	Trace of a tensor

Subscripts

∞	Extrapolation value
abs	Absorbed
act	Activation
BP	Burke-Plummer
$cell$	TPMS cell
CF	Relative to the C_F
e	Electric
F	Inertial drag factor
h	Hydraulic
i	i-th grid
in	Inlet
inc	Incident

K	Relative to the K_{rel}
KC	Kozeny-Carman
MW	Microwave
num	Numerical
$o-i$	Between outlet and inlet
p	Particle
rel	Relative
rev	Reversed
s	Superficial
t	Turbulent
th	Thermal
tot	Total
TC	Thermocouple
VM	Von Mises
w	Wall
21	Between the finest and the second finest mesh
32	Between the second finest and the third finest mesh

Number sets

$\mathbb{R}$	Real numbers

Superscripts

$'$	Fluctuating part
21	Between the finest and the second finest mesh
t	Turbulent

Abbreviations and acronyms

ADS	Accelerator Driven Subcritical
CFD	Computational Fluid Dynamics
CFETR	China Fusion Engineering Test Reactor
CI	Confindence Interval
CPC	Compound Parabolic Concentrator
CSP	Concentrated Solar Power
CW	Continuous Wave
DTT	Divertor Tokamak Test
EAST	Experimental Advanced Superconducting Tokamak
EB	Elliptic Blending
ECH	Electron Cyclotron Heating
ELU	Exponential Linear Unit
EM	Electromagnetic
EPFL	Ecole Polytechnique Fédérale de Lausanne
FE	Finite Element
FPC	Flat Plate Collector
GCI	Grid Convergence Index
HPC	High Performance Computing
HTF	Heat Transfer Fluid
HX	Heat Exchanger
ITER	International Thermonuclear Experimental Reactor
LBE	Lead-bismuth eutectic

LES	Large Eddy Simulation
LIC	Line Integral Convolution
LPBF	Laser Powder Bed Fusion
MB	Multi-Beam
mf	Mass flow meter
MHD	Magneto-hydrodynamics
MJF	Multi Jet Fusion
ML	Machine Learning
MSE	Mean Squared Error
MW	Microwave
PCHE	Printed Circuit Heat-Exchanger
PDF	Probability Density Function
PFC	Plasma Facing Component
PHE	Plate Heat-Exchanger
PID	Proportional integral derivative
PS	Polymeric Sample
PT	Pressure Transducer
PTC	Parabolic Trough Collector
PV	Photovoltaic
RANS	Reynolds Averaged Navier Stokes
ReLU	Rectified Linear Unit
REV	Representative Elementary Volume
RF	Radio-frequency

RSM	Reynolds Stress Model
SB	Single-Beam
SC	Simple Cubic
SHM	snappyHexMesh
SIMPLE	Semi-Implicit Method for Pressure-Linked Equations
SLA	Stereolithography
SLM	Selective Laser Melting
SLS	Selective Laser Sintering
SPC	Swiss Plasma Center
SST	Shear Stress Transport
TB	Testbed
TES	Thermal Energy Storage
THB	Tokamak Hall Building
TL	Transmission Line
TPMS	Triply Periodic Minimal Surfaces

Chapter 1

Introduction

Effective thermal control is crucial for increasing the operating efficiency and reliability of components and systems in numerous engineering sectors, particularly in the energy industry, but also in fields such as aerospace, electronics, and automotive. In power generation plants, advanced heat exchange assumes a key role in increasing the temperatures of operating fluids, thereby boosting the efficiency of thermodynamic cycles. Achieving efficient heat removal in such contexts is essential not only for maximizing energy conversion efficiency but also for ensuring the structural and operational resilience of materials and components exposed to severe thermal gradients. In addition to the power generation sector, which continues to play a critical role in today energy-intensive society, high-performance thermal control is crucial in many components across all engineering sectors to maintain operational performance. It underpins the reliable function of compact electronic devices, supports the design of lightweight and high-efficiency automotive systems, and enables the thermal stability of aerospace components operating under fluctuating environmental and mechanical loads. In all these cases, maintaining precise temperature regulation is necessary for preventing performance degradation, reducing the risk of material fatigue, and prolonging operational lifespan. Among the energy sectors that require continuous improvement in the operational performance of components are nuclear power, both the more mature fission technology and the newer fusion technology, energy storage, and solar power generation plants.

Addressing the thermal management challenges of these components necessitates the development of advanced cooling frameworks capable of efficiently removing high heat fluxes from compact, intricate geometries while minimizing pressure drop and preserving mechanical strength. Additive Manufacturing (AM) has emerged as a transformative approach in this field, facilitating the fabrication of complex cooling architectures — such as internal channels with variable porosity — that would be impossible or prohibitively expensive to fabricate using conventional manufacturing methods [1]. Periodic cellular lattices emerge among the most promising AM-enabled cooling strategies. These periodic lattices are mainly divided into three categories: beam-based, plate-based and Triply Periodic Minimal Surfaces (TPMS) [2]. Beam (Fig. 1.1a) and plate-based (Fig. 1.1b) structures are generated by the periodic repetition of specific combinations of beams or plates, while TPMS (Fig. 1.1c) are combination of trigonometric functions in 3D. TPMS have smooth structures without sharp edges that can significantly increase the heat transfer surfaces while still theoretically maintaining low pressure drops.

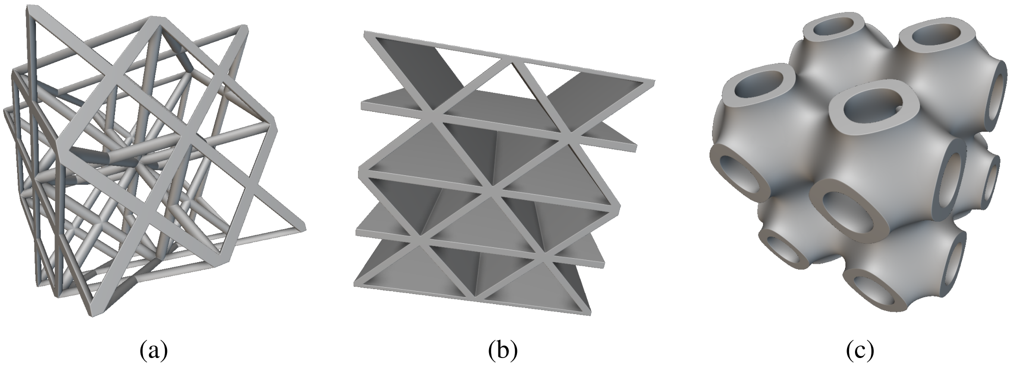
(a) (b) (c)

Fig. 1.1 Example of periodic cellular lattices. (a) Beam-based, (b) plate-based and (c) TPMS.

In this chapter, a general introduction on TPMS is reported in Section 1.1, then the state of the art on the use of TPMS for cooling applications is presented in Section 1.2, with the research gap. A general context is given in Sections 1.3-1.4 on two sectors that could benefit from the use of TPMS, notably Concentrated Solar Power and components in nuclear fusion machines. In Section 1.5, the aim of the thesis and its organization is described.

1.1 Triply Periodic Minimal Surfaces (TPMS)

A minimal surface is a surface that locally minimizes its area for a given boundary: similarly to soap films stretching across wireframes. It is defined as a surface with zero mean curvature at every point. That means the surface is equally curved in opposite directions, resulting in no net bending—like a perfect balance between opposing curves [3].

Mathematically, a minimal surface can be described as follows. Considering a surface $\mathcal{M} \in \mathbb{R}^3$ and being $\mathbf{v}$ a tangent vector of $\mathcal{M}$, the normal curvature of $\mathcal{M}$ in the direction of $\mathbf{v}$ is defined in Eq. 1.1.

$$\kappa(\mathbf{v}) = \mathscr{S}(\mathbf{v}) \cdot \mathbf{v} \tag{1.1}$$

$\mathscr{S}(\mathbf{v})$ is the shape operator, defined as the negative derivative of the unit normal vector field of a surface [4]. In each point of the surface, the maximum and minimum curvatures κ_1 and κ_2 are called the principal curvatures. The mean curvature $\mathcal{H}$ is defined in Eq. (1.2) as the average of the principal curvatures.

$$\mathcal{H} = \frac{1}{2}(\kappa_1 + \kappa_2) \tag{1.2}$$

The mean curvature of a minimal surface is null in any point of the surface, therefore $\kappa_1 = -\kappa_2$, and the Gaussian curvature $\mathcal{K} = \kappa_1 \kappa_2 \leq 0$, indicating that $\mathcal{M}$ is a planar or saddle surface.

A *Triply Periodic* Minimal Surface (TPMS) is a minimal surface that is translationally invariant in three directions.

The term TPMS generally refers to closed geometries with triply periodic minimal surfaces. The first type of TPMS was discovered in the late 19th century by Neovius [5] but several topologies of TPMS can be defined as combination of trigonometric functions in the 3D space. Indeed, TPMS are characterized by an analytical equation $fun(x, y, z)$, such as Eq. (1.3), describing the Gyroid TPMS. The most common types of topologies are presented through their equations in Eqs. (1.4-1.10): Diamond, SplitP, Lidinoid, IWP, FKS, Neovius, respectively.

$$fun_{Gyroid}(x, y, z) = sin(X)cos(Y) + sin(Y)cos(Z) + sin(Z)cos(X) \tag{1.3}$$

$$\begin{aligned} fun_{Diamond}(x,y,z) =& sin(X)sin(Y)sin(Z)+sin(X)cos(Y)cos(Z) \\ &+cos(X)sin(Y)cos(Z)+cos(X)cos(Y)sin(Z) \end{aligned} \tag{1.4}$$

$$\begin{aligned} &fun_{SplitP}(x,y,z) = \\ &1.1(sin(2X)sin(Z)cos(Y)+sin(2Y)sin(X)cos(Z)+sin(2Z)sin(Y)cos(X)) \\ &-0.2(cos(2X)cos(2Y)+cos(2Y)cos(2Z)+cos(2Z)cos(2X)) \\ &-0.4(cos(2X)cos(2Y)cos(2Z)) \end{aligned} \tag{1.5}$$

$$fun_{Primitive}(x,y,z) = cos(X)+cos(Y)+cos(Z) \tag{1.6}$$

$$\begin{aligned} &fun_{Lidinoid}(x,y,z) = \\ &sin(2X)cos(Y)sin(Z)+sin(2Y)cos(Z)sin(X)+sin(2Z)cos(X)sin(Y) \\ &-cos(2X)cos(2Y)-cos(2Y)cos(2Z)-cos(2Z)cos(2X)+0.3 \end{aligned} \tag{1.7}$$

$$\begin{aligned} &fun_{IWP}(x,y,z) = \\ &cos(X)cos(Y)+cos(Y)cos(Z)+cos(Z)cos(X)-sin(X)sin(Y)sin(Z) \end{aligned} \tag{1.8}$$

$$\begin{aligned} &fun_{FKS}(x,y,z) = \\ &cos(2X)sin(Y)cos(Z)+cos(X)cos(2Y)sin(Z)+sin(X)cos(Y)cos(2Z) \end{aligned} \tag{1.9}$$

$$\begin{aligned} &fun_{Neovius}(x,y,z) = \\ &3\,(cos(X)+cos(Y)+cos(Z))+4cos(X)cos(Y)cos(Z) \end{aligned} \tag{1.10}$$

X, Y and Z are defined in Eq. 1.11. The parameter L_c controls the cell size.

$$
\begin{aligned}
X &= \frac{2\pi x}{L_c} \\
Y &= \frac{2\pi y}{L_c} \\
Z &= \frac{2\pi z}{L_c}
\end{aligned}
\tag{1.11}
$$

In the literature, the characteristic equation for the Diamond is also found in the form of Eq. 1.12, which can be derived from Eq. 1.4 through a translation of the coordinate axes.

$$
fun_{Diamond*}(X,Y,Z) = cos(X)cos(Y)cos(Z) - sin(X)sin(Y)sin(Z) \tag{1.12}
$$

The isosurface $fun(x,y,z) = 0$ cuts a certain cubic volume of length L_c in two or three subvolumes, that could (as for the Gyroid and Diamond) or could not (as for the SplitP and Lidinoid) be equivalent. Offsetting the isosurface of a certain value c translates the surface and creates two (or three) different subvolumes, each of them called *solid*-TPMS. When two subvolumes are created, one subvolume can be used as a fluid channel, and the other as solid material (Fig. 1.2). If the isosurface is offset in both normal direction of the same value c, a wall volume is created (Fig. 1.3a) in addition to the two (or three) subvolumes (Figs. 1.3b-1.3c), and the geometry is labeled as *sheet*-TPMS. In this case, the two subvolumes can be employed as fluid within two channels, very useful for heat-exchangers. By varying the isovalue c, different porosity levels can be achieved, producing structures that are fairly dissimilar even within the same topology, which may therefore have significantly different thermal and hydraulic characteristics.

The above characteristic equations are defined in the cartesian space, but they can be transformed to create TPMS conformal to any surface shape. For example, L_c or c could be defined as varying with the position, to achieve a variable size or porosity of the unit cell. Moreover, a coordinate transformation can be performed to obtain for instance a cylindrical lattice. In this case, the Gyroid characteristic equation must be transformed as follows: Eq. (1.3) becomes Eq. (1.13), where ξ is the radius and β the polar angle, ranging from 0 to 2π.

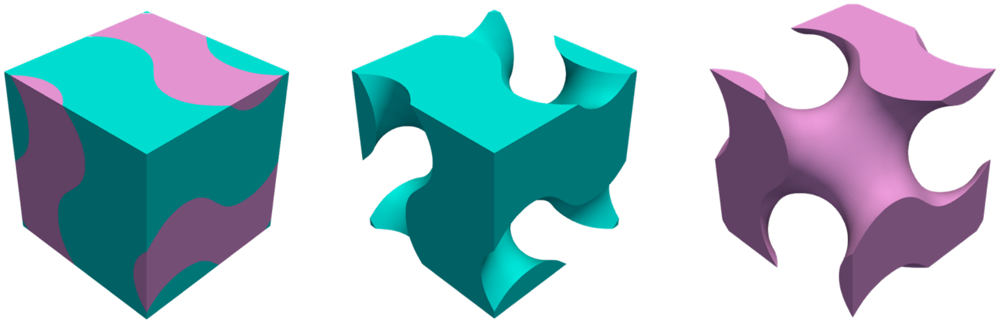

(a) (b) (c)

Fig. 1.2 Solid-Gyroid: (a) both subvolumes together, (b) and (c) view of the two subvolumes separately.

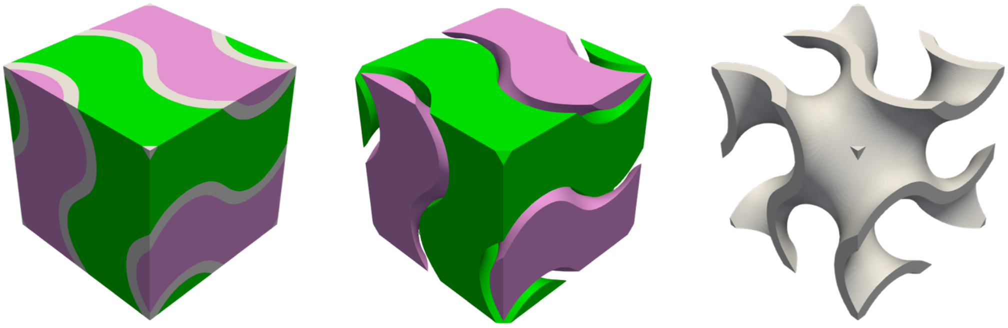

(a) (b) (c)

Fig. 1.3 Sheet-Gyroid: (a) the three subvolumes together, (b) the two subvolumes equal to a solid-Gyroid and (c) wall.

$$\begin{aligned} fun(\xi,\beta,z) &= sin\left(\frac{2\pi\xi}{L_\xi}\right)cos\left(\frac{2\pi\beta}{L_\beta}\right)+ \\ &+sin\left(\frac{2\pi\beta}{L_\beta}\right)cos\left(\frac{2\pi z}{L_z}\right)+sin\left(\frac{2\pi z}{L_z}\right)cos\left(\frac{2\pi\xi}{L_\xi}\right) \end{aligned} \tag{1.13}$$

Conversely to the cartesian lattice which is exactly periodic in the three principal directions, the cylindrical lattice has an increasing azimuthal cell size so to maintain constant the number of TPMS cells in the polar direction with increasing radius, as it might be remarked in Fig. 1.4.

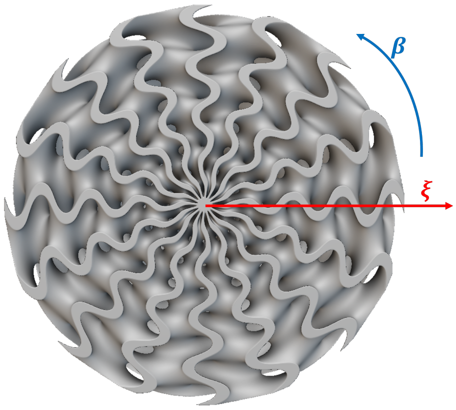

Fig. 1.4 Example of a cylindrical Gyroid.

1.2 State of the art on TPMS-based cooling systems and research gap

Research on TPMS has been rapidly growing [6–8] in recent years. On one hand, TPMS are studied from a mainly analytical point of view in order to characterize them, first hydraulically and then thermally. On the other hand, much research is focused on designing new TPMS-based cooling systems or heat-exchangers to be compared with more traditional structures, without performing extensive parametric analyses on geometric variables or topologies.

Concerning theoretical studies, the first step in characterizing a structure is to delve into hydraulic, even prior to thermal, behavior, which was extensively investigated by many researchers, most of them treating TPMS as structured porous media, so that they can be modeled as homogeneous and continuous media. This approach should be based on the use of a Representative Elementary Volume [9] that can be generalized. Several works focused on the sole viscous (Darcian) regime, in order to evaluate the permeability of TPMS and its variation with porosity, such as Montazerian et al. [10] in 2017, who studied both the radial and longitudinal permeabilities and managed to fit their CFD results using a power law and the Kozeny-Carman relationship for the longitudinal permeability of solid-Gyroid, IWP, Primitive, and Diamond TPMS. They computed the Kozeny-Carman law coefficient as a quadratic function of porosity. Zhianmanesh et al. [11] in 2019 investigated the permeability of different TPMS with both uniform and variable porosity, including solid-Gyroid. For uniform porosity, they developed power law correlations for each

TPMS, with distinct coefficients and exponents. Lu et al. [12] in 2020 performed a regression study on solid-Gyroid, Diamond, Primitive, FKS, and FRD, to compute different porosity-permeability relations specific to each topology, such as power law, exponential law, or polynomial law. They also used the Kozeny-Carman relation for permeability without tuning the coefficient, finding significant discrepancies with the CFD results. Asbai-Ghoudan et al. [13] in 2021 studied the sheet-FKS, Gyroid, and Primitive at a single Reynolds number of one to correlate permeability with porosity (ranging from 50% to 90%) and pore size, developing a model encompassing all the TPMS they investigated. However, the pore size they used is not an easily quantifiable parameter and cannot be known a priori for a certain TPMS structure at a given porosity.

However, the Darcian regime is limited to extremely small Reynolds numbers, which are normally of little use in industrial applications. Thus, TPMS behavior has also been investigated in the transition from viscous to inertial regime, by means of the Darcy-Fochheimer equation. In 2023, Piedra et al. [14] analyzed the sheet-Primitive and IWP TPMS through a CFD study and found that the flow within these structures can be accurately described by Darcy-Forchheimer law. They compared the predictions of their model with the CFD simulations and found mean errors of 5-11%. Though, their results cannot be easily generalized to a porous medium, as they studied a single TPMS unit cell (without using periodic conditions) within in a long channel and they did not explore geometries beyond those used for the regression analysis. In the same year, Ahmed and Bottaro [15] focused on six different sheet-TPMS (Gyroid, IWP, Primitive, SplitP, FKS, and Neovius) at various porosities. They analytically investigated the transition from Darcy regime by examining changes in permeability but did not attempt to relate it to any geometric parameters. The Ergun equation has also been used as an alternative to the Darcy-Forchheimer equation in some studies, as for instance by Hawken et al. [16] in 2023, who compared experimental results to several theoretical friction correlations and developed their own correlation by fitting Ergun coefficients. Their study focused solely on the solid-Diamond structure, investigating different porosities within the Reynolds number range 60-600. Similarly but from a numerical perspective, Cheng et al. [17] found that a different fit was required for each TPMS in the Ergun equation, with distinct coefficients for each topology investigated. Their study focused on solid-Gyroid, Diamond, IWP and Primitive with Reynolds numbers between 10 and 130. The simulation setup of Cheng et al. [17] is, however, questionable: they simulated an array of six TPMS cells and applied wall boundary conditions to the external boundaries (which are periodic) and neither they tried to verify the fully developed conditions within the TPMS.

For what regards studies on the thermal behavior of TPMS, The primary effort has been the development of correlations for the Nusselt number. However, in most cases, parametric studies are not performed, and the results are usually not easily generalizable, also due to the non clear definition of dimensionless numbers. For example Cheng et al. [17] also investigated the thermal behavior of TPMS, and developed a correlation for the Nusselt number with a power law dependence on Reynolds, quadratic dependence on porosity and Prandtl number to the power of one third. However, they did not specify the formula for calculating the Nusselt number and they did not use the pore velocity (usually widely utilized in porous media domain) for velocity scaling of the Reynolds number, but the superficial velocity, which does not account for the actual porosity of a porous structure. Similarly, Wang et al in 2023 [18] and Zhang et al. in 2025 [19], tried to insert the porosity (that Wang et al. called the volume share) within their correlations for the Nusselt number [18] and the Colburn-J factor [19], using a parabolic dependence on the porosity and a power law dependence on the Reynolds number. Wang et al. [18] numerically studied four solid-TPMS: IWP, Primitive, Neovius and FKS. Their results were valid for Reynolds numbers within 1000 and 21000, depending on the TPMS type. They investigated three porosity values, 30%, 50% and 70%. This correlation could be one of the most attractive in the literature; however, Wang et al. did not mention the standard deviation of their fits or other parameters of correlation quality, and their analyzed structures are not among the most interesting from the point of view of thermal enhancement, i.e. Primitive, IWP and Neovius. Zhang et al. [19] numerically investigated solid-Gyroid, FKS and IWP at different porosity between 50% to 80% at Reynolds number between 1000 and 5000 and they computed low average errors on the correlations. However, their definition of the Reynolds number and friction factor was based on the superficial velocity, which does not take into account the porosity of the structure. In 2024, Dube Kerme et al. [20] experimentally studied in water three sheet-Gyroid with different cell sizes (15, 25 and 32 mm) and porosities (75, 85 and 90%) and Reynolds number ranging between 240 and 700. They found a root square relationship between the Reynolds and the Nusselt numbers. Again, their research was not very general as the TPMS cell size was large compared to the sample dimensions (37.5 x 37.5 x 12.7 mm).

As for what concerns real applications of TPMS, many researchers designed heat-exchangers or cooling systems filled with TPMS for a wide range of fields, and some of them also tried to develop their own models for the thermal efficiency of these lattice structures. For example, in 2021 Li et al. [21] explored different TPMS topologies as heat-exchangers for supercritical carbon dioxide cooling, demonstrating a substantial increase in the mean heat transfer coefficient compared to a Printed Circuit Heat Exchanger (PCHE). In the same year Attarzadeh et al. [22] simulated in laminar regime a sheet-Diamond for electronic chip cooling, by varying porosity over four values. In 2022 Khalil et al. [23] designed and printed in AlSi10Mg three 80% TPMS-based heat sinks, solid-Diamond and solid-Gyroid and sheet-Gyroid, with unit size of 10 mm. They hydraulically tested the structures in air and compared the experimental results with the numerical simulations, finding good agreement. They then used the numerical model to compute the heat transfer capability of the TPMS and developed a power-law correlation for the Nusselt number as function of Reynolds and Prandtl, without considering any change in the geometric parameters. Also in 2022, Iyer et al. [24] numerically compared seven TPMS topologies (among which Gyroid and Diamond) for heat-exchanger applications, by considering an infinitesimal wall thickness between the two fluid channels, which is physically unfeasible. They also developed correlations for the Nusselt number for each TPMS, in a Dittus-Boelter style, without considering varying porosity.

In 2023, Wang et al. [25] numerically compared two HX based on sheet-IWP and sheet-Primitive TPMS to a PCHE, using only three porosity values, for the utilization in an accelerator-driven subcritical system (ADS) with Lead-bismuth eutectic (LBE) coolant. They found that TPMS-based HX had two to three times the heat transfer rate of the PCHE, with only half of its volume. Gao et al. [26] compared from numerical and experimental perspectives a 5 mm cell size Diamond-based HX and a Plate Heat-Exchanger (PHE). They printed the TPMS HX in both AISI 316L and Copper. They used water-to-water with Reynolds number below 1000. They found similar fluid outlet temperatures between simulations and tests, but not always within the uncertainty ranges, and promising improvements in the heat transfer rate with respect to the PHE. However, they only used one wall thickness, thus one porosity value. Dong Liang et al. [27] designed a 82% porosity HX using Primitive, Gyroid and Diamond, between 2000 and 9000 Reynolds numbers. They discovered that heat transfer performance of the Diamond and Gyroid HXs was comparable with other 3D-printed heat exchangers, such as lung-inspired.

In 2024, Barakat et al. [28] compared four cartesian sheet-TPMS (Gyroid, Diamond, SlitP, Lidinoid) with different cylindrical sheet-Gyroid structures, by varying the number of repetitions along the azimuthal and radial directions, in heat sink applications. However, they only focused on one porosity per structure, without effectively analyzing a wide range of parameters. In this case, Reynolds numbers were between 100 and 1200. They assessed the validity of their thermal numerical model by testing the structures in air, but they were not able for all cases to find agreement between numerical and experimental values. Kruzel et al. [29] designed and printed in AISI 316L a HX filled with Gyroid with a single porosity value. They correlated the Nusselt numbers to the Reynolds, Prandtl and Grashof numbers (even if the tests were explicitly in forced convection), using a Dittus-Boelter-like relationship. In 2025, Yijin Zhang et al. [30] numerically and experimentally investigated the use of four sheet-TPMS topologies (Primitive, IWP, Gyroid and Diamond) as heat-exchangers between 3000 and 9000 Reynolds numbers, generating the structures with both cartesian and cylindrical periodicity. They found that the cylindrical TPMS had improved performance with respect to the cartesian geometry, but only used one porosity value. Balderrama Prieto et al. [31] designed a self-heated hexagonal assembly filled with sheet-Gyroid to model nuclear fuel assembly and simulated and tested it (using Ohmic heating). They only investigated one porosity value within the Reynolds number range 700 - 3500. Zhihui Zhang et al. [32] numerically compared 70% porosity sheet-Gyroid, IWP, FKS and Primitive versus pin-fins heat sinks, at very large Reynolds numbers, 10000 to 50000. Su et al. [33] conceived a compact and modular air-to-air heat-exchanger filled with sheet-Gyroid and Diamond. Again, only one porosity of 81% and cell size of 5 mm was studied. They experimentally found Nusselt numbers three or four times larger than in PCHE for Reynolds number values between 200 and 800. They observed an increasing numerical-experimental discrepancy in the pressure drop and heat exchange effectiveness coefficient, up to 67% for hydraulic and 4.2% for thermal results, that they attributed to roughness. Zou et al. [34] designed a water-to-water Diamond heat-exchanger with cell size of 23 mm and fitted the hydraulic and thermal results in terms of friction factor and Nusselt numbers in their Reynolds numbers range up to 50000. They developed two power-law correlations, depending on Reynolds (and also Prandtl number for Nusselt), but did not attempt to investigate different design parameters, such as the porosity or cell size, neither thought that the geometry of the heat exchanger could influence the results. They found good agreement between numerical and experimental results. Dutkowsi et al. printed in AISI 316L and tested a Gyroid-based water-to-water HX with cell size of 20 mm. The studied Reynolds numbers range was 250-1200. They investigated the difference behavior of the cold and hot sides of the HX. Reynolds et al. [35] printed the same Gyroid-based HX at 72% porosity in five materials, aluminum, sintered alumica ceramic, cured resin, alumina and nylon to experimentally characterize the different heat performance of the materials. They also used two different HX configurations, water-to-water and air-to-water. However, they did not try any variation on the structure geometry. Also in 2025, based on numerical results of Reynolds numbers between 5000 and 50000, Brambati et al. [36] strove to combine three sheet-topologies (Diamond, Primitive and Gyroid), cell sizes, porosities and working fluids into a single correlation, which nevertheless had errors larger than 20% in many cases. Moreover, their method to compute the Nusselt number from local heat transfer coefficient is not feasible for real cases, where the distribution of local parameters such as fluid bulk temperature, wall temperature and heat flux cannot be directly measured, but only integral values or point values can be measured.

HX designs were also proposed with modified TPMS, with non-uniform cell sizes in the three directions. In 2024 G. Yan et al. [37] proposed a stretched-Diamond and in 2025 K. Yan et al. [38, 39] a stretched-Gyroid. G. Yan et al. [37] investigated three different stretched configurations by starting from the same porosity Gyroid cell, and developed friction factor and Nusselt number correlations for each configurations, based only on Reynolds (and Prandtl for Nusselt). K. Yan et al. [38, 39], on the other hand, varied the cell sizes and stretching for a total of five configurations and developed a unified correlation for the Nusselt number and friction factor accounting also for an aspect ratio of the TPMS cell.

As mentioned above, between all those studies that focused on applications of TPMS to real cases, some researchers also attempted to fit their experimental or numerical results to power-law correlations for the friction factor or Nusselt number, but most of them did not take into account the porosity or other geometrical parameters [23, 29, 24, 34, 40, 41]. Few of them also tried to incorporate geometrical parameters, such as the aspect ratio of the stretched cells, as previously stated [39], but they used an insufficient number of cases to create a significant database.

This literature review showed that numerous studies have been conducted on TPMS, seeking to explore several aspects from both a phenomenological and analytical perspective. However, frequently the assumptions on which they are based are weak, and the results are scarcely generalizable or repeatable, partly due to insufficient detail in the descriptions or inconsistent definitions of dimensionless numbers. For example, in most cases the tests were performed on structures with few TPMS cells, where the effect of the walls is not negligible compared to the TPMS themselves. Simulations are built with questionable boundary conditions (as the use of symmetry instead of periodicity on the periodic faces of the TPMS) or with an insufficient number of TPMS cells to ensure that inlet effects were not present. Furthermore, although the use of four or five stacked TPMS cells is very common in these studies, any researchers did not actually evaluate the validity of the fully developed hypothesis. There is a lack of clear and detailed systematic analysis that starts from fluid dynamics, seeking to investigate the behavior of different TPMS and then subsequently studying the thermal characteristics in light of the hydraulic findings.

Nonetheless, at the same time, the aforementioned research encourages the investigation of TPMS in other innovative fields where thermal management plays a vital role. The promising results obtained not only for traditional multipurpose heat-exchangers but also for more specialized applications — such as supercritical carbon dioxide HX [21], nuclear fuel assemblies [31], and liquid metal HX [25] — further highlight their potential for broader implementation, as for instance nuclear fusion field or advanced solar applications.

1.3 Concentrated Solar Power plants

Within the spectrum of solar technologies, Concentrated Solar Power (CSP) emerges as a particularly promising solution for large-scale electricity generation [42, 43]. CSP technology combines a traditional thermal cycle for electricity generation to a receiver/absorber where sunlight is concentrated by means of mirrors or concentrators [44–46]. CSP technology works by concentrating sunlight onto a receiver that absorbs the heat through a Heat Transfer Fluid (HTF) which is then coupled with a traditional power cycle. Unlike photovoltaic (PV) systems, energy production from CSP plants possesses significantly greater thermal inertia, as they can straightforwardly be combined to a thermal storage system [43, 47]. Indeed, Thermal Energy Storage

(TES) can, for instance, be constituted directly by the coolant fluid in CSP applications. This allows CSP to reach quite larger availability factors [47, 48].

The receiver is the heart of every CSP system, a critical component that acts as a heat exchanger, intercepting concentrated sunlight and converting it into useful thermal energy for thermodynamic cycles [49, 50]. The receiver design is fundamental to the overall efficiency and operational lifespan of the power plant. While *tubular receivers* are the most common in current commercial applications, they face challenges related to high, non-uniform temperatures and thermal stresses induced by highly concentrated solar fluxes [49, 51]. Tubular receivers are simple structures in which solar energy is directly absorbed by the solid tubes and transmitted to the HTF. To overcome these limitations and enhance performance, *volumetric receivers* have emerged as a promising alternative [50, 52, 53].

Volumetric receivers consist of a porous material absorbing concentrated solar radiation within its volume [52, 54, 55], rather than solely on its external surface. The absorbed heat is then transferred to the HTF as in the tubular receivers. Volumetric receivers allow larger solar fluxes to be absorbed and they can achieve very high working fluid outlet temperatures, up to 700°C - 1000°C when air is used [52]. Ceramic materials like silicon carbide (SiC) and various porous foams have been extensively studied for these applications [52, 53, 56, 57]. However, the effective design of these materials presents challenges, such as flow homogeneity and minimization of thermal stresses caused by non-uniform flux distribution, which could lead to "hot spots" and structural damage.

In this context, periodic lattice structures [52] and in particular TPMS [56, 58] represent an innovative frontier for volumetric receiver design. TPMS geometries offer a more ordered and efficient thermal network compared to traditional metal foams [56, 59]. These structures might not only improve thermal conductivity but also enhance mechanical properties [56].

1.4 Nuclear fusion and heating of plasma

Nuclear fusion energy harnesses the fusion of light atomic nuclei within an extremely hot and ionized gas, the plasma. The energy released from fusion reactions should then be extracted and converted to electrical power through traditional thermodynamic cycles. Among the possible fusion fuels, the combination of the two hydrogen isotopes deuterium-tritium is the most promising due to its highest fusion reaction cross-section at relatively low temperatures compared to the other fuel combinations such as deuterium-deuterium or deuterium-helium-3. Fusion machines still face many challenges [60], including development of suitable Plasma Facing Components (PFC) as the plasma is expected to reach temperatures on the order of 100 million degrees; further development of superconducting magnets to maintain the very high magnetic fields for the plasma confinement; power exhaust management; tritium breeding; and the achievement of ignition. Ignition occurs when the produced energy within the plasma (in the form of helium-4, or alpha particles) compensates the energy required to initiate the fusion reaction.

To reach ignition conditions in magnetic-confined devices like Tokamaks or Stellarators, including ITER (International Thermonuclear Experimental Reactor), DTT (Divertor Tokamak Test), EAST (Experimental Advanced Superconducting Tokamak), W7-X (Wendelstein 7-X), KSTAR or CFETR (China Fusion Engineering Test Reactor), external heating of the plasma is essential, at least in the beginning phases. Initially, Ohmic heating — caused by plasma electrical resistance — helps raising the plasma temperature. However, as the plasma heats up, its electrical resistivity decreases significantly, making Ohmic heating ineffective. The two main methods to elevate plasma temperature to ignition levels include injecting high-energy neutral beams and resonantly absorbing radio frequency electromagnetic waves. The latter can be achieved through waves near the ion cyclotron or electron cyclotron.

The Electron Cyclotron Heating (ECH) system consists of sources of electromagnetic (EM) waves, which are then transmitted and launched into the plasma to heat it up. In addition to the heating and current drive purpose, the ECH system also provides other functions [61–65] that are critical to the operation of the fusion reactor, due to its ability to inject power into specific locations of the plasma, such as:

- Assistance to ramp-up and ramp-down of the plasma current
- Magneto-hydrodynamic (MHD) control via plasma instabilities suppression
- Wall cleaning and mitigation of impurity within the plasma

The EM sources are gyrotron devices [66, 67] producing radio-frequency (RF) beams with a frequency close to the gyro-frequency of the plasma electrons. The

EM beams is then transmitted through a Transmission Line (TL) and then launched into the plasma by the antennae [68–72]. The TL concept may either consist of corrugated waveguides, as in ITER [73], EAST [74] and CFETR [75], or be based on Gaussian beam propagation via reflecting mirrors, as in W7X [76, 77] and DTT [78]. All the components of the ECH systems, as the gyrotron cavity and the reflecting mirrors, require enhanced active cooling to work, due to the very large heat loads they must sustain during their operations while avoiding substantial deformations. Thus, innovative heat removal systems designed with TPMS could be beneficial.

1.5 Aim of the thesis

The scope of the present thesis is to conduct an in-deep analysis on three TPMS topologies from hydraulic and thermal perspectives, beginning with a more analytical study to investigate the fundamental phenomena responsible for momentum and energy transfer in TPMS and to develop concentrated-parameters frameworks employable in place of large and computationally expensive pore-scale simulations. This thesis also aims at proposing TPMS structures as advanced cooling systems in innovative technology fields where effective heat removal is required, in particular Concentrated Solar Power and nuclear fusion applications. The three TPMS extensively studied in this work - Gyroid, Diamond, and SplitP — were chosen for the goal of studying both widely recognized structures and the less explored (SplitP) geometry. In the first analytical part the TPMS studied are restricted to solid-types, as the sheet-types are topologically equivalent to the solid-types, thus their analysis should first be based on a thorough understanding of solid topologies. The analytical study on the hydraulic and thermal characteristics of TPMS is restricted to low Reynolds numbers in the viscous and inertial regime, as the starting point for fluid dynamics analysis must always be the investigation of the most basic cases, before moving on to more complex ones, such as turbulence. In the applications of TPMS in CSP and fusion components, both sheet and solid frameworks are analyzed, and also larger Reynolds number regime, to comply with the use of water as coolant in such complex heat removal systems.

The thesis is thus structured as following:

- Chapter 2 is devoted to the systematic analysis of solid-TPMS from a numerical point of view to investigate their hydraulic and thermal behavior, seeking to study the applicability of models previously observed in the literature, such as the equivalent porous medium model and correlations for heat exchange capacities
- In Chapter 3 two TPMS topologies are proposed for CSP cooling applications
- Chapter 4 investigates the use of TPMS in the cooling of mirrors for reflecting microwave beams in fusion devices
- The main conclusions of the thesis are drawn in Chapter 5, with possible future perspectives of the study

Chapter 2

Numerical characterization of different TPMS lattices at low Reynolds numbers

This chapter presents a numerical investigation of the thermal-hydraulic behavior of TPMS at low Reynolds numbers, considering a single cell as a computational unit. First, some brief remarks are given on the transport equations that will be used for modeling the thermal-hydraulic fluid flow in the chapter. The second part comprehends geometrical considerations on the chosen topologies of TPMS. Then, a purely hydraulic study in Section 2.3, while the thermal behavior is also included in Section 2.4. In the last Section 2.5, some final observations on this chapter results are drawn.

Four types of solid-TPMS are considered: Gyroid, Diamond and both subvolumes (which are not equivalent) of SplitP. The investigation is carried out on a single cubic cell domain of dimension L, representing an infinite periodic medium, with five porosity values, for a total number of twenty configurations, as in Fig. 2.1.

Portions of this chapter were published or presented in the following scientific papers and conferences:

- E. Gajetti, G. Boccardo, L. Savoldi, and L. Marocco, "Hydrodynamic characterization of Gyroid, Diamond and Split-P Triply Periodic Minimal Surfaces as porous medium". *International Journal of Heat and Mass Transfer*. 2025. [79]

- L. Savoldi, A. Cammi, E. Gajetti, and L. Marocco, "Investigating the Reynolds analogy for Triply Periodic Minimal Surfaces in low-Reynolds flow regime" *Presented at the 11th Internal Symposium on Turbulence, Heat and Mass Transfer - THMT25*. 2025. [80]

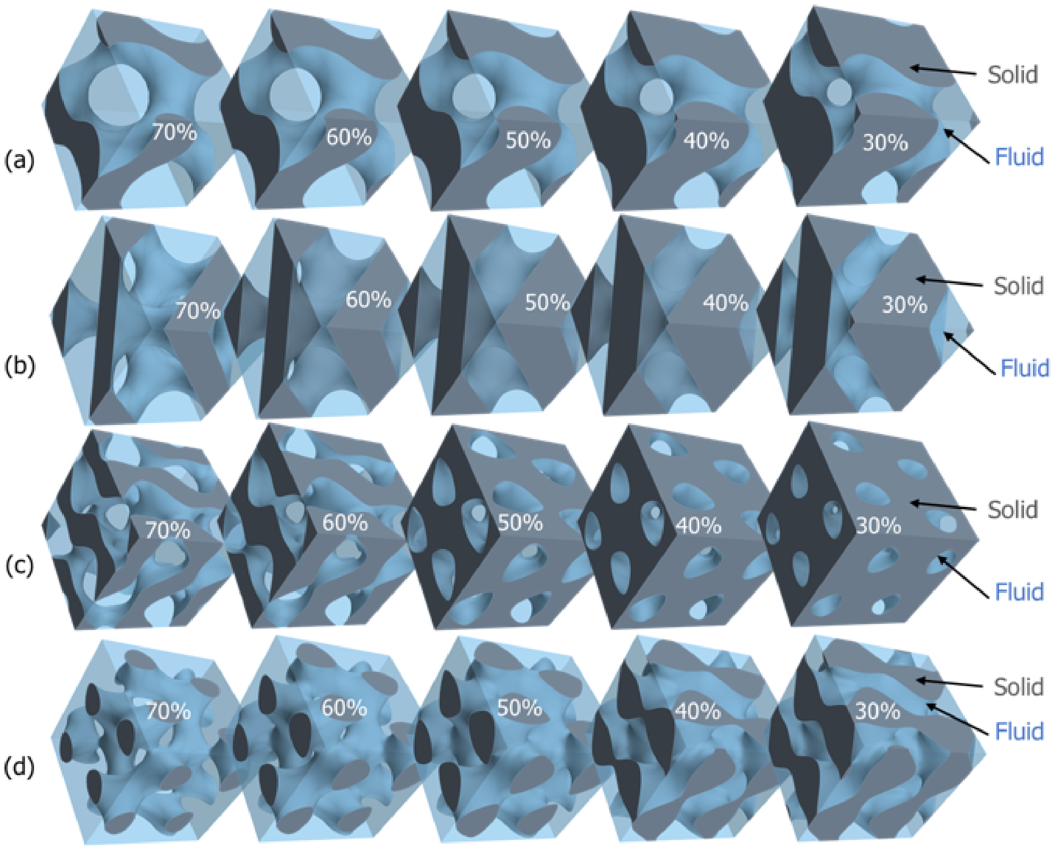

Fig. 2.1 Analyzed TPMS geometries at 30, 40, 50, 60 and 70% porosities. a) Gyroid, b) Diamond, c) SplitP 1, d) SplitP 2. Fluid and solid domain (not simulated) are indicated by arrows. Modified from [79].

2.1 Fundamental equations

In the present chapter, the steady-state continuity (Eq. (2.1)) and momentum conservation (Eq. (2.2)) equations for the laminar flow of an isothermal incompressible

Newtonian fluid, neglecting gravity, are numerically solved for the hydraulic characterization. In OpenFOAM, the CFD code used for the present work, the actual implemented equation of the incompressible, steady-state momentum equation is with the flux form of Eq. (2.3), where the identity of Eq. (2.4) and the incompressible continuity enforcement are used.

$$\nabla \cdot \boldsymbol{u} = 0 \tag{2.1}$$

$$\rho(\boldsymbol{u} \cdot \nabla)\boldsymbol{u} - \nabla \cdot \mathcal{R} = -\nabla p \tag{2.2}$$

$$\nabla \cdot (\boldsymbol{u} \otimes \boldsymbol{u}) - \frac{1}{\rho}\nabla \cdot \mathcal{R} = -\frac{\nabla p}{\rho} \tag{2.3}$$

$$(\boldsymbol{u} \cdot \nabla)\boldsymbol{u} = \nabla \cdot (\boldsymbol{u} \otimes \boldsymbol{u}) - \boldsymbol{u}(\nabla \cdot \boldsymbol{u}) \tag{2.4}$$

In Eqs. (2.1-2.2), $\boldsymbol{u}$ is the velocity vector, p the pressure, ρ the density and $\mathcal{R}$ is the viscous stress tensor, defined in Eq. (2.5) as twice the deviatoric part of the strain rate tensor $\mathcal{S}$ of Eq. (2.6). $\mathcal{I}$ is the identity tensor, tr the trace of a tensor and μ is the dynamic viscosity.

$$\mathcal{R} = \mu\left(2\mathcal{S} - \frac{2}{3}tr(\mathcal{S})\mathcal{I}\right) = \mu\left(2\mathcal{S} - \frac{2}{3}(\nabla \cdot \boldsymbol{u})\mathcal{I}\right) \tag{2.5}$$

$$\mathcal{S} = \frac{1}{2}\left(\nabla\boldsymbol{u} + (\nabla\boldsymbol{u})^T\right) \tag{2.6}$$

From the definition of the strain rate tensor, $tr(\mathcal{S}) = tr(\nabla\boldsymbol{u}) = tr\left((\nabla\boldsymbol{u})^T\right)$.

It must be noted that for incompressible fluids (and constant properties), Eq. (2.5) becomes Eq. (2.7) and the divergence of the viscous stress tensor Eq. (2.8).

$$\mathcal{R} = \mu(2\mathcal{S}) \tag{2.7}$$

$$\nabla \cdot \mathcal{R} = \mu\left(\nabla^2\boldsymbol{u} + \cancel{\nabla(\nabla \cdot \boldsymbol{u})}\right) = \mu\nabla^2\boldsymbol{u} \tag{2.8}$$

When thermal behavior is also accounted for, the steady-state, incompressible, scalar transport equation of the temperature field is solved, as in Eq. 2.9.

$$\boldsymbol{u} \cdot \nabla T = \frac{\lambda}{\rho c_p} \nabla^2 T + \mathcal{R} \cdot \nabla \boldsymbol{u} \tag{2.9}$$

Where λ and c_p are the thermal conductivity and specific heat capacity.

2.2 Geometric parameters

The TPMS could be considered as structured periodic porous media and thus be described by the relevant parameters of porous media field, such as hydraulic diameter D_h (Eq. (2.10)) [81, 16], porosity φ (Eq. (2.11)), tortuosity ζ (Eq. (2.14)).

$$D_h = 4 \frac{Vol_f}{A_{wet}} \tag{2.10}$$

$$\varphi = \frac{Vol_f}{Vol_{cell}} \tag{2.11}$$

In the previous equations, Vol_f is the fluid volume, while Vol_{cell} is the volume of the cell - solid and fluid. A_{wet} is the area wetted by the fluid.
The Reynolds number is defined with respect to the hydraulic diameter as in Eq. (2.12), where U_s/φ represents the characteristic velocity within the TPMS. U_s is the superficial velocity defined as the flow rate $\dot{V}$ divided by the total flow area, i.e in the case of a single cell, the square of the cell length L_c^2, as in Eq (2.13).

$$Re_{D_h} = \frac{U_s D_h \rho}{\varphi \mu} \tag{2.12}$$

$$U_s = \frac{\dot{V}}{A} = U_s = \frac{\dot{V}}{L_c^2} \tag{2.13}$$

The tortuosity is computed as the ratio of the volume-averaged velocity magnitude $\langle U \rangle_V$ to the volume-averaged velocity in the main direction $\langle u_x \rangle_V$, as expressed in Eq. (2.14). This definition is equivalent to the traditional tortuosity definition, i.e. the ratio of the actual path length to the straight-line distance at very low Reynolds numbers ($Re_{D_h} \approx 1$), where viscous forces dominate and the flow paths reflect the geometric constraints of the structure [82–85]. The evaluation of tortuosity in this regime ensures that intrinsic geometric properties are captured, providing a robust measure linked to the network structure and unaffected by inertial effects.

$$\zeta = \frac{\langle U \rangle_V}{\langle u_x \rangle_V} \tag{2.14}$$

As TPMS are structured porous media described by analytical equations, it is also crucial to correlate the geometric factors with the equation parameters, in particular the isovalue c, which offsets the isosurface, with the porosity, as it is shown in Fig. 2.2a. The variations of A_{wet}/L_c^2, D_h/L_c and ζ with the porosity φ are depicted in Fig 2.2b-2.2d.

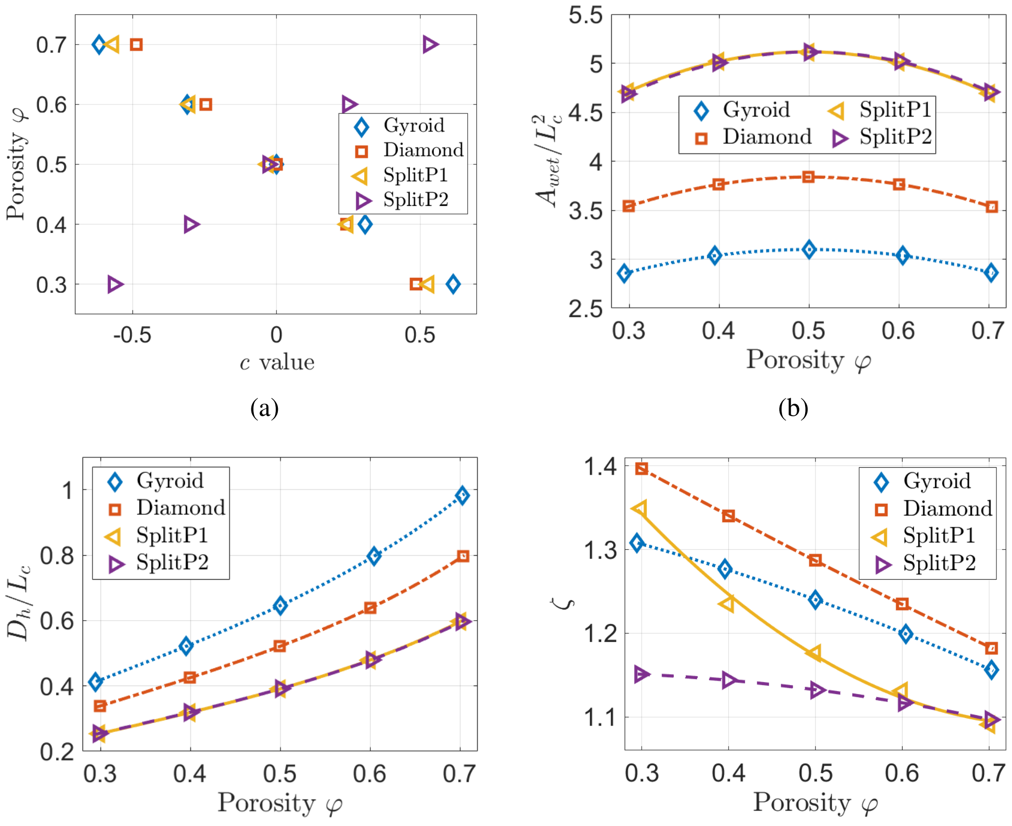

(a) (b)

(c) (d)

Fig. 2.2 Geometric parameters: (a) c value, (b) A_{wet}, (c) D_h and (d) ζ. Modified from [79].

The relationship between porosity and the level set parameter c is linear (see Fig. 2.2a). This linearity is expected, as offsetting the isosurface by a certain value proportionally increases (or decreases) the domain volume relative to the offset, at least for small offsets. This observation is consistent with previous findings in literature: Montazerian et al. [86] demonstrated similar proportionality for the solid-Gyroid and solid-Diamond, and Fisher et al. [87] corroborated these findings.

The wetted area A_{wet} shows a quadratic dependence on porosity, as illustrated in Fig. 2.2b, with a parabolic trend peaking at 50% porosity. This behavior reflects a symmetry in the wetted surface area around a porosity value of 50%. Specifically, A_{wet} is maximum at the value c=0, corresponding to 50% porosity, where the fluid and solid volumes are equal. As the iso-surface offset increases or decreases from c=0, the wetted area decreases symmetrically for equal positive and negative values of the offset. Thus, the wetted area at 60% porosity is the same as at 40% porosity. This symmetry suggests that changes in the solid-to-fluid volume ratio are mirrored for both higher and lower porosities relative to the midpoint, resulting in an equivalent reduction in the wetted surface area on either side of the 50% porosity value. These observations align with the findings of Lu et al. [12].

As illustrated in Fig. 2.2d, tortuosity decreases with increasing porosity across all TPMS structures, in contrast to the behavior of hydraulic diameter. This indicates that as porosity rises, the fluid pathways within the lattice become less convoluted, providing more straightforward flow channels. However, the degree and manner in which tortuosity declines differ among the various structures, reflecting their unique geometries.

For the Diamond, Gyroid, and SplitP2 structures, tortuosity decreases nearly linearly with increasing porosity, suggesting a steady simplification of flow paths as the fluid domain expands. This results in easier fluid flowing with fewer directional changes or obstacles. Among these, the Diamond structure exhibits the highest tortuosity over the porosity spectrum, pointing to more complex flow paths, while the Gyroid falls in the middle. Conversely, SplitP1 shows an almost parabolic relationship between tortuosity and porosity within the measured range. At lower porosities (around 30%), tortuosity in SplitP1 is higher than in SplitP2, but as porosity grows, tortuosity rapidly decreases, eventually aligning with SplitP2 values near 70% porosity. This parabolic pattern reflects a significant shift from complex to more streamlined flow behavior within the SplitP1 configuration, suggesting notable geometric changes affect fluid pathways as porosity increases.

These findings highlight the significance of tortuosity as a key metric for assessing fluid transport complexity in TPMS lattices. While hydraulic diameter offers a consistent measure of scale across different configurations, tortuosity reveals critical variations in the flow field. Previous research by Dolamore et al. [88] and Gado et al. [89] reported comparable hydraulic diameter and tortuosity values for Gyroid and Diamond structures. Such results underline the limitation of models that consider only hydraulic diameter or porosity, as they may overlook the nuanced fluid dynamics present in TPMS lattices. Comprehensive pore-scale investigations are therefore vital to fully understand the interplay between tortuosity, structural features, and porosity and their collective impact on flow behavior.

Another important geometric parameter is the pore diameter [81], which can be related to the hydraulic diameter via Eq. (2.15). D_p is also referred to as the equivalent particle diameter, usually considered for sphere packing.

$$D_p = 6(1-\varphi)\frac{Vol_{cell}}{A_{wet}} \tag{2.15}$$

2.3 Hydraulic behavior

Flows in porous media differ from internal flows in pipes or conduits by the strong influence of solid-liquid interfaces, reason why defining the motion regimes that characterize porous media is much more complex [90]. Indeed, a sudden change from laminar to turbulent regime does not occur within porous media but a qualitative progressive variation might be identified in the flow field across different Reynolds number ranges. Recently, Wood et al. [90] proposed an attractive classification into five distinct motion regimes within different kinds of porous media:

1. Darcian or creeping regime ($Re_{D_h} \lesssim 10-15$). In this regime, viscous effects are predominant, and the flow behavior closely follows Darcy law (Eq. (2.16)), which describes a linear relationship between the pressure gradient and the superficial velocity. Inertial resistance is negligible.

2. Inertial regime ($15 \lesssim Re_{D_h} \lesssim 250$). As the Reynolds number increases, inertial effects begin to manifest significantly, leading to deviations from Darcy linear law. In this regime, convection becomes important, and pore spaces can be

dominated by inertial cores. Steady vortical structures and recirculation zones have been observed, and the velocity distribution within the pores differs markedly from the Darcy regime. The relationship between hydraulic gradient and velocity becomes non-linear, often described by binomial (Forchheimer) equation, as in Eq. (2.17) [91].

3. Unsteady laminar regime ($250 \lesssim Re_{D_h} \lesssim 500$). This regime is characterized by the emergence of unsteady, transitional flows, where periodic vortices may be sustained, and large-scale structures can exhibit intermittency. Flow at early times and near the entrance of a porous medium can involve a mixture of wave and diffusive behaviors.

4. Turbulent regime ($500 \lesssim Re_{D_h} \lesssim 2300$). In this regime, the flow structure within the pore space begins to resemble more conventional turbulent flows, defined by significant turbulent motions. Inertial and advective effects become dominant, and viscous effects may be neglected, particularly in fully developed turbulence. This regime is associated with increased energy losses due to friction and mechanisms of eddy formation and trapping. The hydraulic gradient is thus related only to the square of the velocity, as seen in the Burke-Plummer equation (Eq. (2.18)) [92] or the inertial term of the Forchheimer equation.

5. Asymptotic regime ($2300 \lesssim Re_{D_h}$). At very high Reynolds numbers, the turbulence can be approximated as being locally isotropic over most of the fluid volume within the pore space. Under these conditions, Kolmogorov similarity theory may allow for reasonable estimation of turbulence characteristics [93].

$$\nabla p = -\frac{\mu}{K}\boldsymbol{U}_s \tag{2.16}$$

$$\nabla p = -\frac{\mu}{K}\boldsymbol{U}_s - \frac{\rho C_F}{\sqrt{K}}{\boldsymbol{U}_s}^2 \tag{2.17}$$

$$\nabla p = -\frac{C_{BP}}{D_h}\rho {\boldsymbol{U}_s}^2 \tag{2.18}$$

In the above equations, ∇p is the pressure gradient, K the permeability and C_F the inertial drag factor. C_{BP} is a coefficient in the Burke-Plummer equation. The permeability is a measure of the ease of a porous medium to be passed through by a fluid. If solely one direction of motion is considered, Eqs.(2.16-2.18) become Eqs. (2.19-2.21), being $\Delta p/L$ the linear pressure drop along the flow direction.

$$\frac{\Delta p}{L} = -\frac{\mu}{K} U_s \tag{2.19}$$

$$\frac{\Delta p}{L} = -\frac{\mu}{K} U_s - \frac{\rho C_F}{\sqrt{K}} U_s^2 \tag{2.20}$$

$$\frac{\Delta p}{L} = -\frac{C_{BP}}{D_h} \rho U_s^2 \tag{2.21}$$

The primary objective of this section is the study of the hydraulic characteristic of TPMS at relatively low Reynolds number (below 100), both from a qualitative point of view of flow distribution and from a quantitative point of view, in particular within the Darcian and inertial regimes.

2.3.1 Computational methodology

Boundary conditions and simulation setup

The open-source code OpenFOAM v2212 was used for the present analysis. The use of OpenFOAM is motivated by the fact that the following analysis required numerous simulations to be performed, thus benefiting from the use of an open-source code, which could be more easily automated than proprietary commercial software tools. The computational domain consisted of a single unit cell of TPMS, which is geometrically periodic in all three principal directions, as illustrated in Fig. 2.3. The cell size is $L_c = 10\,mm$. To model a fully-developed flow with a specified flow rate, a pressure drop is imposed in one periodic direction. Periodic boundary conditions with zero pressure gradient are applied in the other two directions, as depicted in Fig. 2.3.

The use of a single periodic cell is justified when the characteristic size of the entire structure, such as the diameter of a pipe or device equipped with TPMS, is significantly larger than the size of the unit cell. In such cases, it is reasonable to assume that macroscopic boundary effects do not influence the representative

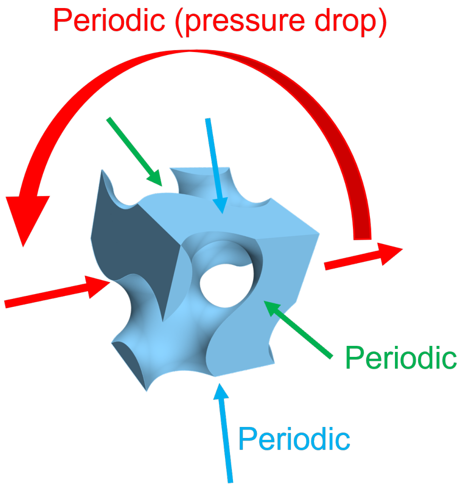

Fig. 2.3 Fully developed periodic boundary conditions for the inlet/outlet section. Taken from [79].

periodic volume, assuming thus a sort of *infinite medium*. This approach of using a single periodic TPMS unit cell has been previously employed in studies, such as by Pires et al. [94].

The pressure-velocity coupling was performed by using the SIMPLE algorithm of OpenFOAM [95]. A linear upwind discretization scheme was used for the convective terms and a central difference scheme for the diffusive terms. Simulations were conducted for different Reynolds numbers, defined in Eq. (2.12), in the range of $0.3-100$, and for porosity values of 30%, 40%, 50%, 60% and 70%. Water at 20°C was considered as fluid.

As stated in the ASME standard [96], the recommended approach is to reduce the iterative error until it becomes negligible compared to the discretization error, without necessarily converging the solution to near machine precision. Therefore, it was considered satisfactory that the normalized residuals of the simulations of the present chapter reached $10^{-7}-10^{-8}$.

Mesh generation and mesh convergence analysis

When studying flow problems where fully developed turbulence has to be treated, it is customary to use meshes with clearly defined boundary layers. As the main objective of this chapter is instead the analysis of flow within TPMS in laminar regime or at the beginning of the transition zone between regimes, without exploring full turbulence, a polyhedral mesh without boundary layers was used. The mesh was generated using STAR-CCM+, version 17.02.008-r8.

To assess the accuracy of the results, four grids were created for the 30% porosity geometries and the volume average of the velocity magnitudes $\langle U \rangle_V$ within the TPMS computed with the different grids were checked and plotted in Fig. 2.4. Here, velocities were normalized to the finest mesh results (*Ref1*) as well as the average cell size, Δh, defined in Eq. (2.22), where N_{mesh} is the number of polyhedral cells composing the grid.

$$\Delta h = \sqrt[3]{Vol_f / N_{mesh}} \tag{2.22}$$

The number of cells of each grid and TPMS is shown in Table 2.1 and some views of the meshes are presented in Fig. 2.5. The Gyroid has the less intricate structure, thus a coarser mesh is sufficient to capture its flow features nicely, with respect to the other TPMS. SplitP2, on the other hand, is the most complicated.

Table 2.1 Number of polyhedral cells in the 30% porosity TPMS.

	Ref1	**Ref2**	**Ref3**	**Ref4**
Gyroid	72k	36k	20k	8.7k
Diamond	75k	31k	18k	8.7k
SplitP1	90k	51k	28k	11k
SplitP2	99k	54k	29k	15k

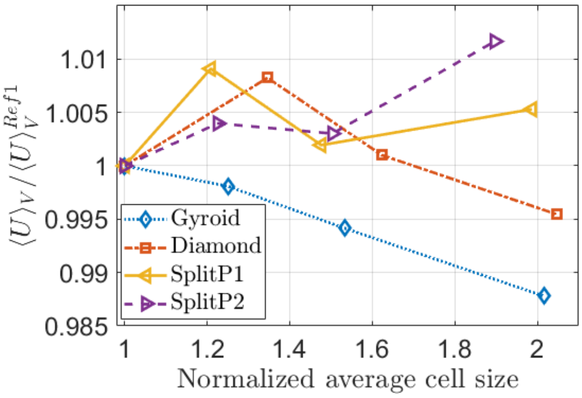

Fig. 2.4 Normalized velocities vs normalized average cell size. Modified from [79].

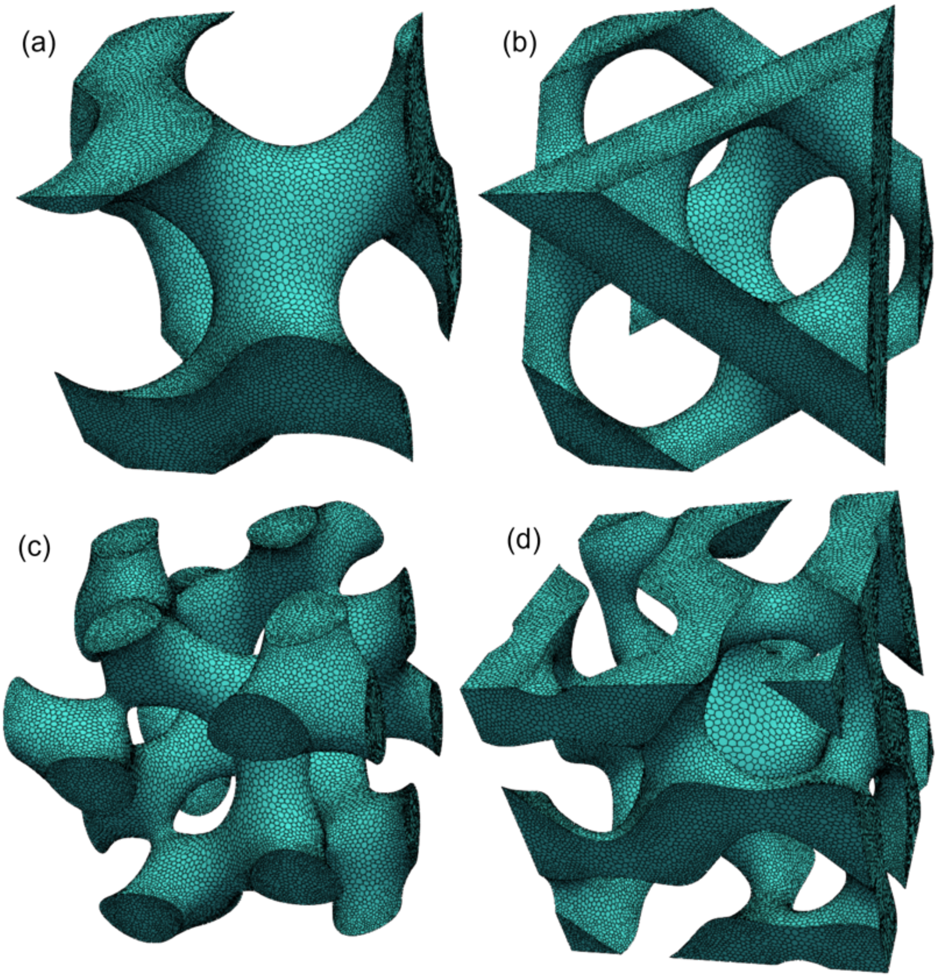

Fig. 2.5 Surface mesh views: (a) Gyroid, (b) Diamond, (c) SplitP1 and (d) SplitP2. Taken from [79].

The numerical uncertainties on the velocities were computed following the ASME standard [96]. The uncertainty evaluation strictly based on the Richardson extrapolation method is valid only within the asymptotic regime. However, for highly complex problems, non-monotonic and not fully convergent results may occur, leading to oscillatory behavior in the solution. In such cases, a least-squares approach can be employed, as prescribed by the ASME standard [96], to determine an "effective" order of convergence, with the additional provision of limiting the computed order to the theoretical one. For problems where a fully non-monotonic trend cannot be clearly observed, fitting the data with a polynomial of degree higher than the discretization order may yield misleading results. Consequently, the computed order of convergence is limited to the theoretical order of convergence, in accordance with the standard. It is thus assumed that the discretization error might be approximated as one-term expansion, as given by Eq. 2.23. $\langle U_i \rangle_V$ is the average velocity calculated with the i-th grid, $\langle U_\infty \rangle_V$ is the extrapolated value, α is a proportionality coefficient, and γ is the calculated order of convergence. The parameters $\langle U_\infty \rangle_V$, α and γ are computed employing a least squares approach, based on the minimization of the function in Eq. 2.24.

$$\langle U_i \rangle_V - \langle U_\infty \rangle_V \approx \alpha \Delta h_i^\gamma \tag{2.23}$$

$$\mathcal{L}(\langle U_\infty \rangle_V, \alpha, \gamma) = \sqrt{\sum_{i=1}^{3} \left(\langle U_i \rangle_V - \langle U_\infty \rangle_V - \Delta h_i^\gamma \right)^2} \tag{2.24}$$

Considering that most of the numerical uncertainty is given by errors due to discretization, its estimate is given by Eq. 2.25. The *GCI* is the Grid Convergence Index, and it is defined in Eq. 2.26, where er_a^{21} is the absolute error between the results of the finest and second finest meshes and r_{21} is the ratio of the average cell sizes of the finest and second finest meshes. The factors 1.15 and 1.25 in Eq. (2.25)-(2.26) are recommended by [96].

$$un_{num} = \frac{GCI}{1.15} \tag{2.25}$$

$$GCI = \frac{1.25 \cdot er_a^{21}}{r_{21}^\gamma - 1} \tag{2.26}$$

For the maximum Reynolds number studied, specifically $Re_{D_h} \approx 100$, the calculated numerical uncertainties are less than 5%. Table 2.2 presents the volume-averaged velocity magnitudes through the TPMS with 30% porosity at this Reynolds number, alongside their numerical errors. In Table 2.3, the computed orders of convergence are shown, for each TPMS. As stated in the standard of ASME [96], even convergence order values lower than 1 can be considered acceptable, as they likely indicate that the coarsest grid is not fully within the asymptotic region. This condition leads to higher estimated numerical uncertainties, thus maintaining a conservative approach.

Table 2.2 Volume-average velocity magnitudes flowing through the 30% porosity TPMS (in cm/s) with their numerical uncertainties

Gyroid	**Diamond**	**SplitP 1**	**SplitP 2**
(2.57 ± 0.04)	(3.2 ± 0.1)	(3.77 ± 0.08)	(3.9 ± 0.2)

Table 2.3 Computed order of convergence γ for the flow within the four TPMS topologies.

Gyroid	**Diamond**	**SplitP 1**	**SplitP 2**
1.17	1.15	0.85	1.25

This numerical uncertainty assessment was only performed for the void fraction of 30%, as those are the geometries with the highest velocities for the same Reynolds number. The $Ref1$ computational grid was used in the following study for the 30% porosity, and the cells with different porosities were meshed using the same grid generation parameters of $Ref1$.

2.3.2 Results and discussion

In this section, the results of the hydraulic study on the single periodic cell are presented. First, an initial qualitative analysis of the fluid flow throughout the different TPMS was conducted, to improve comprehension of the velocity distribution and fluid path within the different topologies, and then a concentrated parameter analysis in which the TPMS were considered as porous media to develop lumped models.

Velocity and flow complexity

The purpose of this first section is to investigate the promotion of vorticity within TPMS and the distinctions between different topologies, at high - $Re_{D_h} \approx 100$ - and low - $Re_{D_h} \approx 0.3$ - Reynolds numbers. First, the normalized velocity field along the flow direction was studied and presented in Fig. 2.6, together with the normalized vorticity (Fig. 2.7), for the 50% porosity. Then, also the helicity angle is analyzed, which could give a more quantitative insight about the amount of flow swirling
As it can be remarked in Fig. 2.6, at low Reynolds numbers all TPMS configurations exhibited smooth and stable flow profiles, indicating dominance of viscous forces. As the Reynolds number increased, the velocity profiles became more complex, reflecting the growing influence of inertial forces. Increasing the Reynolds, localized regions of negative velocity appeared in the Gyroid structure, signaling minor flow separation or flow reversal near certain surfaces and highlighting increased flow complexity due to inertia. Conversely, the Diamond structure maintained a relatively uniform velocity distribution even at higher Reynolds numbers, indicating a more stable flow regime with minimal signs of separation. The SplitP1 and SplitP2 geometries demonstrated significantly more complex flow at higher Re_{D_h}, showing substantial velocity fluctuations and broader areas of negative velocity that indicate flow reversal. The intricate design of these SplitP structures appeared to amplify inertial effects, producing more varied and complex flow patterns.

Fig. 2.7 depicts the Line Integral Convolution (LIC) of the normalized vorticity. The vorticity vector $\boldsymbol{\varpi}$ is defined in Eq. (2.27) as the rotor of the velocity vector [97] and describes the infinitesimal circulation of the velocity field.

$$\boldsymbol{\varpi} = \nabla \times \boldsymbol{u} \tag{2.27}$$

At low Reynolds numbers, the Gyroid, Diamond, and SplitP1 exhibited well-organized flow fields, characterized by stable and regular vorticity patterns that reflect the dominance of viscous forces. In contrast, the SplitP2 structure already showed more irregular and intricate flow features under the same low Reynolds conditions, suggesting that its geometry inherently promoted greater flow complexity even in the viscous regime. As the Reynolds number increased to approximately 100, all structures displayed a significant rise in flow complexity. The vorticity fields became more intricate and variable, with intensified swirling and the emergence of

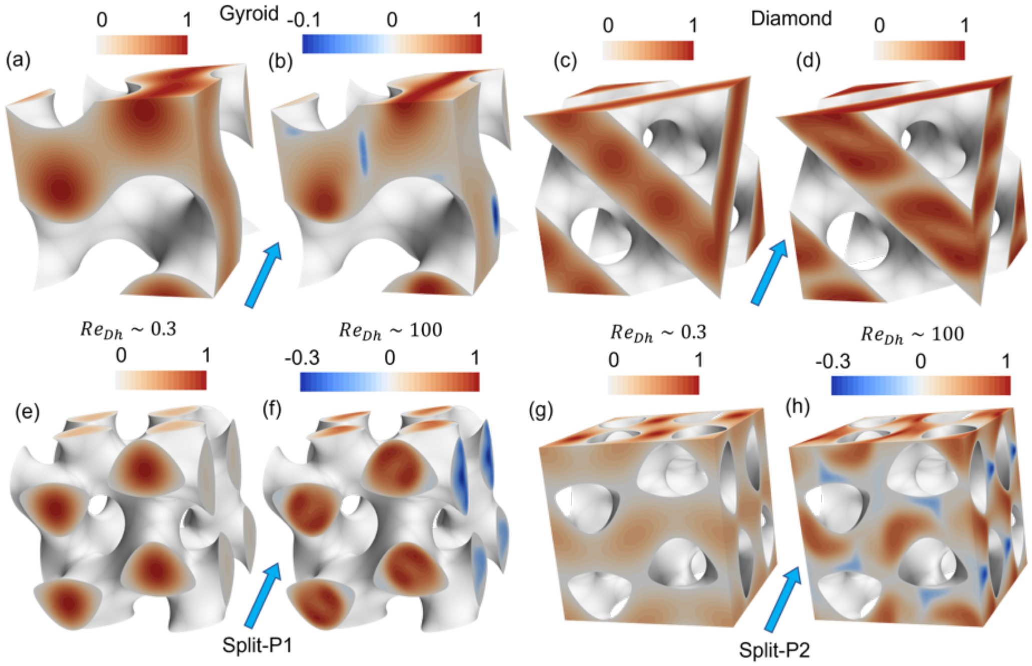

Fig. 2.6 Normalized velocity in the flow direction for 50% porosity. (a), (c), (e), (g) $Re_{D_h} \approx 0.3$, (b), (d), (f), (h) $Re_{D_h} \approx 100$ for the Gyroid (a),(b), Diamond (c),(d), SplitP1 (e),(f) and SplitP2 (g),(h), respectively. Taken from [79].

increasingly irregular features across the domain — clearly illustrating the growing influence of inertial forces on flow behavior. Among the geometries, the SplitP configurations produced more pronounced variations in the flow field compared to the Gyroid and Diamond, highlighting their enhanced capability for promoting internal mixing. It is also important to note that while the vorticity fields are normalized at each Reynolds number, the actual (dimensional) maximum vorticity at $Re_{D_h} \approx 100$ is roughly 1000 times greater than at $Re_{D_h} \approx 0.3$. This underscored the substantial increase in rotational motion intensity in the inertial regime, which is visually evident in the LIC images as areas of high vorticity became more distinct and complex.

In order to better assess the degree of swirling within the TPMS cells at different Reynolds numbers, the helicity angle Θ was also investigated, as defined in Eq. (2.28). When this angle between the velocity and vorticity vectors is near $\pi/2$ (90°), the fluid flow is prone to greater curvature and helical structures [98], because the fluid flow is primarily characterized by transverse rotational motion relative to the local flow direction, which could theoretically enhance mixing. Conversely, when the helix angle approaches 0° or 180°, the velocity and vorticity vectors are aligned

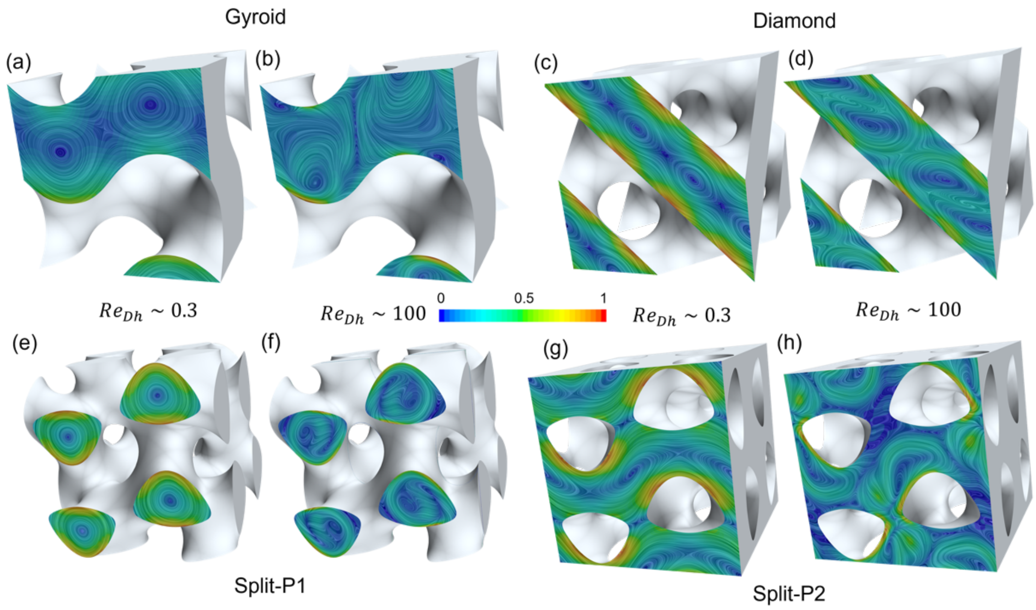

Fig. 2.7 Line convolution integral of the normalized vorticity for 50% porosity. (a), (c), (e), (g) $Re_{D_h} \approx 0.3$, (b), (d), (f), (h) $Re_{D_h} \approx 100$ for the Gyroid (a),(b), Diamond (c),(d), SplitP1 (e),(f) and SplitP2 (g),(h), respectively. Taken from [79].

along the main axis of the flow, giving rise to helical (corkscrew-shaped) motions. These coherent and stable structures tend to maintain the separation between fluid layers, reducing the effectiveness of transverse mixing.

$$\Theta = acos\left(\frac{\boldsymbol{\varpi}\cdot\boldsymbol{u}}{|\varpi||u|}\right) \tag{2.28}$$

In Fig. 2.8 the probability density function (PDF) of the helicity within the TPMS was plotted, for the highest (orange bars) and lowest (blue bars) Reynolds numbers, for all the structures. It might be remarked that for all the cases Θ was peaked around $\pi/2$, but how it was more broadly distributed at $Re_{D_h} \approx 100$ with respect to $Re_{D_h} \approx 0.3$. Although this may suggest a favorable potential for mixing, in low Reynolds number regimes, dominated by viscosity, the available energy was limited, and the flow remained structured and stable. This limited the interactions between fluid layers and therefore reduced the intensity of mixing, despite the orthogonal orientation.

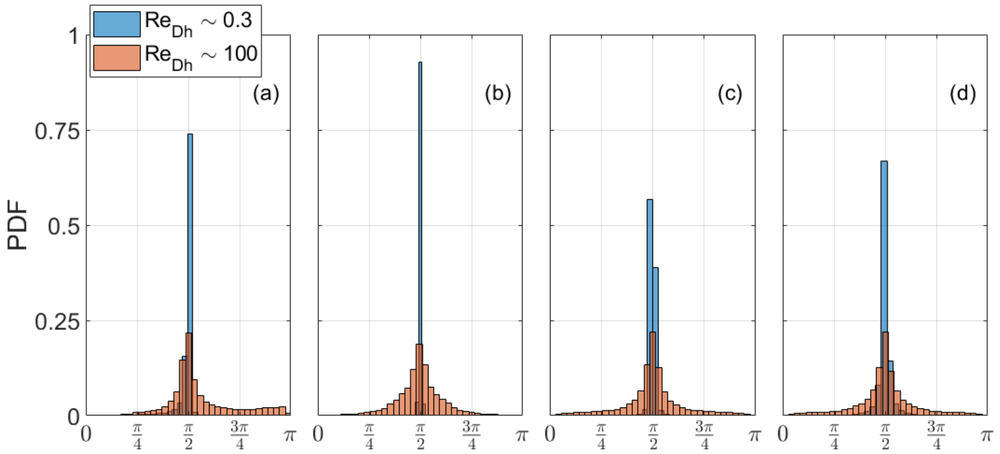

Fig. 2.8 Probability density function (PDF) of the helicity in the fluid domain. (a) Gyroid, (b) Diamond, (c) SplitP1 and (d) SplitP2. Taken from [79].

Darcy and Darcy-Forchheimer law

As already discussed above, the fluid flow through porous media might be described by the Darcy-Forchheimer equation. Figure 2.9 shows the relationship between linear pressure drop and surface velocity for the TPMS geometries analyzed, with porosities of 30%, 40%, 50%, 60% and 70%. The results referred to a water flow at 20°C. In all configurations, a linear correlation between pressure drop and surface velocity was observed up to approximately 10, represented by the fourth data point in each graph. This linear regime indicated that Darcy law (represented by the dotted lines) accurately described the flow resistance in this low-velocity range, which was dominated by viscous phenomena. It is important to note that this threshold was constant across different types of TPMS and porosity levels, establishing a clear limit within which Darcy law remains valid.

When the Reynolds number exceeded 10, the relationship between pressure drop and velocity became non-linear. In this regime, Darcy-Forchheimer law (indicated by the dashed-dotted lines) provided a more accurate representation, including an additional inertial term that allowed the quadratic increase observed in pressure drop with increasing velocity to be modeled.

To quantify the flow resistance parameters for each TPMS geometry and porosity level, the results of simulations at different Reynolds numbers were fitted to both Darcy and Darcy-Forchheimer equations. This fitting process made it possible to

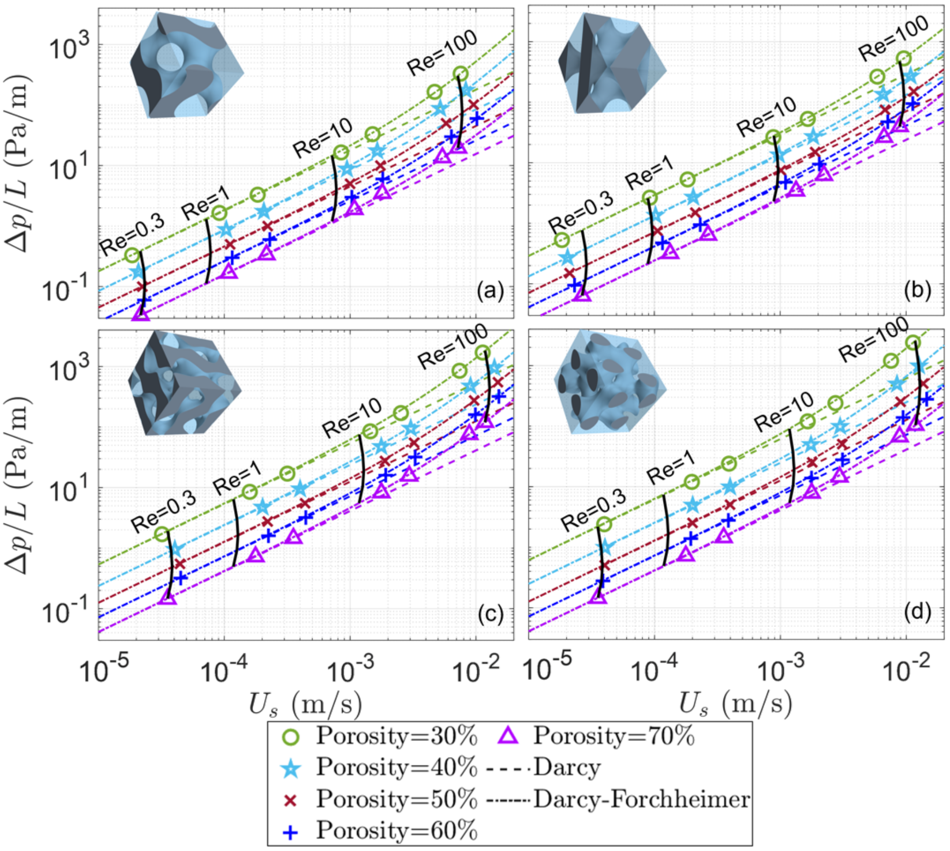

Fig. 2.9 Linear pressure drop vs superficial velocity. (a) Gyroid, (b) Diamond, (c) SplitP1 and (d) SplitP2. The continuous black lines refer to isolines of constant Reynolds number. Modified from [79].

extract the permeabilities and inertial resistance factors, as summarized in Table 2.4. These parameters characterize the viscous and inertial contributions to flow resistance for each configuration.

To facilitate the comparison of permeability values over different characteristic lengths, the concept of relative permeability was introduced. In this study, it was calculated by scaling the dimensional permeability by the square of the cell size L_c, set as 10 mm. This approach was in line with the methodologies adopted by Asbai-Ghoudan et al. [13] and Callens et al. [99]. The Gyroid structure was also investigated at different cell sizes, notably 5 mm and 15 mm, and the normalized permeability and drag inertial factor were consistent to the results for the 10 mm structure.

Table 2.4 Power law fitting parameter - K and C_F, for all TPMS and porosities

φ (%)	**Gyroid**		**Diamond**		**SplitP 1**		**SplitP 2**	
	K_{rel}	C_F	K_{rel}	C_F	K_{rel}	C_F	K_{rel}	C_F
30	5.6e-4	0.81	3.5e-4	0.52	1.9e-4	1.20	1.6e-4	1.70
40	1.2e-3	0.53	7.6e-4	0.30	4.3e-4	0.65	4.1e-4	0.85
50	2.2e-3	0.31	1.4e-3	0.20	8.1e-4	0.46	8.0e-4	0.50
60	3.9e-3	0.20	2.4e-3	0.19	1.4e-3	0.34	1.4e-3	0.31
70	6.5e-3	0.13	4.2e-3	0.15	2.4e-3	0.25	2.4e-3	0.20

The permeability K_{rel} increased with porosity in all TPMS structures, reflecting a reduction in flow resistance in more open configurations. Conversely, the inertial drag factor C_F decreased as porosity raised, indicating a lower impact of inertial effects in high-porosity structures. This trend was consistent across all geometries analyzed, with Gyroid and Diamond generally exhibiting higher permeability and lower inertial drag factors than the more complex SplitP structures. This difference in behavior highlighted the influence of TPMS geometry on flow characteristics, with simpler structures such as Gyroid and Diamond allowing for smoother flow paths and therefore lower resistance. The high coefficients of determination R^2, close to 1, obtained in all cases underscored the accuracy of the Darcy-Forchheimer model in describing the flow behavior in the range of TPMS structures porosity levels and Reynolds numbers analyzed.

Ergun equation

A frequently used framework for characterizing porous media within the transition regime is the Ergun equation [81, 16], as documented in Eq. (2.29). This equation incorporates both first and second-order dependencies on the superficial velocity, thus addressing both viscous and inertial components. Eq. (2.29) may be reformulated in a dimensionless form, as illustrated in Eq. (2.30), with Re^* and Δp^* defined in Eq. (2.31) and Eq. (2.32), respectively.

$$\frac{\Delta p}{L} = 150\left(\frac{\mu U_s}{D_p^2}\right)\frac{(1-\varphi)^2}{\varphi^3} + \frac{7}{4}\left(\frac{\rho U_s^2}{D_p}\right)\left(\frac{1-\varphi}{\varphi^3}\right) \tag{2.29}$$

$$\Delta p^* = \frac{150}{Re^*} + \frac{7}{4} \tag{2.30}$$

$$\Delta p^* = \left(\frac{\Delta p}{\rho U_s^2}\right)\left(\frac{D_p}{L}\right)\left(\frac{\varphi^3}{1-\varphi}\right) \tag{2.31}$$

$$Re^* = \frac{\rho D_p U_s}{\mu(1-\varphi)} \tag{2.32}$$

Ergun equation is a semi-empirical correlation derived from simple idealized models and adapted to be employed for packed-bed columns. Its advantage lies in that it can reliably predict pressure drops over a wide range of conditions with a somewhat simple relationship, dependent only on few parameters of the porous medium, meant to be easily measurable experimentally, i.e., porosity and porous granulometry. Herein also lies its weakness, as this (otherwise commonly used) relationship may struggle to predict pressure drops in cases where more geometrical parameters have an impact or where these integral equivalent parametric descriptors are not adequate for the system investigated: this could be the case of TPMS. Indeed, the primary aim of this section is the comparison of the predicted pressure drop from Ergun equation with the CFD results on the investigated TPMS cells.

In Fig. 2.10, the Ergun equation was plotted with the numerical results for the 30% and 60% porosities of the four TPMS topologies. The relative deviations of the CFD results from the Ergun predictions were also highlighted, showing significant inadequacy in modeling the hydraulic impedance of TPMS, even at very low Reynolds numbers, where viscous effects dominated. The error bars indicated that for all TPMS configurations, including simpler geometries like Gyroid and Diamond, the relative error is already above 30-50% at low Re^*. This discrepancy became even more pronounced for more complex structures, such as the two SplitP configurations. While the difference between CFD results and Ergun equation decreased for the Gyroid and Diamond structures at higher porosity and Reynolds numbers, it overall remained unacceptably large, particularly for the SplitP structures. These observations underscored the insufficiency of Ergun equation in accurately modeling pressure drop in intricate TPMS configurations.

In literature, some authors tried to adapt the Ergun equation to the TPMS by varying the coefficients 150 and 7/4 with a fit from numerical CFD results, as for example Hawken et al. [16] and Cheng et al. [100], shown in Fig. 2.11. The correlation of Cheng et al. [100], which was developed for both Gyroid and

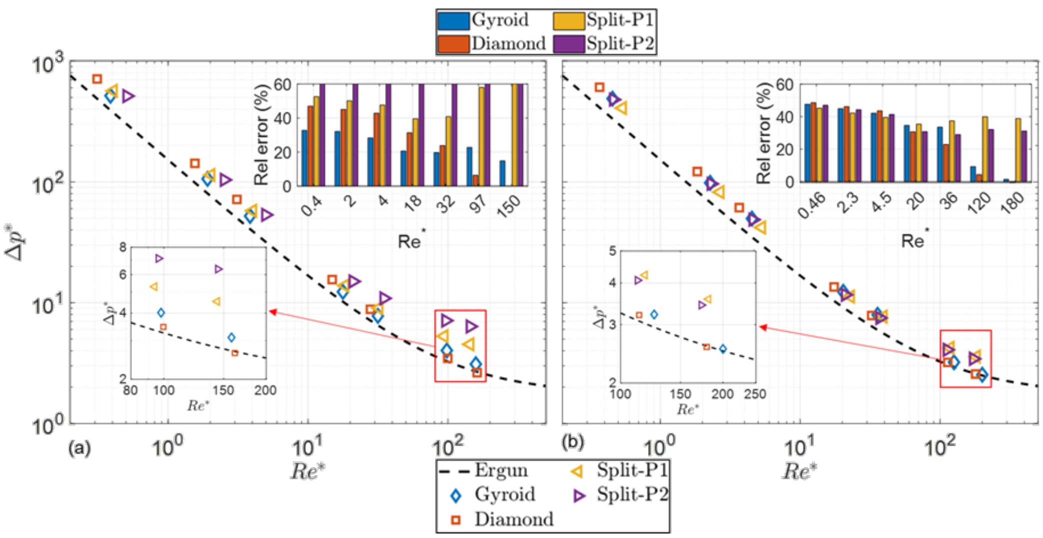

Fig. 2.10 Comparison of TPMS results with the Ergun equation at different porosities with zooms in the inertial region: (a) 30% and (b) 60%. The relative errors for SplitP2 in (a) exceed the maximum value of the axis and are well beyond 100% for the highest Re^* value. Taken from [79].

Diamond, tended to better capture the pressure drop for the Gyroid, in the higher Re^* region, while significant discrepancies were evident at low Re^*. However, for the Diamond structure, the Cheng's model showed significant deviation at higher Reynolds numbers, indicating an increasing mismatch as inertial effects dominated. For the Diamond structure, the model of Hawken et al. [16] was in agreement with the CFD data of the present work in the high Re^* range. However, it still did not fully capture the detailed flow resistance across all Reynolds number ranges, especially at lower Re^*, where viscous effects were significant. These observations imply that neither of the two modifications was fully adequate for accurately modeling pressure drops in TPMS structures like Gyroid and Diamond across all flow regimes.

Consequently, it is imperative to develop an innovative framework to enhance the predictive capability of the available models.

Porosity-dependent correlations for relative permeability and inertial drag factor in TPMS structures

Assessing the permeability and inertial drag factor of each TPMS at different porosity levels is essential for their characterization [94]. Subsequently, K_{rel} and C_F were associated with porosity through a power law relationship, consistent with the

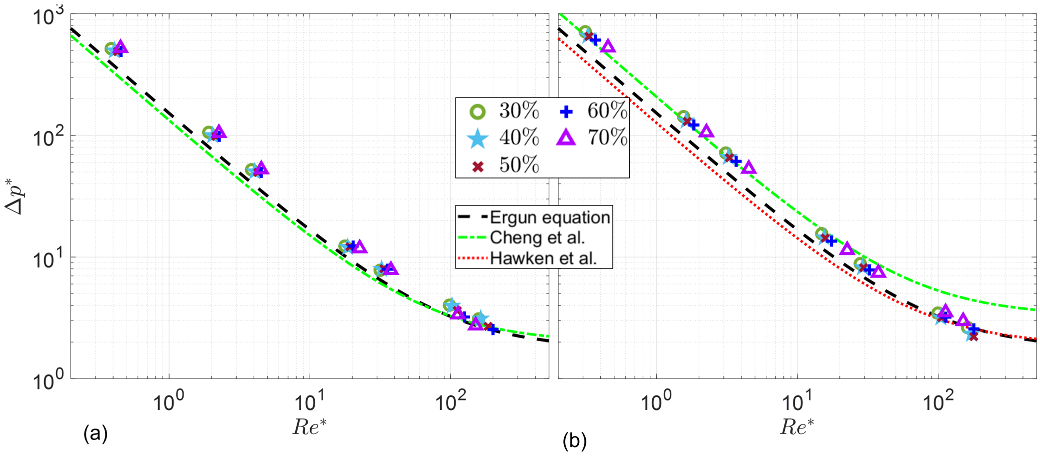

Fig. 2.11 Comparison of CFD results with modified Ergun equations by Hawken et al. [16] and Cheng et al. [100] (a) Gyroid, (b) Diamond. Modified from [79].

formulae outlined in Eq. (2.33) and Eq. (2.34). Figure 2.12 shows the CFD results for the different geometries and the fitting curves.

$$K_{rel} = a\varphi^n \tag{2.33}$$

$$C_F = b\varphi^m \tag{2.34}$$

Table 2.5 Power law fitting parameter - K_{rel} and C_F

TPMS	**Gyroid**	**Diamond**	**SplitP1**	**SplitP2**
a	0.0189	0.0126	0.00771	0.00794
n	3.08	3.14	3.26	3.34
$R^2_{K_{rel}}$	0.9976	0.9984	0.9980	0.9982
b	0.0837	0.0739	0.129	0.0916
m	-1.88	-1.59	-1.82	-2.41
$R^2_{C_F}$	0.9874	0.9751	0.9970	0.9996

All TPMS had similar power laws for permeability, with an exponential coefficient spanning around three: the characteristic equation parameters are displayed in Table 2.5, where R^2 is the R-squared, i.e., the coefficient of determination. In the same table, also the coefficients for the correlation of the C_F are presented.

The Gyroid permeability was the highest one, probably because of the simplest characteristic equation, resulting in a simpler geometry, whereas the two SplitP,

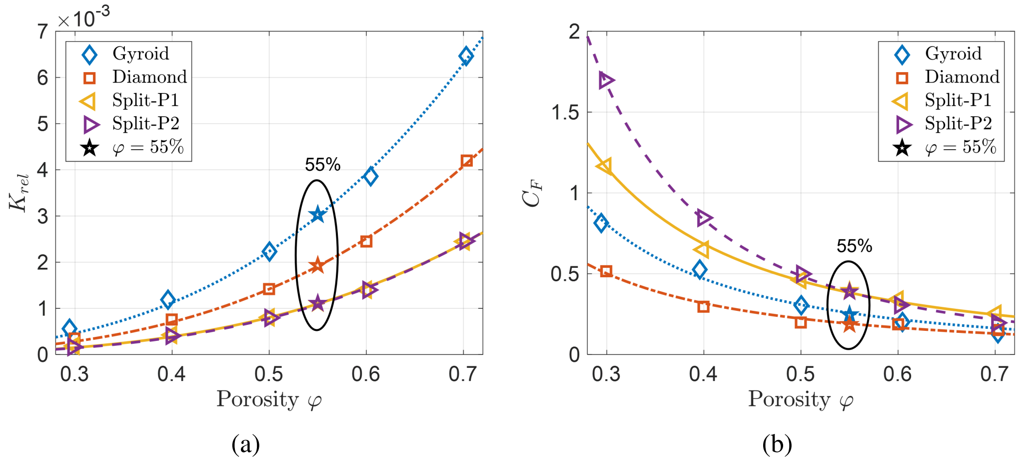

Fig. 2.12 Normalized permeability (a) and inertial drag coefficient (b) as function of porosity, for the four TPMS topologies, using Eqs. (2.33) and (2.34). The symbols are the computed results, the line the power law fitting. Modified from [79].

having a more complex structure, had the lowest permeability. Indeed, the Gyroid appeared to have a straight channel running through it, if one of the lattice axes was aligned with the main flow direction, and this affects the permeability.

It's interesting to remark that the two complementary SplitP types presented almost the same permeability but different inertial coefficient. Indeed, the discrepancies between the fits of K_{rel} of the two SplitP were within the numerical uncertainty. At the same Re_{D_h}, wetted area and porosity, the two structures had the same flow rate, but induced the same pressure drop only in viscous regime, while in inertial regime the SplitP2 had larger pressure losses. This was caused by the different cross-sectional areas that the fluid passed through in the two structures. In Fig. 2.13 the normalized cross-sectional area A_c/L_c was computed at different cut sections of the TPMS along the flow direction x, for both SplitP at 50% porosity. The integral of the two curves of Figure 2.13a was equal, corresponding to the porosity. However, the trend of A_c/L_c of SplitP1 had higher peaks, while SplitP2 presented lower minimum A_c/L_c. Therefore, also the trend of the mean velocity in the flow direction $\bar{u}_x$ within the TPMS was different (see Figure 2.13b, for $Re_{D_h} = 100$), while remaining equal its average along the cell length $\langle \bar{u}_x \rangle_{L_c}$. In the viscous regime, the pressure loss is linearly dependent to the velocity, thus the two SplitP showed the same Δp, having the same $\langle \bar{u}_x \rangle_{L_c}$. On the other hand, in inertial regime the pressure losses are largely influenced by the square of the velocity, whose average on the cell length $\langle \bar{u}_x^2 \rangle_{L_c}$ was not equal between SplitP1 and SplitP2. The trend of the square of the velocity in the flow direction is shown in Figure 2.13c: SplitP2, which had the largest $\langle \bar{u}_x^2 \rangle_{L_c}$, caused the largest Δp. This behavior was amplified at lower porosities, and inverted at 60% porosity, where SplitP1 presented slightly greater $\langle \bar{u}_x^2 \rangle_{L_c}$, reflecting on the inertial factor of Table 2.4. The pattern of the cross areas is peculiar, having an angular point in the middle of the cell, probably due to the characteristic equation of the SplitP, which has a factor of two in some of the sine/cosine functions.

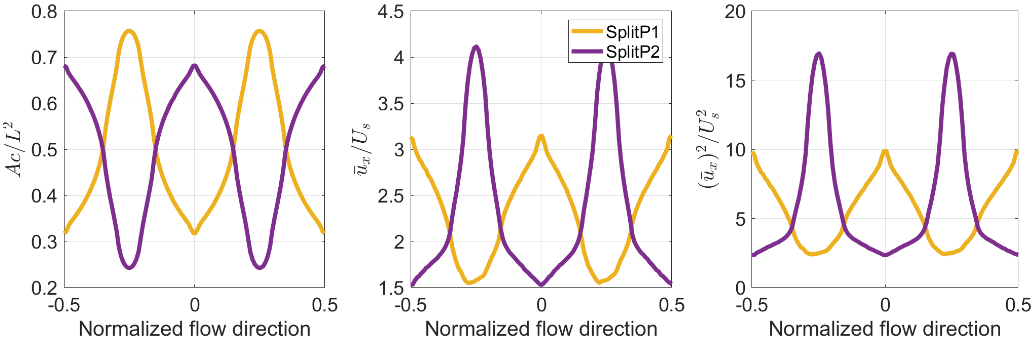

(a) (b) (c)

Fig. 2.13 Comparison between the two SplitP structures at 50% porosity and $Re_{D_h} = 100$: (a) normalized cross sectional area, (b) normalized velocity in the flow direction and (c) square of the normalized velocity in the flow direction. Taken from [79].

In Figure 2.14a, which shows the Gyroid permeability, the correlation of Lu et al. [12] (red dotted line) fell within the 95% confidence interval (CI) of the correlation obtained in the present study for the entire range of porosity. Lu et al. [12] did not explicited the Reynolds they used for their calculations, but claimed it was laminar. The results of Zhianmanesh et al. [11] (calculated at $Re_{D_h} < 10$ and $20\% < \varphi < 80\%$) and Dolamore et al. [88] (computed in in Stokes regime, below $Re_{D_h} < 1$) also fell largely within the confidence limits of the current study, indicating a high degree of consistency in the predicted permeability behavior for the Gyroid structure. This agreement between multiple sources reinforced the validity of the correlation proposed in this work for the Gyroid, supporting its predictive capability in the analyzed porosity range.

On the other hand, Figure 2.14b, representing the Diamond permeability, showed a different trend. In this case, the correlation of Lu et al. [12] fell within the 95% confidence interval of the present study only for the central porosity around 50%, whereas it predicted higher permeability values for $\varphi < 45\%$ and $\varphi > 65\%$. However, Dolamore et al. [88] presented a much closer match with the correlation of the present study, remaining firmly within the confidence interval, especially for medium to high porosities. This consistency with Dolamore et al. [88] supported the accuracy of the correlation reported in this work for the Diamond structure. The 95% confidence interval is equivalent to considering plus or minus two standard deviations of the fit. It served as a reliable reference, encompassing most of the permeability trends reported in the literature for both Gyroid and Diamond structures. The fact that the values of Lu et al. fell within the confidence interval for Gyroid but outside it for some of the Diamond porosities highlights the importance of geometry-specific assessments and the possible variability introduced by different modeling approaches.

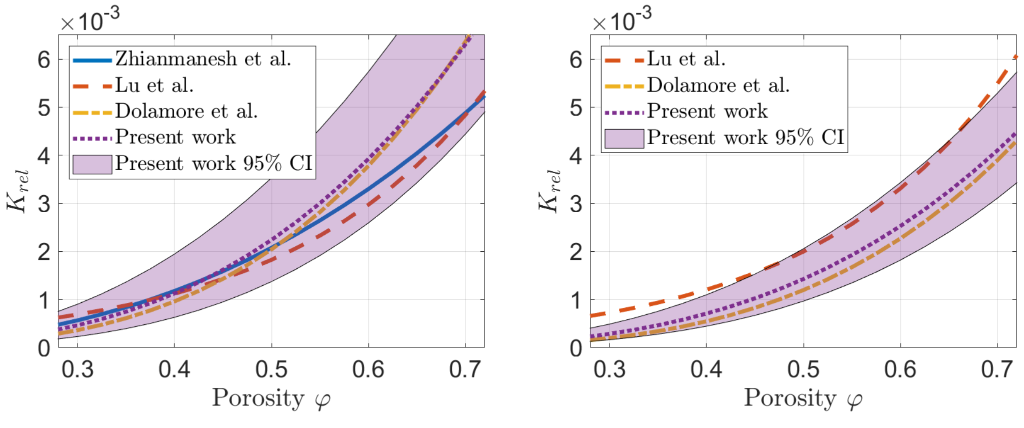

(a)

(b)

Fig. 2.14 Comparison in terms of relative permeability between results from literature and present work. a) Gyroid, b) Diamond. Taken from [79].

Application of the Kozeny-Carman equation to permeability-porosity relations in TPMS Structures

In the Darcian regime, another way to investigate the porosity-permeability coupling lies in the use of the Kozeny-Carman relation, as in Eq. (2.35) [10].

$$K_{KC} = C_K \frac{\varphi^3}{S_V^2} \tag{2.35}$$

C_K is a dimensionless coefficient and S_V is the surface-to-volume ratio, equal to $4/D_h$. The Kozeny-Carman equation was developed for computing the permeability of packed beds. As Montazerian et al. [86] pointed out, C_K could be nicely described as a parabolic function of the porosity, i.e. $C_K = c_0 + c_1\varphi + c_2\varphi^2$: see Fig. 2.15a. The

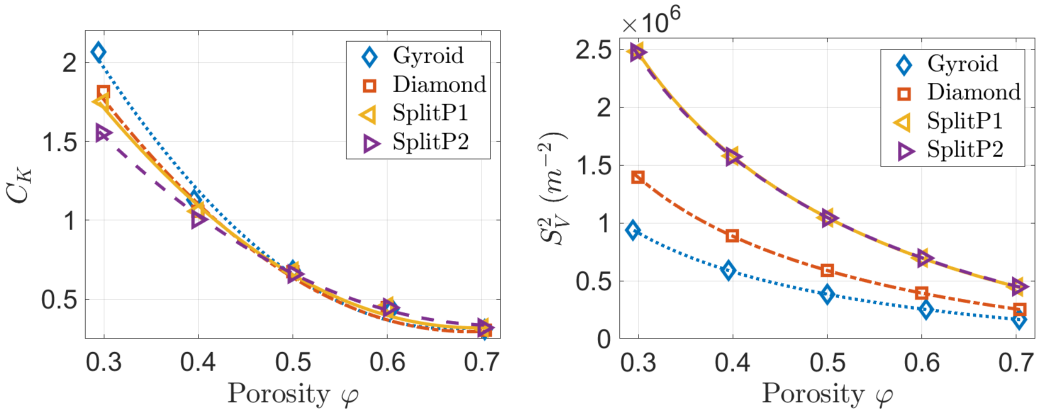

(a) (b)

Fig. 2.15 C_K (a) and S_V^2 (b) vs porosity φ for the different TPMS unit cells investigated here. Taken from [79].

fit parameters for C_K of the present study are shown in Table 2.6, with their R-square values. Note that the quadratic dependence of C_K on the porosity might be explained by the fact that also the surface to volume ratio S_V^2 had a quadratic dependence on the porosity. Indeed, the surface to volume ratio is computed as $\frac{A_{wet}}{V_{fluid}} = \frac{A_{wet}}{\varphi V_{cell}} = \frac{1}{V_{cell}} \frac{A_{wet}}{\varphi}$. As the wetted area scales as $-\varphi^2$, S_V^2 scales as $((-\varphi)^2/\varphi)^2 = \varphi^2$, as can also be seen in Fig. 2.15b. The Kozeny-Carman relationship might be, thus, a substitute to the power law coupling for the permeability.

Table 2.6 C_K quadratic fitting coefficients

TPMS	**Gyroid**	**Diamond**	**SplitP1**	**SplitP2**
c_0	5.78	4.93	4.64	3.86
c_1	-16.4	-13.5	-12.5	-9.80
c_2	12.3	9.83	9.02	6.81
R^2	0.9916	0.9940	0.9960	0.9986

Therefore, in accordance with the results of the previous section, for a given porosity value, the Gyroid structure had the highest permeability, followed by Diamond, SplitP1, and SplitP2. Fig. 2.15a shows that Gyroid and Diamond had relatively higher values at low porosities, with Gyroid showing the highest values among the TPMS structures analyzed. As porosity increased, the values of all structures tended to converge. This convergence was particularly evident for porosity values between 0.55 and 0.7, where the values of the different structures were almost identical.

Porosity-tortuosity-dependent correlations for relative permeability and inertial drag factor in TPMS structures

The porosity is not the only geometrical parameter that influences the permeability and the inertial drag factor: the tortuosity (among other descriptors) could be accounted for, too.

Thus, the results on the relative permeability and inertial drag factor of the different TPMS were fitted to find a power law as Eqs. (2.36) and (2.37) [101], [102].

$$K_{rel} = a_K \varphi^{g_K} \zeta^{l_K} \tag{2.36}$$

$$C_F = a_{CF} \varphi^{g_{CF}} \zeta^{l_{CF}} \tag{2.37}$$

For each TPMS a Least-Squares approach was employed to find the factor a_K, g_K, l_K and a_{CF}, g_{CF}, l_{CF} for K_{rel} and C_F, respectively, which are presented in Tab. 2.7. The dependence of K_{rel} and C_F on the porosity and tortuosity are illustrated in Figs. 2.16 and 2.17.

Table 2.7 Fitting coefficients for $K_{rel} - \varphi - \zeta$ and $C_F - \varphi - \zeta$ relationships

TPMS	Gyroid	Diamond	SplitP1	SplitP2
a_K	2.48e-02	2.07e-02	0.78e-02	1.39e-02
g_K	2.57	1.72	2.78	2.54
l_K	-3.02	-5.93	-2.10	-9.02
$R^2_{K_{rel}}$	0.9986	0.9999	0.9981	0.9999
a_{CF}	2.18e-02	2.41e-01	1.42e-01	4.78e-02
g_{CF}	-0.733	-3.27	-0.269	-2.16
l_{CF}	10.1	-9.48	5.93	6.83
$R^2_{C_F}$	0.9992	0.9932	0.9998	0.9999

The coefficient g_K represented the sensitivity of the permeability to porosity. The Diamond had the lowest value, suggesting that permeability in this structure was less affected by changes in porosity than the others. The coefficient l_K governed the influence of tortuosity on permeability. The negative values suggested that the decrease in tortuosity significantly amplified an increase in permeability, as the geometry became less and less complicate.

For the Diamond, despite its sharp decrease in C_F with porosity, the large negative tortuosity coefficient smoothed this decline. The combination of these effects resulted

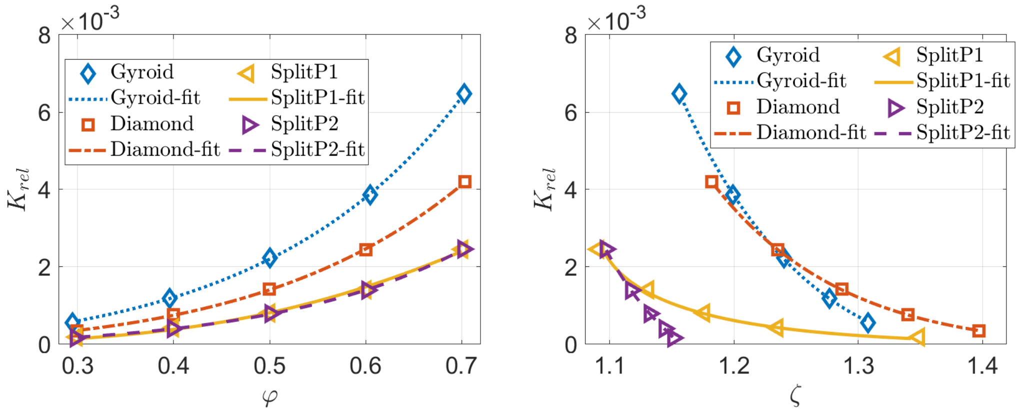

(a) (b)

Fig. 2.16 Relative permeability as function of porosity φ and tortuosity ζ, using Eq. (2.36). Modified from [79].

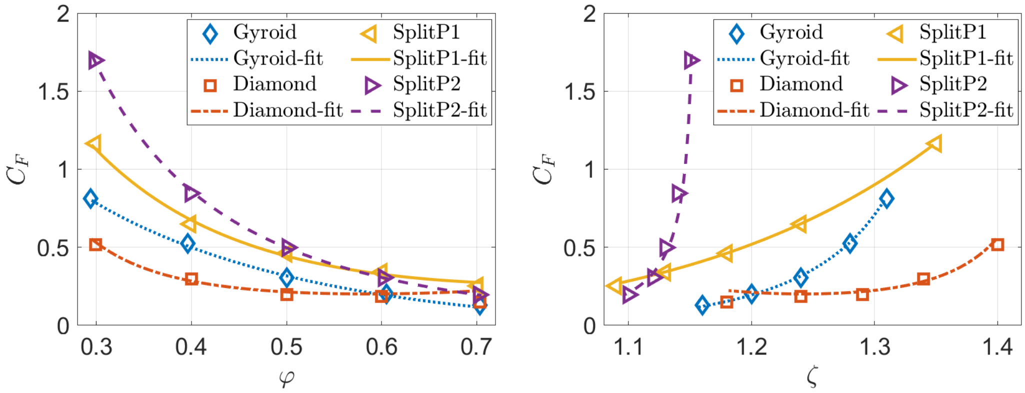

(a) (b)

Fig. 2.17 Relative permeability as function of porosity φ and tortuosity ζ, using Eq. (2.37). Modified from [79].

in a more gradual decrease in C_F, as seen in Fig. 2.12b, where the Diamond exhibited the least pronounced reduction in C_F, compared to other TPMS, at increasing porosity. For the remaining structures the positive l_{CF} coefficients associated with tortuosity further contributed to the decrease in C_F as porosity increased, reinforcing the trend driven by the g_{CF} coefficients.

Assessment of the models predictive capability against CFD results

To test the developed models for the Darcy and Darcy-Forchheimer regimes within TPMS, the predictive capability of the correlations described above were compared against CFD results on two different test-cases. The expected values of pressure drop were calculated using the permeability and drag inertial coefficient power laws determined in the previous sections, incorporating all the models examined: the power law associated with the correlation $K-\varphi$, $C_F-\varphi$, the power law for the correlation $K-\varphi-\zeta$, $C_F-\varphi-\zeta$, and the Kozeny-Carman relationship. Moreover, also the Ergun equation was compared to the performed regression analyses.

First, the same geometry described in Section 2.3.1 was used, with a porosity of 55%, i.e. a value different from the four values employed in the previous discussion. The values of K_{rel} and C_F were computed from the simulation results, and they were shown in Fig. 2.12 to lie pretty close to the fitting line. The relative errors between CFD and predicted values (computed as in Eq. (2.38)) were collected in Fig. 2.18.

$$\text{Relative error}(\%) = (\Delta p_{CFD} - \Delta p_{corr})/(\Delta p_{CFD}) \cdot 100 \tag{2.38}$$

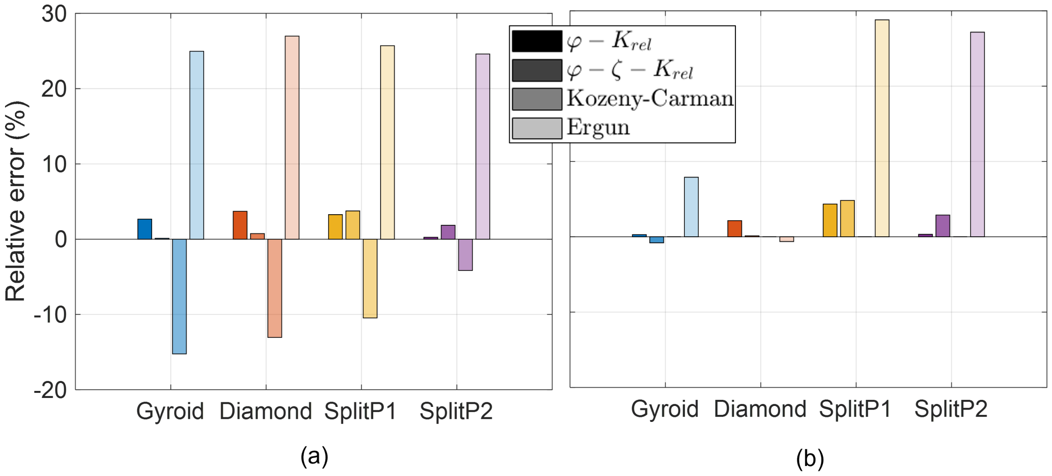

(a) (b)

Fig. 2.18 Comparison of predicted pressure drop for the unit cell with 55% porosity using the developed models and CFD results. (a) $Re_{D_h} \approx 5$, (b) $Re_{D_h} \approx 100$. Taken from [79].

The computed errors of the $K_{rel}-\varphi$, $C_F-\varphi$, $K_{rel}-\varphi-\zeta$, $C_F-\varphi-\zeta$ power laws were small - consistently below 10% - while the Kozeny-Carman relationship lead to larger discrepancies. The similar performance of these models suggested that

incorporating the tortuosity ζ in addition to porosity φ did not significantly enhance the predictive accuracy. This could be attributed to the interdependence of φ and ζ, as discussed in the previous section. Since ζ and φ are not entirely independent variables, the simpler $K_{rel} - \varphi$ model is sufficient for practical use, providing nearly identical results with reduced computational complexity.
The Ergun equation, while widely used for porous media, performed poorly across all Reynolds numbers and TPMS structures. At low Reynolds numbers, it consistently underpredicted pressure drop, with large errors particularly for the SplitP geometries, where the complex flow pathways deviated significantly from the assumptions underlying the Ergun model. Even at higher Reynolds numbers $Re_{D_h} \approx 100$, where inertial effects dominated, the Ergun equation showed only marginally improved accuracy for the Gyroid and Diamond structures but remained unreliable for SplitP geometries. This indicated that the Ergun model lacked the ability to account for the geometric complexity and tortuosity of TPMS.

In a second step, two circular pipes were designed, with diameters of 20 mm and 40 mm and periodic boundary conditions at inlet-outlet to reduce the computational burden, for a total length of 50 mm and a TPMS unit cell size $L_c = 5\,mm$, smaller than the 10 mm unit cell size used in the development of the correlations. This design choice enabled testing the scalability of the developed K_{rel} correlations to L_c different from those used during their formulation. The internal and external walls were set as no-slip. The geometry of the 40 mm diameter is displayed in Fig. 2.19. The TPMS filled within the pipes had a porosity of 60%. The mesh was prepared similarly to the grid of the single cells, already discussed previously. The expected values of pressure drop within those pipes were computed using the permeability and drag inertial factor power laws and compared to the CFD results.

The predicted pressure drops for a water flow at 20°C were compared to CFD simulations under two flow regimes ($Re_{D_h} \approx 5$ and $Re_{D_h} \approx 100$). Fig. 2.20 provides an overview of these comparisons, highlighting the relative errors and model performance under varying conditions. The numerical uncertainty of the CFD results on the pipes filled with TMPS has been considered equal to the numerical uncertainty computed for the single periodic cell. The developed $K_{rel} - \varphi$ and $K_{rel} - \varphi - \zeta$ correlations demonstrated superior accuracy compared to the Ergun and Kozeny-Carman equations. The relative errors for the developed models were consistently less than 10% across all configurations and Reynolds numbers, with the exception of SplitP1, where the error reached a maximum of 21%. In contrast, the Ergun

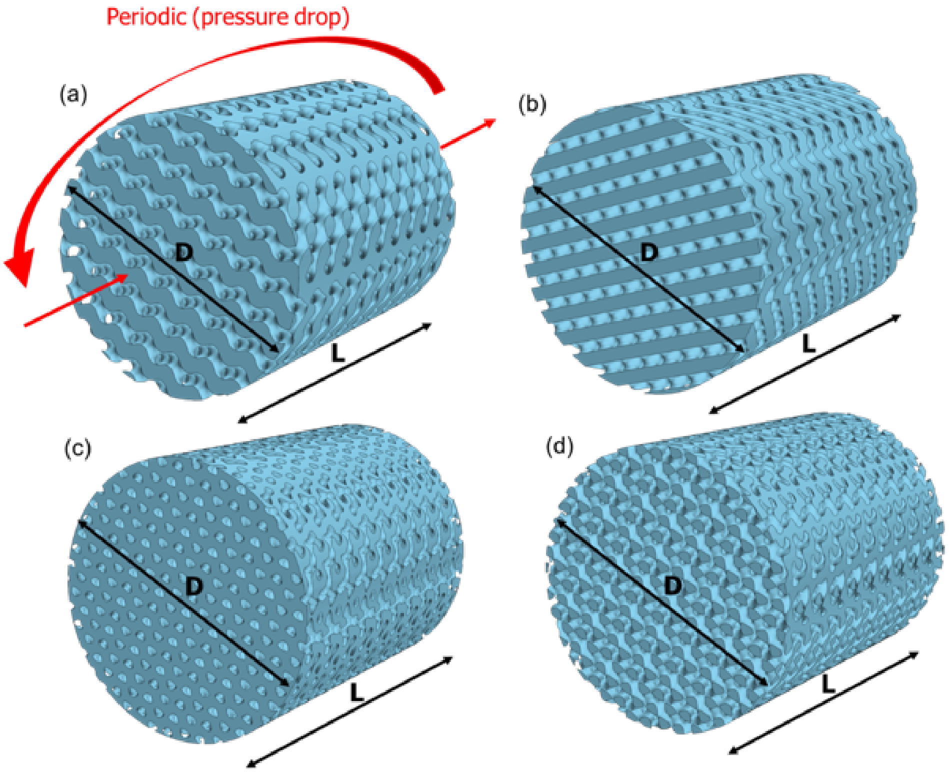

Fig. 2.19 Geometry and boundary conditions of the pipes D = 40 mm diameter (and L = 50 mm). a) Gyroid, b) Diamond, c) SplitP1 and d) SplitP2. Taken from [79].

equation produced errors as high as 30%, particularly for SplitP geometries. This highlighted once again the inability of the Ergun equation to capture the flow behavior within the complex geometries of TPMS structures. In the low Reynolds number regime ($Re_{D_h} \approx 5$), the Kozeny-Carman relation performed similar or worse than the developed correlations. Also here a notable agreement existed between predictions made using $K_{rel} - \varphi$ and $K_{rel} - \varphi - \zeta$ correlations, for the same reasons discussed before for the single unit cell. Consequently, the simpler $K_{rel} - \varphi$ correlation is recommended for practical applications due to its comparable accuracy and lower computational complexity.

The differences in pressure drop results between the pipe geometries and the single unit cell can be partially explained by the variation in hydraulic diameter D_h. In the pipes, the presence of the external wall modified the wetted area A_{wet} compared to the single cell configuration, resulting in deviations in D_h. These differences were more pronounced for simpler geometries like Gyroid or Diamond, where the wall significantly alters A_{wet}, while more complex geometries exhibited

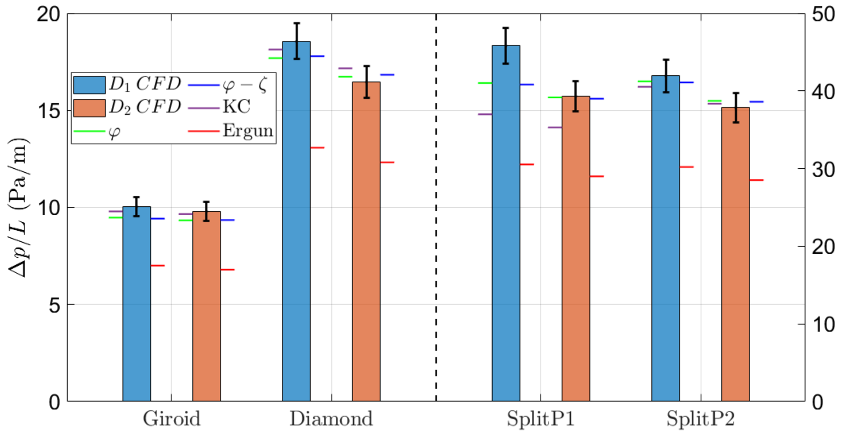

(a)

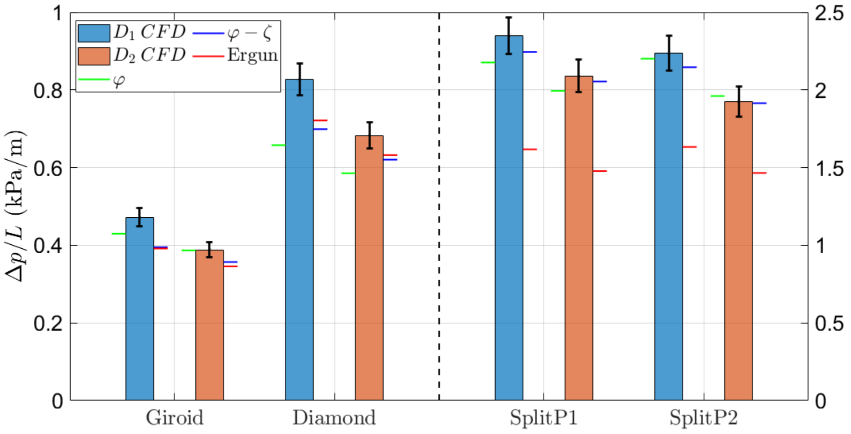

(b)

Fig. 2.20 Comparison of predicted linear pressure drops of water in the pipes at (a) $Re_{D_h} \approx 5$ and (b) $Re_{D_h} \approx 100$, using the developed models and CFD results. φ and $\varphi - \zeta$ in the legend refer to the developed power laws for the permeability, one depending only on porosity, and the other on porosity and tortuosity. KC refers to the Kozeny-Carman equation. The horizontal lines refer to the models predictions. Taken from [79].

less sensitivity to the wall effects. The smaller D_h in the pipe configurations, at the same Re_{D_h}, lead to a higher superficial velocity and, consequently, a higher linear pressure drop. This effect was particularly noticeable in the smaller diameter pipe $D_1 = 20\,mm$, where the reduced D_h amplifies the velocity and thus pressure drop compared to the larger diameter pipe $D_2 = 40\,mm$. Despite these geometric differences, the model predictions were within the uncertainty of the CFD results for both pipe sizes (except for SplitP1 with $D_2 = 20\,mm$). This results highlighted the scalability of the developed correlations to configurations beyond single unit cells, demonstrating their potential for use in practical engineering applications. The relatively small influence of pipe diameter on the predictive performance further emphasized the generalizability of the models.

The proposed correlations are, however, topology-dependent. Consequently, future studies will aim to identify additional governing parameters to establish generalized formulations capable of encompassing different TPMS topologies within a unified correlation framework. In this regard, the parameters L_c and c were not considered in the present study, as their inclusion would not meaningfully contribute to such generalization. Specifically, L_c represents the characteristic cell size, and all extensive quantities can be normalized with respect to it, thereby making the results independent of its value. Similarly, the isovalue c cannot be easily correlated with the geometric and hydraulic characteristics of TPMS structures — those responsible for momentum and heat transfer — and exhibits only limited variation across different topologies. Moreover, the inherent complementarity of the two SplitP values further restricts its usefulness as a governing parameter.

2.4 Thermal behavior

As highlighted in the Introduction, in the literature, many studies on the thermal capabilities of various TPMS are present, but most of them are problem-specific, without attempting to develop general correlations able to span different parameter spaces. This section seeks to investigate the thermal characteristics of solid TPMS in parallel with their hydraulic characteristics, so that thermal behavior can be inferred from hydraulic behavior.

2.4.1 Reynolds analogy

When a fluid flows near a surface, viscous effects occur at the solid-fluid interface. At relatively high Reynolds numbers, when the inertial effects predominate, viscous phenomena are confined to a very thin region adjacent to the surface, named the *boundary layer* [97]. The fundamental assumption of the boundary layer theory [103] is that its thickness is very small compared to the characteristic size of the domain over which the fluid is flowing, being external or internal flow. Thus, velocity and temperature fields must vary from the superficial to the free-stream values in such extremely thin layers. For that, gradients normal to the surface are substantially larger than the gradients parallel to it, thus diffusive terms along the surface can be neglected and the mass, momentum and energy conservation equations simplified. In this framework, the dimensionless characteristic equations of the thermal and hydraulic fields have closely resembling functional forms, as the mechanisms responsible for mixing within the fluid promote both momentum transport and heat transfer similarly. The hypothesis that analogous profiles of velocity and temperature develop within the flow is referred to as *Reynolds analogy*, and can allow to predict heat transfer capabilities from measured hydraulic impedance.

The Reynolds analogy is commonly expressed as in Eq. (2.39), where C_f is the friction coefficient and St is the Stanton number defined in Eq. (2.40). The Prandtl number is given in Eq. (2.41). Eq. (2.39) is rigorously valid only when $Pr = 1$ and in laminar regime when the normalized free-stream pressure gradients are negligible. However, for turbulent flows, the assumption of negligible pressure gradients can be relaxed, and the analogy still holds approximately.

$$\frac{C_f}{2} = St \tag{2.39}$$

$$St = \frac{Nu}{Re\,Pr} \tag{2.40}$$

$$Pr = \frac{\mu\, c_p}{\lambda} \tag{2.41}$$

For TPMS, the friction coefficient can be defined by considering as reference velocity U_s/φ, as in Eq. (2.42).

$$C_f = \frac{\bar{\boldsymbol{\tau}}_w}{\frac{1}{2}\rho(U_s/\rho)^2} \tag{2.42}$$

The wall shear stress vector $\boldsymbol{\tau}_w$ is defined as the projection of $\mathcal{R}$ on the wall normal versor $\boldsymbol{n}$.

$$\boldsymbol{\tau}_w = \mathcal{R} \cdot \boldsymbol{n} \tag{2.43}$$

When averaged over the entire wall of the TPMS, the only relevant direction in which it is not zero is the fluid direction, thus here $\overline{\tau}_w = \langle \boldsymbol{\tau}_w \hat{\boldsymbol{x}} \rangle_{A_{wet}}$, with $\hat{\boldsymbol{x}}$ the x-axis versor.

Concerning the Nusselt number Nu, it can be defined for the constant wall temperature or constant wall heat flux, as in Eqs. (2.44-2.45).

$$Nu_{T_w} = \frac{\overline{q}_w}{\Delta T_{LM}} \frac{D_h}{\lambda} \tag{2.44}$$

$$Nu_{q_w} = \frac{q_w}{\overline{T}_w - \langle T_b \rangle_V} \frac{D_h}{\lambda} \tag{2.45}$$

In the above equations, for the imposed constant wall temperature T_w, the logarithmic mean temperature is defined in Eq. (2.46) and the average wall heat flux over the TPMS in Eq. (2.47).

$$\Delta T_{LM} = \frac{T_{b,o} - T_{b,i}}{ln\left(\frac{T_w - T_{b,i}}{T_w - T_{b,o}}\right)} \tag{2.46}$$

$$\overline{q}_w = \lambda \langle \nabla T \cdot \boldsymbol{n} \rangle_{A_{wet}} \tag{2.47}$$

$T_{b,o}$ and $T_{b,i}$ are the outlet and inlet bulk temperatures, with T_b the mass flow average of the temperature for a constant properties fluid, defined in Eq. (2.48), where A_c is the fluid cross section and u_x the velocity in the flow direction x.

$$T_b = \frac{\int_{A_c} u_x T dA}{\int_{A_c} u_x dA} \tag{2.48}$$

For the imposed constant wall heat flux q_w, the average wall temperature over the TPMS is defined in Eq. (2.49) and the mean bulk temperature is defined in Eq. (2.50), as an approximation of the exact integral mean of $T_b(x)$ over L_c.

$$\overline{T}_w = \langle T_w \rangle_{A_{wet}} \tag{2.49}$$

$$\langle T_b \rangle = \frac{\int_{TPMS} u_x T dVol}{\int_{TPMS} u_x dVol} \approx \frac{\int_{L_c} \left(\frac{\int_{A_c} u_x T dA}{\int_{A_c} u_x dA} \right) dx}{L_c} \tag{2.50}$$

The founding hypotheses of the Reynolds analogy - namely, the assumptions of a very thin boundary layer thickness relative to the characteristic size and negligible pressure gradients - do not hold to TPMS in the transitional regime, object of the present study. This is because TPMS feature continuous varying surfaces, tiny pores and, in this work, flow conditions have not yet reached a fully turbulent state. Nonetheless, it is reasonable to assume that a parallelism between momentum and energy transport exists. Thus, the purpose of this section is the derivation of a modified analogy that could establish a direct connection between the friction factor and the Stanton number.

2.4.2 Computational methodology

The open-source code OpenFOAM v2212 was used for the analysis, which again required a wide range of parameters to be investigated, so an automated algorithm (this time not only for running simulations but also in grid production) was used, exploiting the potential of the open-source code. For more information on the automated process, refer to Appendix C.2 .

Boundary conditions and simulation setup

As in the previous section, a single periodic cell was employed for both hydraulic and thermal analysis. Thermal periodicity was enforced on the normalized temperature θ along the flow direction, defined in Eq. (2.51) [103] - for more information about this boundary condition implementation, refer to Appendix B.

$$\theta = \frac{T_w - T}{T_w - T_b} \tag{2.51}$$

On the other two directions, the standard periodicity on the temperature field was enforced. To impose the flow, a momentum source was used along the x-axis, while the thermal driver consisted of a uniform constant temperature or heat flux at the wall. Again, the SIMPLE algorithm [95] of OpenFOAM v2212 and its scalar transport solver [104] were used. A linear upwind discretization scheme was used for the convective terms and a central difference scheme for the diffusive terms. Fig. 2.21 shows the applied boundary conditions

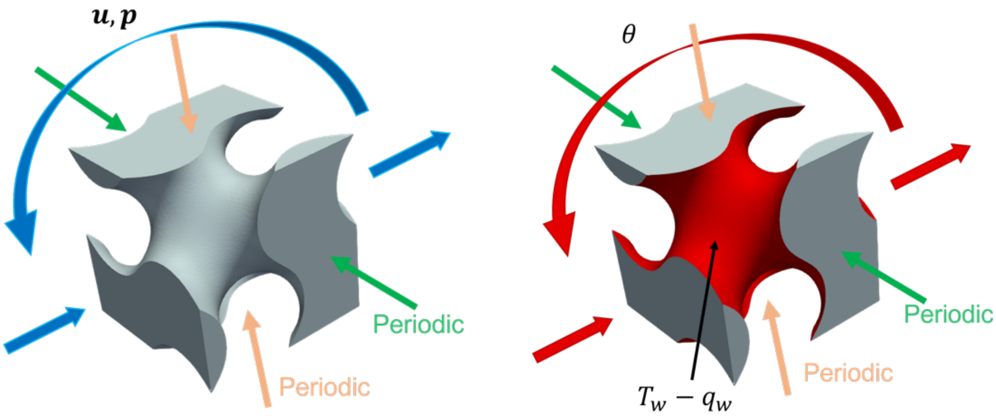

(a) (b)

Fig. 2.21 Thermal-hydraulic boundary conditions.

Conversely from the previous section, whose analysis focused on water, this section studies an artificial fluid with $Pr = 1$.

Simulations were conducted for different Reynolds numbers, defined in Eq. (2.12), in the range of $20-100$, and for porosity values of 30%, 40%, 50%, 60% and 70%. Below $Re_{D_h} < 20$, conduction prevailed over convection, leading to values of ΔT_{LM} or $\overline{T}_w - \langle T_b \rangle_V$ that were far too small, resulting in numerical cancellation in the calculation of the Nusselt numbers.

Mesh generation and mesh convergence analysis

The computational grid was constructed as in the previous section, but by means of the OpenFOAM mesher snappyHexMesh [105], thus producing a hexahedra-dominant mesh rather than polyhedral as created by the STAR-CCM+ mesher. Again, since the analysis is purely laminar, boundary layers were not constructed. For more detail on the mesh generation of TPMS in OpenFOAM, refer to Appendix C.2.2.

The numerical uncertainty of the results was calculated using a grid convergence analysis, similar to Section 2.3.1. Four meshes were created for the TPMS at 30% porosity and their information are presented in Tab. 2.8. Due to the characteristics of the OpenFOAM mesher, which is less efficient than STAR-CCM+ one, producing coarse but good quality grids is more difficult. Therefore, the *Ref4* grids contains a larger number of cells than the polyhedral *Ref4* in Tab. 2.1.

Table 2.8 Number of hexahedral cells in the 30% porosity TPMS.

	Ref1	**Ref2**	**Ref3**	**Ref4**
Gyroid	518k	154k	65k	38k
Diamond	518k	154k	65k	56k
SplitP1	539k	194k	100k	72k
SplitP2	664k	241k	93k	64k

In this case, being the *Ref1* grid excessively refined, the *Ref2* was selected as the employed numerical mesh for the rest of the analysis. The chosen meshes for the 30% porosity are shown in Fig. 2.22.

The GCI for the second finest mesh is thus calculated as Eq. 2.52.

$$GCI = \frac{1.25 \cdot er_a^{32}}{r_{32}^{\gamma} - 1} \tag{2.52}$$

At the maximum Reynolds number considered of 100 and 30% porosity, the numerical uncertainties on the pressure drop, mean wall shear stress in the fluid direction $\overline{\tau}_w$, mean wall heat flux $\bar{q}_w$ and bulk temperature raise $\Delta T_{o-i} = T_{b,o} - T_{b,i}$ were computed, in the configuration with imposed constant wall temperature.

The trend of the normalized Δp, $\overline{\tau}_w$, $\overline{q}_w$ and ΔT_{o-i} with respect to the normalized average cell size is shown in Fig. 2.23, and the calculated respective uncertainties are reported in Tab. 2.9, whereas the computed orders of convergence are displayed in Tab. 2.10. Note that when using the least-square approach recommended by ASME standard [96], slightly larger values than the theoretical order of convergence are tolerated, as in this case 2.05 for a second-order discretization scheme. With respect to the hydraulic study, slightly larger computed order were found, probably because the grids were hexahedral-dominant - generally more accurate than polyhedral grids, having lower artificial diffusivity - and were generated with a larger number of cells.

The trend is convergent for all parameters but for the shear stress of the Gyroid, which is anyway decreasing, thus conservative, and that has a variation of less than

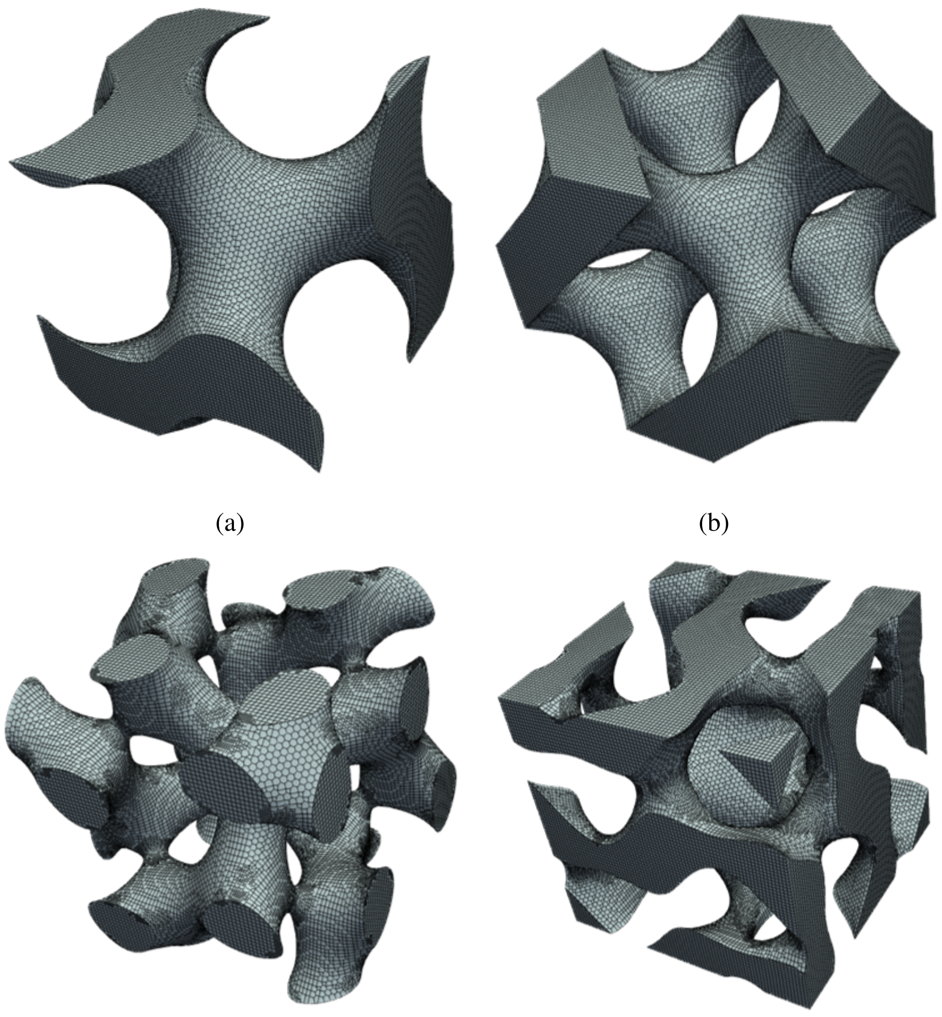

(a) (b)

(c) (d)

Fig. 2.22 Numerical grid employed for the thermal-hydraulic simulations. (a) Gyroid, (b) Diamond, (c) SplitP1, (d) SplitP2.

5% between the two most refined meshes. The Gyroid $\overline{\tau}_w$ has indeed the largest numerical uncertainty.

2.4.3 Results and discussion

This section reports the results of the analysis of similarities between hydraulic and thermal fields in TPMS: first, a study on the dimensional quantities for the different TPMS topologies and then on the dimensionless variables. The analysis

Table 2.9 Relative numerical uncertainties of the considered quantities.

	Δp	$\overline{\tau}_w$	$\overline{q}_w$	ΔT_{o-i}
Gyroid	1%	7%	0.3%	0.2%
Diamond	2%	2%	0.9%	0.2%
SplitP1	2%	3%	2%	1%
SplitP2	3%	4%	0.7%	2%

Table 2.10 Computed orders of convergence γ for the considered quantities.

	Δp	$\overline{\tau}_w$	$\overline{q}_w$	ΔT_{o-i}
Gyroid	1.48	1.33	2.00	2.05
Diamond	2.05	1.50	1.58	2.05
SplitP1	2.00	1.50	2.05	2.05
SplitP2	2.00	2.01	2.05	2.05

was performed on global or average quantities, because the aim of the work is the extension to real cases, in which the measurable quantities are global quantities such as pressure drop and flow rate.

Analysis of dimensional quantities

With Reynolds numbers ranging between 20 and 100, the four TPMS topologies at the porosities 0.3 - 0.7 were simulated.

At $Re_{D_h} = 20$ and 100 for the mid-porosity Gyroid, the velocity magnitude and normalized temperature field are shown in Figs. 2.24 and 2.25. Both U and θ were normalized with respect to their maximum value, hence $U^* = U/max(U)$ and $\theta^* = \theta/max(\theta)$.

To compute T_b, 80 slices were created along the flow direction and the bulk temperature of each slice was computed approximating Eq. (2.48) as in Eq. (2.53). The number of slices was chosen as the number of discrete blocks created by the OpenFOAM mesher along the three principal direction, i.e. the maximum number of discretization points of the generated mesh in each principal direction.

$$T_b = \frac{\int_{slice} u_x T dVol_{slice}}{\int_{slice} u_x dVol_{slice}} \tag{2.53}$$

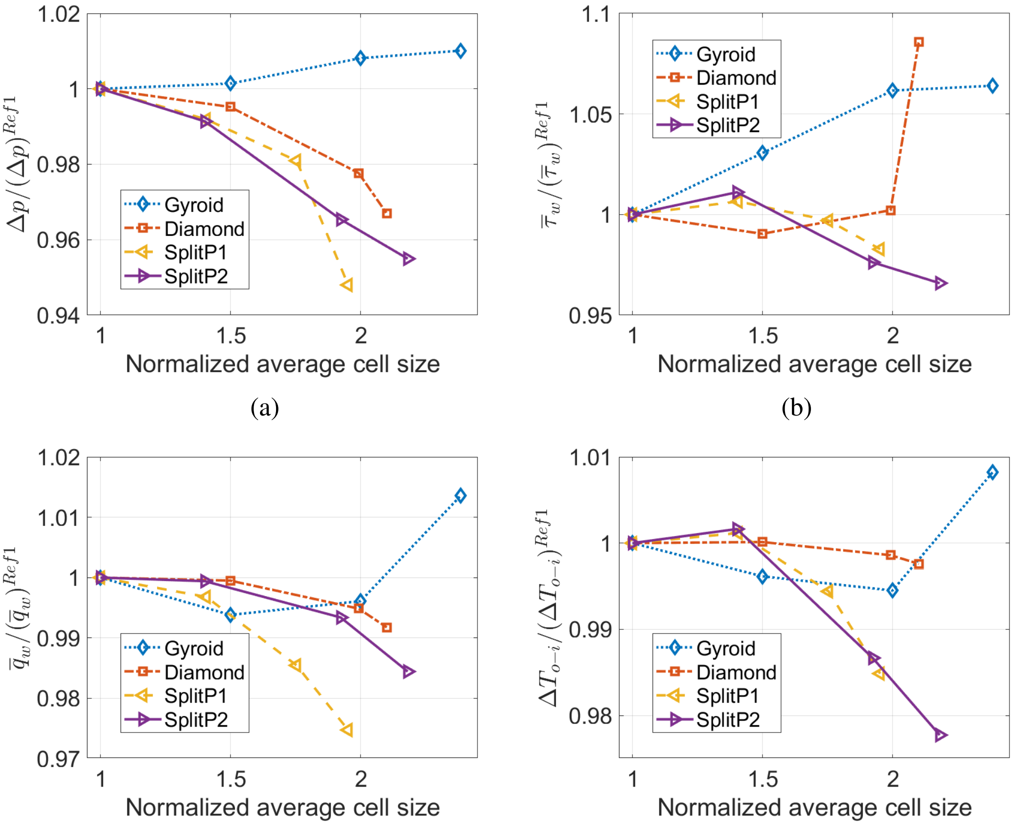

(a) (b)

(c) (d)

Fig. 2.23 Grid convergence results for the computational mesh used in the thermal-hydraulic simulations.

The contrast in U and θ fields between the two Reynolds numbers can be remarked. At the high Reynolds number, the flow appeared less influenced by the presence of the wall, generating a more uniform profile along the flow direction. For both Re_{D_h}, the temperature and velocity fields are qualitatively similar, as expected.

The average wall shear stress, linear pressure drop and average wall heat flux (at constant wall temperature) are plotted in Figs. 2.26-2.28 as function of the Re_{D_h}.

Similarly to the results of Section 2.3, the TPMS having the largest flow impedance is the SplitP2. Note that the values of the linear pressure drop are different from Fig. 2.9 because the fluid properties are different. Figs. 2.26-2.27 have different y-axis limits because the range of the SplitP was excessively large for the Gyroid and Diamond. Both SplitP1 and SplitP2 have greater values of $\frac{\Delta p}{L}$ and $\overline{\tau}_w$ than Diamond and Gyroid, at all the porosities. For large porosities, the hydraulic results of SplitP1

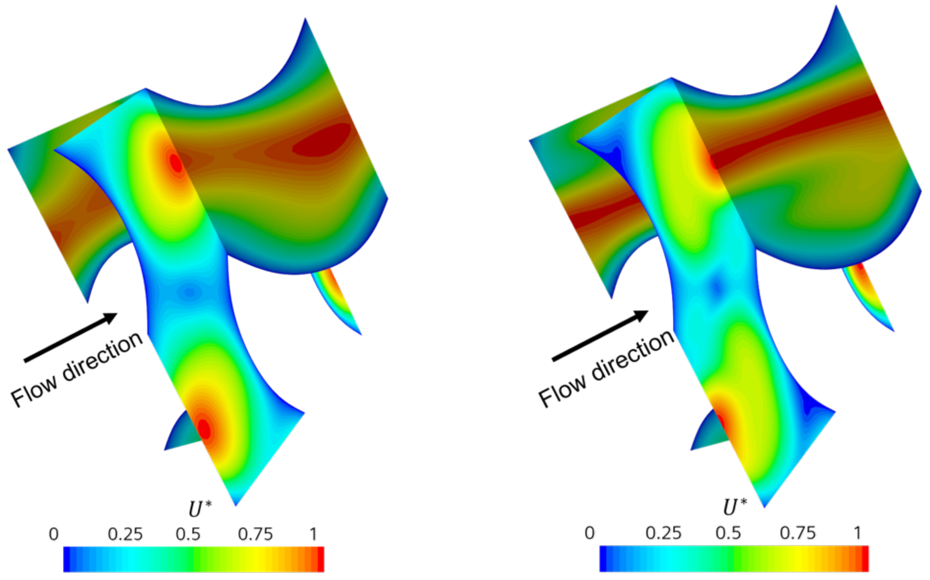

(a) (b)

Fig. 2.24 Normalized temperature in Gyroid, 50% porosity, computed on two cut sections (parallel and normal to the flow direction, respectively). (a) $Re_{D_h} = 20$ and (b) $Re_{D_h} = 100$.

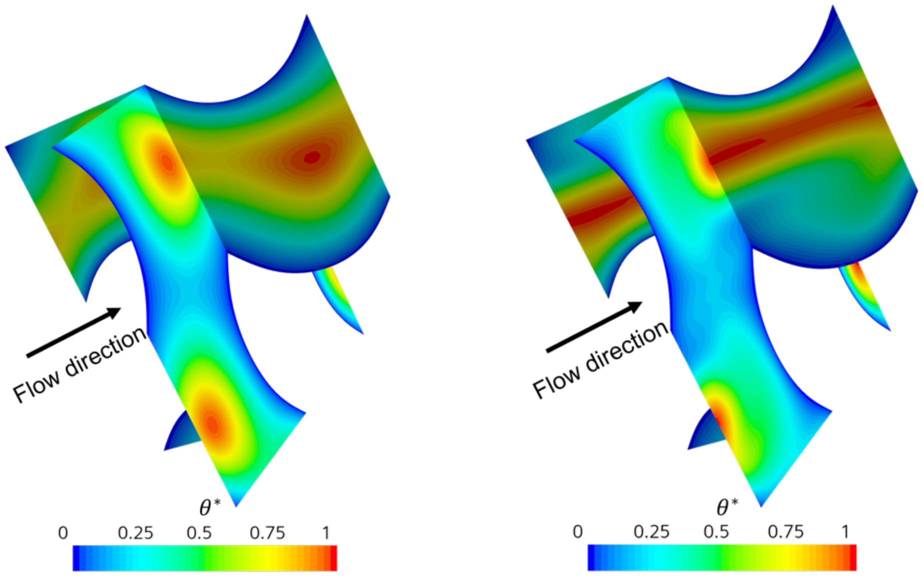

(a) (b)

Fig. 2.25 Normalized velocity magnitude in Gyroid, 50% porosity, computed on two cut sections (parallel and normal to the flow direction, respectively). (a) $Re_{D_h} = 20$ and (b) $Re_{D_h} = 100$.

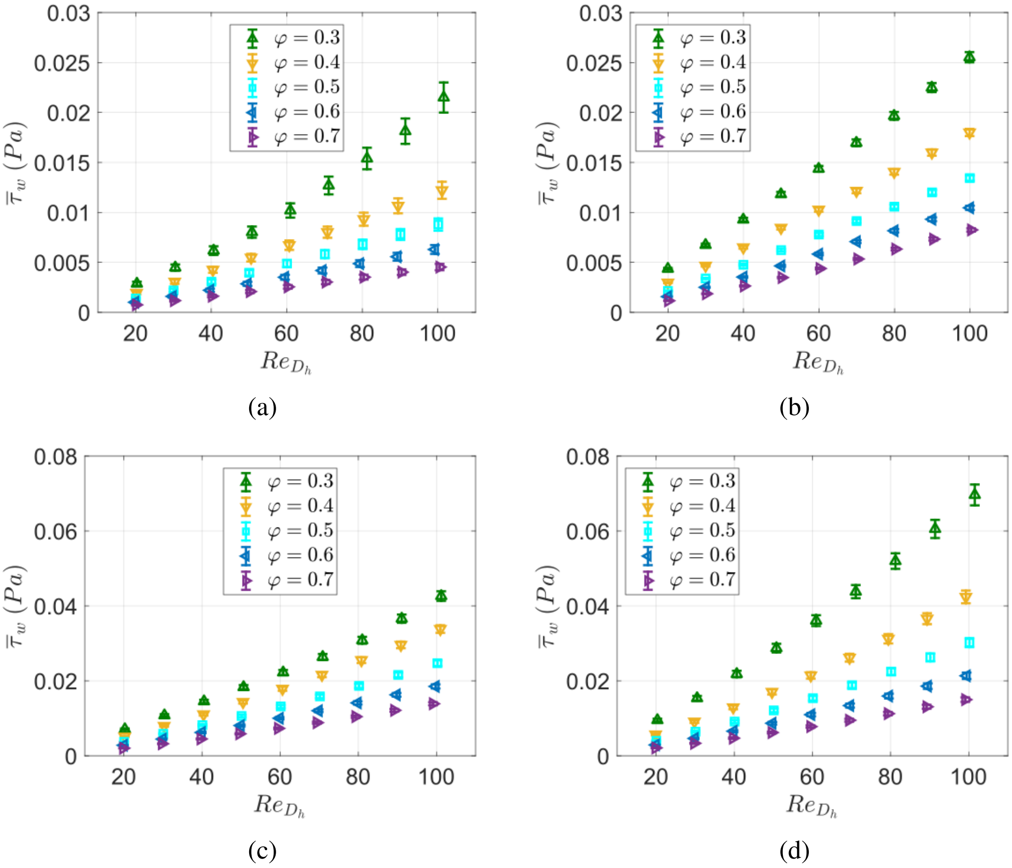

(a) (b) (c) (d)

Fig. 2.26 Average wall shear stress on the four TPMS and porosities. (a) Gyroid, (b) Diamond, (c) SplitP1 and (d) SplitP2.

and SplitP2 appeared similar, as was found also in the previous section, for C_F. Both linear pressure drop and shear stress increased with Reynolds number and decreased with porosity, as the porosity diminished the flow path became more complex and the hydraulic diameter decreased, too.

In a first-order approximation, stress can be roughly estimated using Eq. (2.54), by considering that the velocity should reduce from the mean value U_s/φ to zero at wall within the boundary layer thickness δ.

$$\overline{\tau}_w \sim \mu \frac{U_s/\varphi}{\delta} \tag{2.54}$$

Although it is extremely challenging to estimate the boundary layer thickness in a structure as complex and constantly evolving as TPMS, δ can be assumed to

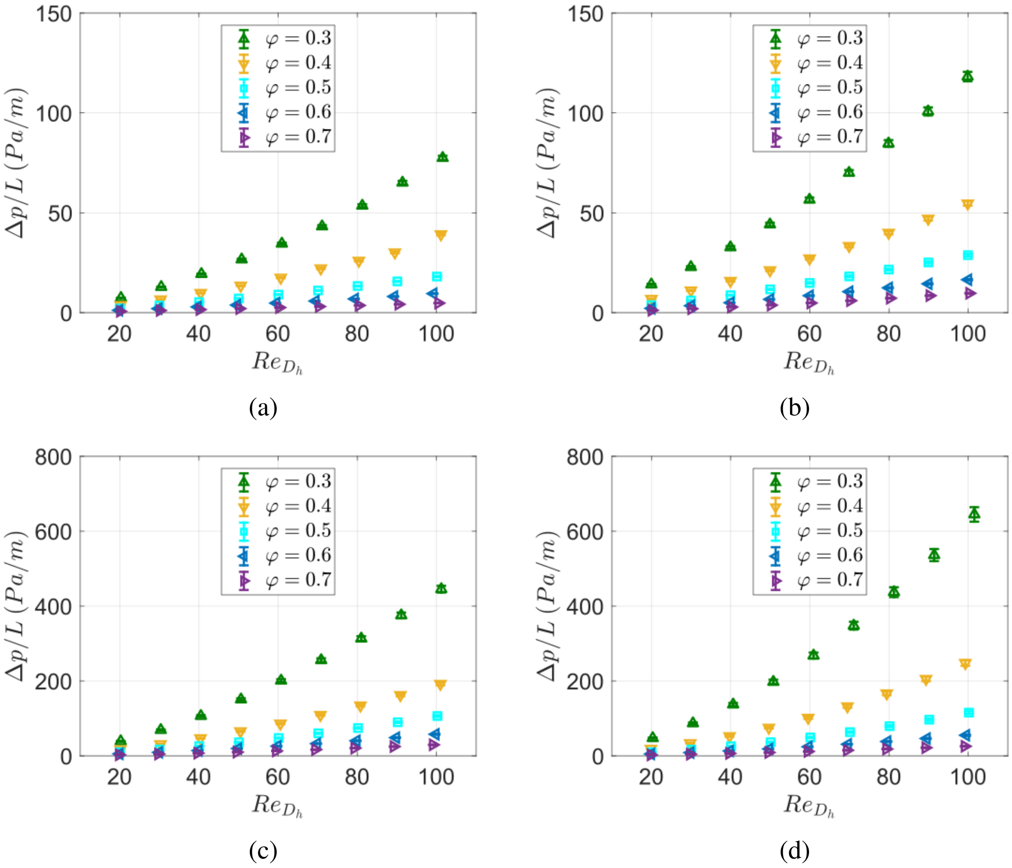

(a) (b)

(c) (d)

Fig. 2.27 Linear pressure loss on the four TPMS and porosities. (a) Gyroid, (b) Diamond, (c) SplitP1 and (d) SplitP2.

increase with the hydraulic diameter, and so with porosity, which is the reason why the shear stress rose as porosity diminished. On the other hand, probably $\mathscr{d}$ decreases with Reynolds number, as it is also highlighted by Figs. 2.24-2.25.

Concerning the average wall heat flux, it had a behavior close to the hydraulic variables: the exchanged heat flux raised with Reynolds number and reduced with porosity. The order of magnitude was similar for the four topologies, but the Diamond presented quite analogous values at varying porosity levels, while the other structures had more accentuated differences.

It is interesting to notice that the structure with the largest heat flux for all porosity was SplitP1, not in line with the largest impedance structure. It should also be remarked that the wetted areas of the TPMS are different, having the SplitP the largest A_{wet} and the Gyroid the smallest (see Fig. 2.2b). Thus, even if the heat fluxes

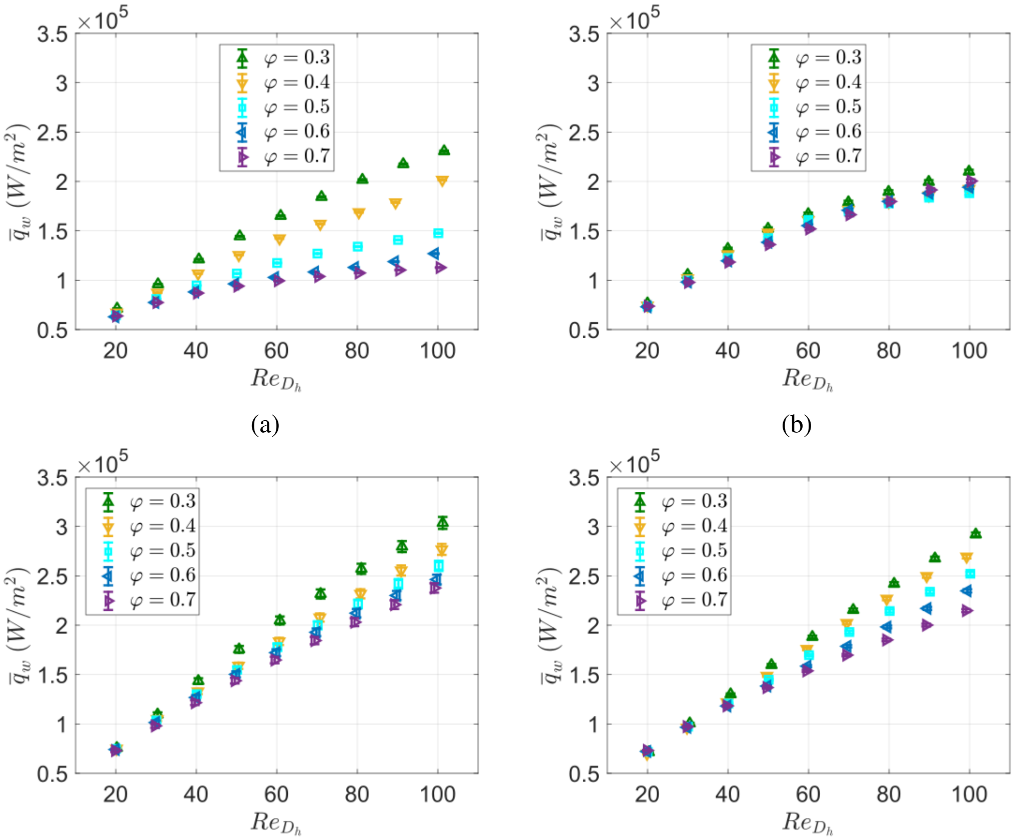

(a) (b)

(c) (d)

Fig. 2.28 Average wall heat flux on the four TPMS and porosities. (a) Gyroid, (b) Diamond, (c) SplitP1 and (d) SplitP2.

were similar between the structures, the actual heat transfers $Q = \overline{q}_w A_{wet}$ resulted considerably higher in SplitP than Gyroid and Diamond.

Analysis of dimensionless quantities

In Fig. 2.29 the friction coefficient is plotted, for the four TPMS structures.

From Eqs. (2.42) and (2.54), Eq. (2.55) might be written, where Re_{δ} is the Reynolds number referred to the boundary layer thickness.

$$C_f \sim \frac{2\mu}{\delta \rho U_s/\varphi} \sim \frac{2}{Re_{\delta}} \tag{2.55}$$

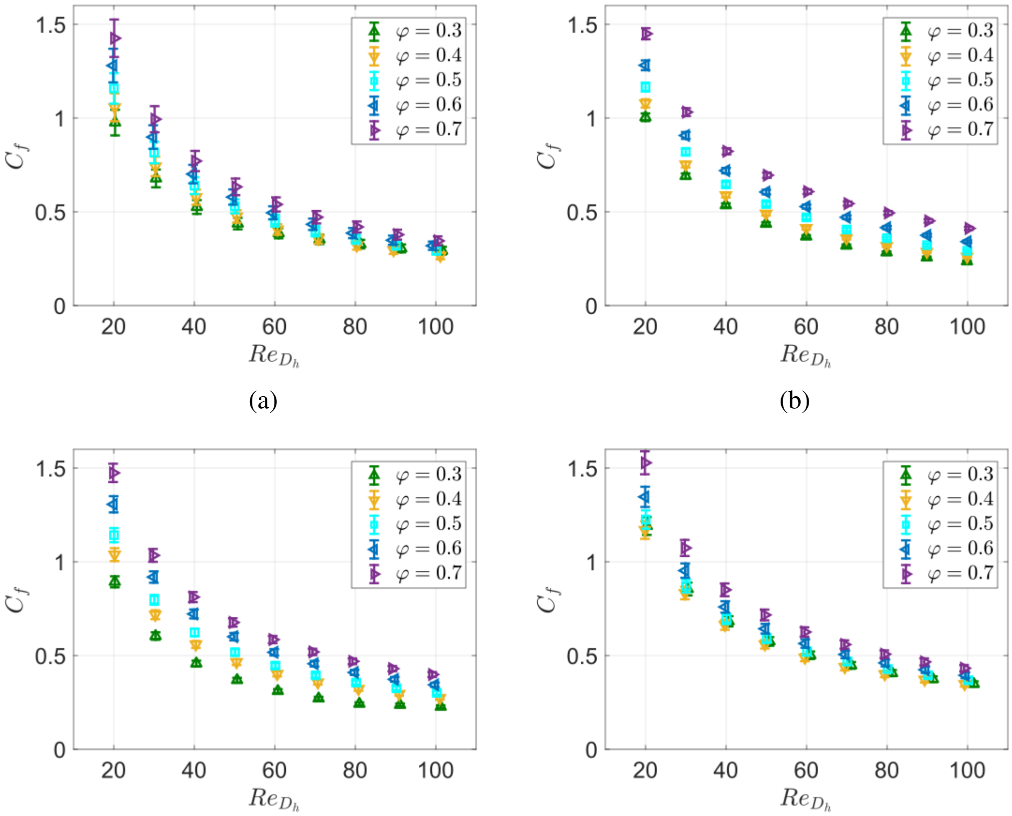

(a) (b) (c) (d)

Fig. 2.29 Friction coefficient of the four TPMS and porosities. (a) Gyroid, (b) Diamond, (c) SplitP1 and (d) SplitP2.

Considering again that δ is some increasing function of D_h, Re_δ is expected to be an increasing function of Re_{Dh}. This can explain the inverse trend of the friction coefficient with the Reynolds number. It is, however, far more difficult to make assumptions on the actual dependence of the boundary layer thickness on the porosity. If we consider that $\delta \sim D_h^n$, with $0 < n < 1$, similar to the Prandtl hypothesis [97], then Eq. (2.55) becomes Eq. (2.56), which could explain the increase in C_f with D_h and φ.

$$C_f \sim \frac{2D_h^{1-n>0}}{Re_{D_h}} \tag{2.56}$$

Another useful dimensionless quantity is the friction factor, defined in Eq. (2.57). By starting from the Darcy-Forchheimer equation (2.20), it might be found a correlation of f with respect to the permeability K and the inertial drag coefficient C_F, as in Eq. (2.58).

$$f = \frac{\Delta p}{L} \frac{D_h}{\frac{1}{2}\rho(U_s/\varphi)^2} \tag{2.57}$$

$$f = \frac{1}{Re_{D_h}} \left(\frac{2\varphi D_h^2}{K} \right) + \left(\frac{2\varphi^2 D_h C_F}{\sqrt{K}} \right) \tag{2.58}$$

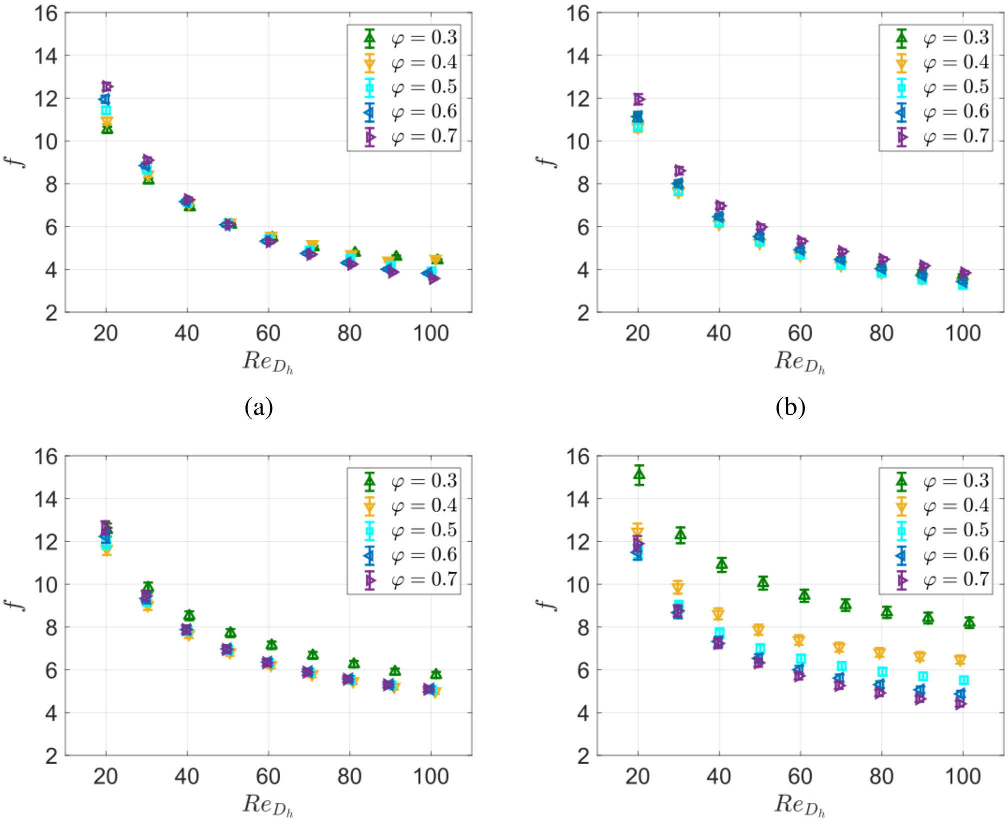

(a) (b)

(c) (d)

Fig. 2.30 Friction factor of the four TPMS and porosities. (a) Gyroid, (b) Diamond, (c) SplitP1 and (d) SplitP2.

The friction factor is plotted against the Reynolds number for the studied TPMS in Fig. 2.30. The trend of f with Re_{D_h} was clearly inverse, as highlighted in Eq. (2.58), but it did not show a monotonic trend with porosity. This is explained by the power exponents of K and C_F, from Tab. 2.4, where approximately $K_{rel} \sim \varphi^3$ and

$C_F \sim \varphi^{-2}$. Thus, substituting those trends within Eq. (2.58) and considering that $D_h = 4\varphi L^3/A_{wet}$ resulted in Eq. (2.59).

$$f \sim \frac{1}{Re_{D_h}}\left(\frac{\varphi^3}{A_{wet}^2\varphi^3}\right)+\left(\frac{\varphi^3\varphi^{-2}}{A_{wet}\sqrt{\varphi^3}}\right) \sim \frac{1}{Re_{D_h}A_{wet}^2}+\frac{1}{A_{wet}\varphi^{0.5}} \tag{2.59}$$

The wet area has a parabolic trend such as $A_{wet} = c_0 + c_1\varphi - c_2\varphi^2$, with parameters c_0, c_1 and c_2 depending on TPMS. If we operate a change of variable $w = 1/\varphi > 1$, then $A_{wet} = (c_0w^2 + c_1w - c_2)/w^2$ and Eq. (2.59) becomes Eq. (2.60).

$$f \sim \frac{w^4}{Re_{D_h}(c_0w^2+c_1w-c_2)^2}+\frac{w^{2.5}}{c_0w^2+c_1w-c_2} \tag{2.60}$$

The first term of the above equation decreases with w, i.e increases with porosity, conversely to the second term, increasing with w and diminishing with φ.
The very large deviations between TPMS in the linear pressure drop were smoothed out in the friction factor by the presence of the hydraulic diameter in f definition, so that the friction factor values appear closer.

The Nusselt and Stanton numbers as function of Reynolds numbers are presented in Figs. 2.32-2.33. The small uncertainties are not plotted for graphical clarity. In these two figures the results at imposed T_w and q_w are shown.

The Nusselt number almost always increased with the Reynolds number, while the Stanton number had an inverse proportionality, closely mirroring the trend of the C_f. The trend at imposed constant temperature was similar to that at imposed constant heat flux in all topologies, as expected.
Looking at the Gyroid - Fig. 2.32a - the Nu growth rate with Re_{D_h} decreased as φ increased and the porosity effect was more pronounced at low Re_{D_h}.
The other three TPMS had a more significant dependence on porosity, with Nu almost always increasing with φ. At low porosities, SplitP1 and SplitP2 had slightly crossing Nusselt values, which however remained within theirs numerical uncertainty (2%). This increasing trend with φ could be explained with some general considerations on the Nusselt number significance, as in Eq. (2.61). The Nusselt number is the ratio between the convective (i.e. total) and conductive heat transfer rate at a boundary [103].

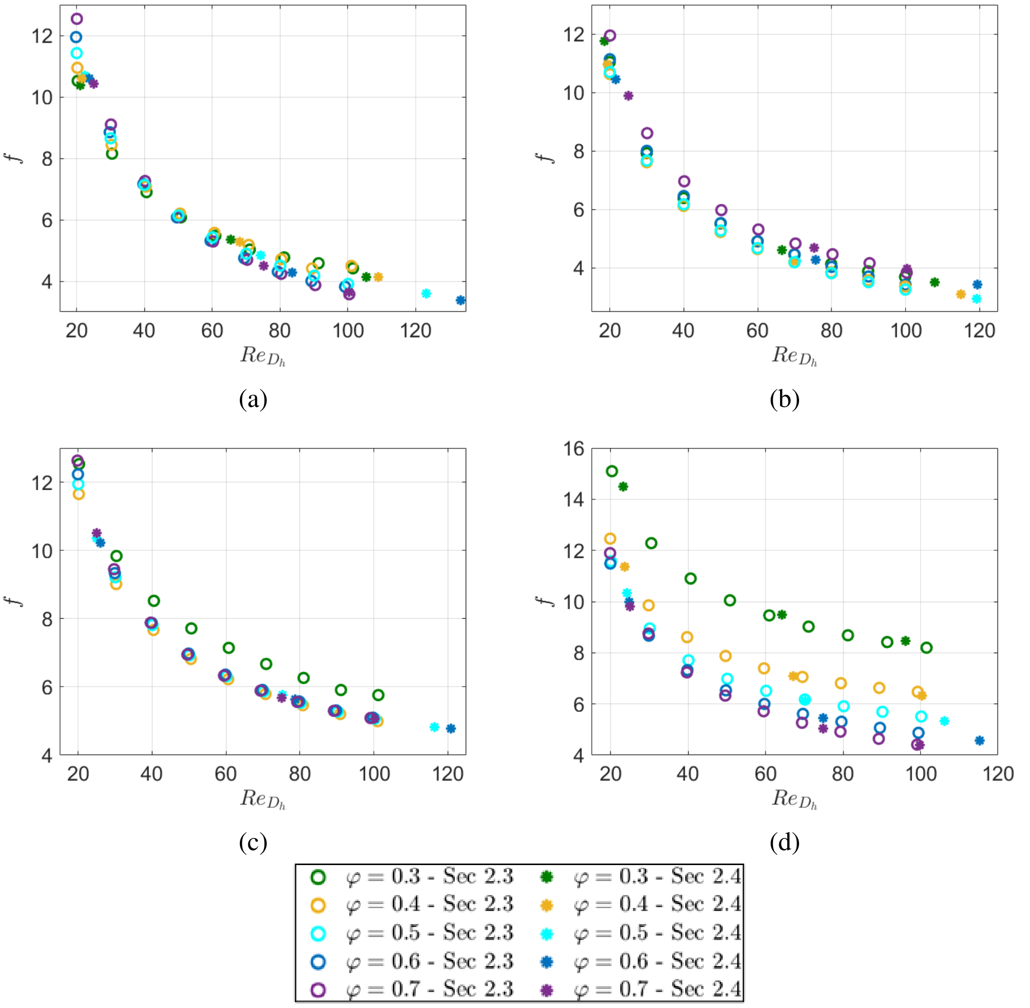

(a) (b) (c) (d)

Fig. 2.31 Comparison of the friction factor computed within the purely hydrodynamic analysis of Section 2.3 and the present section study.(a) Gyroid, (b) Diamond, (c) SplitP1 and (d) SplitP2.

$$Nu = \frac{Convective\ heat\ transfer\ rate}{Conductive\ heat\ transfer\ rate} \tag{2.61}$$

Thus, Nusselt number can be interpreted as $Nu = (\frac{Q}{A_w})/(\frac{\lambda}{D_h})$. Being $D_h = 4L^3\varphi/A_w$, $Nu \sim \frac{Q\varphi}{A_w^2}$. As before, using the variable change $w = 1/\varphi$ and considering the wet area parabolic trend, the Nusselt number scales as Eq. (2.62), which, at constant power Q, decreases with w, thus increasing with φ.

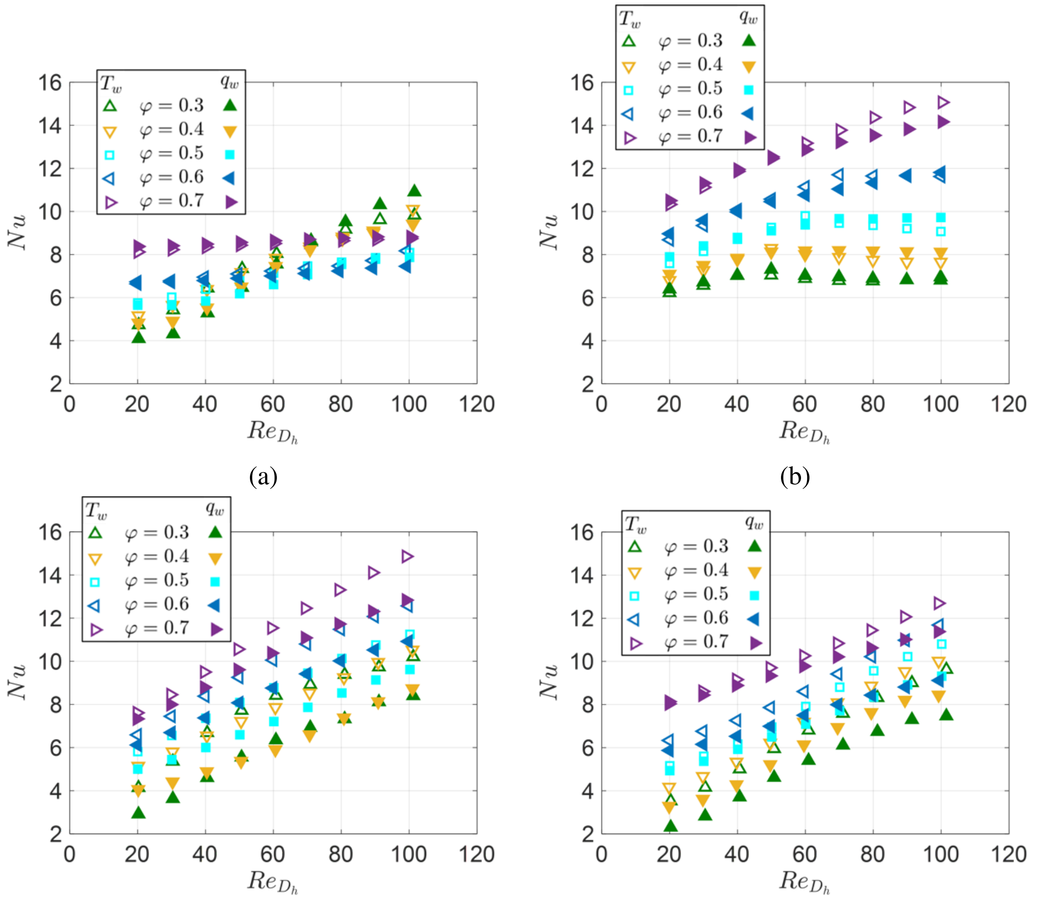

(a) (b)

(c) (d)

Fig. 2.32 Nusselt number of the four TPMS and porosities. (a) Gyroid, (b) Diamond, (c) SplitP1 and (d) SplitP2. T_w and q_w refer to the imposed constant T_w and q_w, respectively.

$$Nu \sim Q \frac{w^3}{(c_0 w^2 + c_1 w - c_2)^2} \tag{2.62}$$

The calculated Nu were compared to the results from Cheng et al. [17], that used a correlation with a quadratic dependence on the porosity, as in Eq. (2.63). They fitted Diamond and Gyroid results at approximately the same Re_{D_h} and φ range of the present study. If the order of magnitude is the same, their correlation results differ significantly from the present study. However, Cheng et al. [17] did not use the *infinite* porous medium assumption with periodic boundaries, but arranged eight cells in an array, applied symmetry instead of periodicity and inlet and outlet as extruded square channels. This configuration can significantly impact the results on

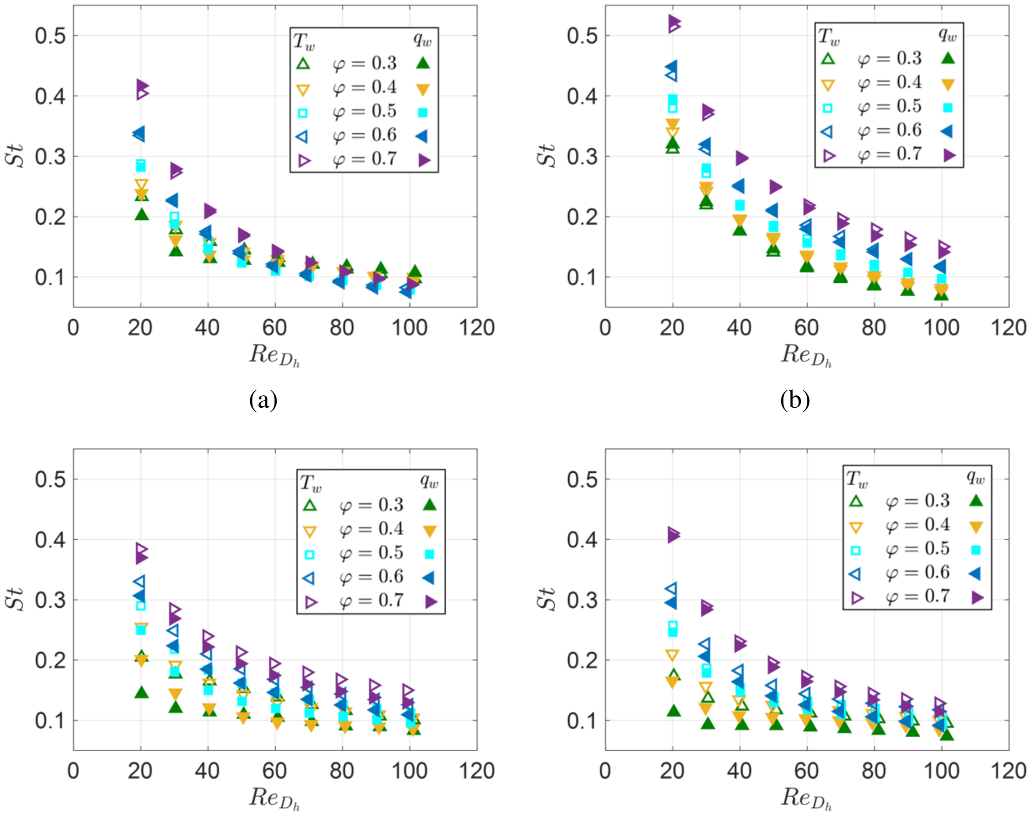

(a) (b)

(c) (d)

Fig. 2.33 Stanton number of the four TPMS and porosities. (a) Gyroid, (b) Diamond, (c) SplitP1 and (d) SplitP2. T_w and q_w refer to the imposed constant T_w and q_w, respectively.

the first and last TPMS cells, where the fully developed hypothesis is certainly not verified, thus influencing the overall Nusselt calculations.

$$Nu = (a + b\varphi + c\varphi^2)Re^d \tag{2.63}$$

As previously mentioned, the pure Reynolds analogy compares the C_f and the St. However, in real applications, the measurable quantity is the pressure drop rather than the shear stress, so in Figs. 2.34-2.37 , the St was compared not only with C_f but also with f, in the original form $2St/C_f$ or $2St/f$.

It appears clear that the pure Reynolds analogy, even considering f instead of C_f, was not sufficient to describe the relationship between the hydraulic and thermal behavior in TPMS. Indeed, for all TPMS there was a dependence on the Reynolds

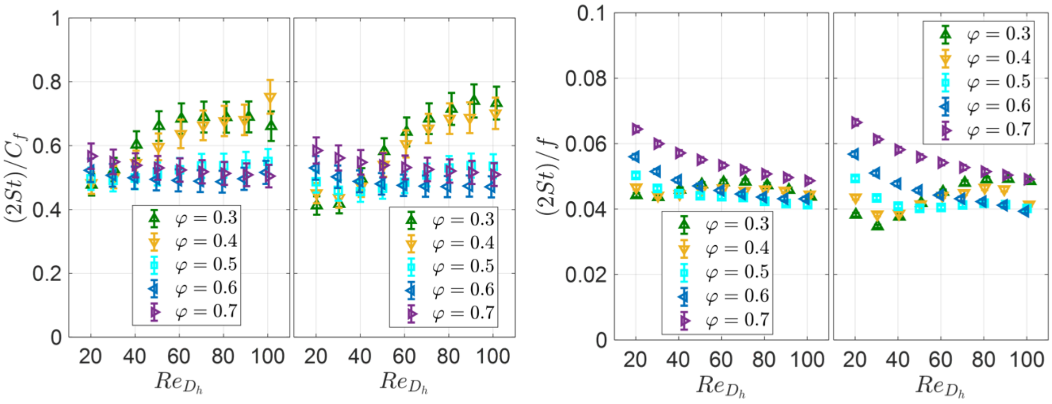

(a) (b) (c) (d)

Fig. 2.34 Reynolds analogy considering C_f (a)-(b) and f (c)-(d) for the Gyroid. (a) and (c) imposing T_w and (b) and (d) imposing q_w.

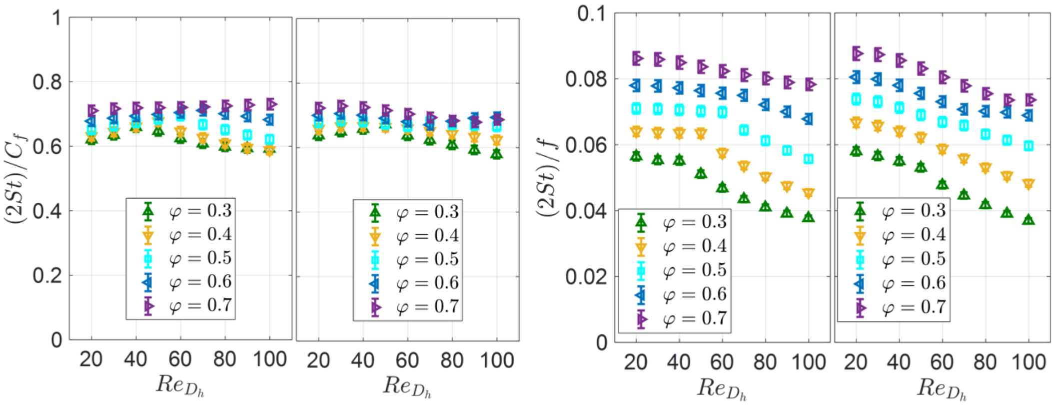

(a) (b) (c) (d)

Fig. 2.35 Reynolds analogy considering C_f (a)-(b) and f (c)-(d) for the Diamond. (a) and (c) imposing T_w and (b) and (d) imposing q_w.

number, more or less accentuated depending on the topology, but it was difficult to determine a similar trend for St/C_f. On the other hand, $(2St/f)$ presents a similar behavior as Nu, with the Gyroid having the different porosities results crossing each others and the other topologies a monotonic increasing trend with φ. This growing trend could be viewed as a growing efficiency in heat transfer compared to momentum transfer as porosity increases, since the Reynolds analogy compares the efficacy of heat and momentum transfer within a fluid.

A modified Reynolds analogy is proposed here, so to account for the porosity (and Reynolds) impact in each TPMS topology. Three different correlations, defined

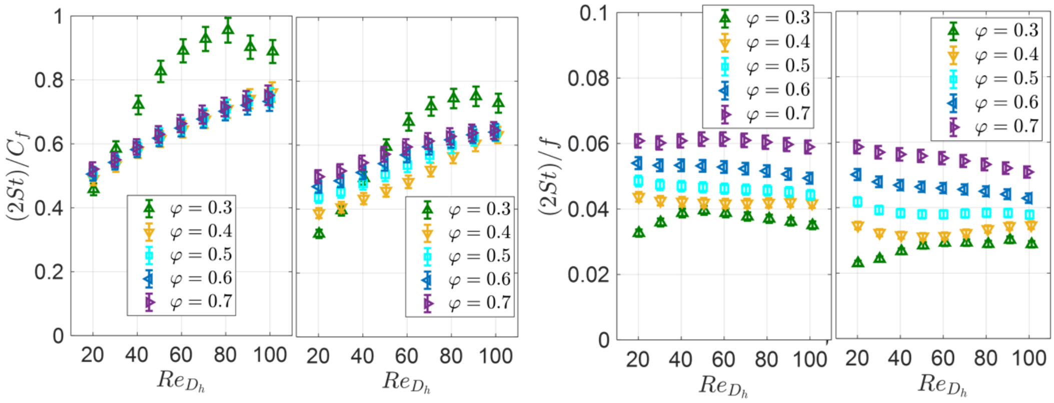

(a) (b) (c) (d)

Fig. 2.36 Reynolds analogy considering C_f (a)-(b) and f (c)-(d) for the SplitP1. (a) and (c) imposing T_w and (b) and (d) imposing q_w.

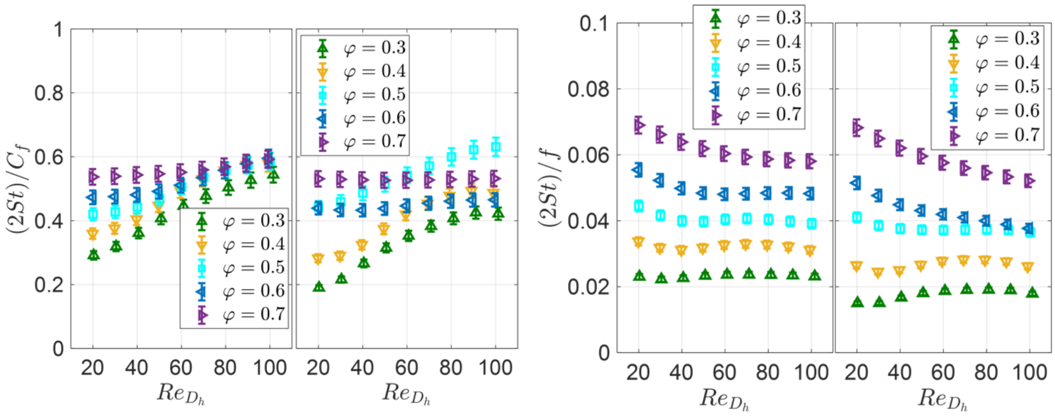

(a) (b) (c) (d)

Fig. 2.37 Reynolds analogy considering C_f (a)-(b) and f (c)-(d) for the SplitP2. (a) and (c) imposing T_w and (b) and (d) imposing q_w.

in Eqs. (2.64-2.66) were investigated for all topologies. The computed data were fitted by employing together the results at $T_w = const$ and $q_w = const$, considering that they should produce two limits for the thermal behavior of a real application, where usually neither the temperature or the heat flux is constant. The friction factor was only used, instead of the friction coefficient, being more exploitable in real case scenarios.

$$St = a_1 \varphi^{n_1} f \tag{2.64}$$

$$St = a_2 \varphi^{n_2} Re^{m_2 - \varphi} f \tag{2.65}$$

$$St = a_3 \varphi^{n_3} Re^{m_3 - b_3 \varphi} f \tag{2.66}$$

Moreover, being the friction factor described by Eq. (2.57), the results of Section 2.3 were utilized to fit f and to insert its dependence on Re_{D_h} and φ within the correlations for St, resulting in Eqs. (2.67-2.69).

$$St = a_1 \varphi^{n_1} \left(\frac{1}{Re_{D_h}} \left(\frac{2\varphi D_h^2}{K} \right) + \left(\frac{2\varphi^2 D_h C_F}{\sqrt{K}} \right) \right) \tag{2.67}$$

$$St = a_2 \varphi^{n_2} Re^{m_2 - \varphi} \left(\frac{1}{Re_{D_h}} \left(\frac{2\varphi D_h^2}{K} \right) + \left(\frac{2\varphi^2 D_h C_F}{\sqrt{K}} \right) \right) \tag{2.68}$$

$$St = a_3 \varphi^{n_3} Re^{m_3 - b_3 \varphi} \left(\frac{1}{Re_{D_h}} \left(\frac{2\varphi D_h^2}{K} \right) + \left(\frac{2\varphi^2 D_h C_F}{\sqrt{K}} \right) \right) \tag{2.69}$$

The results are plotted in Figs. 2.38-2.41 for the four TPMS. Note that only the correlation with the smallest standard deviation is shown here, for each TPMS. The black dotted lines refers to the fitting coefficients a_1, a_2 or a_3, while the magenta dotted lines are the standard deviations of the fits. The fitting coefficients are shown in Tab. 2.11. $stdev$ are the standard deviations of the fits.

For all the TPMS, all the proposed correlations had standard deviations below 20%. It's interesting how the correlation of Eq.(2.64) and Eq. (2.66) had the same standard deviation for all TPMS but the Diamond, even if they have a different number of fitting parameters. Indeed, normally a larger number of fit parameters enable a better fit quality. This could be an indication that the simplest Eq. (2.64) was adequately able to model the differences between porosity and Reynolds numbers.

For the Gyroid, two structures at additional porosities of 45% and 65% were constructed and simulated at $Re_{D_h} = 45, 85$, to test the above correlations. Their results were plotted in Fig. 2.38 as red stars and blue crosses. The four additional setpoints were almost always within the fitting deviations or slightly beyond, for all developed correlations, with the maximum error below 20%, for Eq. (2.67) at

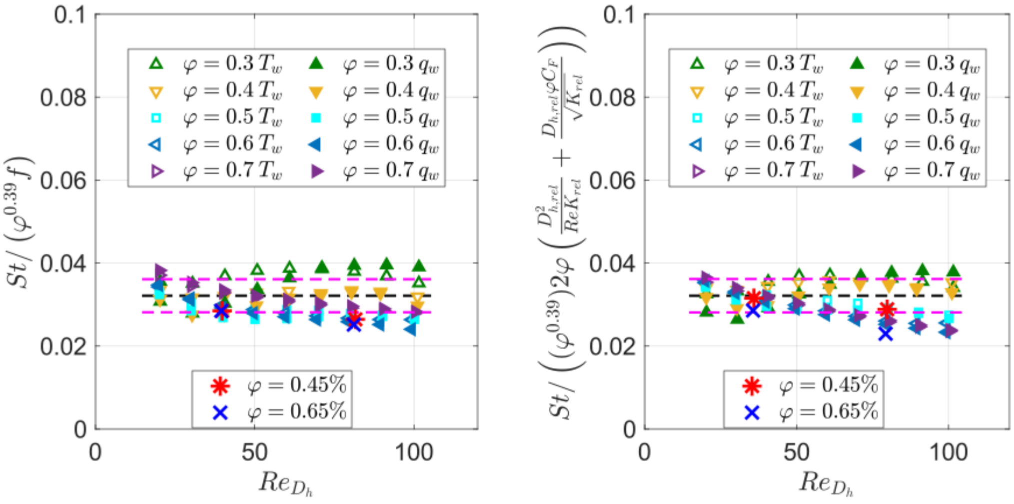

(a) (b)

Fig. 2.38 Modified Reynolds analogy of Eq. (2.64) for Gyroid. (a) With computed f and (b) using the f correlation.

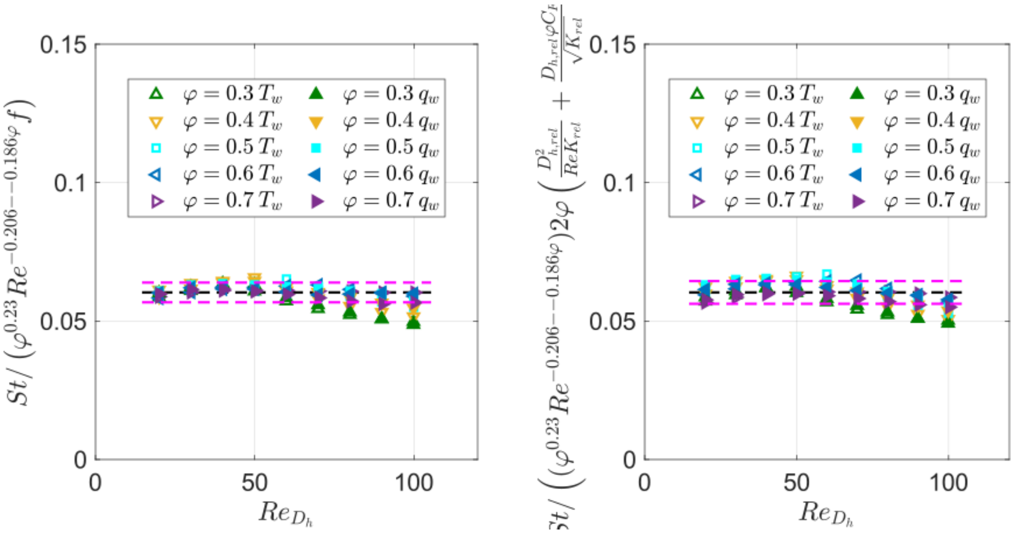

(a) (b)

Fig. 2.39 Modified Reynolds analogy of Eq. (2.66) for Diamond. (a) With computed f and (b) using the f correlation.

$\varphi = 65\%$ and $Re_{D_h} = 85$. This corroborates the developed correlations, as most empirical correlations found in the literature [103] have always an uncertainty greater than 20%.

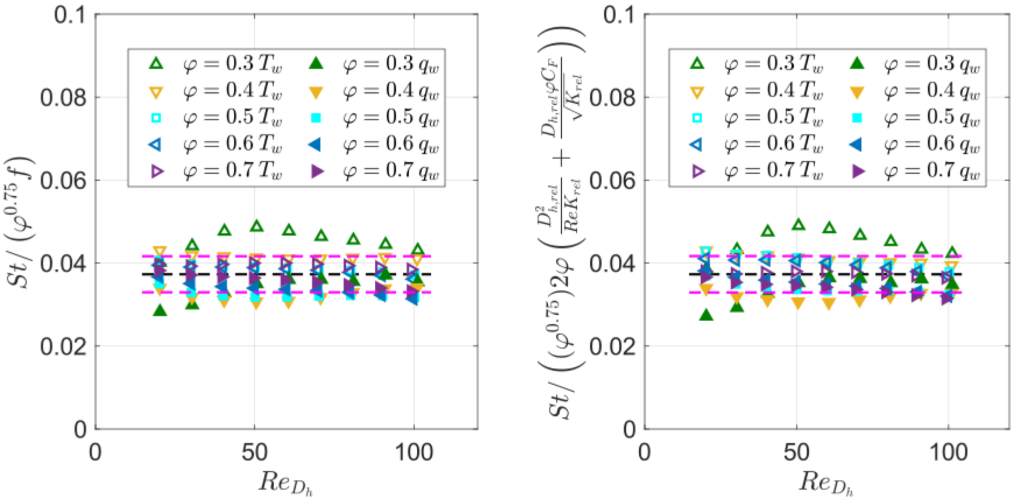

(a) (b)

Fig. 2.40 Modified Reynolds analogy of Eq. (2.64) for SplitP1. (a) With computed f and (b) using the f correlation.

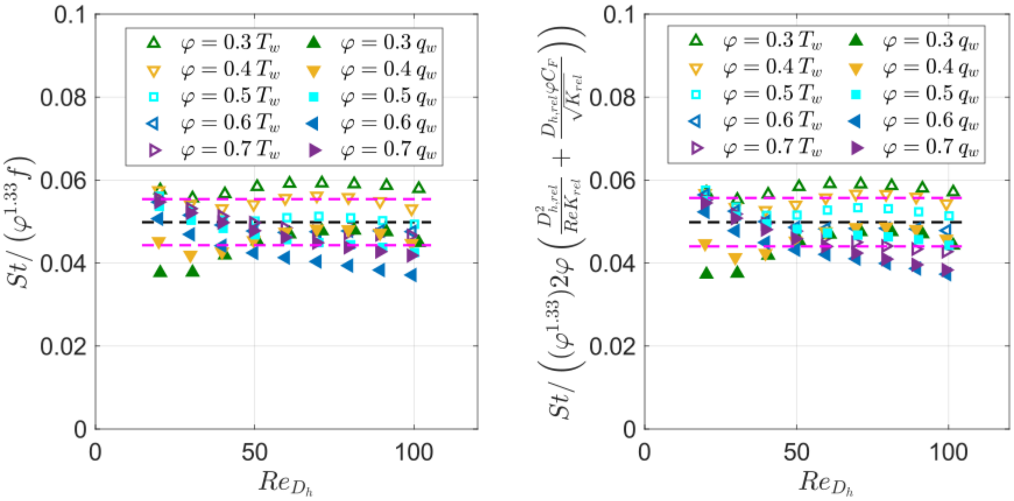

(a) (b)

Fig. 2.41 Modified Reynolds analogy of Eq. (2.64) for SplitP2. (a) With computed f and (b) using the f correlation.

Table 2.11 Parameters of the fitting correlations for the modified Reynolds analogy of Eqs. (2.64-2.69).

	Gyroid	**Diamond**	**SplitP1**	**SplitP2**
a_1	0.032	0.051	0.037	0.050
n_1	0.39	0.56	0.76	1.33
$stdev_1$	12%	10%	14%	11%
a_2	0.147	0.223	0.13	0.211
n_2	2.12	2.3	2.55	3.14
m_2	0.423	0.443	0.522	0.455
$stdev_2$	15%	15%	18%	13%
a_3	0.05%	0.06	0.039	0.094
n_3	0.53	0.23	0.78	1.8
m_3	-0.057	-0.0206	-0.017	0.052
b_3	-0.083	-0.186	-0.019	-0.263
$stdev_3$	12%	6%	14%	11%

2.5 Chapter summary

In this chapter, an analytical and numerical investigation of triply periodic minimal surface (TPMS) structures was carried out to characterize their hydraulic and thermal behavior and to develop predictive correlations for flow and heat transfer within these complex geometries. Four solid TPMS configurations at different porosity levels were analyzed over a Reynolds number range from 1 to 100 (with thermal analysis starting from $Re = 20$). Hydraulic performance was quantified through correlations for permeability and inertial drag coefficient, expressed as power-law functions of key geometric parameters such as porosity and tortuosity. These correlations were compared with existing models from the literature, revealing notable discrepancies that were interpreted based on geometric and flow-structure interactions. The proposed models were further validated against numerical simulations of larger-scale domains, confirming their reliability within the investigated low-Reynolds number regime. Beyond empirical fitting, theoretical insights were introduced to rationalize the observed trends. For instance, the divergence in hydraulic resistance behavior between SplitP1 and SplitP2 structures, transitioning from viscous to inertial regimes, was linked to differences in cross-sectional area evolution despite identical wetted surfaces. Thermal behavior was assessed through the development of Stanton number correlations for each TPMS topology. These correlations were constructed by aggregating data across multiple porosity levels and were successfully tested against additional cases not included in the fitting procedure.

While this chapter primarily focused on conventional analytical correlations for thermal-hydraulic performance, the thesis also explores alternative modeling strategies. In particular, Appendix C presents a machine learning-based approach to predict flow behavior, while Appendix D discusses geometric and hydraulic relationships between sheet-TPMS and solid-TPMS configurations.

The thermal analysis identified the SplitP structure as the most effective configuration for heat removal. Based on this outcome, subsequent chapters focus on comparative analyses involving this topology: Chapter 3 evaluates SplitP against Diamond structures in solar receiver applications, while Chapter 4 compares it with Gyroid structures in reflective components for fusion systems. Furthermore, the hydraulic correlations developed here will be validated against full-domain simulations in the following chapter.

Extending the proposed thermal–hydraulic correlations to fluids with Prandtl numbers different from unity is identified as a key direction for future research. This development would make it possible to investigate Reynolds–Stanton analogies for a broader range of working fluids with different thermal diffusivities, increasing the generality and applicability of the proposed models to practical engineering systems

Chapter 3

Triply Periodic Minimal Surfaces for Concentrated Solar Power

This chapter aims to analyze two volumetric receivers filled with TPMS, from the design (and manufacturing) stage in Section 3.1 to experimental thermal (Section 3.2) and hydraulic (Section 3.3) characterization, including an assessment of the numerical models performance (Section 3.4). Concluding remarks for the chapter are drafted in Section 3.5.

Portions of the present chapter were published or presented in the following scientific papers and conferences:

- A. Mortazavi, A.L. Ávila-Marín, H. Ebadi, E. Gajetti, C. Piatti, L. Marocco and L. Savoldi, "Experimental investigation of Triply Periodic Minimal Surfaces for high-temperature solar receivers". *Case Studies in Thermal Engineering*, 60:104771, 2024-08. [106]
- E. Gajetti, G. Boccardo, A. Buffo, V. Gentile, A. Lucchini, L. Marocco, C. Piatti, A. Quamori Tanzi and L. Savoldi, "Assessment of numerical tools and models for the simulation of flow through TPMS structures". *Presented at the 9th European Congress on Computational Methods in Applied Sciences and Engineering - ECCOMAS2024.* [107]
- E. Gajetti, G. Boccardo, A. Buffo, V. Gentile, A. Lucchini, L. Marocco, C. Piatti, A. Quamori Tanzi and L. Savoldi, "Experimental investigation of fluid

flow through Triply Periodic Minimal Surfaces structures". *Presented at the 41st UIT International Heat Transfer Conference, 2024.* [108]

3.1 Design and manufacture of the receivers

Two planar volumetric receivers were designed in accordance with their employ in the solar simulator of IMDEA Energy Institute in Madrid, Spain. The two samples (Fig. 3.1) consisted of an external parallelepiped measuring 50 mm and filled with 40 mm length of TPMS, connected to two circular tubes measuring 15 mm each via two manifolds of 10 mm length, for a total sample length of 10 cm. The two filling TPMS are the sheet-Diamond and sheet-SplitP. The external envelope was drawn using SolidWorks [109], and the TPMS in nTop [110], with unit cell size of 10 mm and 1 mm of wall thickness. This cell size was not derived from a dedicated optimization study; it was selected as a value known to be manufacturable and suitable for preliminary testing of TPMS structures in a solar field context.

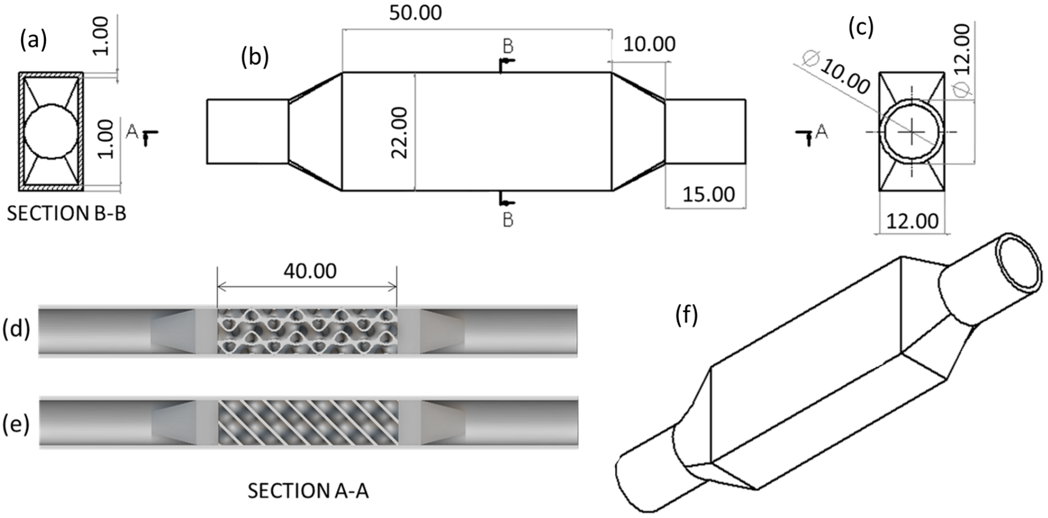

Fig. 3.1 Samples geometry. (a)-(c) Drawing of the envelope and transversal cross-section views, longitudinal cross-section view with (d) the Diamond and (e) the SplitP lattice and (f) the external envelope geometry. Dimensions are in millimeters.

The two samples were manufactured in AISI 316L (Figs. 3.2a-3.2b) by the private company Ellena S.p.A. via Additive Manufacturing, using the Laser Powder Bed Fusion (LPBF) method - also called Selective Laser Melting (SLM) - employing a 240 W printer with a spot of 0.1 mm. They were also printed with Stereolithography (SLA)

(Figs. 3.2c-3.2d) using a photopolymer at the Energy Department of Politecnico di Torino. The used photopolymer is a liquid mixture of bismethacrylate (75%), acrylic acid (24%) and phenylphosphine oxide (1%). The photosensitive liquid polymer is exposed to a laser beam generated with a 405 nm violet diode and a maximum output of 250 mW that activates a photo-crosslinking among the different constituents and monomers, solidifying the liquid polymer along the designed path and generating layer by layer the TPMS geometry. The samples were printed in two materials to explore the impact of different printing techniques, but evidently only the metal samples were thermally tested, while the hydraulic tests were performed on both materials. The two metallic samples were not covered by any coating.

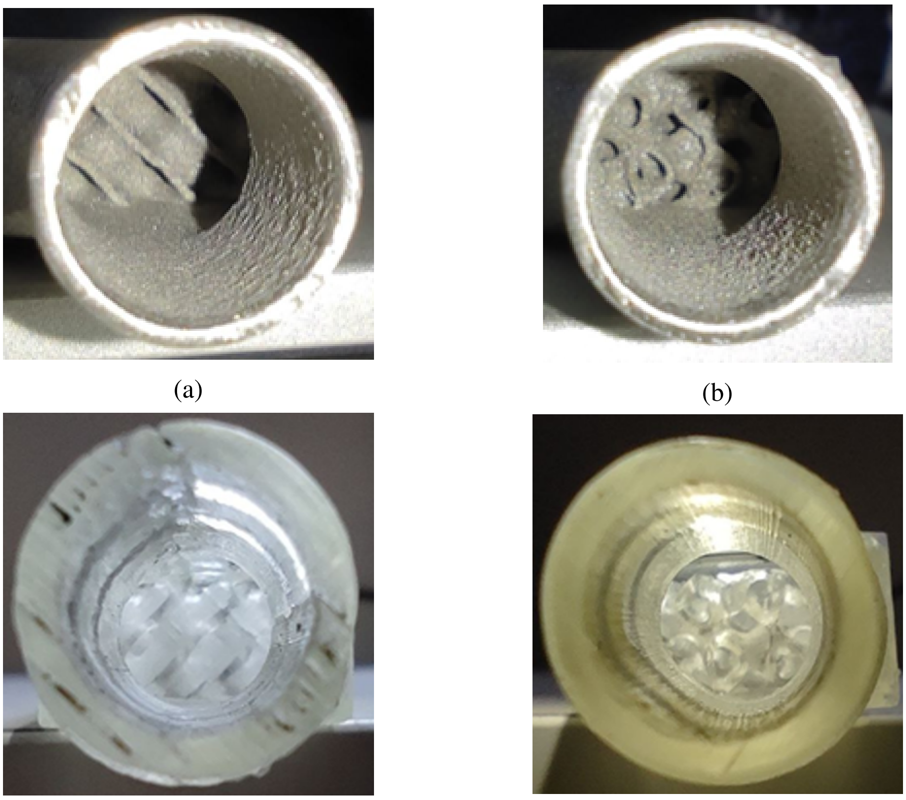

(a) (b)

(c) (d)

Fig. 3.2 Geometric parameters: (a) c value, (b) A_{wet}, (c) D_h and (d) τ.

The design data of the two samples is displayed in Tab. 3.1. It should be noted that at the same cell size and wall thickness, the SplitP presents a larger surface-to-volume ratio, and thus lower porosity, than the other topology. This is consistent with the findings of the previous chapter, in Fig. 2.2c, in which the hydraulic diameter (the inverse of the surface-to-volume ratio) of the Diamond is much larger than the SplitP at the corresponding solid porosity, i.e. around 35%. The fact that the S_V of the SplitP is larger than the Diamond can be an indication of better thermal performance.

Table 3.1 Design data of the planar receivers.

	Diamond	**SplitP**
φ	76.8%	73.7%
S_V (mm^{-1})	1.06	1.43

3.2 Test of thermal performance in air

The thermal tests were conducted within the SFERA III project, funded by the European Union, at IMDEA Energy Institute in Madrid, Spain, through a high-flux solar simulator.

3.2.1 Experimental setup

IMDEA high-flux solar simulator, KIRAN-42 [111], is equipped with seven Xenon short-arc lamps, arranged in a hexagonal symmetry and featuring elliptical reflectors. The emission spectrum of the KIRAN-42 closely resembles that of sunlight. At its maximum capacity, the simulator delivers a total radiation power of $14\,kW$, achieving a peak heat flux of $3.6\,MW/m^2$ at its focal plane. For the purposes of this study, only the central lamp was employed, as the tested heat flux range did not exceed $350kW/m^2$. A movable testbed was employed to reach different heat flux, depending on its position with respect to the central lamp focal point. The testbed was motioned by an actuator that could move in the Cartesian space with an accuracy of $1\,mm$. It was exposed to the Xenon lamps through a large-aperture window fitted with a blind shutter, and another large window allowed for observation and control from the control room - see Fig. 3.3.

An open-loop circuit was constructed to study the thermal behavior of the planar solar receivers, as shown in Fig. 3.4a. The working fluid was synthetic air, composed of 79% Nitrogen and 21% Oxygen, supplied from a compressed air bottle. The inlet pressure of the air was maintained approximately around $10\,bar$ by a pressure regulator valve (V). A thermal flow meter (mf) was used to measure the flow rate

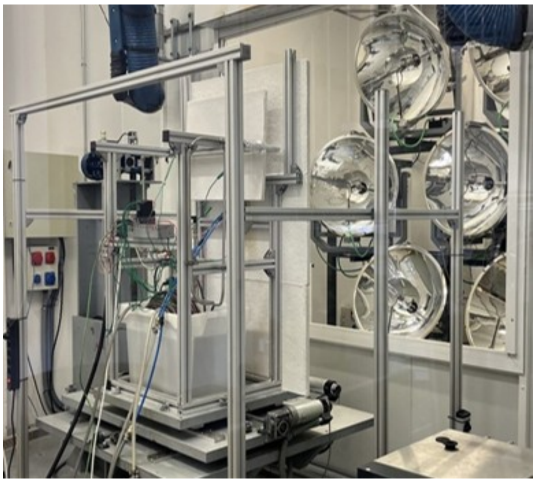

Fig. 3.3 The test table with the Xenon lamps. Taken from [106]

of the synthetic air. Inlet and outlet pressure and temperatures of the sample air were measured through pressure transmitter (P) and thermocouples (T). The heated air exiting the sample was cooled down in a heat exchanger (HX) integrated into a secondary loop with the aid of a chiller, before being exhausted. The exhaust air temperature was also measured, and the room temperature. The radiative heat flux from the Xenon lamp (L), directed to the sample, was measured by a thermogage, also called Gardon Gauge.
Four thermocouples were placed directly on the sample: two on the backside surface (*TC1* near the inlet and *TC3* near the outlet) and two on the bottom edge (*TC2* and *TC4*), as shown in Fig 3.4b. A sensor holder was built to ensure proper contact for the bottom-side thermocouples, as in Fig. 3.4c. It is important to note that only the readings from *TC3* were considered comparable between the two tested samples due to difficulties in securely positioning *TC1*, *TC2* and *TC4*, which led to slight alterations in their positions. Even if pressure sensors were available, they were solely used for the operating pressure (to compute the air properties) rather than computing the pressure losses, as the very small flow rates provided negligible pressure drops with respect to the uncertainty of the instruments.

The instrumentation utilized for data collection is presented in Tab. 3.2. All data from the various sensors was recorded simultaneously at a frequency of $0.5\,Hz$, and to reach steady-state conditions all configurations were tested for about 5-10 minutes.

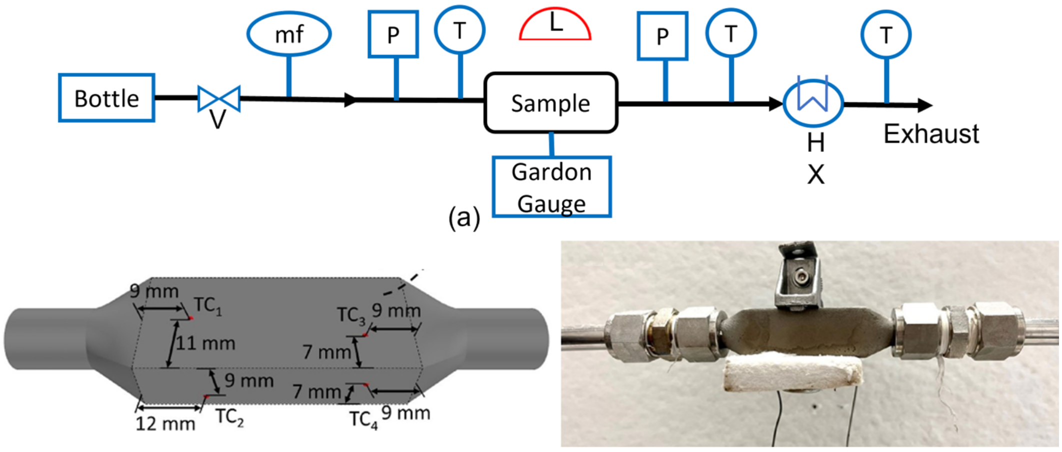

(a)

(b)

(c)

Fig. 3.4 Sketch of the experimental air circuit at IMDEA. (a) Positions of the thermocouples on the samples on the back and lateral side and (b) front side of mounted sample. Modified from [106].

Table 3.2 Instrumentation data for the thermal tests of the planar receivers.

Instrument	**Type**	**Accuracy**
Thermocouples	K-type	0.5 K
Mass flowmeter	Thermal mass flowmeter	0.5% r.v.
Heat flux sensor	Thermogage circular-foil heat flux transducer	10% r.v.
Pressure sensors	Pressure transmitters	0.08 bar

3.2.2 Data reduction and uncertainty evaluation

The heat flux distribution in a solar simulator follows a Gaussian shape. The first testing day, different values of heat flux were measured with the thermogage at different vertical positions of the testbed. Then, the exact heat flux distribution was mapped from these point, as in Eq. (3.1), where $B = 94.43\,kW/m^2$, $C = 245.08\,kW/m^2$ and $stdev = 15.575\,mm$, computed from the fit of the Gaussian equation to the measured values. The heat flux distribution is depicted in Fig. 3.5, with the location of the sample for a nominal desired peak heat flux of $100\,kW/m^2$ and $325\,kW/m^2$.

$$q = B + C\,e^{-0.5\left((\frac{x}{stdev})^2+(\frac{y}{stdev})^2\right)} \tag{3.1}$$

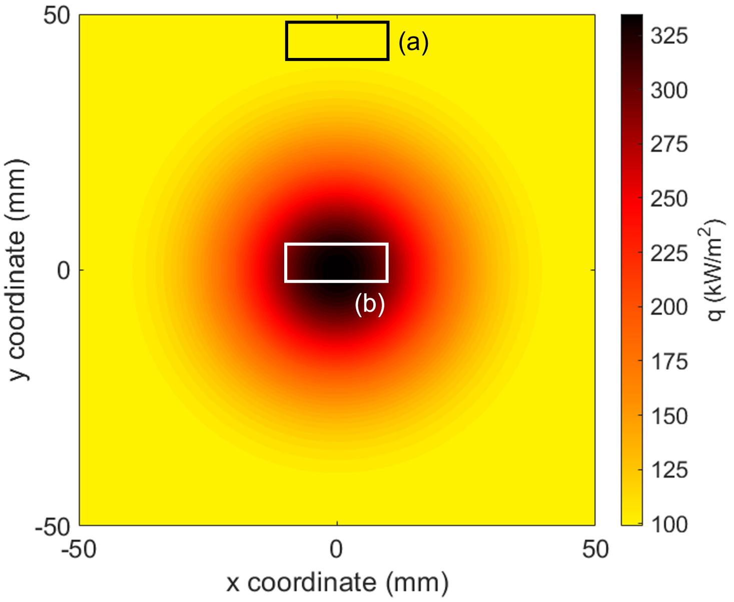

Fig. 3.5 Heat flux field as in Eq. (3.1), and the position of the sample for a nominal heat flux of (a) 100 kW/m^2 and (b) 325 kW/m^2.

Thus, the incident power on the receiver Q_{inc} is the surface integral of Eq. (3.1). Not all the heat incident on the receiver is absorbed by the system, but a fraction is lost to the environment due to reflection and emission from the surface as well as convective heat transfer to the ambient air. Considering the losses to the environment through radiation and convection, the actual power absorbed by the receiver might be computed as a power balance, assuming steady-state conditions, as in Eq. (3.2).

$$Q_{abs} = \dot{m} c_p (T_{out} - T_{in}) \tag{3.2}$$

In Tab. 3.3 the vertical positions of the testbed for the different nominal heat flux levels considered in the experiment are shown, together with the incident power on the receiver.

In the following Tab. 3.4 the tested conditions are presented, for the Diamond and SplitP.

Given the incident power and the power effectively absorbed by the receiver, an absorption efficiency η_{th} can be defined as in Eq. (3.3).

Table 3.3 Vertical positions of the testbed y_{TB} (origin at x = 0 and y = 0) associated to each nominal heat flux level q and the incident power Q_{inc} from Eq. (3.1)

Nominal $q\ (kW/m^2)$	$y_{TB}\ (mm)$	$Q_{tot}\ (W)$
100	38	120
125	33	130
150	28	150
200	20	190
250	14	230
300	9	250
325	6	270

$$\eta_{th} = \frac{Q_{abs}}{Q_{inc}} \tag{3.3}$$

The thermocouples readings T_{TC} were reduced by subtracting the inlet temperature T_{in} for each test, as in Eq. (3.4), to compute the temperature increases ΔT.

$$\Delta T = T_{TC} - T_{in} \tag{3.4}$$

The evaluation of the standard uncertainty of the measurements was performed by following the guidelines provided by the Joint Committee for Guides in Metrology [112]. The uncertainty of a measurand estimate ($un(x)$) was calculated by combining the statistical uncertainties from the random oscillations ($un_{A-type}(x)$) in the experiments and the accuracy of the instrumentation ($un_{B-type}(x)$) in Eq. (3.5). $un_{A-type}(x)$ is computed as the standard deviation of the mean of the measurements and $un_{B-type}(x)$ using the instrumentation accuracy as reported by the manufacturer. $un_{B-type}(x)$ is evaluated by considering that the accuracy provides symmetric bounds within which the measurand value has an equal probability to lie. The two bounds $-ac$ and $+ac$ therefore delimit a rectangular distribution, with mean value equal to zero and variance equal to $ac^2/3$.

$$un(x) = \sqrt{un^2_{A-type} + un^2_{B-type}} = \sqrt{\frac{\sum_i (x_i - \bar{x})^2}{n(n-1)} + \frac{ac^2}{3}} \tag{3.5}$$

Thus, the uncertainty of the temperature increase ΔT is computed as the combination of uncertainty of the two measured temperatures as in Eq. (3.6).

Table 3.4 Tests information containing the mass flow rates and heat flux levels for Diamond and SplitP samples.

Diamond sample

$\dot{m}\,(g/s)$	$q\,(kW/m^2)$
0.5	100
	125
	150
	200
1	100
	125
	150
	200
	250
	300
1.5	100
	125
	150
	200
	250
	300
	325
2	100
	125
	150
	200
	250
	300
	325

SplitP sample

$\dot{m}\,(g/s)$	$q\,(kW/m^2)$
0.5	100
	125
	150
	200
1	100
	125
	150
	200
	250
	300
	325
1.5	100
	125
	150
	200
	250
	300
	325
2	100
	125
	150
	200
	250
	300
	325

$$un(\Delta T) = \sqrt{un^2(T_{TC}) + un^2(T_{in})} \tag{3.6}$$

The uncertainty of the incident power $un(Q_{inc})$ is assumed equal to the uncertainty of the Gardon gauge of 10%. The uncertainty of the absorbed power $un(Q_{abs})$, on the other hand, is depicted in Eq. (3.7), where ΔT_{o-i} is the temperature difference between inlet and outlet. From Eq. (3.7), the uncertainty of the thermal efficiency can be calculated as Eq. (3.8);

$$\frac{un(Q_{abs})}{Q_{abs}} = \sqrt{\left(\frac{un(\dot{m})}{\dot{m}}\right)^2 + \left(\frac{un(c_p)}{c_p}\right)^2 + \left(\frac{un(\Delta T_{o-i})}{\Delta T_{o-i}}\right)^2} \tag{3.7}$$

$$\frac{un(\eta_{th})}{\eta_{th}} = \sqrt{\left(\frac{un(Q_{abs})}{Q_{abs}}\right)^2 + \left(\frac{un(Q_{inc})}{Q_{inc}}\right)^2} \tag{3.8}$$

3.2.3 Results and discussion

As already mentioned, data of each mass flow rate for both samples was acquired for a long period, so to ensure steady-state within the considered heat flux values. Thus, within the measured data, both transient and steady-state conditions are present, as can be remarked in Fig. 3.6, showing the Diamond and SplitP sample tested at 0.5 g/s. In this figure, the temperature increase refers to the inlet temperature, which was consistently equal to the ambient temperature within the uncertainty of the thermocouples. Coherently with the position of the thermocouples, *TC1* and *TC3* were lower than the thermocouples placed on the side, *TC2* and *TC4*. Moreover, the thermocouples situated closer to the outlet measured higher values, because of the larger power absorbed. The temperature profile of the inlet and ambient temperatures are not shown here because they were almost constant with respect to the other distributions. In Fig. 3.6 also the cooling phase is shown, during which the Xenon lamp was shut down while continuously cooling the system. The temperature increases of the Diamond sample were pretty similar to the SplitP, with the exception that the Diamond reached lower temperatures in the fluid and in the thermocouples on the side and back of the sample, indicating lower actual power absorption. Besides, during the cooling phase, the SplitP cooled down to temperature equal to 2% of their values within a time 10% shorter than the time needed by the Diamond sample. This could already denote the superior heat transfer efficiency of the SplitP structure. In Figs. 3.7 and 3.8 the temperature rise of $TC3$ and T_{out} and the useful absorbed power are shown. As expected, the absorbed power increased with increasing mass flow rates and increasing incident heat fluxes for both samples. However, with raising heat flux, the absorbed power progressively deviated more from the ideal condition (where absorbed power equals total incident power - black line in Fig. 3.7). This was possibly caused by the higher temperature levels reached by the samples, leading to increased heat losses to the ambient. On the other hand, increasing the flow rate

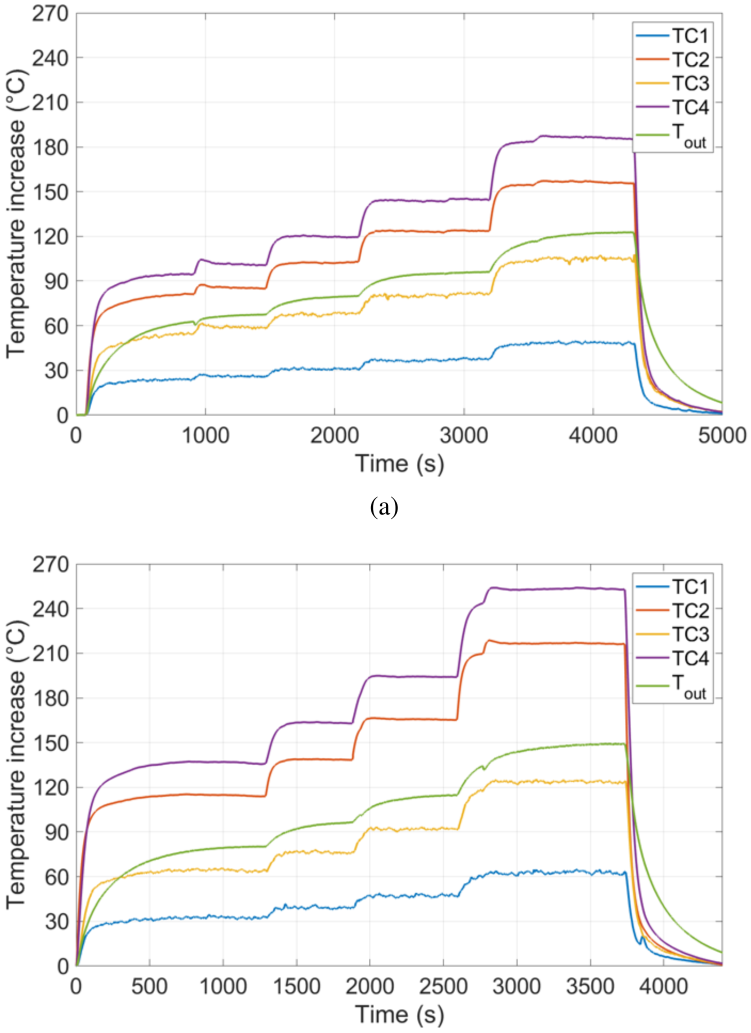

(a)

(b)

Fig. 3.6 Example of the acquired data at the mass flow rate of 0.5 g/s for the sample filled with (a) Diamond and (b) SplitP. The temperature increase is referred to the inlet temperature.

approached the curve to the ideal condition of zero power losses to the environment. This could probably be explained since a more effective cooling of the receiver limited the temperature rise of the solid material for a given incident heat value. By keeping the receiver material temperature lower, the heat loss to the ambient decreased. This improved cooling allowed the fluid to carry away a larger fraction of the incident power, leading to an overall increase in useful absorbed power and improved thermal efficiency.

Across all tested mass flow rates and incident heat fluxes, the sample filled with

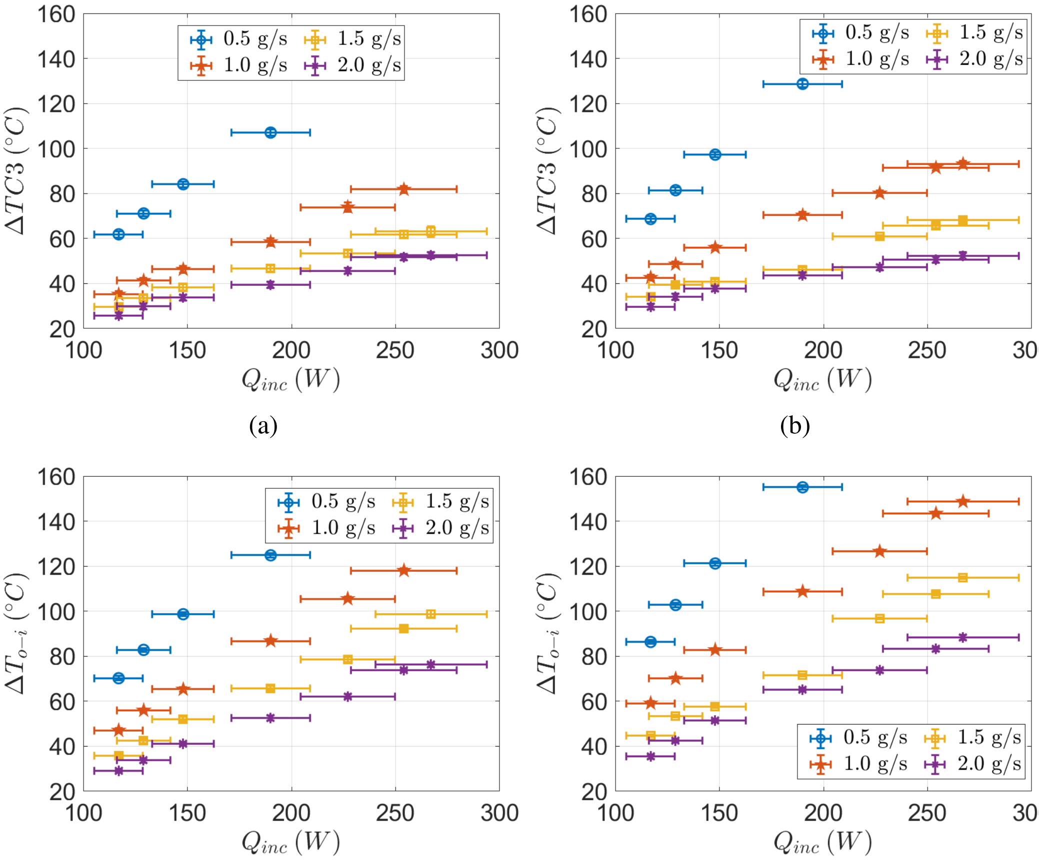

(a) (b) (c) (d)

Fig. 3.7 Temperature rise with respect to room temperature in TC3 (a,b) and at the outlet (c,d) for Diamond (a,c) and SplitP (b,d).

SplitP demonstrated an enhancement of the heat removal with respect to the sample filled with Diamond. For what concerns the thermal efficiency, it increased for both samples with higher mass flow rates, stabilizing at the highest value. The SplitP sample demonstrated superior thermal performance, achieving a maximum thermal efficiency of approximately 70% at a mass flow rate of 2 g/s. In comparison, the Diamond sample reached nearly 60% thermal efficiency under the same conditions. This highlights the significant improvement offered by SplitP. These efficiencies are relatively high compared to what can be found in the literature: as mentioned in the review of He et al. [55], the maximum efficiency found in volumetric porous receivers in air can reach values larger than 80%, as for example studied by Roldan et al. [57], but with larger air flow rates and temperatures of the present study. For example, Roldan et al. [57] simulated an air flow rate of 13 g/s, an order of magnitude

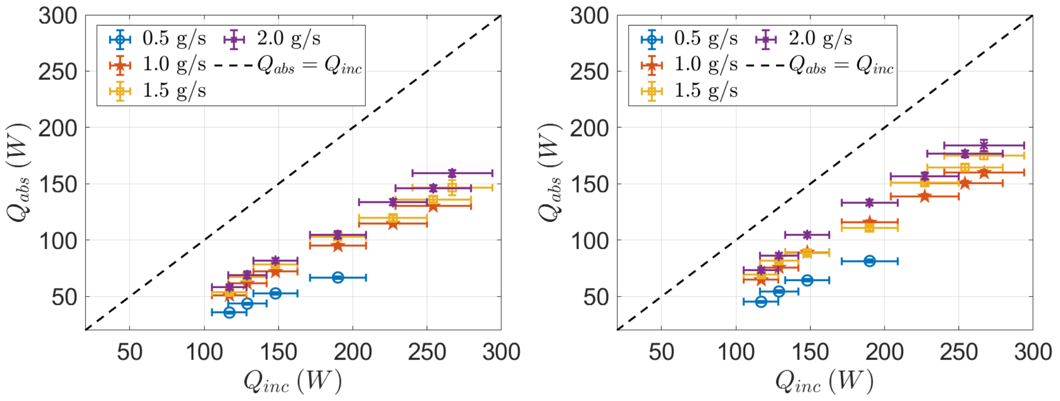

(a) (b)

Fig. 3.8 Heat absorbed for different incident heat for (a) Diamond and (b) SplitP samples.

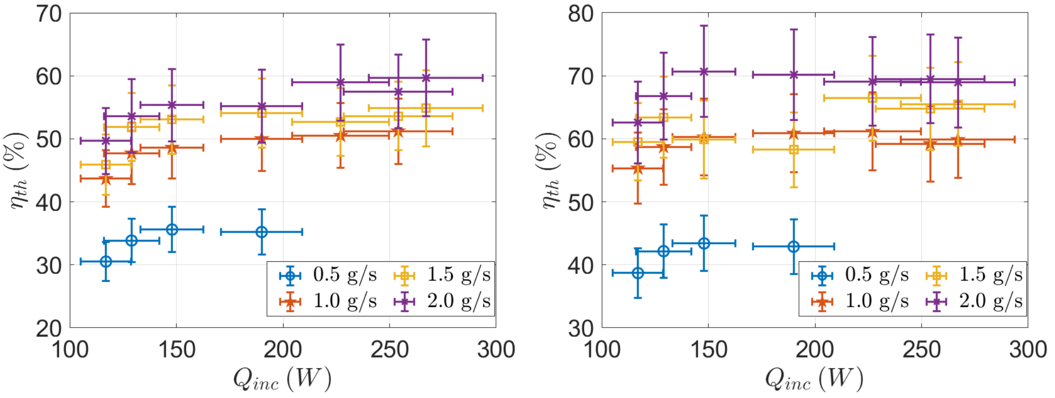

(a) (b)

Fig. 3.9 Thermal efficiency for (a) Diamond and (b) SplitP samples

larger than the present work, and air temperature up to 500°C. When compared to analyses performed on solar absorbers with analogous conditions, the efficiencies found in the literature are quite lower typically below 50%. For example, for a Compound Parabolic Concentrator (CPC) [113] with an air flow rate of 0.002 m^3/s - approximately equivalent to $\sim 4g/s$ at 2.5 bar - Wang et al. [113] found $\eta_{th} \sim 50\%$; Nems et al. [114] found $\eta_{th} \sim 45\%$ with a similar flow rate of Wang et al. [113] within a Parabolic Trough Collector (PTC) with internal fins; Afaq [115] observed an efficiency of 15% with a mass flow rate of 3 g/s within a double-pass unglazed Flat Plate collector (FPC), and they also reported increasing efficiency with the flow rate.

3.3 Experimental analysis in water: hydraulic performance

Since during thermal testing at the IMDEA institute the pressure drops were too small compared to the accuracy of the sensors, a hydraulic characterization of the samples was performed in a subcooled water circuit at the Energy Department of Politecnico di Milano, for Reynolds numbers within 1400-7000. In addition to the metallic samples, polymeric samples were also tested for comparison, to explore the impact of the manufacturing method on their hydraulic characteristic.

3.3.1 Experimental setup

The experimental loop at the laboratory *Frigorifero* of Politecnico di Milano is shown in Fig. 3.10. The AISI sample was connected to a differential pressure transducer (PT) through copper pipes, in parallel to a channel with a safety valve (V2). This latter should be closed to perform the measurements, but can be opened in emergency cases, when the pressure drop is accidentally higher than the maximum tolerated by the transducer, to avoid spoiling of the instrument. The differential pressure transducer was calibrated before starting the tests using a relative pressure sensor. The cross-shaped joints also connected two short vertical pipes that allow to expel the air contained in the circuit before starting the tests.

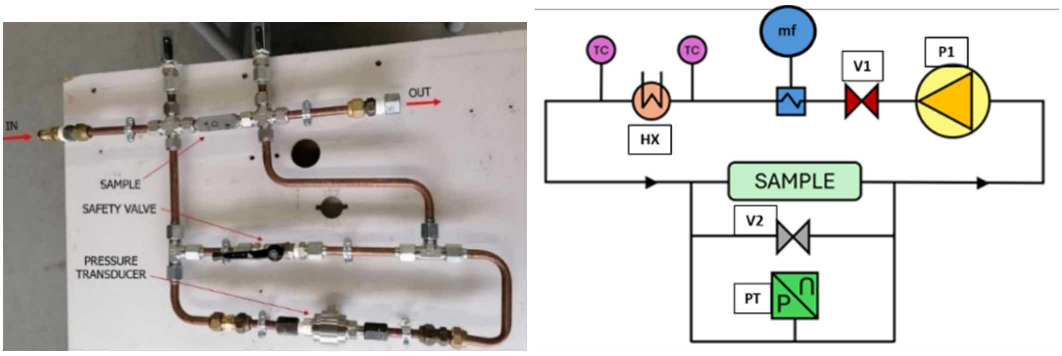

(a) (b)

Fig. 3.10 Hydraulic circuit used for the tests of AISI samples: (a) photo, (b) sketch

The test section was then connected to a close circuit that included a pump (P1) and a Coriolis mass flow meter (mf). The mass flow rate was manually controlled

through the valve V1. To avoid the temperature rise due to energy dissipation from the pump, the circuit was equipped with a heat exchanger (HX) and a secondary cooling loop (containing a solution of water and Glycol). The heat exchanger maintained the water temperature around the desired value of 20°C by means of a PID (proportional integral derivative) system.
The instrumentation parameters are displayed in Tab. 3.5

Table 3.5 Measuring instruments for the hydraulic circuit of laboratory *Frigorifero* at Politecnico di Milano.

Type	**Range**	**Accuracy**
Mass flow meter	0-108 l/min	0.3% r.v.
Relative pressure transducer	0-100 kPa	0.2 kPa
Type K thermocouples	0-50°C	0.5 °C

In the experimental circuit of the metallic devices, the samples were directly connected to cross-shaped joints, which were also directly connected to the pressure transducer. However, inserting the polymeric samples in the same circuit was unfeasible because of the metallic connectors. Thus, longer connection pipes to the pressure transducer were needed and an additional connector was placed to employ plastic pipes to join the polymeric samples. The modified version of the testing circuit is presented in Fig. 3.11a. In this case, pressure measurements were influenced by the localized pressure drop of the additional connector and, to a smaller extent, by the distributed pressure losses before and after the sample. Therefore, the circuit section was short-circuited (Fig. 3.11b), by removing the polymeric sample and inserting a plastic pipe of length equal to the connection pipes plus the sample.

3.3.2 Data reduction and uncertainty evaluation

Several flow rates were tested within the four samples. Moreover, the metallic samples were also tested reversing the flow direction within the TPMS. The tested flow rates are listed in Tabs. 3.6-3.7. The slight discrepancies in the superficial velocities at the same flow rate within the same sample are due to tiny differences in water temperatures.

(a) (b)

Fig. 3.11 Hydraulic circuit used for the tests of polymeric samples (a) and short-circuited section (b).

Table 3.6 Tested mass flow rates and corresponding superficial velocities for the metallic and polymeric Diamond samples.

Metal				**Polymer**	
Normal direction		Reversed direction		Normal direction	
$\dot{m}$ (kg/s)	U_s (m/s)	$\dot{m}$ (kg/s)	U_s (m/s)	$\dot{m}$ (kg/s)	U_s (m/s)
0.13	0.62	0.14	0.69	0.11	0.53
0.14	0.70	0.17	0.84	0.13	0.60
0.15	0.76	0.19	0.98	0.14	0.64
0.17	0.84	0.22	1.11	0.15	0.72
0.18	0.91	0.25	1.26	0.17	0.80
0.19	0.97	0.28	1.40	0.18	0.87
0.21	1.04			0.19	0.95
0.22	1.11			0.21	1.00
0.24	1.18			0.22	1.07
0.25	1.26			0.24	1.14
0.26	1.32			0.25	1.20
0.28	1.39			0.26	1.27
0.29	1.45				
0.31	1.53				
0.32	1.60				

The data reduction of the measurements of the polymeric samples (Δp_{PS}) is provided in Eq. (3.9): the pressure losses measured in the short-circuited section ($\Delta p_{P-circuit}$) were subtracted from the pressure losses measured in the circuit with the polymeric sample ($\Delta p_{short-circuited}$). The subscript PS refers to the polymeric

Table 3.7 Tested mass flow rates and corresponding superficial velocities for the metallic and polymeric SplitP samples.

Metal				**Polymer**	
Normal direction		Reversed direction		Normal direction	
$\dot{m}$ (kg/s)	U_s (m/s)	$\dot{m}$ (kg/s)	U_s (m/s)	$\dot{m}$ (kg/s)	U_s (m/s)
0.10	0.49	0.11	0.57	0.10	0.49
0.11	0.55	0.14	0.69	0.11	0.56
0.13	0.63	0.17	0.84	0.13	0.64
0.14	0.70	0.19	0.98	0.14	0.71
0.15	0.77			0.15	0.76
0.17	0.84			0.17	0.84
0.18	0.90			0.18	0.91
0.19	0.98			0.19	0.98
0.21	1.04			0.21	1.03
0.22	1.11				
0.24	1.17				

sample without the contribution of the connectors and $P-circuit$ the loop with the polymeric sample.

$$\Delta p_{PS} = \Delta p_{P-circuit} - \Delta p_{short-circuited} \tag{3.9}$$

Eight set points were measured in the short-circuited section, and a quadratic fit is displayed in Fig. 3.12, together with the measurements in the circuits with the samples. It may be remarked how the pressure losses in the short-circuited section are quite important with respect to the overall losses in the circuits with the samples. The pressure drop in the piece of pipe of equivalent length to the TPMS sample is, on the other hand, negligible

The tested samples are not completely filled with TPMS, but they comprehend inlet and outlet parts with diverging and converging manifolds. However, by evaluating inlet and outlet pressure drops within the sample by appropriate literature coefficients, these amount to less than 2%. Thus, the measured Δp values refer practically only to the pressure drop due to TPMS.

The uncertainty evaluation of the measured values follows the guidelines of the JCGM [112], as reported in Section 3.2.2. Thus, while the pressure losses in the metallic sample circuit were directly acquired from the differential pressure

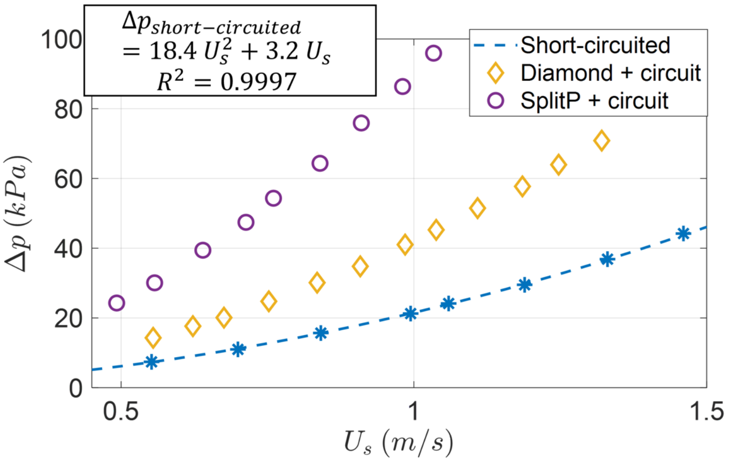

Fig. 3.12 Pressure losses in the polymeric circuit and short-circuited section.

transducer, in circuit with the polymeric sample, the uncertainty from pressure losses of the short-circuited loop must be accounted for, as in Eq. (3.10).

$$un(\Delta p_{PS}) = \sqrt{un(\Delta p_{P-circuit})^2 - un(\Delta p_{short-circuited})^2} \tag{3.10}$$

The uncertainty of the friction factor and Reynolds number was computed using the uncertainty propagation formula of Eq. (3.11), where y is the dependent variable and x_i the i-th independent variable.

$$un(y) = \sqrt{\sum_i \left(\frac{\partial y}{\partial x_i} un(x_i)\right)^2} \tag{3.11}$$

3.3.3 Results and discussion

In Fig. 3.13, the hydraulic characteristics of the Diamond and SplitP metallic samples are plotted. In Fig. 3.13a the error bars were not inserted as they were smaller than the marker size, and thus not visible. The Diamond and SplitP samples had similar porosity ($\varphi \sim 70\%$) but very different hydraulic characteristics: the SplitP had a quite larger hydraulic impedance, which could be related to its smaller hydraulic diameter (2.4 mm against 3 mm of the Diamond) and thus higher surface area-to-volume ratio. It must be noted that the SplitP samples were tested with lower flow rates - and thus lower superficial velocities - than the Diamond devices because of the range of the pressure transducer. The larger flow impedance of the SplitP TPMS compared to Diamond confirms the findings shown (for laminar regime) by Chohuan and Gunji [116], who conducted an experimental study on the pressure drop of 32 sheet-TPMS samples (Gyroid, Diamond, Lidinoid and SplitP) printed via SLA with an air circuit and they showed that SplitP lattice had a larger flow impedance than Diamond. The larger pressure losses within SplitP were also shown in Chapter 2.

The TPMS being periodic structures which are invariant in the translation in three principal directions, and since the total length of the TPMS insert in those samples was a multiple of the unit cell, inverting the direction of the flow within those samples should produce the same pressure losses, and every difference must be reported to discretization and printing errors. Thus, the samples were tested inverting the flows and the results are denoted with the subscript "rev" in Fig. 3.13, giving substantially the same hydraulic characteristics for both TPMS topologies, as expected. Also, the $f - Re_{D_h}$ curves of the two flow directions lied within the error bars. From the test results, it turned out that in the Reynolds numbers range 3000-4000, the friction factor of the SplitP sample was almost twice that of the Diamond sample.

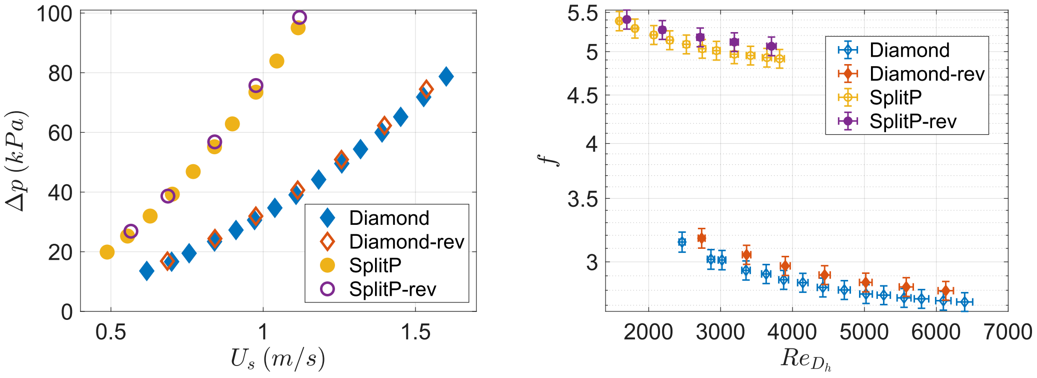

(a) (b)

Fig. 3.13 Hydraulic impedance of metallic samples in dimensional form U_s vs Δp (a) and dimensionless form f vs Re_{D_h} (b).

The friction factors for the two samples were plotted in Fig. 3.14, for both the metallic and polymeric materials. For both topologies, it might be noticed that the polymeric sample had lower friction factors than the metallic one, which can be explained by the different roughness of the two materials. Indeed, while the steel samples can have a large roughness, the SLA technique produces very precise objects, allowing smoother surfaces compared to other techniques, as already remarked by

Zimmer et al. [117] and Hawken et al. [16] in a lower Reynolds number range than the present experimental campaign.

The difference between the polymeric and metallic sample is definitely more pronounced for Diamond than for SplitP, as the Diamond samples had friction factor discrepancies around 50% between the two materials, while within the SplitP only around 10%. The SplitP having a more complex structure, its hydraulic impedance due to the pressure stresses on wall surfaces normal to the flow could be more significant than the viscous shear stresses. This would explain why the relative differences between polymer and metal due to roughness were reduced in SplitP compared to Diamond.

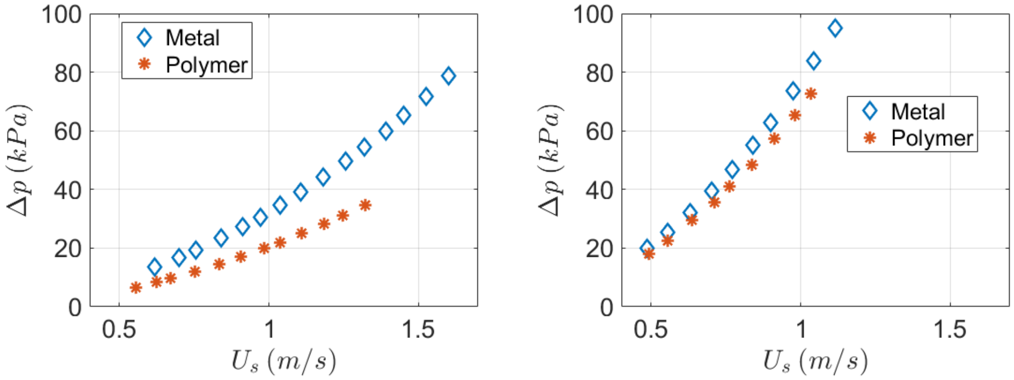

(a)

(b)

Fig. 3.14 Hydraulic characteristic for the Diamond (a) and the SplitP (b) sample, respectively.

3.4 Comparison to expectations from simulated results

This section aims at comparing and assessing computational fluid dynamics (CFD) models performance against the obtained experimental results in the hydraulic test campaign of Section 3.3. While in the previous chapter the open-source code OpenFOAM was used for a single cell under laminar conditions, in the case under consideration, with a more complex geometry and turbulent flow conditions, several CFD codes are compared in order to identify the best choice.

3.4.1 Computational methodology

In the computational model, only the receiver geometry was considered, being the rest of the circuit negligible for the pressure losses. A polyhedral grid was generated in STAR-CCM+ [118], and suitable boundary conditions were applied, as shown in Fig. 3.15a: inlet flow rate and pressure outlet, where 2 bar of outlet condition was set, coherently with the experimental values. Only the fluid domain was simulated, and the interface fluid-solid was set as non-slip walls. In Fig. 3.15b a detail of the employed mesh in the Diamond sample is presented.

As discussed in the previous chapter, following the ASME guidelines , the iterative error was reduced until it became negligible compared to the discretization error, without requiring convergence to machine precision. Consistently with this criterion, in the present simulations involving more complex geometries, the normalized residuals were reduced until flatness, reached at values on the order of $10^{-4} - 10^{-5}$.

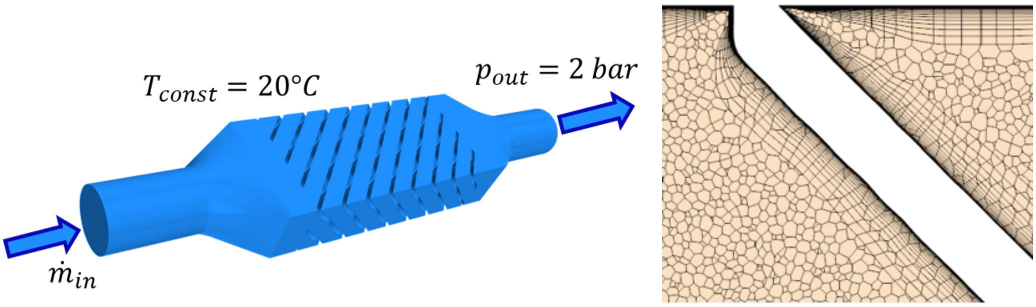

(a)

(b)

Fig. 3.15 Numerical domain of the Diamond sample, with inlet and outlet conditions highlighted (a) and mesh detail (b).

Because of the high Reynolds numbers, attaining values of 4000 for the SplitP and 6500 for the Diamond, the flow regime was turbulent, thus 17 boundary layers were inserted to capture the near-wall behavior and the first cell y^+ was approximately 1. Three CFD applications were tested and compared against the experimental results, STAR-CCM+ [118], Ansys Fluent [119] and OpenFOAM [120]. Once decided on a code, different Reynolds Averaged Navier Stokes (RANS) models were employed, namely Realizable $k-\varepsilon$, $k-\varepsilon$ Lag Elliptic Blending (EB) and Shear Stress Transport (SST) $k-\omega$ turbulence models.

The softwares solved the 3D, steady-state Navier Stokes equations for water with constant properties, using the SIMPLE algorithm (Semi-Implicit Method for

Pressure-Linked Equations). For the turbulence a discretization scheme of the 1^st order was used, and of 2^{nd} order for the convection (with the exception of the $k-\omega$ model, for which a 1^{st} order discretization scheme for the convection was used because of convergence issues).

A grid convergence analysis was performed to generate the suitable computational grid for the analysis. Four grids (see Tab 3.8) were generated and the results in terms of pressure losses at the maximum flow rate are shown in Figure 3.16. The plotted pressure drop is normalized with respect to the pressure drop of the finest mesh, labeled as *Ref1*. The Grid convergence study was performed for the three investigated turbulence models in STAR-CCM+, and also with the Realizable $k-\varepsilon$ model in Ansys Fluent for the Diamond sample.

The simulations for all the turbulence models have been performed on the same mesh for simplicity. The numerical grids were refined to such an extent that, as the cell size decreased, all models exhibited a convergent trend, albeit not a monotonic one. Indeed, each turbulence model could benefit from a different computational grid but, given the large amount of conducted simulations the same set of grids has been used. Moreover, this also helped in comparing the three models at similar computational costs.

Table 3.8 Number of polyhedral cells in the receiver grids.

	Ref1	**Ref2**	**Ref3**	**Ref4**
Diamond	12.2M	5.6M	3.9M	2.0M
SplitP	13.3M	9.3M	5.6M	3.3M

From Fig. 3.16 the convergent trend of the different grids results is clear for the Diamond sample, while if not completely convergent for the SplitP, the results of the two finest meshes are practically very close. When non-otherwise explicitly stated, the following plots refer to STAR-CCM+. It is also interesting to notice that the Realizable $k-\varepsilon$ model has a similar qualitative trend while refining the mesh for both the commercial CFD softwares. In order to verify that the results were within the asymptotic regime, an additional grid coarser than the four meshes used in the convergence study was generated. The corresponding results were compared with those obtained from the grids employed in the convergence analysis, revealing significantly different outcomes, as shown in 3.17.

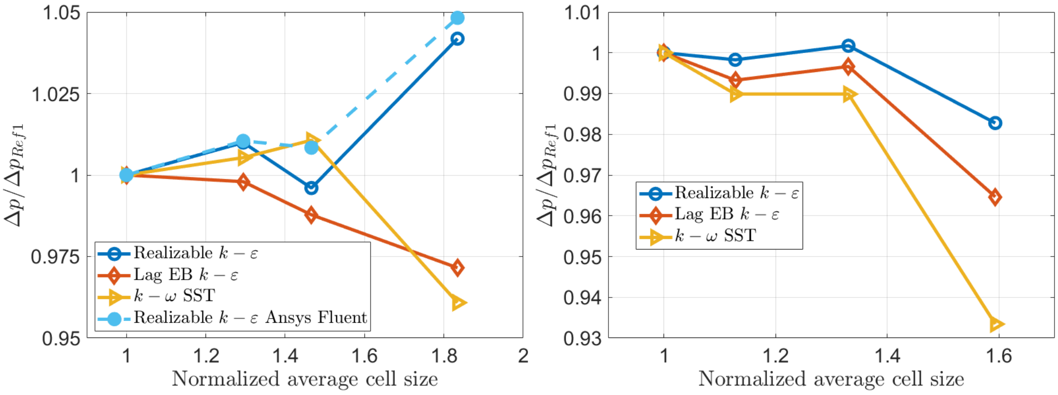

(a) (b)

Fig. 3.16 Grid convergence results on the normalized pressure drop within the samples: (a) Diamond and (b) SplitP.

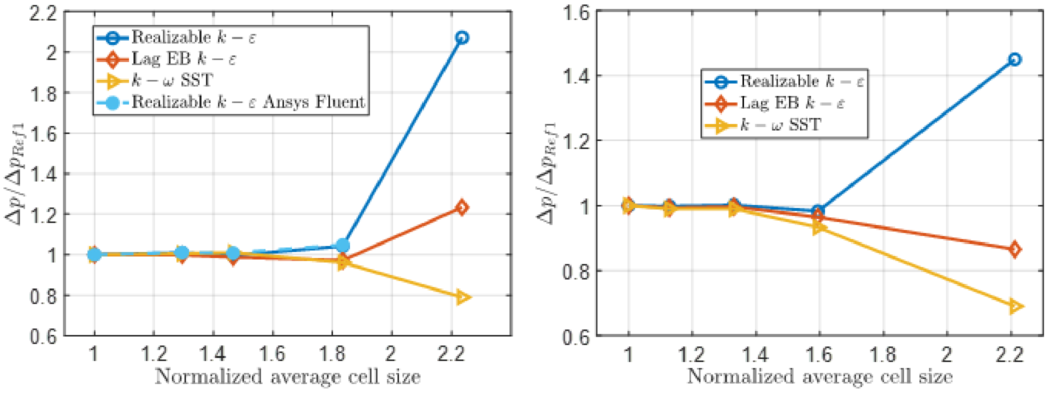

(a) (b)

Fig. 3.17 Grid convergence results on the normalized pressure drop within the samples, with the addition of the coarser grid for the verification of the asymptotic range attaining: (a) Diamond and (b) SplitP.

Following the same procedure used in Section 2.3.1, prescribed by the ASME V&V Standard [96], the numerical uncertainties due to discretization were computed and are depicted in Tab. 3.9, while the computed order of convergence are reported in Tab. 3.10. The order of convergence of the SST $k-\omega$ model has been limited to 1, as only a 1st order discretization scheme has been employed

Table 3.9 Numerical uncertainty due to discretization in the receiver models.

	Realizable $k-\varepsilon$	**SST $k-\omega$**	**$k-\varepsilon$ Lag EB**	**Realizable $k-\varepsilon$ - Ansys**
Diamond	2%	2%	3%	2%
SplitP	7%	8%	3%	

Table 3.10 Computed order of convergence γ for the different turbulent models.

	Realizable $k-\varepsilon$	**SST $k-\omega$**	**$k-\varepsilon$ Lag EB**	**Realizable $k-\varepsilon$ - Ansys**
Diamond	2.00%	1.00%	1.97%	2.00%
SplitP	1.94%	1.00%	2.00%	

3.4.2 Turbulence models

Considering that the velocity vector can be decomposed in an average and a fluctuating part $\boldsymbol{u} = \mathcal{V} + \boldsymbol{u'}$, to close the Navier-Stokes equations the Reynolds stress tensor $\mathcal{R}^t = -\rho\overline{\boldsymbol{u'} \otimes \boldsymbol{u'}}$ must be modeled. In index notation, $\mathcal{R}^t_{ij} = -\rho\overline{u'_i u'_j}$.

The most widely used RANS turbulence closures are linear eddy viscosity models, relying on the Boussinesq approximation of Eq. (3.12), where the Reynolds stress tensor is approximated by a linear constitutive relationship with the mean strain rate tensor $\overline{\mathcal{S}} = 1/2\left(\nabla\mathcal{V} + (\nabla\mathcal{V})^T\right)$. In index notation and divided by the density, Eq. (3.12) is written as Eq. (3.13).

$$\mathcal{R}^t = 2\mu_t\overline{\mathcal{S}} - \frac{2}{3}\rho k\mathcal{I} \tag{3.12}$$

$$-\overline{u'_i u'_j} = \nu_t\left(\frac{\partial\mathcal{V}_i}{\partial x_j} + \frac{\partial\mathcal{V}_j}{\partial x_i}\right) - \frac{2}{3}k\delta_{ij} \tag{3.13}$$

In Eq. (3.12)-(3.13), μ_t and ν_t are the dynamic and kinematic eddy viscosities. $\nu_t = \mu_t/\rho$ is defined as in Eq. (3.14) or Eq. (3.15) [93] depending on whether it belongs to a $k-\varepsilon$ or a $k-\omega$ model. δ_{ij} is the Kronecker Delta. k is the turbulent kinetic energy, defined in Eq. (3.16). ε is the turbulence dissipation rate, and ω is the specific turbulence dissipation rate.

$$\nu_t = C_\mu\frac{k^2}{\varepsilon} \tag{3.14}$$

$$\nu_t = C_\mu \frac{k}{\omega} \tag{3.15}$$

$$k = \frac{1}{2}\overline{(\boldsymbol{u}' \cdot \boldsymbol{u}')} = \frac{1}{2}\overline{u_i' u_i'} \tag{3.16}$$

Those linear eddy viscosity models rely on two transport equations for k and ε/ω supplementary to the equations of mass and momentum conservation, with the form of Eq. (3.17).

$$\underbrace{\frac{\partial(\rho\Gamma)}{\partial t}}_{\text{Rate of change}} + \underbrace{\nabla \cdot (\rho \Gamma \mathcal{V})}_{\text{Convection}} = \underbrace{\nabla \cdot \left[\rho\left(\nu + \frac{\nu_t}{\varsigma_\Gamma}\right)\nabla\Gamma\right]}_{\text{Diffusion}} + \underbrace{\mathscr{P}_\Gamma}_{\text{Production rate}} + \underbrace{\mathscr{D}_\Gamma}_{\text{Destruction rate}} \tag{3.17}$$

In the above transport equation, Γ is the transported variable, ς_Γ is a constant depending on the turbulent model and $\nu + \frac{\nu_t}{\varsigma_\Gamma}$ is referred to as the effective viscosity.

The Realizable $k-\varepsilon$ model [121] employs the transport equation of Eq. (3.17) for k and ε but adds the realizability constraint [122] to the eddy viscosity and it introduces additional terms in the production term of the ε equation with respect to the standard $k-\varepsilon$ model.

The SST $k-\omega$ model [123], on the other hand, blends a $k-\omega$ model near wall and a $k-\varepsilon$ model in the free-stream, to maximize the efficiency of both models. In STAR-CCM+ [124], the realizability constraint can be optionally selected as well as different constitutive relations to account for the anisotropy of turbulence, i.e. using a non-linear relationship between the Reynolds stress tensor and the mean strain rate tensor.

Finally, the $k-\varepsilon$ Lag EB model [125, 126] was derived from the Elliptic Blending Reynolds Stress model of Lardeau et al. [127], which expanded a Reynolds Stress Model (RSM) with an elliptic equation to describe the near-wall behavior of the flow and from the Lag $k-\varepsilon$ model of Revell et al. [128]. The $k-\varepsilon$ Lag EB model of Lardeau et al. [125] bears resemblance with the standard $k-\varepsilon$ model and it adds a transport equation for the lag ϕ between stress and strain and an elliptic equation for the blending factor. Moreover, it enforces the realizability constraint within the eddy viscosity formulation and has slightly modified definition of the effective viscosity as $\frac{\nu}{2} + \frac{\nu_t}{\varsigma_\Gamma}$. It employs a quadratic constitutive relation between the Reynolds stress tensor and the mean strain rate tensor.

These three models were selected in order to investigate both a $k-\varepsilon$ and $k-\omega$ model (of which the Realizable and SST are the most recent and widely used representatives), and to study a newer model such as Lag EB, that appears promising for experimental validation, as shown by Difonzo et al. [129]. In the literature for the study of TPMS, Realizable $k-\varepsilon$ was used, among the others, in [31, 130–132], SST $k-\omega$ in [25, 30, 31, 132, 133] and $k-\varepsilon$ Lag EB in [31].

3.4.3 Results and discussion

First of all, the three different computational tools were compared over the Realizable $k-\varepsilon$ turbulence model applied to the Diamond sample, using the same grid and the same solvers.

Although the turbulence model is the same, the three codes have different approaches for the near-wall behavior, which is crucial for the gradient calculation at wall, responsible for the pressure losses of internal flows. On one hand, both STAR-CCM+ [134] and Ansys Fluent [119] use the *Two-Layer* approach [135], which divides the near-wall region into a fully turbulent zone and a viscous-dominated layer, based on a modified wall Reynolds number. In the fully turbulent zone, the $k-\varepsilon$ equations are employed, while in the viscous-dominated layer ε is specified. Both STAR-CCM+ and Ansys Fluent adopt an innovative and enhanced wall treatment, respectively named *All* y^+ and *Enhanced wall treatment*. Both of them blend the low y^+ and the high y^+ wall treatments to enhance stability of the solution. In addition, to address turbulence anisotropy induced by strong streamline curvature, a curvature correction was applied in the simulations, modifying the turbulent kinetic energy production term as a function of the local rotation rate and vorticity. A pressure-gradient correction is available in Ansys Fluent but not in STAR-CCM+. Nevertheless, even in the absence of this specific correction, the improved *All* y^+ wall treatment used in STAR-CCM+ is designed to enhance both the accuracy and the numerical robustness of the solution.

OpenFOAM, on the other hand, does not provide a Two-layer approach neither a blended wall treatment comparable to the one used by STAR-CCM+ and Ansys

Fluent, but the *Low Re wall functions* might be used, which adopt a low y^+ wall treatment, that solves the transport equations of turbulent variables down to the wall.

The CFD tools were compared on the same mesh, using the same solvers, on four mass flow rates within the Diamond sample, as shown in Fig. 3.18.
STAR-CCM+ and Ansys Fluent produced very close results, while OpenFOAM was far from the other two softwares. This could be imputed to the dissimilar wall treatment. Furthermore, it must be noted that OpenFOAM had quite large oscillations in the results, up to $4\% - 8\%$, which were used as error bars in the plot. In addition, commercial CFD packages generally proved more suitable for handling complex geometries, thanks to more robust meshing tools; in particular, the STAR-CCM+ mesher performed better than the Ansys Fluent mesher, for which it was not possible to generate a suitable grid for the complex TPMS geometry. Thus, STAR-CCM+ was then used for the rest of the analysis.

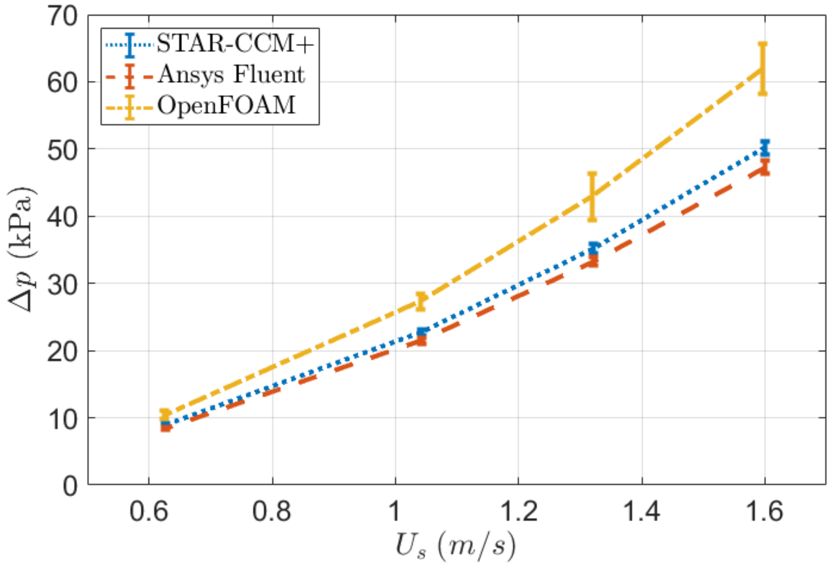

Fig. 3.18 CFD tools comparison on the Diamond hydraulic impedance.

Fig. 3.19 compares the experimental data with the results from the simulations using the different turbulence models. First, it is clear how the two $k-\varepsilon$ models produced similar results ($k-\varepsilon$ Lag EB and Realizable $k-\varepsilon$) in both the Diamond and the SplitP samples, while the SST $k-\omega$ model predicted larger pressure drops than the other two models. Another remarkable point is that the Realizable $k-\varepsilon$ model accurately simulated the experimental data of the Diamond polymeric sample and the SST $k-\omega$ was even above the polymeric curve (but below the metallic one), whereas for the SplitP sample all the models were below the polymeric experimental curve. Thus, the tested RANS models were not always capable to capture the experimental behavior of the TPMS, at least not for the SplitP sample.

Khalil et al. [23] found similar outputs comparing the Realizable $k-\varepsilon$ and SST $k-\omega$ turbulence models against experimental data in the Reynolds number range 2000-7000: the SST $k-\omega$ model predicted larger pressure losses than the Realizable $k-\varepsilon$ model, even larger than the experimental values. However, their study differed from the present one because they tested in air solid-TPMS printed in AlSi10Mg with 80% porosity, with approximately the same cell size of the present study. It is possible that the experimental test of Khalil et al. was very close to the numerical results, even if on metallic samples, because the $S_V < 500$ for a 80% solid-Diamond, value much lower than the S_V of the sheet-Diamond at similar porosity (see Tab. 3.1). Thus, the influence of the roughness on the overall pressure losses could be lower.

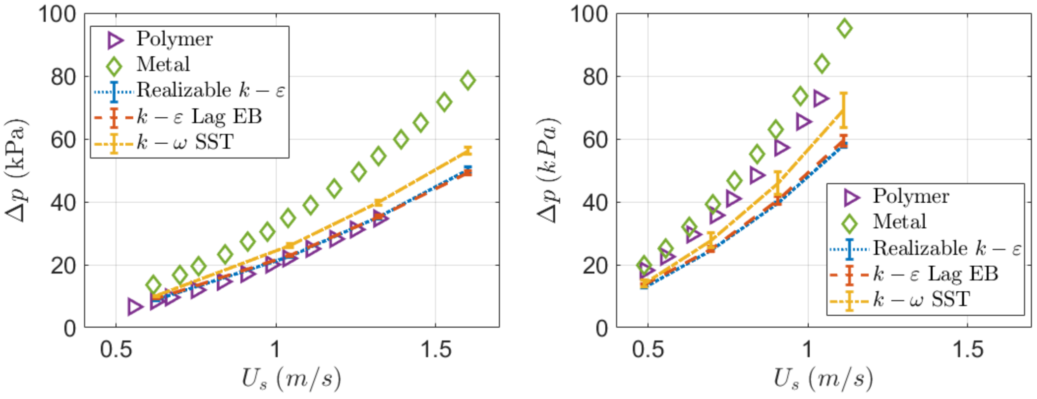

(a)

(b)

Fig. 3.19 Pressure drop vs superficial velocity in the Diamond (a) and SplitP (b) samples - comparison of experimental and numerical results.

Comparing the three tested turbulence models, the $k-\varepsilon$ family proved to be more robust than $k-\omega$, which experienced many fluctuations in the results, as also reported by [31]. Realizable $k-\varepsilon$ is less computationally demanding than Lag EB $k-\varepsilon$ and produced close outputs, within their numerical uncertainties. In the literature, there is not a clear agreement on whether turbulence model is superior for predicting the thermal-hydraulic characteristics of TPMS. For example, Balderrama Prieto et al. [31] found closer results on pressure losses using the SST $k-\omega$, while Xu et al. [132] found that the Realizable $k-\varepsilon$ model was capable of providing more accurate results for the thermal field in thermal-hydraulic tests.

Since the sheet-TPMS can be considered as combination of solid-TPMS, the permeability and inertial drag coefficient of the sheet-type could be calculated from the solid-type at half of their porosity. Following the procedure described in Appendix D, the K and C_F of the sheet-Diamond and sheet-SplitP were computed from the correlation of Section 2.3 and inserted within the Darcy-Forchheimer equation to be compared to the simulation results of the receivers in Fig. 3.20. The values of the permeability and inertial drag factor were plotted with the 68% confidence interval of their fit. A confidence interval of 68% is equivalent to plus or minus one standard deviation of the fit, in statistical terms.

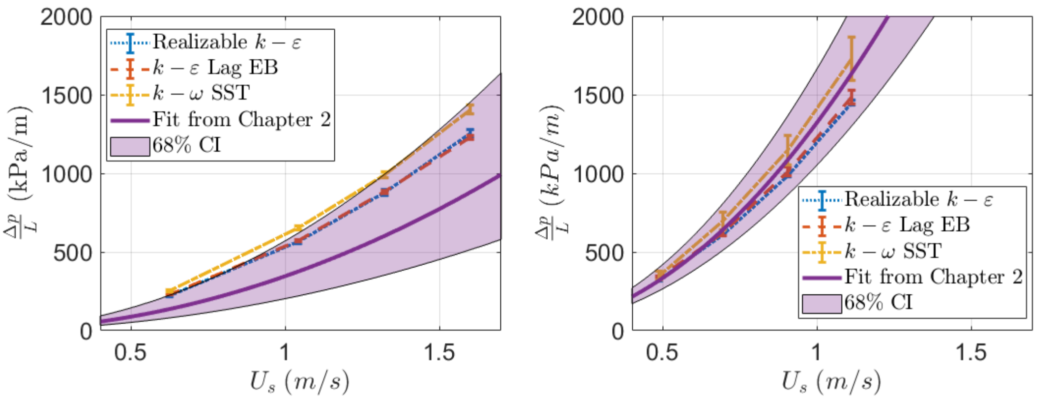

(a) (b)

Fig. 3.20 Linear pressure drop vs superficial velocity in the Diamond (a) and SplitP (b) samples - comparison of CFD results and predictive values for the correlation of the Darcy-Forchheimer parameters (Chapter 2).

In Fig. 3.20 the linear pressure drop is shown instead of the pressure drop so to be consistent with the representation of Section 2.3. The tests of the receivers largely exceeded the ranges for which the correlations were computed, both in terms of superficial velocity and Reynolds numbers - the correlations were developed for $0.3 < Re_{D_h} < 100$. Furthermore, the correlations of Section 2.3 were based on simulations using a laminar model (and the infinite medium model). However, for both the TPMS the turbulence models results and their uncertainties were within the 68% confidence interval of the fit for all setpoints but two. Also, as similarly found in Section 2.3.2 where the correlations were compared to CFD results in circular pipes, the developed model for Diamond underpredicted the CFD results, while being closer for the SplitP (when looking at the large Reynolds results). Indeed, having the

SplitP a larger surface-to-volume ration than Diamond, the relative influence of the external walls of real configurations with respect to the infinite medium (the periodic cell) is lower for SplitP than Diamond.
The larger confidence interval of the Diamond rather than the SplitP is due to the smaller coefficient of determination of the fits of the solid-Diamond with respect than the two solid-SplitP (see Tab. 2.5).

The correlations developed for the Diamond and SplitP structures in Section 2.3 were derived under laminar flow conditions and the Darcy–Forchheimer model is not intended to provide accurate predictions in transitional or turbulent regimes. Nevertheless, the present results showed that, likely due to the presence of the quadratic inertial resistance term, the model can still offer a reasonable approximation of the hydraulic impedance at higher Reynolds numbers. In this sense, the correlations proved capable of reproducing the simulation results obtained under different flow conditions, provided that an appropriate confidence interval is considered. In particular, their validity can be considered within a range corresponding to a confidence interval of 68% of the fitting, which could define the expected uncertainty when extending their use beyond the strictly laminar regime.

3.5 Chapter summary

In this chapter, two sheet-TPMS - Diamond and SplitP - were investigated as volumetric solar receivers. Two absorbers were designed and printed in AISI 316L via SLM and in resin via SLA, and they were hydraulically tested in Politecnico di Milano, Italy, in a dedicated water loop. Discrepancies were found between the polymeric and metallic hydraulic impedance, more pronounced for the Diamond than the SplitP, possibly because the more complex structure of the SplitP produced a larger hydraulic impedance due to normal pressure stresses than viscous stresses, thus reducing the relative effects of roughness, impacting only on shear stresses.

The hydraulic curve was reproduced with three different CFD solvers, OpenFOAM, STAR-CCM+ and Ansys Fluent, and three different turbulence closures. The open-source code OpenFOAM showed less stable solutions due to the wall treatment compared to the commercial solvers STAR-CCM+ and Ansys Fluent, which exhibited quite similar outcomes when using the same solver, turbulence model and computational grid. The correlations developed for the Darcy-Forchheimer equation in Chapter 2.3 were also tested against the pore-scale hydraulic simulations of the receivers filled with TPMS, and it was found that the CFD results of the whole samples fell within the porous medium curve by approximately one standard deviation, i.e. within the 68% confidence interval of the fit.

When comparing the simulation and experimental results, the hydraulic curve of the Diamond receiver printed in polymeric resin could be predicted by the CFD, the metal samples had larger pressure losses compared to the numerical predictions (and polymeric samples), and the polymeric SplitP curve was slightly higher than the tested turbulence models. Thus, further assessment on the metallic surface roughness is envisaged.

On the other hand, the thermal tests at IMDEA Institute in Madrid, Spain, were successful as the TPMS-based receivers showed large thermal efficiency in terms of absorbed versus incident power, higher than the efficiencies reported in the literature for absorbers in similar conditions of flow rate.

Having examined here two out of the three analytically studied topologies - Diamond and SplitP, the next chapter focuses on the Gyroid lattice, comparing it with SplitP under higher heat flux and flow rate conditions.

Chapter 4

Triply Periodic Minimal Surfaces for mirror cooling in nuclear fusion applications

This chapter aims at presenting innovative cooling solutions for the mirrors of DTT ECH system, employing TPMS. Section 4.1 provides a detailed outline of the DTT ECH system and components, focusing on the mirrors involved in this investigation. Section 4.2 concentrates on the design and numerical assessment of TPMS-based cooling systems for the TL and launcher mirrors and Section 4.3 presents the design of a prototype mirror filled with TPMS, an experimental investigation and comparison with simulations results. At the end, Section 4.4 provides a brief synopsis of the findings of this chapter.

Portions of the present chapter were published or presented in the following scientific papers and conference:

- E. Gajetti, M. Bonesso, A. Bruschi, F. Fanale, S. Garavaglia, G. Granucci, A. Moro, A. Pepato, A. Romano and L. Savoldi, "A new efficient mirror cooling for the Transmission Line of Fusion Reactor ECH systems based on Triply Periodic Minimal Surfaces". *IEEE Transactions on Plasma Science*, pages 1-7, 2024. [136]
- E. Gajetti, A. Bruschi, S. Garavaglia, F. Fanale, L. Marocco, A. Romano and L. Savoldi, "Development of a novel TPMS cooling structure for the launcher

mirror M2 of the DTT ECH system". *Presented at the 33rd Symposium on Fusion Technology - SOFT2024*. [137]

- E. Gajetti, A. Bruschi, F. Fanale, W. Ferretto, G. Granucci, A. Lucchini, L. Marocco, A. Romano and L. Savoldi, "Design, manufacture and experimental characterization of a first-of-a-kind DTT ECH mirror equipped with TPMS". *Submitted to IEEE Transactions on Plasma Science, 2025*. [138]
- A. Bruschi, M. Bonesso, D. Busi, C. Cesari, R. Chomicz, R. Dima, F. Fanale, P. Fanelli, G. Favero, E. Gajetti, S. Garavaglia, G. Granucci, A. Pagliaro, A. Pepato, P. Platania, N. Rispoli, A. Romano, A. Salvitti, L. Savoldi, A. Simonetto, M. Turcato and F. Zanon, "Challenges of the DTT ECH Launchers and options under study", *Submitted to IEEE Transactions on Plasma Science, 2025*. [139]

4.1 DTT Electron Cyclotron Heating system

DTT [140–143] is an experimental facility being constructed in Frascati, Italy, for the study of DEMO-relevant power exhaust issues. The DTT ECH system is expected to deliver up to 32 MW [69] in its last operational stage, through 32 170 GHz-gyrotrons [144, 145] grouped in 4 clusters of 8 MW sources each. Each gyrotron (denoted as $\mathcal{G}$) cluster will be organized as in Fig. 4.1, depicting the cluster organizations around a combining mirror via a Single-Beam TL (SBTL) [146]. The combining mirror, or combiner, combines the 8 single beams into a beam bundle which is then transmitted in the Tokamak Hall Building (THB) via the Multi-Beam TL (MBTL) [78]. In the Tokamak Building the beam bundle is split back into single-beams by a splitter mirror and transmitted via another SBTL to the launchers [146].

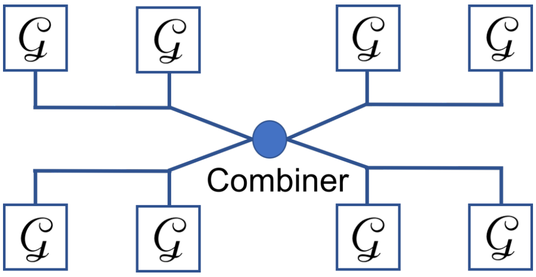

Fig. 4.1 Schematics of a gyrotron cluster and SBTL.

The single-beams are polarized via corrugated polarizing mirrors (polarizer) [146, 78] upstream the antennae. The EM beams from each cluster are injected into the plasma through an equatorial and an upper antenna composed by four and two launchers respectively, in a dedicated DTT sector [62, 61, 69, 68]. Each launcher consists of two mirrors: M1 and M2. M1 is a fixed mirror, focusing the beam from the TL, while M2 is plane and steerable to precisely direct the beam into plasma [147, 62, 148].

Several components of the ECH system stand at the edge of their operational capabilities owing to technological limitations, for quasi-optical transmission [149] of Gaussian waves requires sub-millimeter size tolerances in the production and in any structural deformations. Therefore, almost all the ECH components need active cooling to prevent severe deformations that would prevent their proper functioning.

In particular, during the EM wave reflection on the mirrors, large Ohmic losses are produced in the conductive material. Thus, various cooling solutions have been implemented in the different nuclear fusion facilities, ranging from traditional serpentine cooling of EAST [150], KSTAR [151], ITER [152], CFETR [153] to spiral cooling, proposed for W7-X [154, 77] and for some ITER mirrors [155, 156]. In more recent years, some improved designs have been proposed, such as a heat removal system based on cylindrical fins around which the fluid flows freely, proposed for EAST [157], radial channels [147] or modified spiral structure [148].

These studies and the demand for further improvements in cooling system performance have demonstrated the importance of an innovative approach in this field, such as the use of TPMS. Furthermore, in the case of fixed mirrors such as the combiner, splitter, or M1, a highly conductive material such as copper or a copper alloy can be used but, for steerable mirrors as M2, the proximity to the intense magnetic field of the Tokamak induces high electromagnetic forces that oppose its movement, hence the need for materials with lower electrical (and consequently thermal) conductivity, as Stainless Steel or Inconel.
TPMS systems were proposed for the most loaded mirrors of the TL (combiner, splitter and polarizer) and launcher (M2 mirror) and for a prototype mirror.

For an elliptical electromagnetic wave, the intensity distribution of the beam is given by Eq. (4.1) [158], being $\mathscr{I}_0$ the peak value, which is equal to twice the average value of the intensity module $\frac{Q_{MW}}{\pi w_x w_y}$, thus resulting in Eq.(4.2). w_x and w_y are the wave waist sizes and Q_{MW} the beam power.

$$\mathscr{I} = \mathscr{I}_0 e^{-2\left(\left(\frac{x}{w_x^2}\right)^2 \left(\frac{y}{w_y^2}\right)^2\right)} \tag{4.1}$$

$$\mathscr{I} = \frac{2Q_{MW}}{\pi w_x w_y} e^{-2\left(\left(\frac{x}{w_x^2}\right)^2 \left(\frac{y}{w_y^2}\right)^2\right)} \tag{4.2}$$

The actual heat flux q_{MW} to be removed by the cooling system depends on the absorption coefficient of the mirror $\mathscr{A}$ as in Eq. (4.3). The absorption coefficient accounts for the mirror material, the surface roughness, the air impedance and the incidence angle of the beam [78].

$$q_{MW} = \mathscr{A}\mathscr{I} \tag{4.3}$$

The parameters to compute the heat flux for each mirror of the present analysis are displayed in Tab. 4.1 [147, 148, 159, 160].

Table 4.1 Parameters of the microwave heat flux.

Mirror	$\mathscr{A}$	$Q_{MW}\,(MW)$	$w_x\,(mm)$	$w_y\,(mm)$
Splitter/combiner	0.002	1.0	25	35
Polarizer	0.0055	1.0	20	22
M2	0.0087	1.1	43	67
Prototype	0.005	1.0	31	44

In the case of the launcher mirror, the vicinity to the plasma causes an additional thermal load due to radiation from the plasma, whose modulus varies according to the orientation of the mirror and is considered uniform across its entire surface. Thus, for the M2 mirror $q_{M2} = q_{MW} + q_{plasma}$. The heat fluxes on the surfaces of the mirrors are shown in Fig. 4.2. In this figure, the diverse dimensions of the mirrors can be appreciated, and the peak values of the heat load, whose largest value is found on the polarizer mirror, up to $\sim 7.7 MW/m^2$. Most of the mirrors have an elliptical shape but the polarizer, which is circular and presents corrugations on its reflective surface. The other considered mirrors are plane but the prototype mirror, having a parabolic reflective surface.

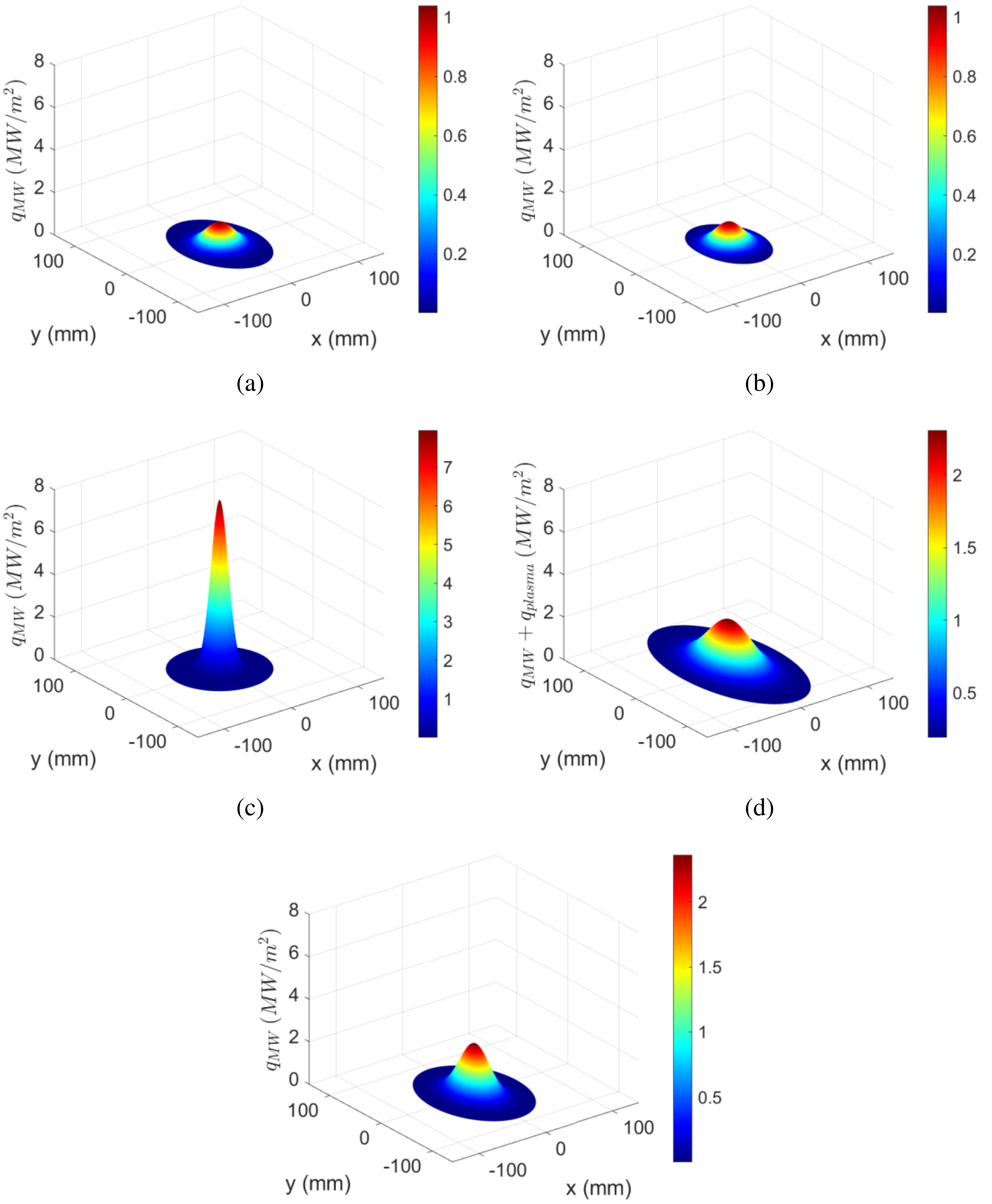

(a) (b)

(c) (d)

(e)

Fig. 4.2 Heat flux on the mirrors surfaces. (a) Splitter, (b) combiner, (c) polarizer, (d) M2 and (e) prototype. The colorbars refer to the heat flux values.

4.2 Design and simulations of the TPMS-based cooling systems

For the above mentioned mirrors in the TL and launcher of the ECH system of DTT, a novel cooling system equipped with TPMS was developed. Initially, a study on the TPMS performance was conducted by varying different geometric parameters of the lattices and comparing two topologies and sheet/solid types. Also, a configuration with cylindrical periodicity was investigated and compared to the cartesian periodicity of the TPMS lattices. A mechanical analysis was performed on those mirrors, too. Then, based on the results of the previous parametric analysis, the cooling system for the M2 and prototype mirror, more loaded, was designed and numerically simulated.

4.2.1 Computational methodology

The mirrors geometries were drawn in SolidWorks [109] and the TPMS generated using nTop [110]. The CFD analyses were carried out in STAR-CCM+ [118] while the thermo-mechanical analyses were performed using Ansys Mechanical [161]. The use of Star-CCM+ is the outcome of the study in the previous chapter, where it became clear that this commercial software is able to handle complex geometries more easily, allowing for more stable results. The computed Reynolds numbers were larger than 400 in the splitter-combiner (with the lowest flow rate) and larger than 800-1000 in the other mirrors. Thus, based on the analysis of the previous chapter, for which the Realizable $k-\varepsilon$ was the most robust model with an accuracy comparable to SST $k-\omega$, Realizable $k-\varepsilon$ was employed. The adopted turbulence model was also consistent with other studies on ECH mirror cooling [147, 148].

For almost all the mirrors, due to the high computational cost associated with modeling the full mirror geometry, symmetry-based simplifications were adopted. Although TPMS structures with Cartesian periodicity do not present any symmetry planes (being periodic and not symmetric), reduced domains corresponding to one half or one quarter of the mirror were generated. To enforce symmetry conditions, a fictitious thin wall was introduced, despite not being physically present in the real configuration. An example is shown in Fig. 4.3, depicting the splitter mirror. This artificial boundary inevitably introduces additional friction and conductive effects. However, the simulations on the splitter and polarizer were intended as preliminary analyses, primarily aimed at design exploration and comparative evaluation among different TPMS configurations. For the final stage, involving manufacturing considerations and experimental validation, the complete mirror geometry was modeled without such simplifications.

All the developed cooling structures had a central inlet, to cope with the peak heat load, while depending on the mirrors one or more outlets were proposed.

Concerning the iterative error, for the less demanding cases, the normalized residuals reached values comparable to those reported in Chapter 3 (on the order of $10^{-4} - 10^{-5}$. However, for the most complex simulations, characterized by very tiny TPMS cells compared to the characteristic size of the devices, with intricate geometries and an extremely large number of cells, the residuals stabilized at values around 10^{-3}.

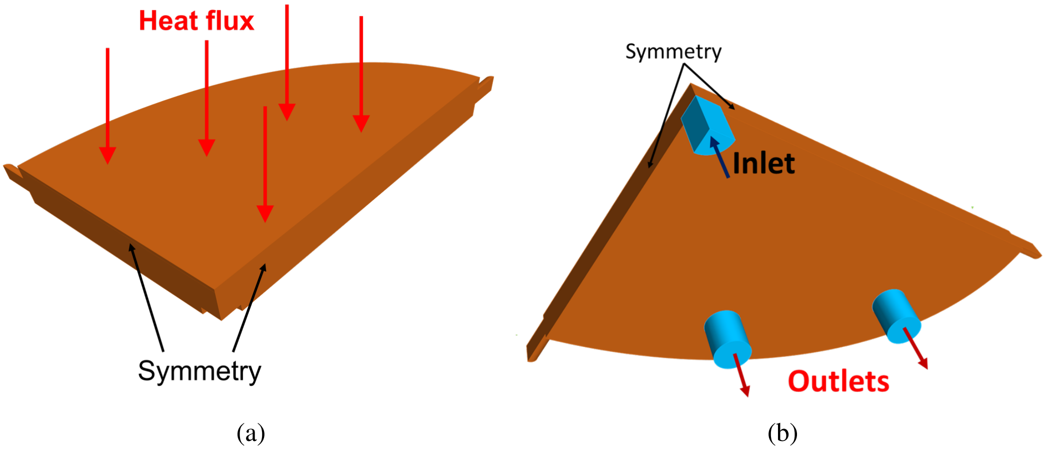

(a)

(b)

Fig. 4.3 Example of the splitter mirror cut in a quarter with imposed symmetry. (a) Heat load on the reflective surface and (b) inlet and outlets locations. Modified from [136].

The steady-state, conjugate heat transfer was solved between the solid and fluid domains, whose properties were set as temperature-dependent [162]. The solid material was mirror-dependent, as previously mentioned, while the fluid was subcooled water, for which the properties were defined according to the IAPWS-IF97 database and already present in STAR-CCM+ [118]. On the reflective layer, the fluxes shown in Fig. 4.2 were imposed, while the other boundaries were considered adiabatic.

For what regards the thermo-mechanical analyses, the temperature distribution in the solid body and the pressure field were used as loads. Depending on the mirror, specific mechanical constraints were implemented. As for the thermal-hydraulic model, symmetry was imposed along the minor and major axes, where the thin walls were inserted. Isotropic, linear, elastic behavior was assumed. Temperature dependent properties were used for all the materials, from [162].

To ensure the convergence of the models, three numerical grids were tested on the splitter mirror, and the parameters of the grid convergence study are presented in Tab. 4.2. The results, in terms of pressure drop and maximum temperature increase on the mirror reflective surface, are shown in Fig. 4.4. Because the finest and the second finest grid computed very similar results, the second finest mesh was chosen (*Ref2*). A similar mesh was then employed for all the mirrors.

Table 4.2 Mesh parameters for the grid convergence evaluation of the mirror model.

	Ref1	**Ref2**	**Ref3**
# Fluid cells	8.9M	6.7M	4.9M
# Solid cells	2.7M	2.1M	1.6M
# Boundary layers	10	8	6

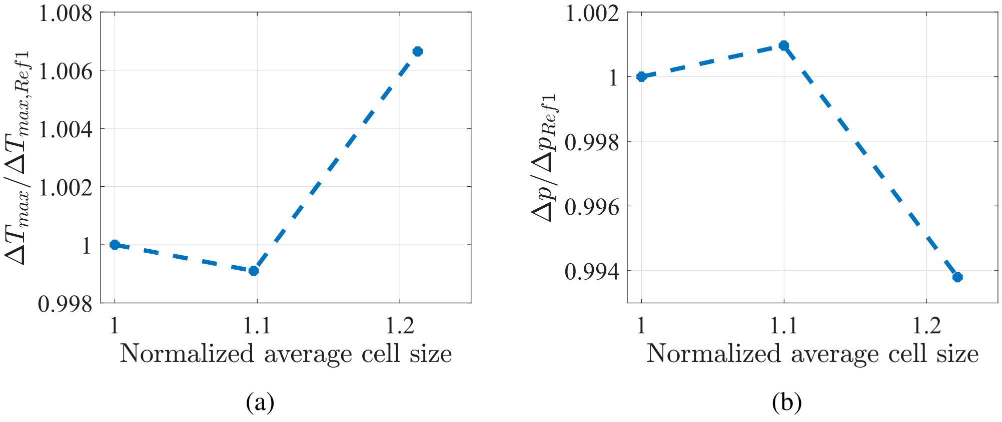

(a) (b)

Fig. 4.4 Grid convergence analysis for the mirror models. (a) Maximum temperature increase and (b) pressure drop. Modified from [136].

4.2.2 Splitter mirror: a parametric study on TPMS thermal performance

A parametric study on the thermal performance of TPMS-based cooling systems was conducted on the splitter mirror, having the combiner and splitter the same microwave heat load and the splitter being larger, thus with greater overall absorbed power. In this study, two TPMS topologies were investigated and namely the Gyroid and SplitP, whose characteristic equations are presented in Eqs. (1.3) and (1.5). Both solid and sheet-Gyroid were studied, and the sheet-SplitP. A quarter of the splitter geometry, as already previously mentioned, was filled with TPMS (see Fig. 4.6) within the L_c space as reported in Fig. 4.5. The reflective surface was 1 mm thick, and with a back width of 2 mm the total thickness of the mirror was equal to the lattice cell size L_c plus 3 mm. The splitter mirror was conceived in CuCrZr.

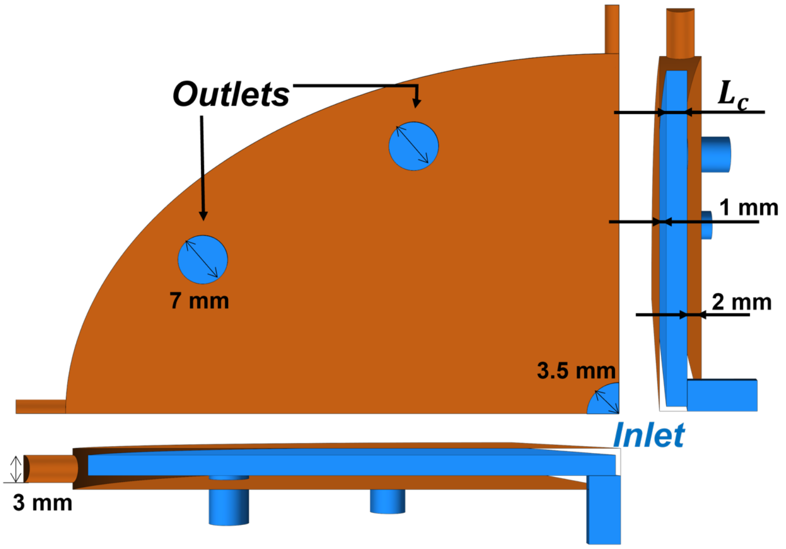

Fig. 4.5 Sketch of the splitter with dimensions of the inlet/outlets, pivots and reflective layer.

TPMS lattices

For each TPMS type, different cell size and porosity were analyzed, as reported in Tab. 4.3. The sheet-Gyroid and sheet-SplitP were referred to as GY and SY, while the solid-Gyroid was named GX.

The surface-to-fluid volume ratio was investigated as relevant geometric parameter for the heat transfer capability of the TPMS. It is plotted versus the porosity in Fig. 4.7a. S_V is defined in Eq. 4.4 and it must scale as $\frac{1}{L_c \varphi}$, considering that the wet area dependence on the porosity is a weaker order than its dependence on the cell size (see Fig. 2.2b and Appendix D).

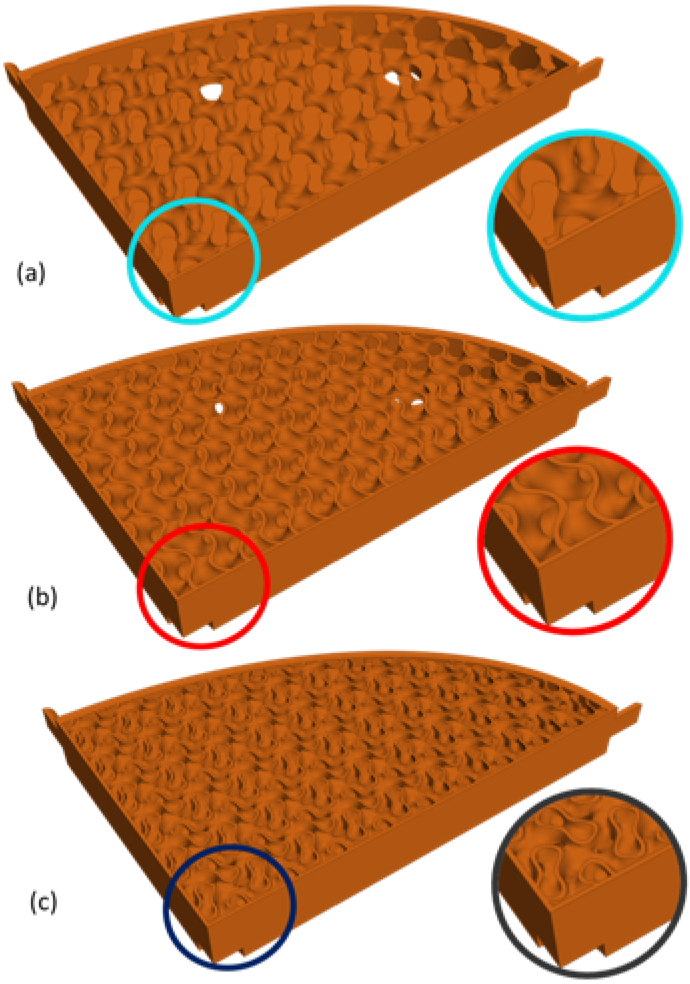

Fig. 4.6 Splitter mirror filled with TPMS. Modified from [136].

$$S_V = \frac{A_{wet}}{Vol_{fluid}} \sim \frac{L_c^2}{L_c^3 \varphi} = \frac{1}{L_c \varphi} \tag{4.4}$$

In Eq. (4.4), the finite-medium influence is disregarded, i.e the fact that the TPMS are enclosed in the mirror envelope. Indeed, the inverse proportionality φL_c vs S_V might be appreciated in Fig. 4.7b.

As visible in Fig. 4.7a, the lattices with the smallest L_c showed the largest S_V and the smallest porosities. For a given value of L_c, the solid-Gyroid had the same porosity of the sheet-Gyroid, but a slightly lower S_V because the sheet-TPMS have twice the area of the solid-TPMS at the same porosity. At similar φL_c values, the

Table 4.3 Geometrical parameters of the TPMS lattices adopted in the parametric study on the splitter mirror.

	$L_c\,(mm)$	c	φ	$S_V\,(m^{-1})$
GX1	3	±0.77	0.50	4.44e3
GY2	3	0	0.50	2.90e3
GX3	5	±0.46	0.70	2.18e3
GY4	5	0.61	0.70	1.31e3
GX5	8	±0.30	0.81	1.26e3
GY6	8	0.94	0.81	7.03e2
GY7	8	0.77	0.75	7.71e2
GY8	8	0.62	0.70	8.27e2
GY9	8	0.46	0.65	8.81e2
GY10	8	0.31	0.60	9.42e2
SX1	4	±0.70	0.49	5.11e3
SX2	6	±0.47	0.66	2.88e3
SX3	8	±0.37	0.74	1.99e3

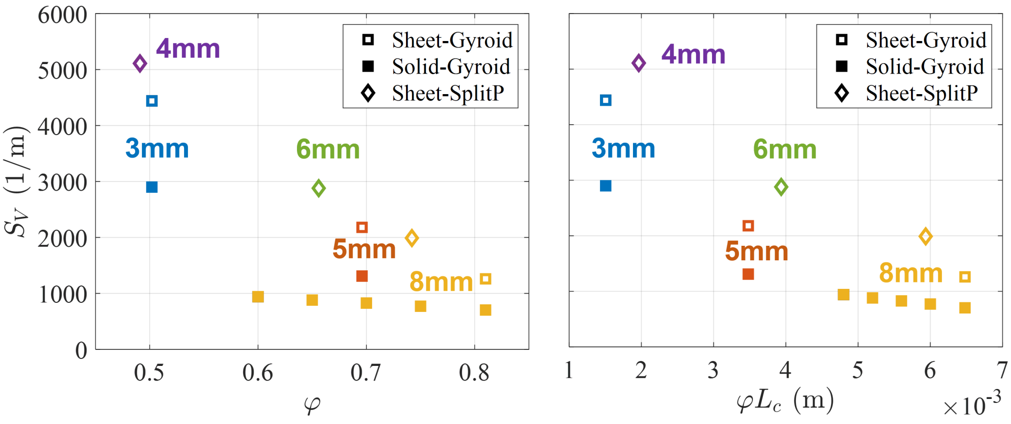

(a) (b)

Fig. 4.7 Surface-to-fluid volume ratio versus porosity (a) and porosity times cell size (b) for the TPMS adopted. Different colors correspond to different values of L_C. Splitter mirror. Taken from [136].

sheet-Gyroid had lower S_V than the SplitP, being the SplitP A_{wet} curve greater than the Gyroid on (see Fig. 2.2b). Focusing on the solid-Gyroid with $L_c = 8\,mm$, the decrease in the porosity was compensated by a tiny increase in the values S_V, in view of the decrease in the fluid volume for a comparable value of the surface, since the wetted area increased with decreasing porosity larger than 50%.

Simulation setup and mesh details

Concerning the operational conditions of the whole mirror, a flow rate of 4.2 l/min entered at 15°C through the central inlet and exited at 7 bar via the two outlets per quarter of Fig. 4.5, and the maximum achievable pressure drop was 4 bar.
As explained in Section 4.2.1, a computational grid with approximately 9M cells was used for the thermal-hydraulic simulations of the splitter. A view of the computational grid is shown in Fig. 4.8, for the sheet-Gyroid configuration.

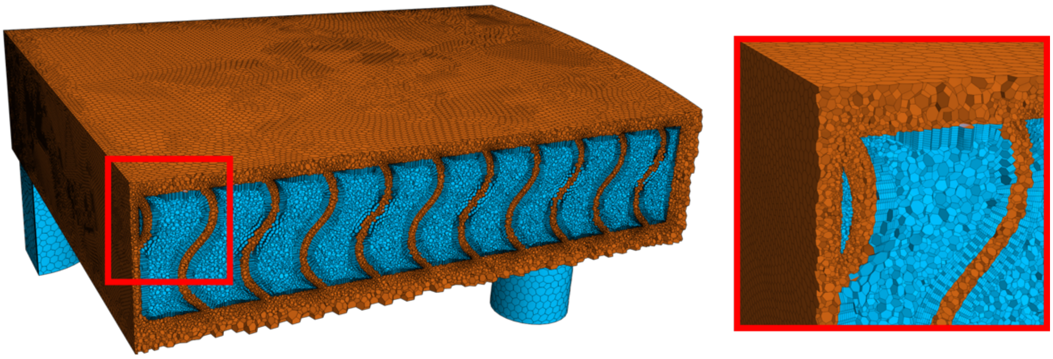

Fig. 4.8 Computational grid for the thermal-hydraulic simulations of the splitter. Configuration GY6. Taken from [136].

Concerning the thermo-mechanical analyses, only the Gyroid structures were simulated, because of computational limitations.
On the major and minor axes, two pivots were inserted for the mechanical constraints: the pivot bases were constrained to move solely along the direction of the axes (vertical displacement for the minor axis and horizontal displacement for the major axis). Symmetry was imposed on the thin walls on the minor an major axes, as for the CFD analysis.

The second-order tetrahedral grid used for the Finite Element (FE) analysis is shown in Fig. 4.10, for the GY6 configuration.

Computed thermal-hydraulic results

The streamlines computed along the TPMS structures are shown in Fig. 4.11. The sheet-Gyroid and sheet-SplitP induced a more complex fluid path than the solid-Gyroid, as expected. However, the complexity of the flow did not present qualitative differences between the two sheet geometries. High velocities were found only at the

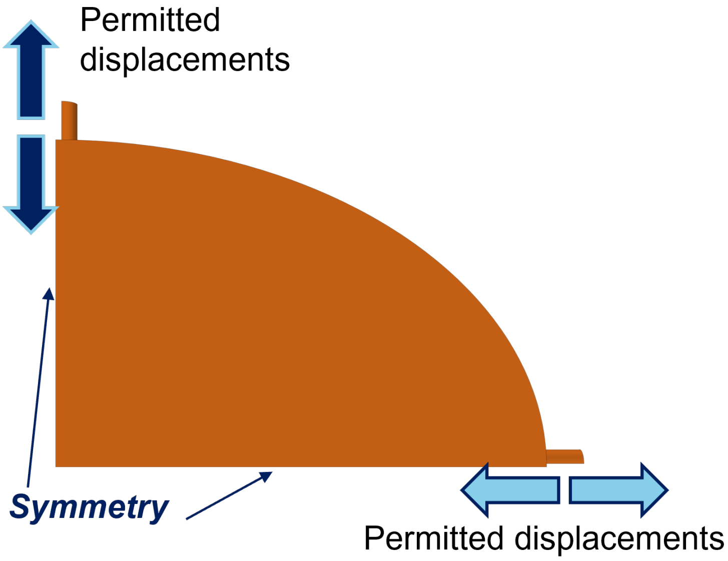

Fig. 4.9 Mechanical constraints of the splitter mirror.

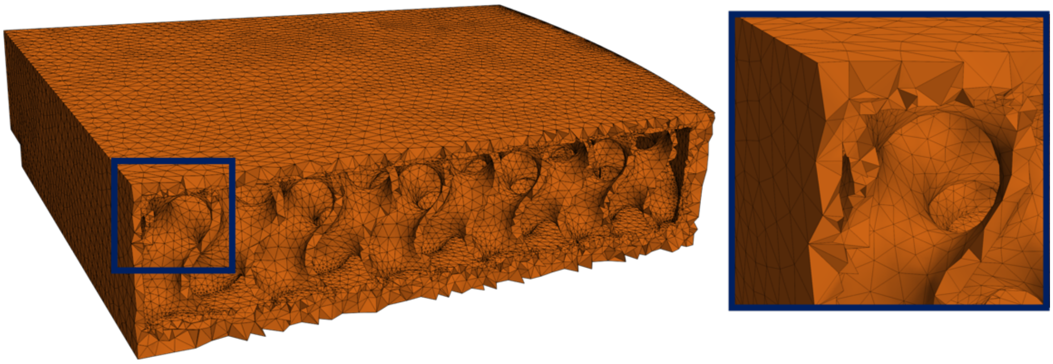

Fig. 4.10 Computational grid for the thermo-mechanical simulations of the splitter. Configuration GY6. Taken from [136].

center of the mirror, where the water was injected by the injector. The mass flow rates at the two outlets were verified to check for correct fluid distribution within the channels in the GX1, GY2, and SX1 configurations. Roughly speaking, the flow was divided between the two outlets in a ratio of 60% (near the minor axis) and 40% (near the major axis). Consequently, all three systems shown in Fig. 4.11 allowed for adequate fluid distribution, with lower velocity on the end of the major axis, where anyway the thermal load was much lower. In fact, the combination of TPMS cooling systems and inlet/outlet positions ensured effective removal of

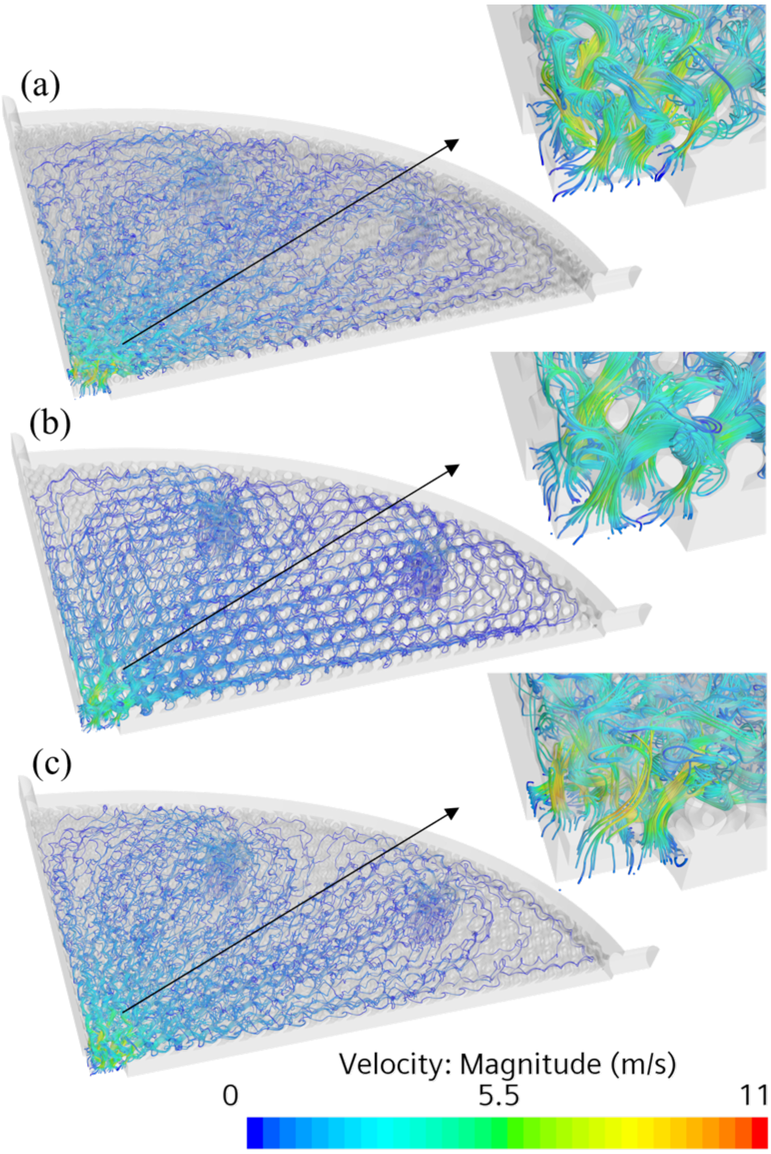

Fig. 4.11 Streamlines computed for the mirror equipped with the cooling structures (a) GX1, (b) GY2, and (c) SX1 colored by velocity. Splitter mirror. Taken from [136].

the Gaussian-distributed heat flow on the mirror layer. However, the imperfect distribution of the flow at the outlets left room for future improvements.

Fig. 4.12 presents the temperature distribution on the mirror layers cooled by GX1, GY2, and SX1, which had the largest S_V values for each structure category, thus expected largest heat removal capability. The position of the temperature peak, which was slightly shifted from the center on the major axis, was due to the Gaussian shape of the thermal load and to the lower exiting flow rate in the outlet closer to

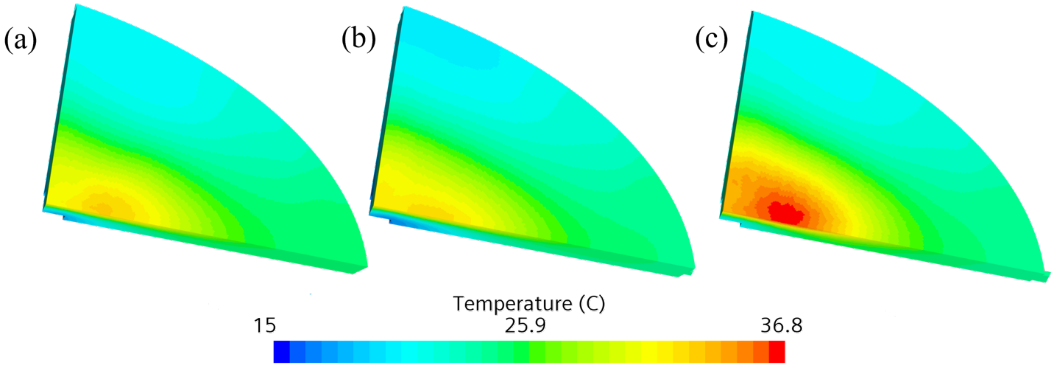

Fig. 4.12 Temperature field on the reflective layer of (a) GX1, (b) GY2 and (c) SY1. Splitter mirror. Modified from [136].

the major axis and it was independent on the TPMS structures, even at the highest porosities.

The solid-Gyroid performed quite poorly compared to the sheet-Gyroid and SplitP, as it had a surface-to-volume ratio less than 1.5 times the sheet-structures S_V, while approximately the same porosity. The sheet-TPMS showed similar results, but we should consider that the SplitP structure was created with an $L_c = 4\,mm$, whereas the tiniest Gyroids had $L_c = 3\,mm$.

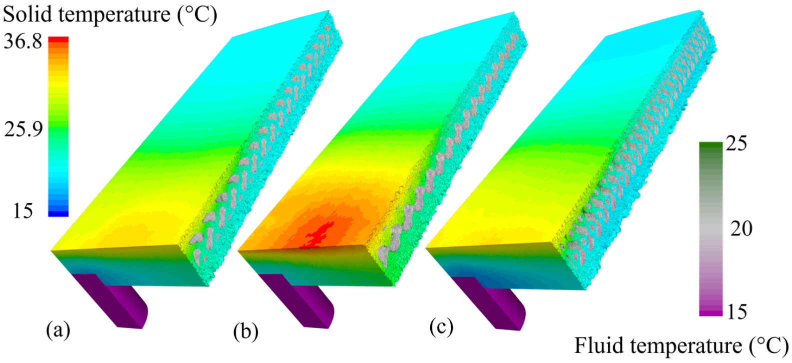

Fig. 4.13 Temperature field of the solid and fluid domain of (a) GX1, (b) GY2 and (c) SY1. Splitter mirror. Modified from [136].

An insight of the fluid temperature is provided in Fig. 4.13. In Fig. 4.14, the maximum temperature increases on the reflective surface (i.e. with respect to the 15°C of the inlet temperature) are plotted against the surface-to-volume ratio and the product of the porosity and cell size, which proved to be reasonable independent parameters to characterize the TPMS cooling ability.

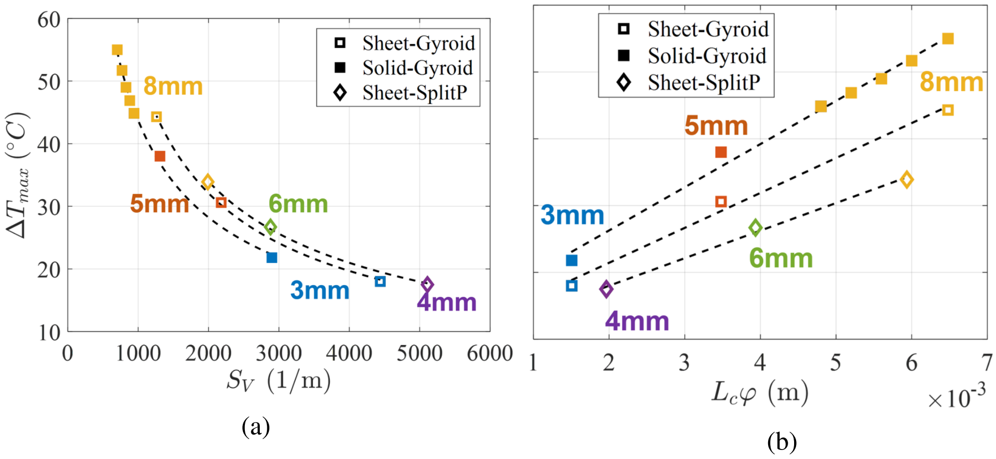

Fig. 4.14 Maximum temperature increase on the reflective surface, computed as a function of S_V and $L_c\varphi$. Splitter mirror. Taken from [136].

The maximum temperature increase could be related to a global heat transfer coefficient H_{global} within TPMS and the wet area, as $\Delta T_{max} \sim Q_{abs}/(H_{global}A_{wet})$. Thus, considering that $A_{wet} = S_V Vol_{fluid}$, results in Eq. (4.5).

$$S_V \Delta T_{max} \sim \frac{Q_{abs}}{H_{global} Vol_{fluid}} \tag{4.5}$$

Hence, considering that in all the configurations the absorbed power Q_{abs} is the same, and that ΔT_{max} exhibited an inverse proportionality with respect to S_V, $H_{global} Vol_{fluid}$ should be roughly constant across all the configurations. The global heat transfer coefficient therefore decreased as the fluid volume increased, since the fluid velocity inside the TPMS also decreased at the same flow rate.
The approximately linear dependency of ΔT_{max} on $L_c\varphi$ is explained by Eq. (4.4), for which $S_V \sim 1/(L_c\varphi)$ in first-order approximation.

To investigate and characterize the TPMS cooling system over a wide operating range, the maximum temperature increase of the mirror reflective surface was reported as a function of the pressure loss calculated along the cooling systems, as shown in Fig. 4.15a. As expected, as the L_c value increased, the cooling systems became less efficient, with higher hot spots, but with lower flow impedance and therefore lower pressure losses. Note that, in all cases, the pressure loss remained significantly below

the imposed constraint of 4 bar. The sheet-Gyroid presented larger pressure losses than the solid-Gyroid at the same porosity, as was found also by Khalil et al. [23] and Yan et al. [163] for Gyroid and Diamond, respectively.
It is also important to note that, in the presence of high porosity and large cell sizes, the greatest contribution to pressure loss was concentrated at the system inlet, as shown in Fig. 4.15b. This explained why the yellow curve in 4.15a showed a net increase at low values of Δp.

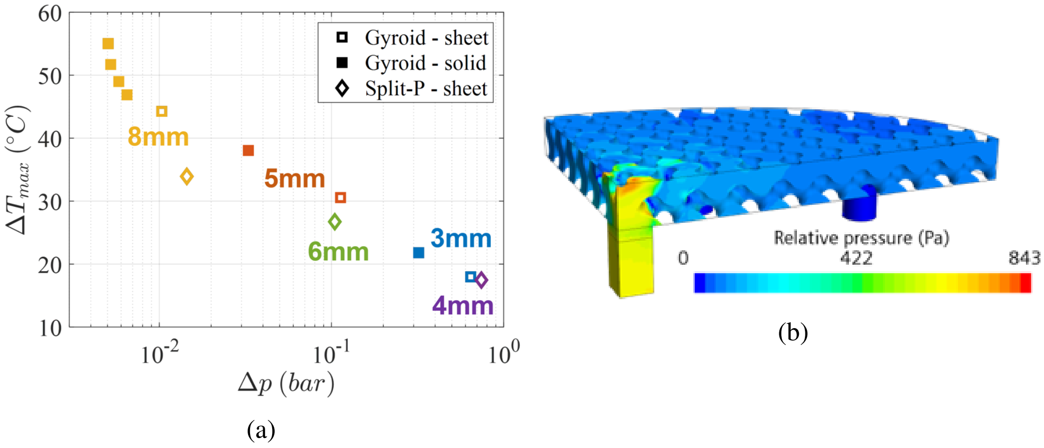

(a)

(b)

Fig. 4.15 Thermal-hydraulic performance: (a) ΔT_{max} vs Δp plot and large localized pressure losses at inlet location for GY6. Splitter mirror. Taken from [136].

The Nusselt number has been computed for the different mirrors as in Eq. 4.6, considering the heated area A_{heated} (where the microwave is reflected) and the average temperature on this surface. It can be remarked that the Nusselt number is larger with the porosity, since the hydraulic diameter increases more than the heat transfer coefficient due to the different TPMS.

$$Nu = \frac{Q}{A_{heated}(\overline{T}_{heated} - T_{in})} \frac{D_h}{\lambda} \tag{4.6}$$

The sheet-SplitP and Gyroid structures at 4 mm and 3 mm cell size, respectively, appeared to be the most promising cooling systems among the considered configurations. The SplitP having tiny improvement with respect to the Gyroid but a more complex structure to be manufactured, the sheet-Gyroid lattice with $L_c = 3\,mm$ was considered as the best trade-off.

Table 4.4 Geometrical parameters of the TPMS lattices adopted in the parametric study on the splitter mirror.

TPMS	Nu
GX1	25
GY2	44
GX3	44
GY4	64
GX5	60
GY6	81
SX1	26
SX2	35
SX3	44

Computed thermo-mechanical results

The mechanical performance of the TPMS-based cooling structures were also investigated by analyzing the deformations of the mirror, as reported in Fig. 4.16. Conversely to the peak temperature, the maximum displacement was found in the center of mirror (since the hotspot is only sightly shifted with respect to the center and the central point is the least constrained), as can be remarked in Fig. 4.16b. The deformation distribution followed an elliptic trend due to the mirror shape as well as the temperature distribution, in turn depending on the Gaussian heat flux.

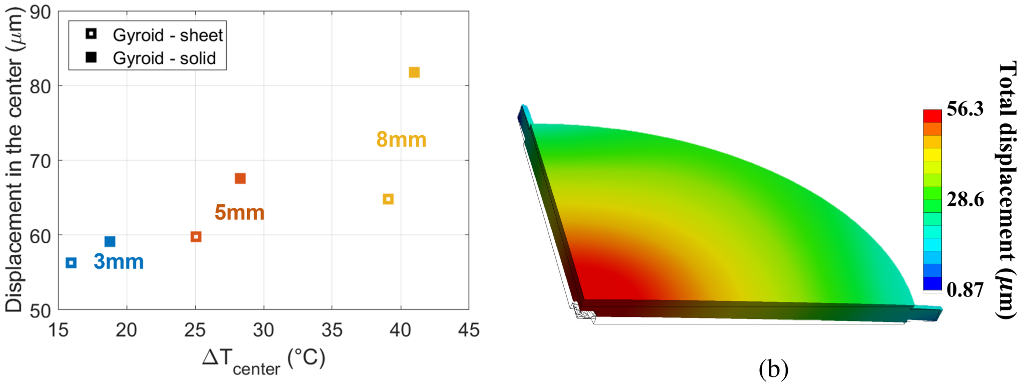

(a)

(b)

Fig. 4.16 Maximum displacement versus central temperature increase for the Gyroid structures. The visual deformation is greater than the actual value for graphic purposes. Splitter mirror. Taken from [136].

in Fig. 4.16a, the maximum displacement is plotted for each configuration of the Gyroid versus the temperature increase in the same location. The approximately linear relationship between temperature increase and displacement was expected as the coefficient of thermal expansion did not vary significantly within the temperature windows of the analysis, thus remaining approximately constant. The solid-Gyroid appeared to have a larger equivalent coefficient of thermal expansion than the sheet-Gyroid.

It must be noted that the stresses induced by the fluid pressure and by the thermal deformations were pretty small, being the temperature rise low as well as the overall, and local, pressure drop.

The sheet-Gyroid proved to have a superior behavior than the solid-one also from a mechanical point of view.

4.2.3 Polarizer mirror

The polarizer mirror is the most loaded mirror in the ECH system of DTT, as it must bear peak heat fluxes up to $\sim 7.7\, MMW/m^2$. With respect to the mirror analyzed in the previous section, the polarizer has a circular geometry and smaller dimensions. Because of mechanical constraints and structural requirements, the mirror width should be 20 mm and a single outlet is envisaged instead of multiple ones. The coolant being non-demineralized subcooled water, it is crucial to maintain the fluid temperature below approximately 70°C.

Based on the results of Section 4.2.2, the sheet-Gyroid lattice with cell size of 3 mm was employed to this different mirror to investigate its efficiency in a different configuration than its parametric study. Furthermore, a different TPMS with cylindrical periodicity was investigated to compare its performance in an axial-symmetric geometry to the cartesian lattice.

Because of structural constraints reported by the intended manufacturers of the mirror (INFN Padova, DIAM group), the reflective layer was increased to 2 mm thickness. The inlet and outlet pipes had diameter equal to 7 mm, as for the previous analysis. This value was suggested by the DTT team.

Cartesian lattice

Owing to the requirement of the single outlet, the mirror was filled with TPMS only in the central part, leaving a circular annulus collector to allow for better radial distribution of the flow. The absence of TPMS in the most peripheral portion of the mirror did not pose any issues with heat removal, as the thermal load was exponentially lower than in the center, given its Gaussian shape.
The geometry of the TPMS is depicted in Fig. 4.17.
For this mirror, the whole domain was simulated, being its geometry quite smaller compared to the previous mirror. Water entered at 15°C and 10 l/min in the central inlet (Fig. 4.17b). As for the splitter system, the desirable pressure loss was lower than 4 bar. As the other TL mirrors, the polarizer was conceived in CuCrZr to exploit its large thermal conductivity (close to Cu) but stronger mechanical properties than the pure Cu, as well as higher softening point [164].

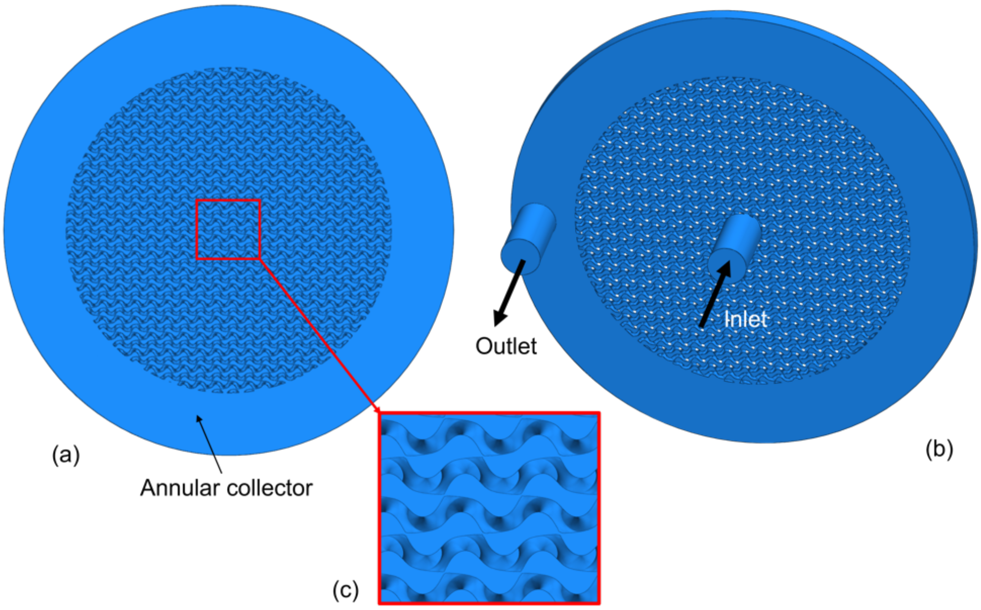

Fig. 4.17 Polarizer geometry filled with cartesian TPMS: (a) top view of the fluid domain, (b) bottom view of the fluid domain and (c) zoom detail. Polarizer mirror.

The surface-to-volume ratio was computed as $S_V = 4.5e3\ m^{-1}$, much close to the GX1 configuration of the splitter, as the employed lattice was the same.
The computational grid was generated with parameters similar to those listed in Section 4.2.1.

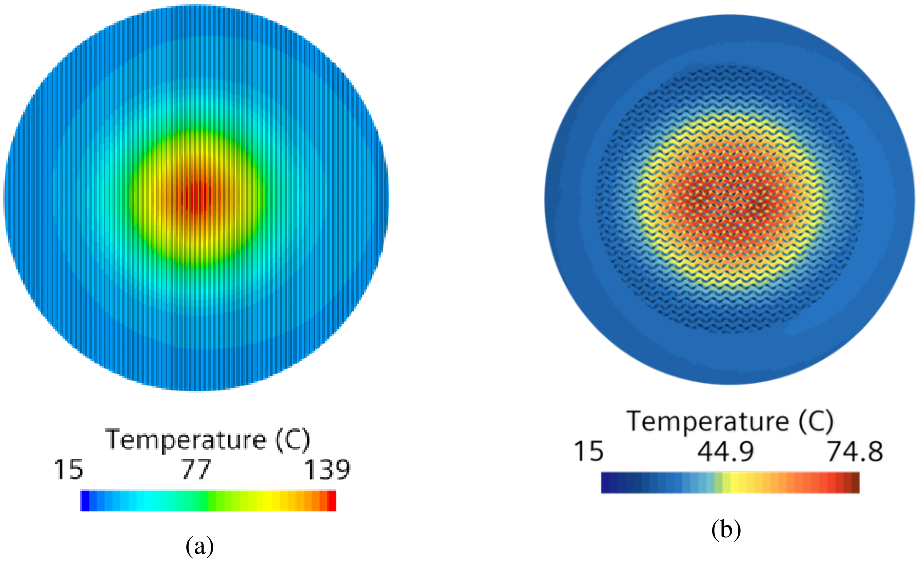

(a)

(b)

Fig. 4.18 Polarizer mirror. Temperature field of the cartesian lattice: (a) reflective surface and (b) solid-fluid interface.

In Fig. 4.18 the temperature maps on the reflective layer and fluid-solid interface are shown. The thermal distribution was fairly uniform, with a colder unbalance towards the outlet position, located on the left in the figure. The computed pressure drop, of 3 bar, remained lower than the maximum achievable for the cooling system. The hotspot temperature was found near the center, similarly to the splitter mirror. The mirror maximum temperature was lower than the softening point of CuCrZr (around 500-600°C [164]). The maximum fluid temperature, at the interface solid-fluid, was at the threshold to avoid the risk of corrosion from non-demineralized water (approximately 70°C). Nevertheless, it must be considered that the hotspot was found in a very localized area and only a very small portion of fluid was actually at that temperature. The computed Nusselt number was around 40.

Cylindrical lattice

As described in Section 1.1, to produce a TPMS conformal to a cylindrical surface the cartesian characteristic equation must be modified as in Eq. 1.13. In cylindrical coordinates the TPMS has an actual azimuthal size extremely tiny in the center, increasing as the radius increases. For this reason, the cylindrical lattice geometry for the cooling system of the polarizer was conceived as the union of two different lattices, a central one with $L_\xi = 3\,mm$ and $L_\beta = 2\pi/8$ and an external one with $L_\xi = 4\,mm$ and $L_\beta = 2\pi/16$. For both lattices, the vertical cell size was $3\,mm$. Moreover, in the center of the mirror a free space was left for the fluid inlet, being the cylindrical structure non-empty in its center.

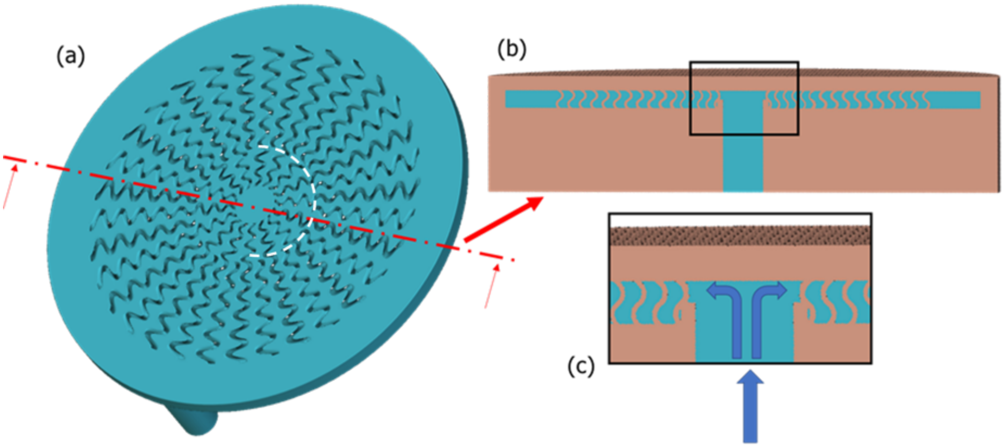

Fig. 4.19 Polarizer geometry filled with cylindrical TPMS: (a) fluid domain, (b) section cut and (c) zoom of the cut section. The white dotted line highlights the transition between the two cylindrical TPMS geometries.

The generated geometry is shown in Fig. 4.19. The two different TPMS lattices were united at $\xi = 12\,mm$. Moreover, the TPMS was vertically translated so to generate radial channels in contact to the solid, which should provide larger heat removal towards the external of the mirror [165].
The computational grid was generated similarly to the previous investigated polarizer cooling system.

The temperature fields computed for this configuration are shown in Figure 4.20. Notwithstanding the measures to improve mirror performance by using cylindrical periodicity, the calculated output appeared worse than the cartesian TPMS mirror. This might be explained by the surface-to-volume ratio value of this cylindrical design, of $2.9e3\,m^{-1}$, lower than the cartesian design.

The most promising lattice solution found on the parametric study of Section 4.2.2 appeared to be satisfactory for another mirror with a significantly larger thermal load.

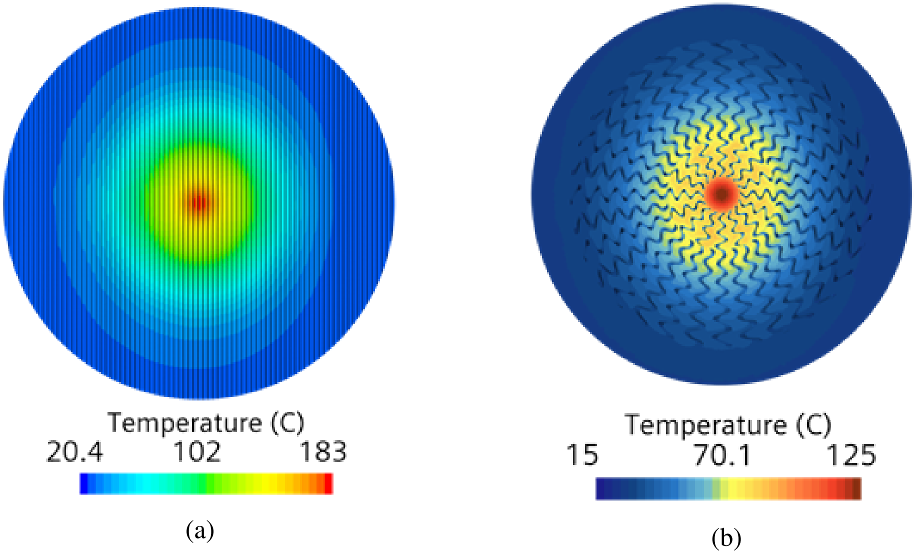

(a)

(b)

Fig. 4.20 Temperature field of the cylindrical lattice: (a) reflective surface and (b) solid-fluid interface. Polarizer mirror.

4.2.4 Launcher mirror M2

The launcher mirrors are quite large compared to the above analyzed mirrors and, as stated before, are subject to high torques from induced eddy currents, the extent of which depends on the electrical conductivity of the material. Especially in the case of the steerable mirror M2, it is highly desirable to opt for a material with high electrical (and unfortunately also thermal) resistance in order to reduce these induced torques, as Stainless Steel.

In a previous study, AISI 316L steel was considered for the bulk material of the M2 cooling system, while a 2 mm-thick layer of copper was inserted for the reflective layer [147]. Subsequent electromagnetic analyses [166] indicated that even a thickness of only 2 mm of Cu or CuCrZr caused too large electromagnetic torques. So, Busi et al. [166] proposed an entirely AISI 316L mirror with a sub-millimetric tungsten coating. Another optional material is Inconel 718 [148], a nickel-chromium alloy presenting withstanding mechanical properties [167].

Both proposals having low thermal conductivity, the use of enhanced cooling systems becomes increasingly urgent, leading to the investigation of the TPMS as heat removal structure. Based on the outcome of the previous Section, a sheet-Gyroid with uniform cell size of 3 mm was generated for the cooling structure of the M2 mirror.

First, a configuration similar to the polarizer structure was investigated in AISI 316L, with an annular collector and a single outlet and then the same geometry with two outlets in AISI 316L and in Inconel 718. A mechanical analysis on both AISI 316L and Inconel 718 mirrors was performed to evaluate the mechanical responses of the structure.
Being the steel and Inconel thermal conductivity considerably lower than the copper alloys, the achieved temperatures were much larger, leading to the risk of boiling. To avoid large corrosion and erosion from the boiling water and considering that modeling and predicting two-phase heat exchange is enormously more complicated than single-phase heat exchange, the saturation temperature should not be exceed. Water enters at 55°C and 11.5 bar and the maximum bearable pressure drop is 6 bar. Thus, considering the lower pressure point of the fluid of 5.5 bar, the saturation point is around 155°C. However, the TPMS system do not reach such a high pressure drops, as it will be shown in the following. A pressure drop of 2 or 3 bars can be retained to estimate the saturation temperature, which is between 170 and 180°C [168].
Inlet and outlet had 7 mm diameters and the reflective layer was 1 mm thick and only half of the M2 domain was simulated to reduce the computational burden.

Single outlet configuration - AISI 316L

The fluid domain for this cooling configuration of the M2 mirror is presented in Fig. 4.21. For this case, also a thin fluid film was left at the major axis location, behind the symmetry wall.

The picture of the M2 mirror compared to the splitter gives an idea of the different eccentricity e, as defined in Eq. (4.7), which is equal to 0.72 for the splitter and 0.82 for the M2. In Eq. (4.7), ξ_{minor} and ξ_{major} are the minor and major semi-axes. The closer the eccentricity is to 1, the more oval the ellipse is and the further it is from the circle. This high eccentricity of the geometry raises the risk of radial flow non-uniformity, which is further increased by the presence of a single outlet.

$$e = \sqrt{1 - \left(\frac{\xi_{minor}}{\xi_{major}}\right)^2} \tag{4.7}$$

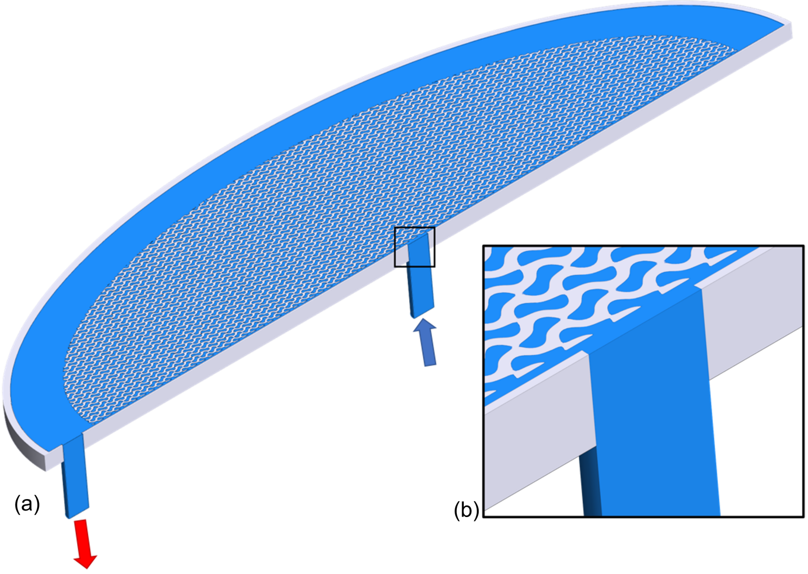

Fig. 4.21 Computational domain with inlet/outlet boundary conditions (a) and zoom on the inlet region (b) - single outlet configuration. The reflective layer has been removed to appreciate the internal structure. M2 mirror.

The thermal-hydraulic results are shown in Figs. 4.22-4.23: the velocity field in a cut section 2 mm below the reflecting surface and the temperature field on the reflective layer and at the solid-fluid interface. The fluid flow might reach large velocities in very small portions of the domain, near the inlet area. The flow distribution was quite inhomogeneous, with a clear imbalance toward the outlet zone (left of the picture), as it was even more remarkable in the thermal field. The maximum fluid temperature is around 200°C, which was higher than the saturation point of water at $\sim 10-11$ bar, around 180°C.

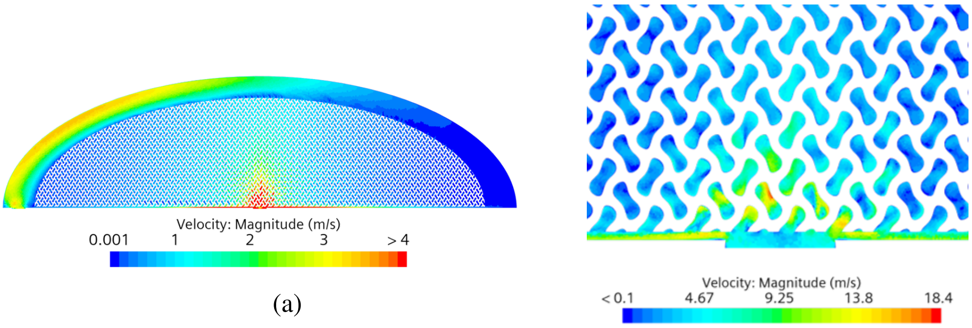

(a)

(b)

Fig. 4.22 Velocity magnitude at 2 mm below the reflective layer, single outlet configuration: whole domain (a) and zoom in the central part (b). M2 mirror.

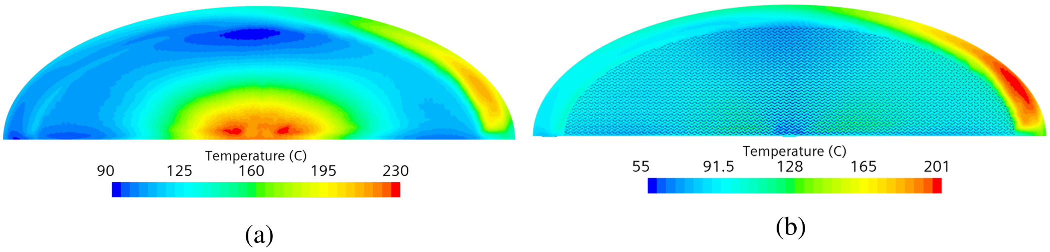

Fig. 4.23 Temperature results of the single outlet configuration: (a) solid temperature and (b) fluid temperature. M2 mirror.

Therefore, to uniformize the flow through the TPMS and in the internal collector, a second outlet was conceived on the opposite side of the major axis.

Two outlets configuration - AISI 316L

The geometry of the two outlets configuration is practically identical to the single outlet case, with a second outlet added on the major axis, as displayed in Fig. 4.24. In this case, the fluid film behind the symmetry wall was removed.

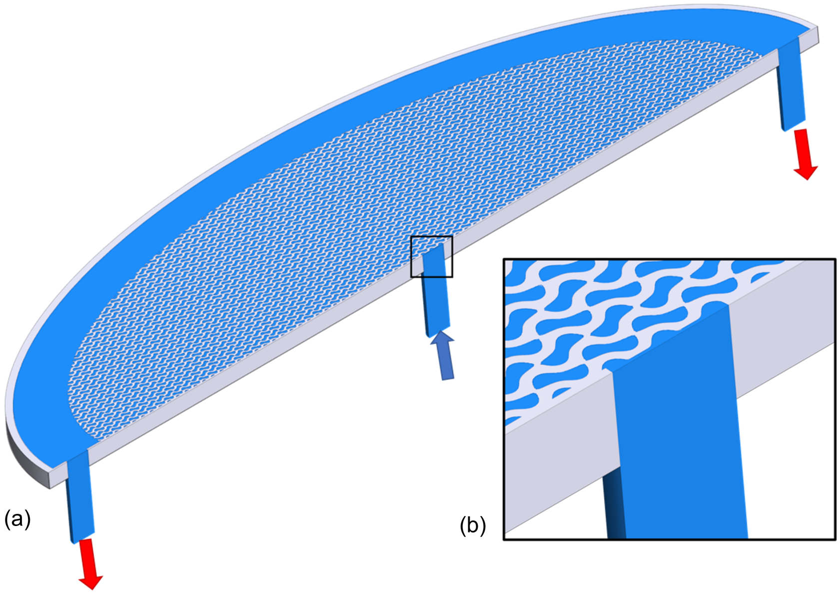

Fig. 4.24 Computational domain with inlet/outlet boundary conditions (a) and zoom on the inlet region (b) - two outlets configuration. The reflective layer has been removed to appreciate the internal structure. M2 mirror.

The velocity and temperature fields were investigated, as for the single outlet configuration, in Figs 4.25-4.26: the flow appeared more uniformly spread within the TPMS and the temperature on the reflective layer is more homogeneous, even if it reached a slightly higher maximum value. Moreover, the maximum fluid temperature in this configuration was 145°C, lower than the saturation point. The computed pressure drop was 2.8 bar. The proposed cooling system for the M2 mirror by Allio et al. [147] (Fig. 4.27a) was examined by updating the materials, i.e., replacing the Cu layer with stainless steel, and the temperature field on the reflective surface is shown in Fig. 4.27b. Allio's proposal consisted of radial channels connecting concentric elliptical channels, for a more homogeneous flow compared to the spiral option. It must be noted that also Allio's configuration had a central inlet and two outlets (placed on the minor axis instead of the major axis).

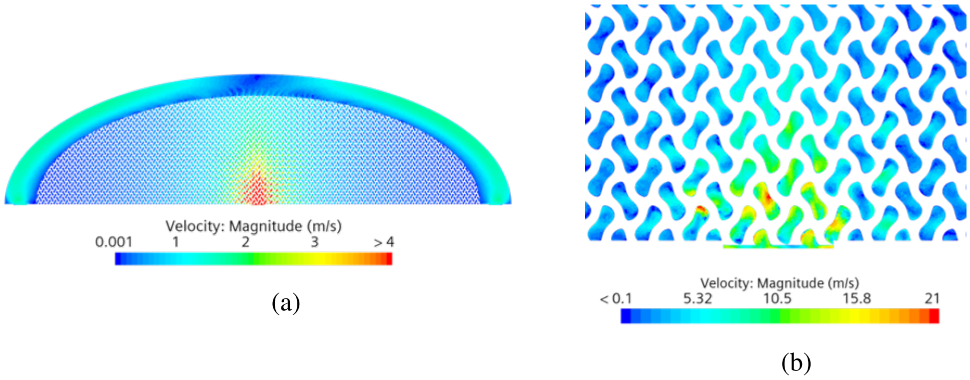

(a) (b)

Fig. 4.25 Velocity magnitude at 2 mm below the reflective layer, two outlets configuration: whole domain (a) and zoom in the central part (b). M2 mirror.

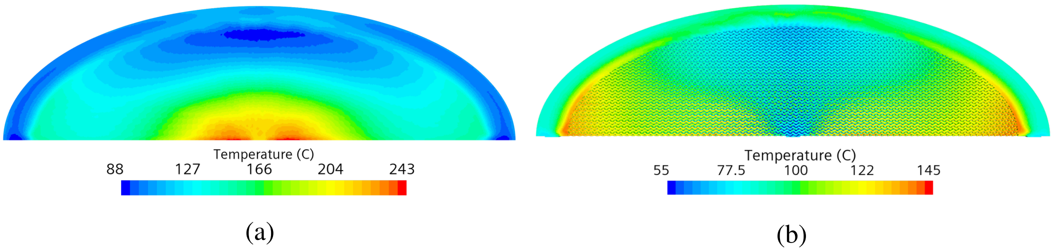

(a) (b)

Fig. 4.26 Temperature results of the two outlets configuration: (a) solid temperature and (b) fluid temperature. M2 mirror.

The maximum reached temperature of the Allio et al. [147] mirror was consistently larger than the TPMS mirror, and the maximum fluid temperature exceeded the

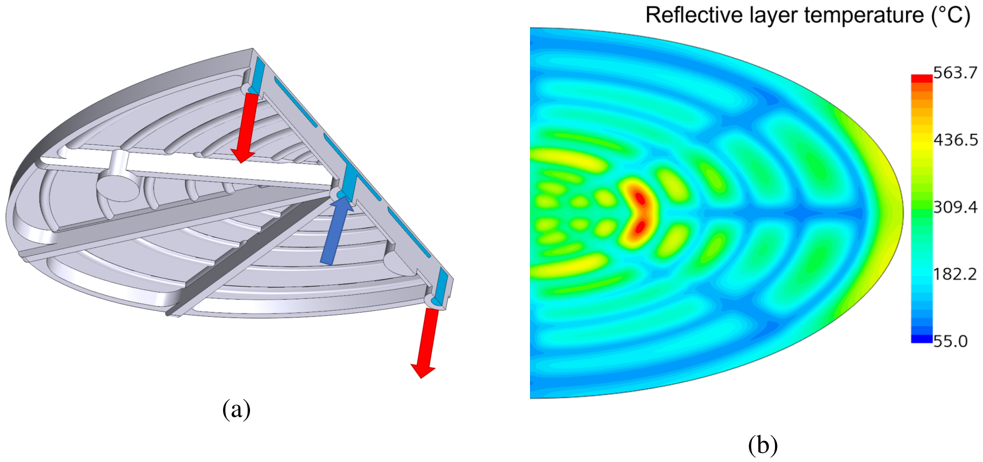

(a)

(b)

Fig. 4.27 Allio et al. proposal [147] of the M2 mirror made of only AISI 316L. (a) Geometry and (b) temperature on the reflective layer.

saturation point. The present cooling solution with TPMS therefore appeared to be among the best available options, significantly improving the previous configuration of Allio et al. and outperforming other recent solutions as reported by Pagliaro et al. [148].

Two outlets configuration - Inconel 718

The same cooling configuration of the previous section, with two outlets, was also simulated with Inconel 718 as solid material, which had a slightly lower thermal conductivity than the AISI 316L, but consistently larger yield strength. The computed temperatures were, indeed, larger than the AISI 316L mirror, as shown in Fig. 4.28.

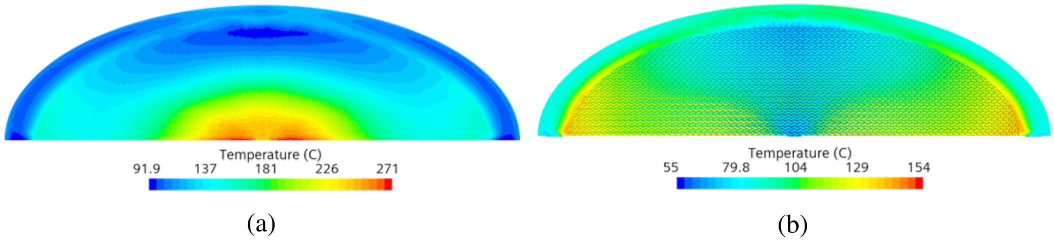

(a)

(b)

Fig. 4.28 Temperature results of the two outlets configuration with Inconel 718: (a) solid temperature and (b) fluid temperature. M2 mirror.

Mechanical analysis

The thermo-mechanical analysis was performed on both AISI 316L and Inconel 718 mirrors. As explained in Section 4.2.1, the solid temperature field and the fluid pressure distribution were exported from the thermal-hydraulic simulations and employed as drivers in the thermal-mechanical simulations. Conversely to the splitter mechanical model, the M2 was constrained only along the minor axis, as visible in Fig. 4.29. Only a quarter of the mirror was simulated for computational reasons.

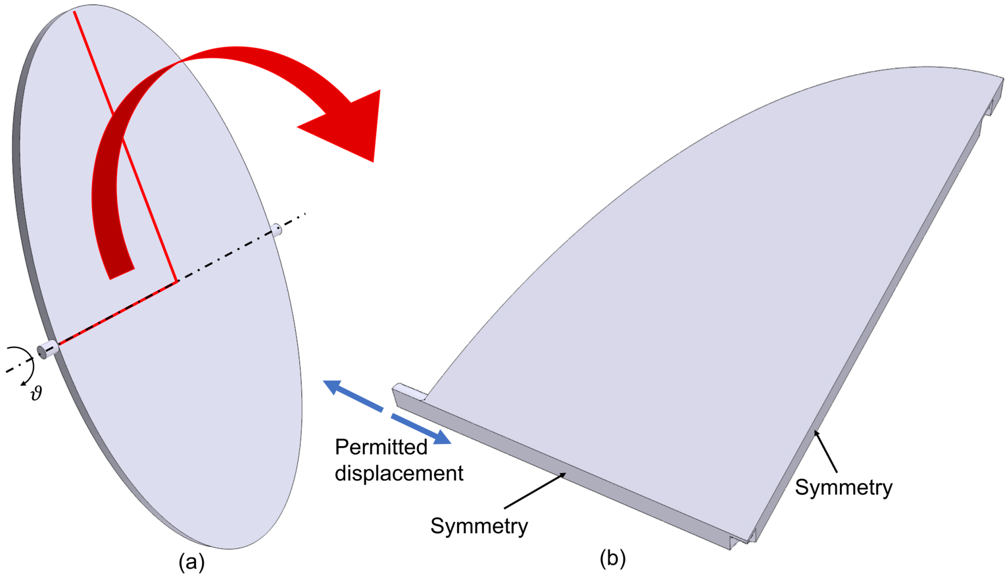

Fig. 4.29 Mechanical boundary conditions on the M2. (a) Whole mirror with the two pivots on the minor axis and (b) a mirror quarter, with the permitted displacement highlighted.

The stress field and the deformation field normal to the reflective surface are displayed in the Figs. 4.30-4.31. The stress being a tensor, the presented value is the Von Mises stress σ_{VM}, defined in Eq. (4.8), where σ_1, σ_2 and σ_3 are the stresses along the principal axes. The graphical deformation is larger than the real values, for better visualization.

$$\sigma_{VM} = \sqrt{\frac{(\sigma_1 - \sigma_2)^2 + (\sigma_2 - \sigma_3)^2 + (\sigma_3 - \sigma_1)^2}{2}} \tag{4.8}$$

The normal deformation of the mirror surface had its maximum in modulus at the edge of the major axis, which was not constrained and was very cold with respect

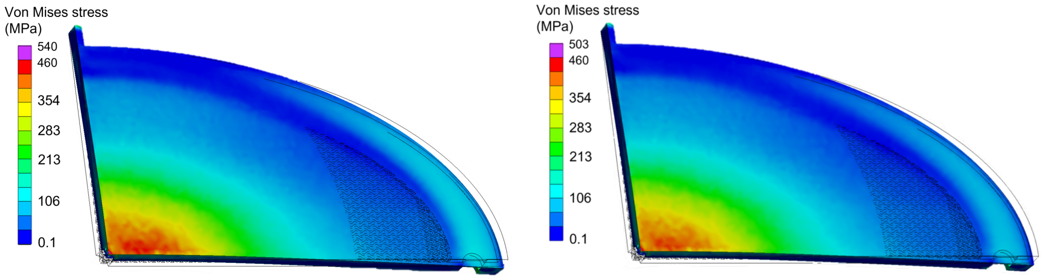

(a) (b)

Fig. 4.30 Von Mises stress field on the M2 mirror. (a) AISI 316L and (b) Inconel 718.

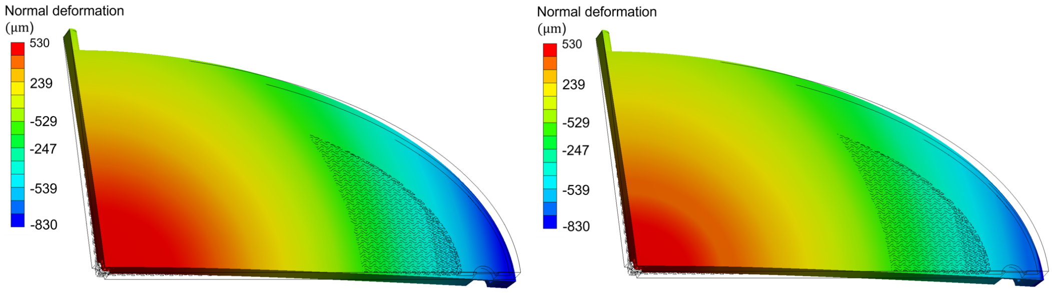

(a) (b)

Fig. 4.31 Deformation field normal to the reflective surface on the M2 mirror. (a) AISI 316L and (b) Inconel 718.

to the rest of the mirror. The center of the mirror was deformed towards the upper direction with values around 530 μm for the steel and 430 μm for the nickel alloy.

The maximum computed values of σ_{VM}, reported in violet in Fig. 4.30, were 540 MPa and 503 MPa for AISI 316L and Inconel 718. They were very localized values in the center of the mirror, computed in very few cells. The maximum stress on steel was larger than the Inconel, being the coefficient of thermal expansion of AISI 316L larger than the Inconel 718, even if the maximum temperature of AISI 316L was slightly lower. The computed fields for the two materials were quite similar, with marginally larger values of AISI 316L σ_{VM} in the central area and in the outer zone of the collector. The presence of the annular collector produced a clearly colder zone in the temperature field compared to the neighboring areas with TPMS, and this temperature gradient caused high deformation of the mirror, and therefore stress.

Although $\sigma_{VM,AISI316L}$ exceeded the yield strength of traditional AISI 316L (around 120 MPa at 250°C), it has been reported in the literature that Additive Manufactured Stainless Steel can achieve much larger strength values, of the order

of 500 MPa [169–172], depending on the printing direction and treatments of the sample. Thus, the maximum reached AISI 316L stress could be within the material limits, considering that with the exception of very few cells, the computed stress was lower than 500 MPa.
The yield strength of Inconel 718 at the maximum mirror temperature of 270°C is around 940 MPa, conservatively larger than the computed maximum stress.

The stress distribution on TPMS structure within the mirrors is presented in Fig. 4.32. Again, the fields of the two materials were almost the same, with slightly larger values in the steel mirror. The maximum values of the Von Mises stresses found on the TPMS structure were lower than the peak values on the reflective layer, being the reflective surface the hottest zone of the mirror.

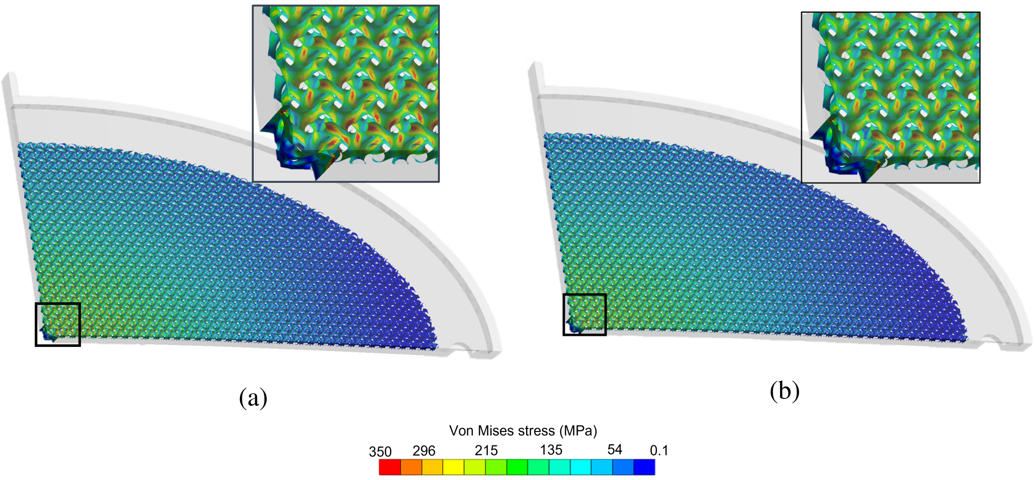

(a)

(b)

Fig. 4.32 Von Mises stress distribution on TPMS-based cooling system within the M2 mirror. (a) AISI 316L and (b) Inconel 718.

From the numerical analysis of the M2 mirror, it appeared that Inconel 718 might be used with a large safety margin within the mirror operating window, while AISI 316L could be employed depending on the type of 3D printing and the treatment applied by the manufacturing company.

4.3 Design, manufacture and test of a prototype mirror equipped with TPMS

Following numerical analyses on the various mirrors for the TL and launcher of DTT ECH system, the design of a prototype mirror was carried out. This prototype was printed in AM in AISI 316L (being the stainless steel a more common material for 3D printing and less expensive than Inconel 718) and tested from a hydraulic and thermal point of view at the Politecnico di Milano. The mirror design targeted the compatibility with a connection line to be installed at the FALCON facility hosted by SPC (Swiss Plasma Center) at EPFL (Ecole Polytechnique Fédérale de Lausanne) [145, 173, 174] in Lausanne. The prototype had smaller dimensions than the M2 and it was just a little bigger than the splitter. Conversely to the previously analyzed mirrors, it had a concave reflecting surface.

4.3.1 Mirror design

Having almost the same thermal load as the M2, the cooling system of the prototype was drawn in parallel with that of the launcher mirror, with the sheet-Gyroid having a cell size varying from 3 mm in the central area to 4.5 mm in the most peripheral area. In this case too, an external annular collector was inserted to ensure radial homogeneity of the flow. Only one outlet was conceived, due to mechanical limitations and because the computed eccentricity was 0.71, lower than the splitter and M2. The geometry is shown in Fig. 4.33.

The characteristic equation of the Gyroid (Eq. (1.3)) became Eq. (4.9) in order to generate the TPMS varying with the concavity of the reflective surface. $L_c(x, y)$ was the varying cell size with x and y coordinates, normal to the reflective surface, as reported in Fig. 4.33a. $L_c(x, y)$ is defined in Eq. (4.11), with a parabolic varying function used also for the isovalue parameter $c(x, y)$ in Eq. (4.11), where $x_0 = 157\,mm$ and $y_0 = 114\ mm$. The variation of $c(x, y)$ was defined so to reduce gradually the wall thickness and increase the porosity towards the periphery of the mirror, where the heat load is lower. The sheet-Gyroid was then generated as in Eq. (4.12).

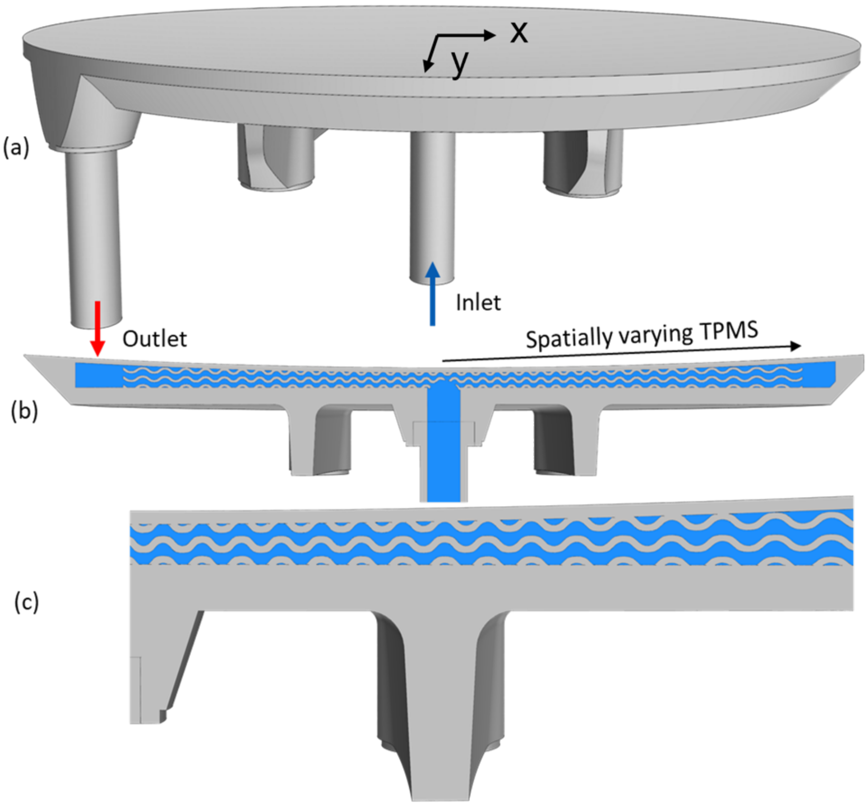

Fig. 4.33 Prototype geometry. (a) Solid domain with inlet/outlet boundary conditions, (b) cut section highlighting the varying TPMS and (c) zoom of the cut section.

$$\begin{aligned} fun(x,y,z) = sin\left(\frac{2\pi x}{L_c(x,y)}\right) cos\left(\frac{2\pi y}{L_c(x,y)}\right) + \\ + sin\left(\frac{2\pi y}{L_c(x,y)}\right) cos\left(\frac{2\pi z}{L_c(x,y)}\right) + sin\left(\frac{2\pi z}{L_c(x,y)}\right) cos\left(\frac{2\pi x}{L_c(x,y)}\right) \end{aligned} \tag{4.9}$$

$$L_c(x,y) = 3 + 3\left(\frac{x^2}{x_0^2} + \frac{y^2}{y_0^2}\right) \tag{4.10}$$

$$c(x,y) = 0.75 - 1.1\left(\frac{x^2}{x_0^2} + \frac{y^2}{y_0^2}\right) \tag{4.11}$$

$$(fun(x,y,z) = c(x,y)) \cup (fun(x,y,z) = -c(x,y)) \tag{4.12}$$

Thus, both the cell size and the isovalue parameter varied with the concave surface, and the resulting average porosity of the TPMS was 48%.

4.3.2 Numerical nominal performance

The thermal-hydraulic performance of the prototype mirror was initially evaluated in the nominal operating conditions of the FALCON facility (inlet water flow rate of $10\,l/min$ at $20\,^{\circ}C$ and Gaussian heat flux with peak of $2.3\,MW/m^2$, see Fig. 4.2e) to verify the compliance to requirements, i.e., maximum fluid temperatures below saturation point at $3-7$ bar (minimum and maximum operating pressure level) and pressure drop lower than *4 bar*.

Computational methodology

The same analysis workflow of the previous analyzed mirrors was used: the fluid and solid domains were meshed with a fine grid resulting in $\sim 80M$ of polyhedral cells, with boundary layers near the wall to capture the near-wall behavior. The Realizable $k-\varepsilon$ turbulence model was used in STAR-CCM+. The conjugate heat transfer problem was solved with temperature-dependent properties for both subcooled water and mirror steel. The heat flux shown in Fig. 4.2e was used as the thermal driver, being all the other mirror boundaries adiabatic.

Numerical results

To assess the flow homogeneity in the mirror, the velocity field in two cut sections was analyzed, as presented in Fig. 4.34-4.35.

It can be remarked how the velocity presented huge values in the center, for the inlet jet effect and the tiny cell size, and the flow radially expanded towards the peripheral zones. Concerning the annular collector, the velocity was larger toward the outlet position, whereas it had the lowest values in the diametrically opposite location. However, this inhomogeneity only marginally affected the thermal field, as it is shown in Fig. 4.36, showing the temperature fields on the reflective layer and at the fluid-solid interface underneath the reflective layer. The maximum solid temperature remained well below the softening point of the AISI 316L of 700°C [175]. The maximum fluid temperature did not exceed the saturation temperature at

3 bar, the minimum pressure level, estimated in 133°C [168].

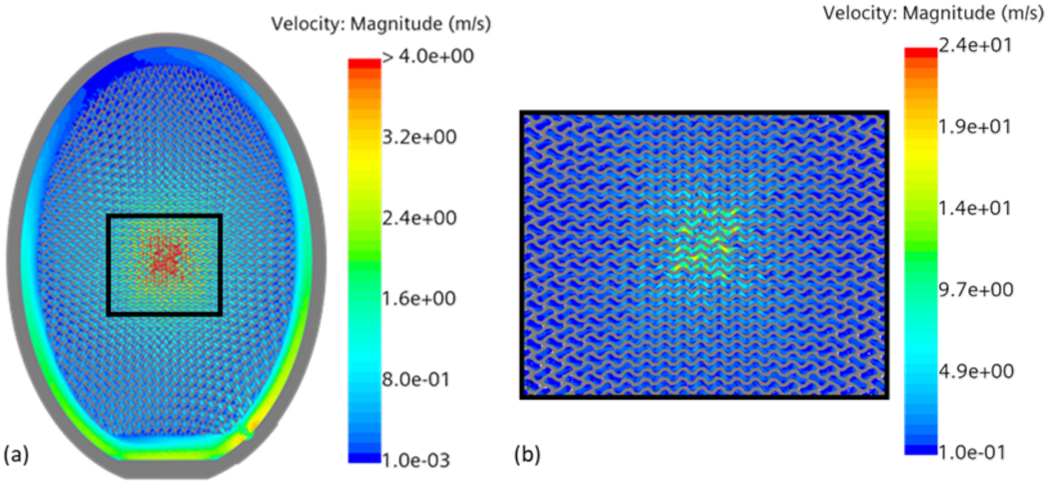

Fig. 4.34 Velocity magnitude, in a cut section 1.5 mm below the concave surface (a) and zoom in the central zone (b) – prototype mirror.

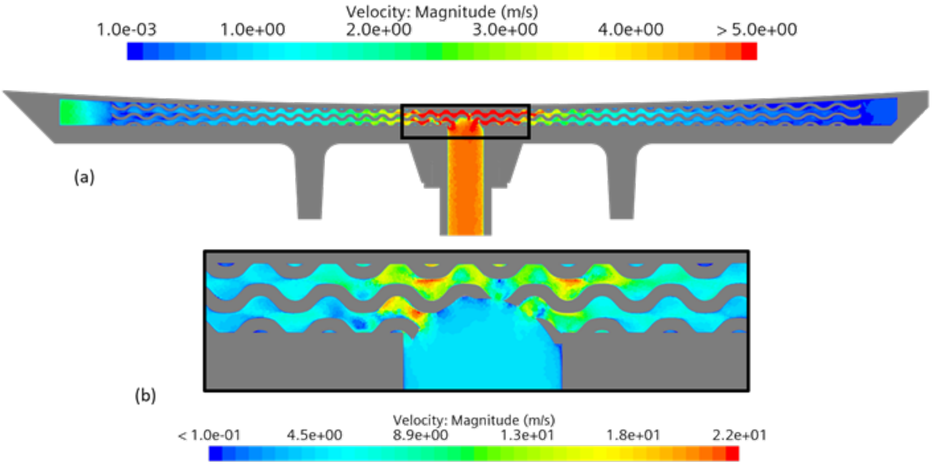

Fig. 4.35 Velocity magnitude, in a cut section normal to the minor axis (a) and zoom in the central zone (b) – prototype mirror.

The reflective layer temperature followed the Gaussian shape of the heat flux, while the fluid-solid interface temperature showed the influence of cooling effects. In particular, the impinging of the fluid arriving with a relative high velocity from the inlet connection was clearly visible. The temperature fields did not present significant inhomogeneity due to the presence of the single outlet, although in Fig. 4.36b the

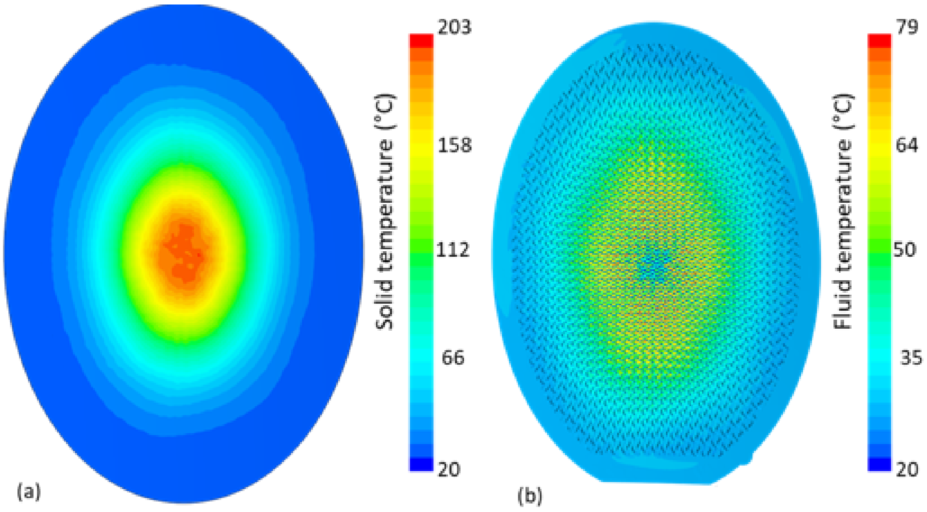

Fig. 4.36 Temperature map of (a) the solid domain and (b) the fluid domains, simulated in the nominal operating conditions at FALCON – prototype mirror.

location of the outlet at bottom right corner in the shown map is revealed by the decrease of fluid temperature. The computed pressure drop at the nominal flow rate was 2.7 bar.

4.3.3 Manufacturing

The prototype mirror was printed by the private company Ellena S.p.a. in AISI 316L, with the same LPBF printer already described in Section 3.1. The resulting part accuracy and surface roughness estimated by the manufacturer are 0.15 mm and $5-15\,\mu m$, respectively. The company also evaluated the relative part density around 99.85% of the bulk material, which ensures that mechanical properties were degradated because of porosity decrease of the metal [176].

The sample was successfully depowdered using a vibrating machine, manually shaken with a rubber hammer, and by injecting compressed air and pressurized water, as well as employing an industrial ultrasonic washing machine. The outer surface of the sample is shown in Fig. 4.37

Fig. 4.37 3D printed prototype mirror after manufacturing and depowdering.

4.3.4 Experimental analysis

In order to validate the mirror design, a preliminary experimental campaign was conducted at the thermal-hydraulic laboratory *Frigorifero* at Politecnico di Milano, Italy. Both hydraulic and thermal tests were carried out in the same water loop of Section 3.4 in order to compare the numerical results with the experimental ones and check the predictability of the model.

Experimental setup

A picture of the experimental hydraulic circuit is shown in Fig. 4.38a, while its operating scheme with also the thermal components is reported in Fig. 4.38b. With reference to Fig. 4.38b, the water loop was composed of a centrifugal pump (*P*); a flow control valve (*V*); a Coriolis mass flow meter (*MF*); a heat exchanger (*HX*) that was fed by a secondary cooling loop to maintain a constant water outlet temperature; two relative pressure transducers (*PT1* and *PT2*) and two thermocouples (TC_{in} and TC_{out}) were employed to measure the pressure and temperature upstream and downstream the test section of the mirror. The mirror was connected to the loop via 10 mm-diameter transparent plastic tubes to the circuit. A resistor (*R*) connected to a variac (an autotransformer employed to impose the voltage difference applied to the resistor terminals) was used to tune the heat flux at the mirror surface, and different thermocouples (TC_x) were utilized. The maximum bearable current in the variac was 8 A. Two mass flow meters were employed, with different range and uncertainty, as reported in Table 4.5 together with the pressure transducers and thermocouples.

To perform the thermal tests, the experimental setup was modified with respect to Fig. 4.38a. Ten thermocouples were positioned on the surface of the mirror using glue and copper tape, as shown in Fig. 4.39a-b. To create a constant heat flux source, sixteen Positive Temperature Coefficient (PTC) resistors were placed on the surface

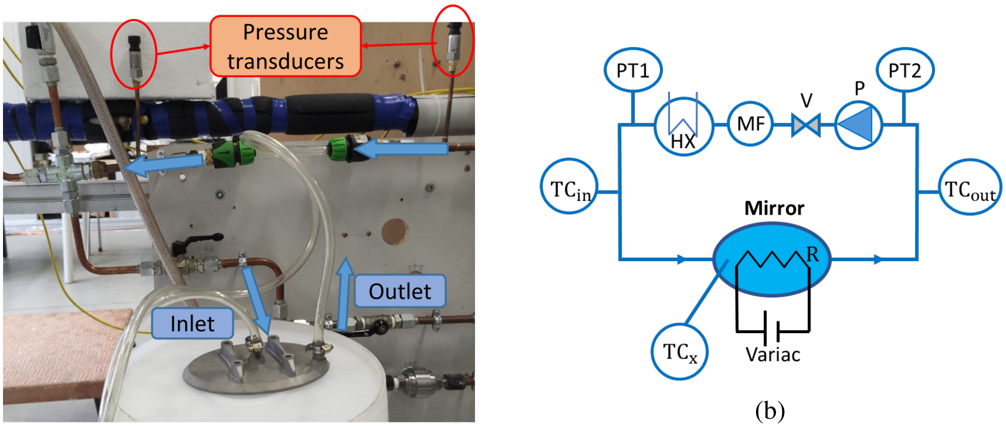

(a)

(b)

Fig. 4.38 Experimental circuit at *Frigorifero* Laboratory, in the Department of Energy of the Politecnico di Milano, used for the experimental tests of the miror prototype. (a) Picture of the hydraulic circuit connected to the sample and (b) Sketch of the equivalent circuit of the experimental setup, with also the thermal components.

Table 4.5 Measuring instruments

Type	**Range**	**Accuracy**
Mass flow meter 1	0 - 6.7 l/min	0.15% r.v.
Mass flow meter 2	0 - 108 l/min	0.3% r.v.
Relative pressure transducer	0.5 - 7 bar	0.07 bar
Type K thermocouples	0-50°C	0.5 °C

(Fig. 4.40a), interposed with a silicon thermal paste (Fig. 4.39c). The thermocouples were placed so to avoid being directly below a heating element, but between two adjacent resistors, such that the readings of the mirror wall temperature should not be affected by the surface temperature of the heaters. To ensure that the resistors and the thermocouples were fixed to the surface, a pressed wood plate was secured to the mirror using screws, pressing the resistors and thermocouples, as shown in Fig. 4.40b. The PTC resistors were connected as two parallel series of eight resistances to the variac, see Fig. 4.40a. Finally, the mirror was thermally insulated, on both sides, by rock wool 10 cm thick, with thermal conductivity of approximately 0.03 $W/(m\,K)$, and connected to the same circuit of the hydraulic tests.

Referring to Fig. 4.39a, *TC1* was located in the mirror center, *TC2-3* and *4-5* on the minor and major axis, respectively. *TC6-9* were positioned diagonally with

(a) (b) (c)

Fig. 4.39 Thermal test preparation: (a) thermocouples, (b) copper tape and (c) silicon thermal paste on the mirror surface.

respect to the axes and *TC10* was placed in correspondence of the outlet. It should be noted that *TC2-3* were placed outside the resistors, thus they were expected to measure quite low temperatures.

For the pure hydraulic experiments, 34 setpoints were tested, spanning from 1.7 l/min to 7.1 l/min, and each of them was acquired at a frequency of 1 Hz for 270 s. Concerning the thermal experiments, different nominal flow rates, with nominal values of 1.7, 2.5, 3.3, 4.2 and 5 l/min, were tested, at two power levels, which nominal voltages are 84 and 94 V. Each test was recorded for 180 s at a frequency of 1 Hz. The tested flow rates and power levels are reported in Table 4.6. The imposed power Q_{abs} was computed from an energy balance as in Eq. (3.2). The uncertainties of Q_{abs} range between 10% and 30%. The power computed from the energy balance was compared for consistency to the electrical power Q_e as in Eq. (4.13) where ΔV was the imposed potential difference to the resistors ends and I the current trough the two series of resistors, measured using a current clamp. The average water inlet temperature was $20°C$. The calorimetric and electrical power resulted the same within their uncertainty bars, see Table 4.6. $\dot{V}$ is the volumetric flow rate.
It must be noted that the resistance characterization of the PTC resistors in a thermostatic bath was not possible because of their non-impermeability.

$$Q_e = 2\Delta V I \tag{4.13}$$

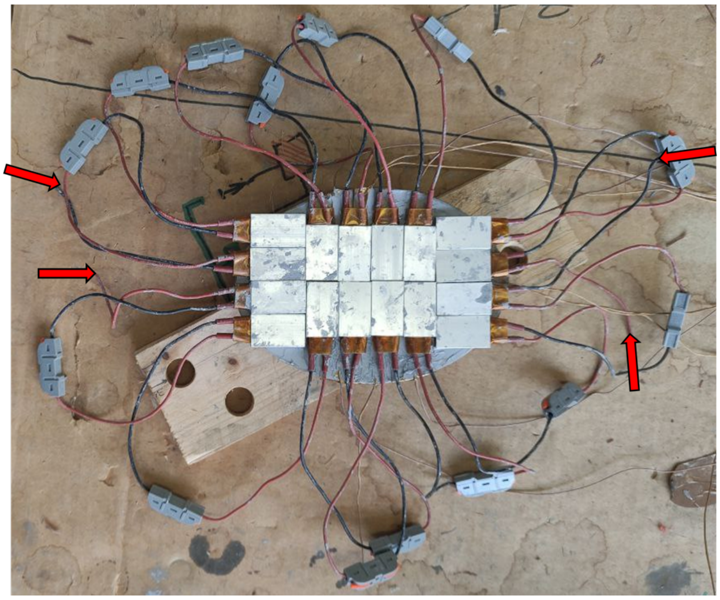

(a)

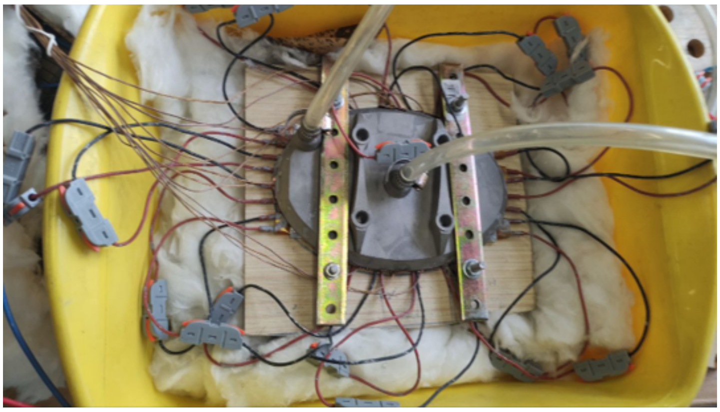

(b)

Fig. 4.40 Thermal test setup: (a) PTC resistors with highlight of the resistors ends and (b) the resistors blocked with a wood plate and inserted into a box filled with rock wool.

Between each thermal test, the variac was switched off and thermocouples were waited for to return to room temperature before continuing. After switching on the variac, several minutes were required for the system to reach a steady state, while monitoring the thermocouples, before starting data acquisition.

Table 4.6 Tested conditions in the thermal experiments.

84 V

$\dot{V}\,(l/min)$	$Q_{abs}\,(W)$	$Q_e\,(W)$
1.48	430 ± 50	450 ± 30
1.77	460 ± 50	460 ± 30
2.57	420 ± 70	430 ± 30
2.59	440 ± 80	450 ± 30
3.34	460 ± 100	440 ± 30
3.46	520 ± 150	480 ± 30
4.17	490 ± 140	450 ± 30
4.30	470 ± 130	440 ± 30
4.88	460 ± 140	440 ± 30
5.18	510 ± 160	440 ± 30

94 V

$\dot{V}\,(l/min)$	$Q_{abs}\,(W)$	$Q_e\,(W)$
1.77	580 ± 70	670 ± 40
2.19	610 ± 60	660 ± 40
2.69	660 ± 80	680 ± 40
2.55	650 ± 80	660 ± 40
2.63	630 ± 80	640 ± 40
3.41	700 ± 100	690 ± 40
3.40	660 ± 100	670 ± 40
3.31	670 ± 110	640 ± 40
4.23	700 ± 120	690 ± 40
4.19	680 ± 120	680 ± 40
4.20	700 ± 140	660 ± 40
5.06	670 ± 180	690 ± 40
5.02	640 ± 170	650 ± 40
4.81	670 ± 140	630 ± 40

Simulation setup

In the simulations, the same numerical setup exposed in Section 4.3.2 was employed. For the modeling of the hydraulic experiments, isothermal conditions were used and not external flux imposed. The pressure drop between inlet and outlet of the mirror as in Fig. 4.33a was extracted and compared to the experimental values. For the thermal tests, to mimic the heating from the PTC resistors, a constant heat flux of the same shape of the resistors was imposed, as in Fig. 4.41.

To reproduce the same conditions of the experiments, the imposed heat flux was computed from the calorimetry values of Tab. 4.6 as Q_{abs}/A_{HL}, where A_{HL} is the heated area. Because the experimental temperature increases were limited, both fluid and solid properties were considered constant in the model.

Data reduction and uncertainty evaluation

The pressure losses in the mirror were computed as the difference between the measured pressures at the inlet and outlet of the test section, as in Eq. (4.14), p_{PT1} and p_{PT2} refer to the two pressure transducers.

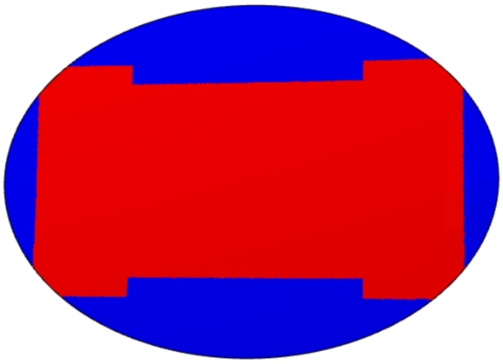

Fig. 4.41 Constant heat flux imposed in the simulations reproducing the experimental tests on the prototype mirror. The red area is where the thermal load is imposed, blue where the surface is considered adiabatic.

$$\Delta p = p_{PT2} - p_{PT1} \tag{4.14}$$

Note that the influence of the pipes and connectors between the mirror and the pressure transducers was also investigated by removing the mirror from the circuit, and negligible effects were revealed, conversely to what was found in Section 3.3, where the total measured pressure losses where lower at larger flow rates. Equivalently to what was done in Section 3.2.2, the temperature increases ΔT in the thermal experiments were computed as in Eq. (3.4) with respect to the inlet temperature.

In order to compare the thermal efficiency of the mirror in the different tests from an average perspective, a modified heat transfer coefficient H^* was calculated as in Eq. (4.15).

$$H^* = \frac{Q_{abs}}{A_{HL}(T_{HL} - T_{in})} = \frac{Q_{abs}}{A_{HL}(\Delta T_{HL})} \tag{4.15}$$

T_{HL} is the mean temperature on the mirror surface. T_{HL} was computed as a weighted average of the TC readings, by considering they affect different portions of the mirror surface, as in Fig. 4.42.

The evaluation of the standard uncertainty of the measurements was performed by following the guidelines provided by the Joint Committee for Guides in Metrology [112], as already described in Section 3.2.2. The uncertainty of the measurand estimate $u(T_{TC})$ was calculated by combining the statistical uncertainties from the

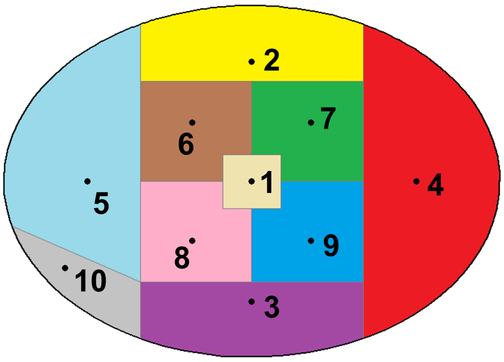

Fig. 4.42 Mirror surface divided into sectors for T_{HL} computation – prototype mirror.

random oscillations in the experiments and the accuracy of the instrumentation in Eq. (3.5). The uncertainty of the temperature increase was computed with the propagation of uncertainty as in Eq. (3.6).

The T_{HL} uncertainty was computed as the root sum square of the TC uncertainties weighted by the fraction of the mirror area they affect. Then, $un(\Delta T_{HL}) = \sqrt{un(T_{HL})^2 + un(T_{in})^2}$ and the uncertainty of the modified heat transfer coefficient was computed as Eq. (4.16).

$$\frac{un(H^*)}{H^*} = \sqrt{\left(\frac{un(Q_{abs})}{Q_{abs}}\right)^2 + \left(\frac{un(\Delta T_{HL})}{\Delta T_{HL}}\right)^2} \tag{4.16}$$

Results of the hydraulic tests

The comparison between the numerical and experimental hydraulic results is shown in Fig. 4.43. As both the pressure drop and flow rate uncertainty was lower than 5% and 1% respectively, they were omitted from the chart for graphical clarity. While the experimental pressure drops measured during tests at the same flow rates measured with the two flow meters agreed, there was a large discrepancy between the tests (blue curve in Fig. 4.43a) and the simulations for the nominal geometry (magenta curve in Fig. 4.43a). It must be noted that the simulations used the Realizable $k-\varepsilon$ model, as described in Section 4.2.1, but also the SST $k-\omega$ turbulence model was investigated, since from the analysis of Chapter 3 it provided larger pressure losses. However, being in lower Reynolds number range than the previous chapter (a maximum of $Re_{D_h} \sim 800$ at the nominal flow rate), the two models produced comparable results.

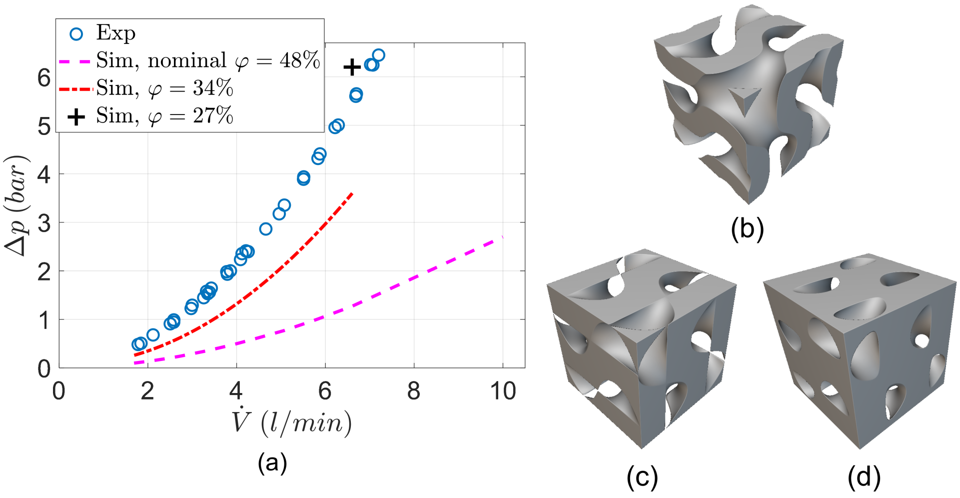

(a)

(b)

(c)

(d)

Fig. 4.43 Comparison of experimental and numerical results: (a) pressure losses, and Gyroid unit cells at different posorities: (b) nominal 48%, (c) 34 % and (d) 27 % – prototype mirror.

Although an underestimation of the simulations compared to the measured hydraulic characteristics was expected — primarily due to the inherent roughness introduced by the printing method, which is quite difficult to capture accurately in the numerical model as already noticed in Section 3.3 — the observed discrepancy was too significant to be explained by surface roughness alone.

Considering the printing accuracy provided by the manufacturer, simulations were also carried out with a smaller lattice porosity, by increasing the wall thickness of the TPMS cell, as in Fig. 4.43b-d. Increasing the wall thickness of 0.2 mm, thus decreasing φ from 48% to 34% resulted in the red dotted curve in Fig. 4.43a, considerably closer to the experimental curve. By further reducing the porosity down to 27%, the curve was slightly exceeded, as noted by the black cross (just one point was simulated for computational cost issues). A second look at Fig. 4.43b-d, allows noting that, as porosity decreased, the topology of the Gyroid structure appears deformed and eventually fluid passages are totally chocked at some locations. Thus, the discrepancy between the experimental and simulation results could be attributed to printing tolerances/defects or local obstructions. A tomography could possibly confirm the speculation, and help in understanding to what extent the internal polishing by abrasive jet [177] could help in reducing the hydraulic impedance of the mirror, increasing the lattice porosity [178, 179].

Results of the thermal tests

The ΔT measured by the different thermocouples are plotted in Fig. 4.44 and 4.45 for the two nominal potential difference. Test1-2-3 refer to the repetitions of the test, as grouped in Tab. 4.6.

Looking at the measured data, if *TC3* had the smallest temperature increase, *TC2* measured a quite large value, that could be possibly explained by a local occlusion within the mirror cooling structure. Consistently with its position at the inlet, *TC1* had a small temperature raise compared to the other thermocouples. *TC4* and *TC5* were at a specular position along the major axis, with *TC5* nearer to the outlet, thus expected lower measured temperature. This expectation was only partially verified as *TC5* was not always lower than *TC4*. In general, TC4 and TC5 had close values, but even considering the uncertainty, there was no compatibility in the measurements. Concerning *TC7-8-9*, they appeared similar but completely offrange with respect to *TC6*, which was nonetheless in a specular position, and detects the highest temperature of the entire mirror.
The only thermocouple surely placed under a heating element was the *TC10*, thus its reading could be the most affected by the temperature of the resistors.
The actual flow rates tested differ from the nominal flow rates, as did the power levels, which vary between the different tests. To compare different tests at the same power rating, six flow rates were selected, cooling approximately the same amount of power around 670 W, and plotted together in Fig. 4.46. In this way, the effect of flow rate on temperature measurements was directly investigated.

While it would be expected that as the flow rate increased, heat exchange would increase, thereby decreasing the temperatures read by the thermocouples, it is clear that this decreasing trend was not present. This brought into question the actual suitability of the experimental setup, which was probably overly biased by the heating elements which, despite the use of thermal paste and compression against the mirror surface, were hotter than the metal surface.

The modified heat transfers are shown in the bar plot of Fig. 4.47. Since it is more difficult to directly compare thermocouple values due to experimental variability in imposing a flow rate or power, the heat transfer coefficient helps to compare different tests together: in particular, at approximately the same flow rate and power, the H^* values were within the uncertainty ranges, which was not the case for Fig. 4.44-4.45.

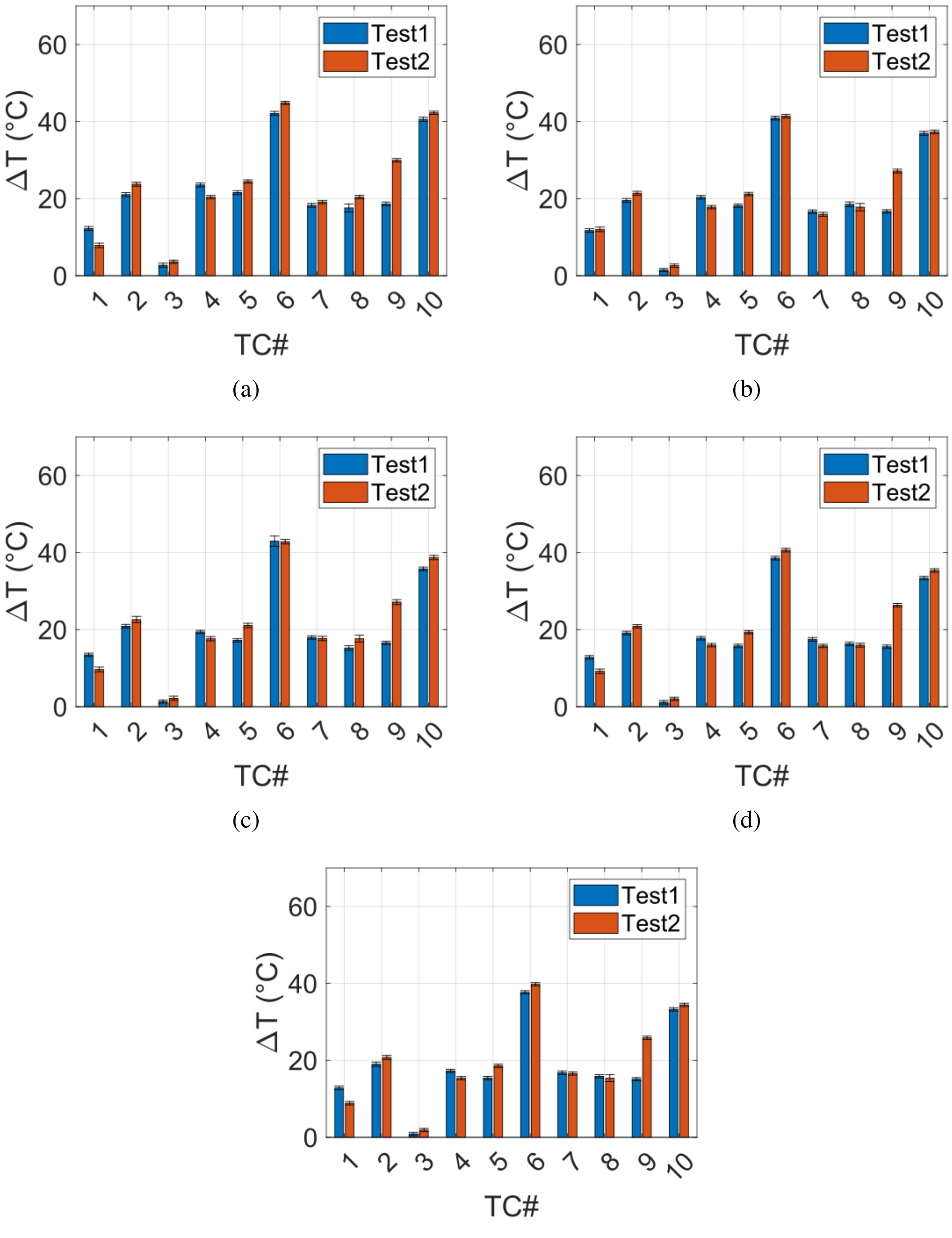

(a) (b) (c) (d) (e)

Fig. 4.44 Measured temperature increases at the nominal voltage of 84 V. Nominal flow rates of (a) 1.7 l/min and 84 V, (b) 2.5 l/min, (c) 3.3 l/min, (d) 4.2 l/min and (e) 5 l/min – prototype mirror.

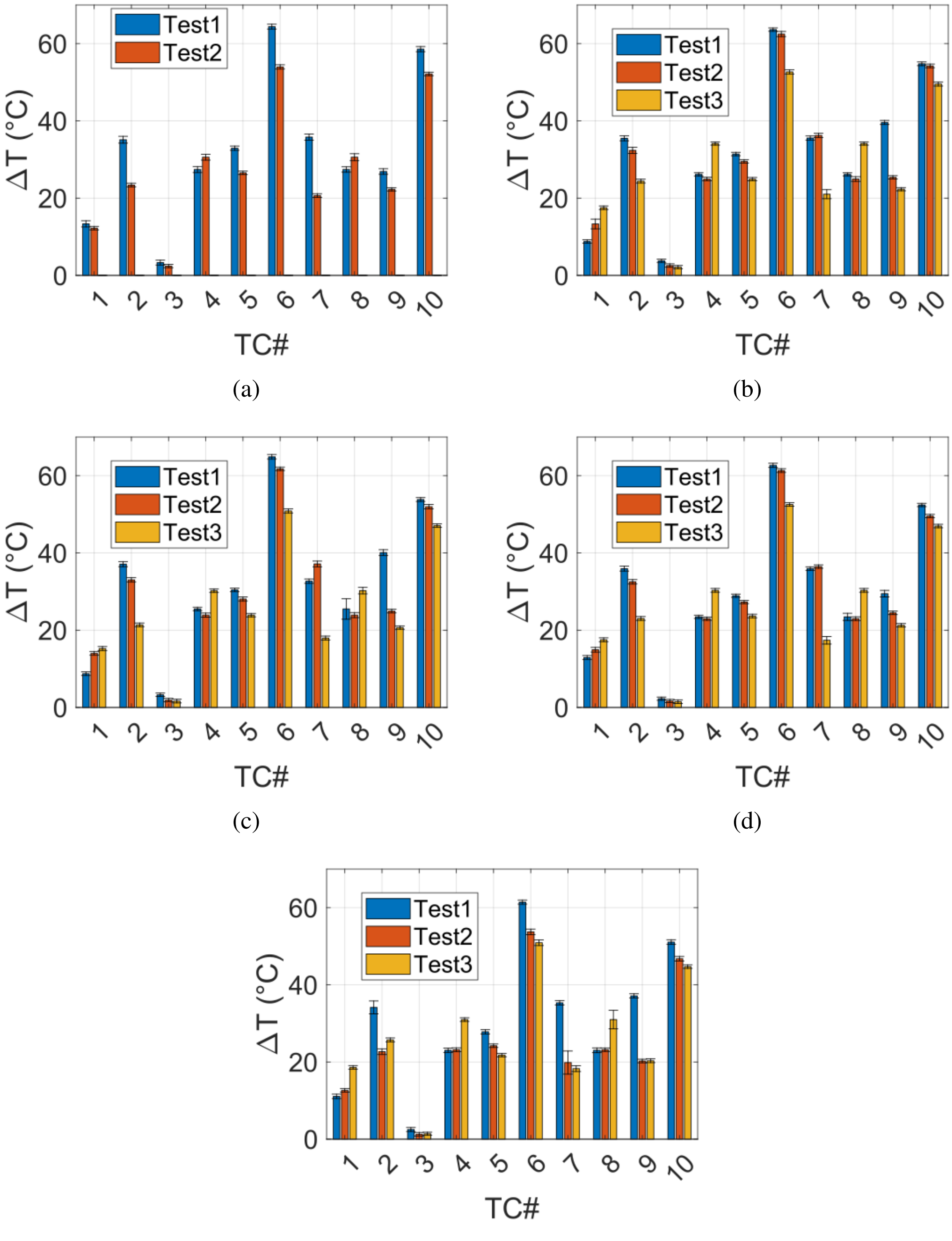

(a) (b) (c) (d) (e)

Fig. 4.45 Measured temperature increases at the nominal voltage of 94 V. Nominal flow rates of (a) 1.7 l/min and 84 V, (b) 2.5 l/min, (c) 3.3 l/min, (d) 4.2 l/min and (e) 5 l/min – prototype mirror.

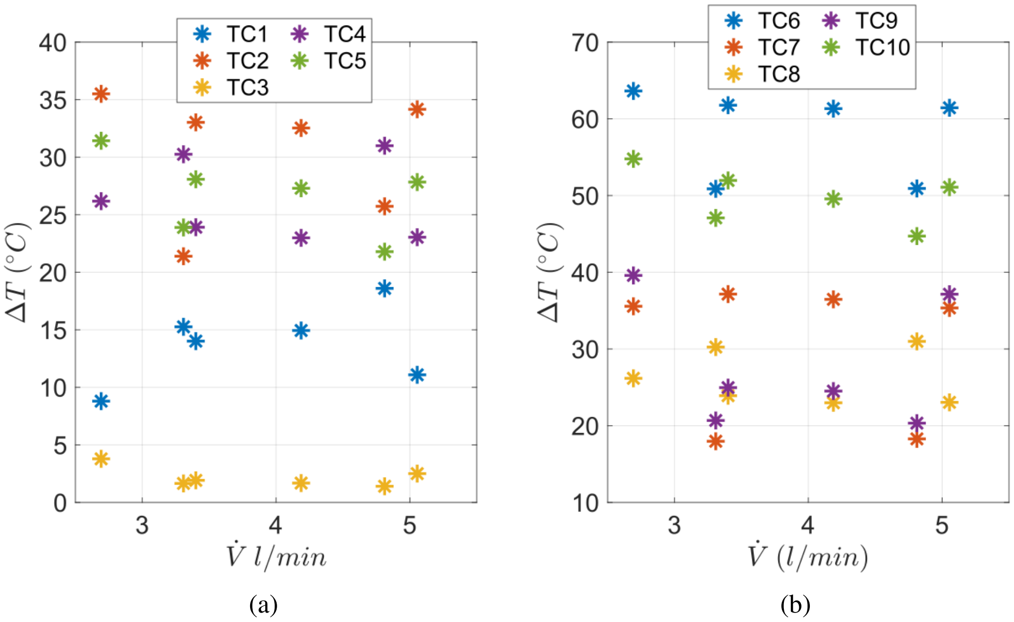

(a) (b)

Fig. 4.46 Measured temperature increase as function of the flow rate, at approximately the same power of 670 W. (a) *TC1-5* and (b) *TC6-10* – prototype mirror.

Furthermore, there was a slight increase in H^* with flow rate, but again this was unclear and within the range of uncertainty.

Note also that, at the nominal potential difference of 94 V, the values of H^* were larger than those computed at 84 V, whereas they were expected to be the same. Indeed, having the material practically constant properties within these temperature windows, at equal flow rate the heat exchange coefficient should be constant also at different power levels. This was again an indication that the influence of the resistors in the thermocouple readings was not negligible.

In Fig. 4.48, the experimental measurements were compared to the simulation results at the lowest flow rate and two power levels. By increasing the power level, the thermocouples readings raised, both in the numerical and experimental results. However, the simulated temperatures were dramatically lower than in the experiments and could not be explained by the experimental uncertainty of the *TC*. The two simulations at the same flow rate and different power levels may also be considered as a sensitivity analysis on the effect of power on *TC*. In fact, the relative increase between 460 W and 580 W of 26% was similar to the uncertainties in the computed Q_{abs}, and yet it did not lead to sufficient increases in the simulations temperatures to explain the numerical-experimental difference.

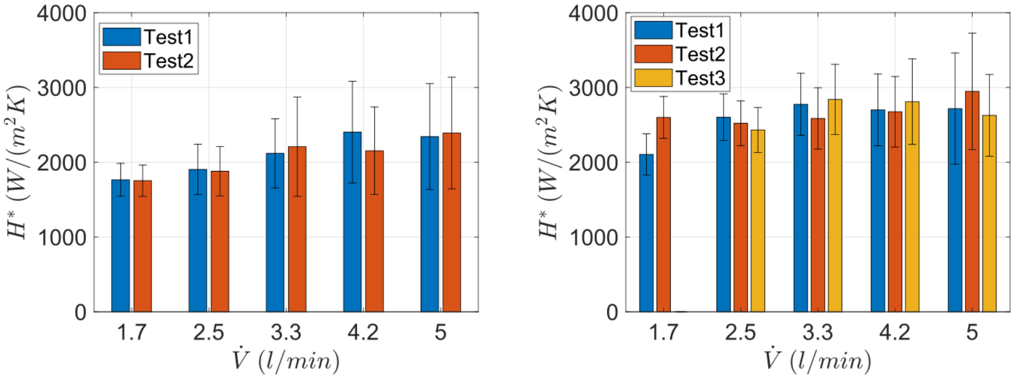

(a) (b)

Fig. 4.47 Comparison of thermal performance of the experimental and numerical results through the heat transfer coefficient. (a) $\Delta V = 84\,V$ and (b) $\Delta V = 94\,V$. The x label refers to the nominal values of flow rates – prototype mirror.

An effect that was parametrically investigated to help explaining the difference between the experimental and computed temperature increase is related to the thermal conductivity of the stainless steel. In the simulations, the bulk material conductivity k_{AISI} was used (taken from ITER database [162]), whereas the conductivity of prototype resulting from the LPBF manufacturing process could be reduced compared to the bulk value [180, 181]. The results of the parametric analysis are shown in Fig. 4.49. Decreasing the conductivity of the stainless steel to 0.6 of its bulk value lead to temperature increases of 20%-50% depending on the thermocouple, which was not sufficient to explain the numerical-experimental difference in the thermocouple readings. The non-significant increase in *TC2-3* is due to their positions outside the heating elements location.

Thus, if the design and initial numerical evaluation of the prototype mirror proved successful, the experimental results were less satisfying. The measured pressure losses within the prototype mirror were much larger than the simulated ones, as previously found in literature for metal-printed samples, possibly due to roughness, printing accuracy or local occlusions. The high experimental pressure drop could be only reproduced numerically if an actual porosity of 27% was assumed. The thermal behaviour of the mirror, including also the experimental assessment of the thermal conductivity of the 3D-printed stainless steel, requires further investigation. Further experiments needs to be carried out with a different setup, for example with a solar simulator such as the IMDEA facility in Madrid [111] and thermal sensors that are not influenced by the heating elements, such as fiber optics [182]. The use of the abrasive jet polishing method is planned for the mirror prototype in the future to evaluate its effectiveness in completing the finishing process of the additively manufactured part.

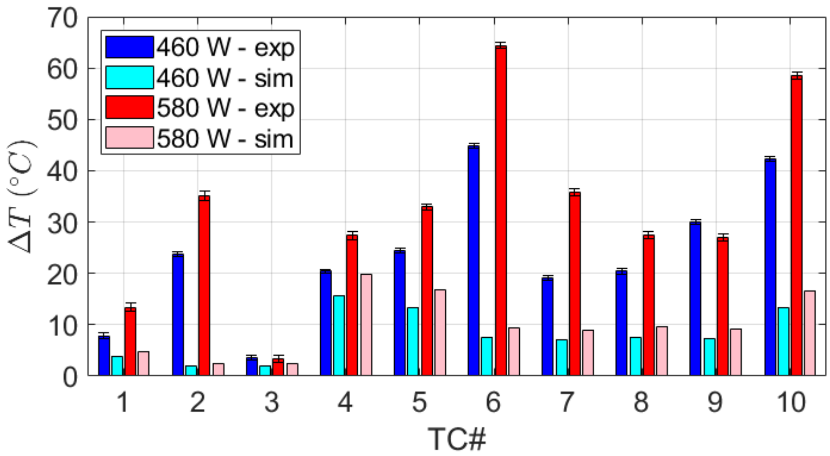

Fig. 4.48 Comparison between simulations and experiments: measured temperature increase at 1.77 l/min and 460 - 580 W – prototype mirror.

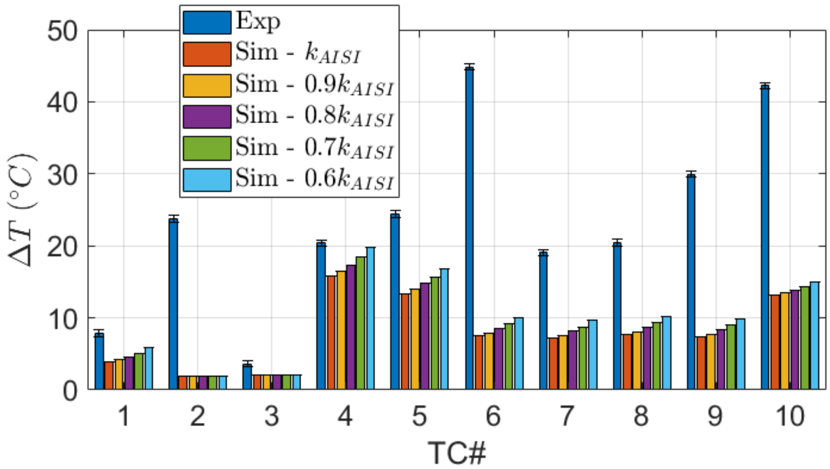

Fig. 4.49 Effect of the thermal conductivity on the numerical results – prototype mirror.

4.4 Chapter summary

In this chapter, TPMS lattices were proposed in several types of reflecting mirrors of DTT ECH system, with different dimensions and thermal conditions. Following the analyses of the previous chapters, the SplitP was chosen, proven to be the most promising, and the Gyroid was selected instead of the Diamond, to investigate also this other lattice performance as well. Because of the stringent operating conditions, a parametric analysis was carried out by varying the cell size and porosity and comparing not only the sheet-Gyroid and sheet-SplitP but also the solid-Gyroid. The best trade-off between thermal performance and structural complexity (that could worsen the printing and depowdering processes) resulted in the 3 mm cell size sheet-Gyroid, which was then used for all the analyzed mirrors. The designed TPMS-based cooling systems proved successful in the numerical analyses, also improving the heat removal capability compared to other proposed cooling structures. Thermo-mechanical analyses were also conducted on the M2 mirror, which is intended to be fabricated from a material with low electrical (and thermal) conductivity due to its proximity to the plasma. The structural simulations revealed that the resulting stresses in the mirror were considerably higher than the yield strength of conventionally manufactured AISI 316L and approximately comparable to that of LPBF-produced AISI 316L. Consequently, the same design was evaluated using Inconel 718, for which a wider safety margin relative to its yield strength was obtained.

When a prototype mirror made in AISI 316L was 3D printed and tested in water at Politecnico di Milano, Italy, the measured pressure losses were, as expected, significantly higher than the simulated values, showing a greater discrepancy with the numerical results than those observed in the receiver tests. This deviation, even larger than what observed in the hydraulic tests of the receivers in the previous chapter, was likely due to the smaller cell size, 3 mm instead of 10 mm, and the larger overall volume, which increased the difficulty of the depowdering process and amplified the effects of possible printing defects and surface roughness. The actual pressure losses could be artificially reproduced by simulating a modified structure with a lower porosity, highlighting the need for further investigation on the surface roughness and potential printing defects, that might be characterized through tomographic scans of the prototype. A systematic polishing process should be carried out to evaluate whether the experimental pressure losses can be reduced to the levels predicted by simulations.

Regarding the thermal tests of the prototype, the experimental setup was arranged to impose a high heat flux on the mirror by means of PTC resistors reaching a total amount of approximately 700 W. This configuration likely caused an excessive influence on the thermocouples, placed between the resistors and the heated surface readings. Their readings were indeed significantly higher than those predicted by numerical simulations. Such discrepancies could not be justified even by considering a lower thermal conductivity of the additively manufactured material. Therefore, further thermal tests should be performed in an experimental facility with a more suitable setup for applying high heat fluxes, such as the solar platform used for the receivers testing. Moreover, different diagnostic techniques could be envisaged, such as fiber optic thermal sensors and infrared thermography.

Chapter 5

Conclusions and future perspectives

This thesis extensively studied Triply Periodic Minimal Surfaces, addressing both mathematical and modeling aspects and practical applications.

In the first chapter, a thorough analysis at Reynolds numbers below 100 of four solid-TPMS structures with different porosities was carried out to develop lumped models that can be used in place of the pore-scale CFD simulations to substantially reduce the computational cost. The entire study was conducted under the infinite medium assumption, using a single unit cell with periodic boundary conditions. For the hydraulic models, this assumption was also assessed to remain applicable when extending the correlations to real geometries, such as circular pipes filled with TPMS structures. The hydraulic correlations were derived within the porous media framework using the Darcy–Forchheimer equation, while the thermal models were developed to correlate the Stanton number with the Reynolds number, the friction factor, and the TPMS porosity.

TPMS were also proposed as cooling systems for real applications, in particular for volumetric receivers in CSP and mirrors in the MW beam transmission in fusion reactors. Diamond and SplitP were investigated as volumetric solar receivers. They were studied both numerically and experimentally and their thermal and hydraulic performance assessed. In particular, the thermal efficiency was evaluated experimentally using a solar simulator, and the TPMS-based receivers showed improved performance with respect to other traditional absorbers at the same flow rate range. The SplitP lattice had higher thermal efficiency than the Diamond, which also resulted in larger flow impedance, in accordance to the thermal-hydraulic analysis of the first chapter. Hydraulic tests in water compared metallic and polymeric samples to evaluate the effects of manufacturing technique and surface roughness, with the printed polymeric surface being much smoother. The difference between the samples made of the two materials was large, more significant for the Diamond than the SplitP, possibly due to the more complicated SplitP structure, which can influence more the overall pressure losses rather than the smoothness of the surface. The turbulent simulations of water flow within the polymeric receivers were satisfactory for the Diamond sample but slightly underestimated the pressure losses in the SplitP sample, while the metallic receivers exhibited much larger pressure drops than modeled, likely due to surface roughness. When comparing the correlations developed in Chapter 2 to the pore-scale results of turbulent flows Chapter 3, the developed Darcy-Forchheimer models could predict almost all the same results within one standard deviation of the fit, which is promising given the different assumptions.

As for the fusion applications, TPMS were proposed for several types of reflecting mirrors, with different dimensions and thermal conditions. For the most loaded mirror, TPMS showed in numerical analyses superior heat removal capabilities compared to other cooling solutions. After a preliminary optimization study on two topologies, numerous TPMS cell sizes and porosities, the sheet-Gyroid was selected as the best compromise between heat removal efficiency and structure complexity, and it was used to design a prototype that was subsequently printed in AISI 316L and tested in the same water loop where the receivers were analyzed. The numerical and experimental curves differed even more than in the case of the receivers, as the TPMS dimensions were much smaller, thus increasing the relative effect of the roughness or possible printing defects. Thermal tests were also conducted on the prototype mirror. The very large heat fluxes on the real component could not be reproduced in laboratory. PTC resistors were employed as heating elements. The thermocouples, positioned between the PTC resistors and the mirror surface, were likely influenced by the high temperatures of the resistors. The experimental outcomes showed larger temperatures than simulations; different from the expectations, as it was assumed that large roughness would have induced better heat transfer. Considering that the 3D printed metals can have reduced thermal conductivity compared to bulk material, a parametric analysis on the conductivity was performed and could not anyway explain these significant deviations.

Future investigations could expand the study of fluid flow and thermal behavior of TPMS to higher Reynolds regimes, including turbulence aspects, for example by performing LES (Large Eddy Simulation) analyses to be used also as reference for comparing different turbulence models. Additional geometrical parameters could be included, as flow direction rotated with respect to the three principal axes of the TPMS. The thermal behavior of sheet-TPMS could be correlated to the solid-TPMS as for the hydraulic fields. The first part of this thesis was devoted to developing dedicated correlations for each topology, thus a valuable direction for future work would be to explore additional geometric parameters to enable the modeling of different topologies within a unified framework.

The developed porous media modeling of TPMS could be also tested against designs with more intricate flow path, such as the reflecting mirrors, where there is not a clear and defined flow direction. Moreover, also the thermal porous media framework may be investigated and its efficiency in modeling thermal behavior of TPMS compared to the correlations for the Nusselt numbers. In addition, an extension of the proposed thermal–hydraulic correlations to fluids with Prandtl numbers different from unity represents an important direction for future research. This would allow the assessment of the analogy between Reynolds and Stanton numbers for a broader class of working fluids with distinct thermal diffusivities, thereby enhancing the generality and applicability of the derived relationships to practical engineering conditions. Surface roughness effects in metal samples should be more deeply addressed, potentially by improving the surface smoothness through post-printing polishing such as abrasive jet polishing. The manufacturing accuracy should be studied via tomography, and sensitivity analysis on the geometric tolerances could be conducted in greater depth. Thermal testing of the prototype mirror could be performed in facilities better suited to deliver large thermal loads, as solar platforms such as the IMDEA Institute. The issue of thermocouples being affected by the heating elements can be overcome by using fiber optic thermal sensors and thermal imaging cameras.

References

[1] O. M. Zaki, R. A. Stavins, M. Wenzel, A. Musser, D. Sharar, S. Elbel, N. Miljkovic, and W. P. King. Additively manufactured compact water-cooled refrigerant condenser. *International Journal of Heat and Mass Transfer*, 244:126836, 2025.

[2] Guide to lattice structures in additive manufacturing. https://www.ntop.com/resources/blog/guide-to-lattice-structures-in-additive-manufacturing/.

[3] C. Magnapera. Minimal Surfaces, a study. Master's thesis, Alma Mater Studiorum, Università di Bologna, 2017. Available at https://amslaurea.unibo.it/id/eprint/13490/1/Minimal_surfaces__a_study%20(1).pdf.

[4] W. Meeks and J. Pérez. The classical theory of minimal surfaces. *Bulletin of the American Mathematical Society*, 48:325–325, 09 2011.

[5] E.R. Neovius. *Bestimmung zweier speciellen periodischen Minimalflächen auf welchen unendlich viele Gerade Linien und unendlich viele ebene geodätische Linien liegen: nebst vier Figurentafeln und zwei Photographien*. Verlag nicht ermittelbar, 1883.

[6] H. Wang, C. Zhao, W. Liu, Z. Liu, H. Bian, and K. Zhang. Advances in triply periodic minimal surface structures for thermal management systems: A comprehensive review. *Applied Thermal Engineering*, 279:127481, 2025.

[7] F. L. Rashid, N. M.L. Al Maimuri, M. A. Al-Obaidi, M. A. Eleiwi, A. Ameen, S. Ahmad, A. Chibani, M. Kezzar, and E. B. Agyekum. Enhancing heat transfer across applications with triply periodic minimal surface (TPMS) structures: A comprehensive review. *Chemical Engineering and Processing - Process Intensification*, 216:110460, 2025.

[8] K. Dutkowski, M. Kruzel, and K. Rokosz. Review of the state-of-the-art uses of minimal surfaces in heat transfer. *Energies*, 15(21), 2022.

[9] M. Bakker and V. Post. *Analytical Groundwater Modeling: Theory and Applications using Python (1st ed.)*. CRC Press, Taylor & Francis Group, 2022.

[10] H. Montazerian, M. Zhianmanesh, E. Davoodi, A.S. Milani, and M. Hoorfar. Longitudinal and radial permeability analysis of additively manufactured porous scaffolds: Effect of pore shape and porosity. *Materials & Design*, 122:146–156, 2017.

[11] M. Zhianmanesh, M. Varmazyar, and H. Montazerian. Fluid permeability of graded porosity scaffolds architectured with minimal surfaces. *ACS Biomaterials Science & Engineering*, 5(3):1228–1237, 2019.

[12] Y. Lu, L. Cheng, Z. Yang, J. Li, and H. Zhu. Relationship between the morphological, mechanical and permeability properties of porous bone scaffolds and the underlying microstructure. *PLOS ONE*, 15, 09 2020.

[13] R. Asbai-Ghoudan, S. Ruiz de Galarreta, and N. Rodriguez-Florez. Analytical model for the prediction of permeability of triply periodic minimal surfaces. *Journal of the Mechanical Behavior of Biomedical Materials*, 124:104804, 2021.

[14] S. Piedra, A. Gómez-Ortega, and J. Pérez-Barrera. Prediction of flow properties of Porous Triply Periodic Minimal Surface (TPMS) structures. *Fluids*, 8(12), 2023.

[15] E. N. Ahmed and A. Bottaro. Flow through porous metamaterials formed by TPMS-based unit cells: Effects of advection. *European Journal of Mechanics - B/Fluids*, 100:202–207, 2023.

[16] M.B. Hawken, S. Reid, D.A. Clarke, M. Watson, C.J. Fee, and D.J. Holland. Characterization of pressure drop through schwarz-diamond triply periodic minimal surface porous media. *Chemical Engineering Science*, 280:119039, 2023.

[17] Z. Cheng, X. Li, R. Xu, and P. Jiang. Investigations on porous media customized by triply periodic minimal surface: Heat transfer correlations and strength performance. *International Communications in Heat and Mass Transfer*, 129:105713, 2021.

[18] J. Wang, K. Chen, M. Zeng, T. Ma, Q. Wang, and Z. Cheng. Investigation on flow and heat transfer in various channels based on triply periodic minimal surfaces (tpms). *Energy Conversion and Management*, 283:116955, 2023.

[19] Y. Zhang, H. Huang, R. Liu, H. Kong, L. Qian, X. Xu, and Z. Zhang. Research on the flow and heat transfer performance of solid-network triply periodic minimal surface structures. *International Communications in Heat and Mass Transfer*, 167:109323, 2025.

[20] E. Dube Kerme, M. Hajialibabei, M. Ziad Saghir, and O. El-Ketan. Experimental investigation of porous gyroid structure: Effect of cell size and porosity on performance. *Thermal Science and Engineering Progress*, 53:102728, 2024.

[21] W. Li, W. Li, and Z. Yu. Heat transfer enhancement of water-cooled triply periodic minimal surface heat exchangers. *Applied Thermal Engineering*, 217:119198, 2022.

[22] R. Attarzadeh, M. Rovira, and C. Duwig. Design analysis of the “Schwartz D” based heat exchanger: A numerical study. *International Journal of Heat and Mass Transfer*, 177:121415, 2021.

[23] M. Khalil, M. Ali, K. Khan, and R. Abu Al-Rub. Forced convection heat transfer in heat sinks with topologies based on triply periodic minimal surfaces. *Case Studies in Thermal Engineering*, 38:102313, 07 2022.

[24] J. Iyer, T. Moore, D. Nguyen, P. Roy, and J. Stolaroff. Heat transfer and pressure drop characteristics of heat exchangers based on triply periodic minimal and periodic nodal surfaces. *Applied Thermal Engineering*, 209:118192, 2022.

[25] J. Wang, K. Chen, M. Zeng, T. Ma, Q. Wang, and Z. Cheng. Assessment of flow and heat transfer of triply periodic minimal surface based heat exchangers. *Energy*, 282:128806, 2023.

[26] S. Gao, J. Ding, S. Qu, H. Liu, and X. Song. Numerical and experimental investigation of additively manufactured shell-lattice copper heat exchanger. *International Communications in Heat and Mass Transfer*, 147:106976, 2023.

[27] D. Liang, C. Shi, W. Li, W. Chen, and M. K. Chyu. Design, flow characteristics and performance evaluation of bioinspired heat exchangers based on triply periodic minimal surfaces. *International Journal of Heat and Mass Transfer*, 201:123620, 2023.

[28] A. Barakat and B. Sun. Enhanced convective heat transfer in new triply periodic minimal surface structures: Numerical and experimental investigation. *International Journal of Heat and Mass Transfer*, 227:125538, 2024.

[29] M. Kruzel, K. Dutkowski, T. Bohdal, A. Litwin, J. Sawicki, and E. Kępa. A new approach for heat transfer coefficient determination in triply periodic minimal surface-based heat exchangers. *International Communications in Heat and Mass Transfer*, 157:107778, 2024.

[30] Y. Zhang, F. Peng, H. Jia, Z. Zhao, P. Wang, S. Duan, and H. Lei. Conformal geometric design and additive manufacturing for special-shaped TPMS heat exchangers. *International Journal of Heat and Mass Transfer*, 247:127146, 2025.

[31] S. A. Balderrama Prieto, N. P. Martin, B. A. Prussack, A. D. Fradeneck, N. E. Woolstenhulme, and M. H. Anderson. CFD modeling of turbulent air flow in self-heated gyroid TPMS structures: Thermal-hydraulic performance and validation. *Applied Thermal Engineering*, 279:127682, 2025.

[32] Z. Zhang, T. Gao, B. Zhang, L. Zhou, P. Yang, J. Gong, and J. Li. Conjugate thermo-hydraulic evaluation of triply periodic minimal surfaces and pin fins. *Applied Thermal Engineering*, 274:126667, 2025.

[33] X. Su, Y. Zhang, Y. Rao, K. Yeranee, and X. Wang. Experimental and Numerical Study on Flow and Heat Transfer Characteristics of Additively Manufactured Triply Periodic Minimal Surface (TPMS) Heat Exchangers for Micro Gas Turbine. *Aerospace*, 12(5), 2025.

[34] Z. Zou, W. Chen, Y. Song, M. Li, S. Li, W. Huang, Y. Sun, X. Tian, and M. Hao. Experimental investigation of the performance of an Industrial-Grade Schwartz-D heat exchanger. *Applied Thermal Engineering*, 270:126243, 2025.

[35] B. Reynolds, F. Lecarpentier, and D. Holland. Heat transfer and topological characterisation of tpms structures using 3d printed materials. *International Journal of Heat and Mass Transfer*, 245:126992, 2025.

[36] G. Brambati, M. Guilizzoni, and S. Foletti. Convective heat transfer correlations for Triply Periodic Minimal Surfaces based heat exchangers. *Applied Thermal Engineering*, 242:122492, 2024.

[37] G. Yan, Y. Liu, Z. Zhang, M. Sun, S. Li, X. Zhang, L. Jiang, S. Xing, and Y. Mao. Thermal-hydraulic performance of modified Schwartz-Diamond solid-networks triply periodic minimal surface structures. *Applied Thermal Engineering*, 249:123384, 2024.

[38] K. Yan, H. Deng, Y. Wu, T. Yu, Y. Xiao, and J. Wang. Gyroid-structured heat exchanger optimization via lattice geometric manipulation for enhanced thermo-hydraulic performance: an experimental and numerical research. *International Journal of Thermal Sciences*, 215:109966, 2025.

[39] K. Yan, H. Deng, Y. Wu, J. Wang, and Y. Huang. Effects of lattice geometric manipulation on thermo-hydraulic performance of gyroid-structured heat exchanger: A numerical study. *International Journal of Heat and Mass Transfer*, 248:127217, 2025.

[40] K. Yan, J. Wang, L. Li, and H. Deng. Numerical investigation into thermo-hydraulic characteristics and mixing performance of triply periodic minimal surface-structured heat exchangers. *Applied Thermal Engineering*, 230:120748, 2023.

[41] L. Ornelas-Ramón, A. Gómez-Ortega, J. Pérez-Barrera, and S. Piedra. Computational analysis and engineering modeling for the heat transfer and fluid flow through the gyroid TPMS structure. *Applied Thermal Engineering*, 268:125865, 2025.

[42] G. Ferruzzi, C. Delcea, A. Barberi, V. Di Dio, M. Di Somma, P. Catrini, S. Guarino, F. Rossi, M. L. Parisi, A. Sinicropi, and S. Longo. Concentrating solar power: The state of the art, research gaps and future perspectives. *Energies*, 16(24):8082, 2023.

[43] A. H. Alami, A. G. Olabi, A. Mdallal, A. Rezk, A. Radwan, S. M. A. Rahman, S. K. Shah, and M. A. Abdelkareem. Concentrating solar power (CSP)

technologies: Status and analysis. *International Journal of Thermofluids*, 18:100340, 2023.

[44] How Concentrated Solar Power Works. https://www.solarpaces.org/worldwide-csp/how-concentrated-solar-power-works/.

[45] E. Okoroigwe and A. Madhlopa. An integrated combined cycle system driven by a solar tower: A review. *Renewable and Sustainable Energy Reviews*, 57:337–350, 2016.

[46] J. Khan and M. H. Arsalan. Solar power technologies for sustainable electricity generation – a review. *Renewable and Sustainable Energy Reviews*, 55:414–425, 2016.

[47] K. M. Kennedy, T. H. Ruggles, K. Rinaldi, J. A. Dowling, L. Duan, K. Caldeira, and N. S. Lewis. The role of concentrated solar power with thermal energy storage in least-cost highly reliable electricity systems fully powered by variable renewable energy. *Advances in Applied Energy*, 6:100091, 2022.

[48] S. H. Madaeni, R. Sioshansi, and P. Denholm. Estimating the Capacity Value of Concentrating Solar Power Plants With Thermal Energy Storage: A Case Study of the Southwestern United States. *IEEE Transactions on Power Systems*, 28(2):1205–1215, 2013.

[49] N. Boerema, G. Morrison, R. Taylor, and G. Rosengarten. High temperature solar thermal central-receiver billboard design. *Solar Energy*, 97:356–368, 2013.

[50] M. Cagnoli, A. De La Calle, J. Pye, L. Savoldi, and R. Zanino. A CFD-supported dynamic system-level model of a sodium-cooled billboard-type receiver for central tower CSP applications. *Solar Energy*, 177:576–594, 2019.

[51] T. Conroy, M. N. Collins, and R. Grimes. A review of steady-state thermal and mechanical modelling on tubular solar receivers. *Renewable and Sustainable Energy Reviews*, 119:109591, 2020.

[52] A. L. Avila-Marin, J. Fernandez-Reche, S. Gianella, L. Ferrari, and D. Sanchez-Señoran. Experimental study of innovative periodic cellular structures as air volumetric absorbers. *Renewable Energy*, 184:391–404, 2022.

[53] A. L. Ávila Marín. Volumetric receivers in solar thermal power plants with central receiver system technology: A review. *Solar Energy*, 85(5):891–910, 2011.

[54] M. Shahabuddin, M.A. Alim, Tanvir Alam, M. Mofijur, S.F. Ahmed, and Greg Perkins. A critical review on the development and challenges of concentrated solar power technologies. *Sustainable Energy Technologies and Assessments*, 47:101434, 2021.

[55] Y. He, S. Du, and S. Shen. Advances in porous volumetric solar receivers and enhancement of volumetric absorption. *Energy Reviews*, 2(3):100035, 2023.

[56] D. Xu and M. Lin. Design controllable TPMS structures for solar thermal applications: A pore-scale vs. volume-averaged modeling approach. *International Journal of Heat and Mass Transfer*, 201:123625, 2023-02.

[57] M.I. Roldán, O. Smirnova, T. Fend, J.L. Casas, and E. Zarza. Thermal analysis and design of a volumetric solar absorber depending on the porosity. *Renewable Energy*, 62:116–128, 2014.

[58] B. Prussack, I. Jentz, T. A. Moreira, E. Pagenkopf, N. Woolstenhulme, G. Nellis, and M. Anderson. Local heat transfer measurement in a volumetrically heated TPMS lattice using distributed optical fiber thermal sensing. *Applied Thermal Engineering*, 269:126101, 2025.

[59] Y. Zhang, X. Zhang, H. Li, S. Li, Z. Zhang, M. Sun, and Y. Song. Improving the efficiency of solar thermal storage systems using TPMS: A pore-scale simulation. *Solar Energy Materials and Solar Cells*, 286:113569, 2025.

[60] J. P. Freidberg. *Plasma Physics and Fusion Engineering*. Cambridge University Press, 2007.

[61] S. Garavaglia, B. Baiocchi, A. Bruschi, D. Busi, F. Fanale, L. Figini, G. Granucci, A. Moro, P. Platania, N. Rispoli, A. Romano, A. Salvitti, E. Sartori, S. Schmuck, and E. Vassallo. Progress of DTT ECRH system design. *Fusion Engineering and Design*, 168:112678, 2021.

[62] S. Garavaglia, L. Balbinot, A. Bruschi, D. Busi, A. Bussolan, F. Fanale, G. Granucci, A. Moro, P. Platania, N. Rispoli, A. Romano, E. Sartori, S. Schmuck, A. Simonetto, and E. Vassallo. Development of the electron cyclotron resonance heating system for Divertor Tokamak Test. *Journal of Vacuum Science & Technology B*, 41(4):044201, 05 2023.

[63] G. Granucci, S. Ceccuzzi, G. Giruzzi, P. Sonato, P. Agostinetti, T. Bolzonella, A. Bruschi, A. Cardinali, L. Figini, S. Garavaglia, R. Maggiora, D. Milanesio, F. Mirizzi, S. Nowak, G.L. Ravera, C. Sozzi, A.A. Tuccillo, and P. Vincenzi. The DTT device: System for heating. *Fusion Engineering and Design*, 122:349–355, 2017.

[64] D.R. Mikkelsen, C.E. Kessel, F.M. Poli, N. Bertelli, and K. Kim. Survey of heating and current drive for K-DEMO. *Nuclear Fusion*, 58(3):036014, jan 2018.

[65] G. Granucci, F. Auriemma, L. Aucone, B. Baiocchi, N. Bonanomi, F. Braghin, A. Bruschi, D. Busi, I. Casiraghi, L.E. di Grazia, F. Fanale, L. Figini, S. Garavaglia, P. Mantica, M. Mattei, A. Moro, S. Nowak, P. Platania, D. Ricci, N. Rispoli, A. Romano, G. Rubino, S. Schmuck, and A. Simonetto. Roles of ECH system in DTT plasma operations. *Nuclear Fusion*, 64(12):126036, oct 2024.

[66] M. K. A. Thumm. MW gyrotron development for fusion plasma applications. *Plasma Physics and Controlled Fusion*, 45(12A):A143, nov 2003.

[67] M. K. A. Thumm, G. G. Denisov, K. Sakamoto, and M. Q. Tran. High-power gyrotrons for electron cyclotron heating and current drive. *Nuclear Fusion*, 59(7):073001, jun 2019.

[68] F. Fanale, B. Baiocchi, A. Bruschi, D. Busi, A. Bussolan, L. Figini, S. Garavaglia, G. Granucci, and A. Romano. Progress on the conceptual design of the antennas for the DTT ECRH system. *Fusion Engineering and Design*, 192:113797, 2023.

[69] F. Fanale, A. Bruschi, S. Garavaglia, A. Moro, B. Baiocchi, M. Bonesso, F. Braghin, D. Busi, R. Dima, P. Fanelli, L. Figini, E. Gajetti, G. Granucci, D. Mascali, S. Passarello, A. Pepato, P. Platania, P. Rebesan, A. Romano, A. Salvitti, L. Savoldi, A. Simonetto, S. Schmuck, G. Torrisi, and M. Turcato. Status of DTT ECH Transmission Lines and Antennae. *IEEE Transactions on Plasma Science*, 52(9):3778–3784, 2024.

[70] M.A. Henderson, S. Alberti, P. Benin, T. Bonicelli, R. Chavan, D. Campbell, S. Cirant, G. Dammertz, O. Dormicchi, O. Dumbrajs, D. Fasel, T.P. Goodman, R. Heidinger, J.-P. Hogge, W. Kasparek, C. Lievin, B. Piosczyk, E. Poli, G. Ramponi, G. Saibene, O. Sauter, A. Serikov, G. Taddia, M. Thumm, M.Q. Tran, A.G.A. Verhoeven, and H. Zohm. EU developments of the ITER ECRH system. *Fusion Engineering and Design*, 82(5):454–462, 2007. Proceedings of the 24th Symposium on Fusion Technology.

[71] Q. Wu, P. Lu, Y. Zheng, H. Du, K. Xu, X. Wang, L. Zhang, and S. Liu. Neutronic analyses of Upper port ECRH antenna system for CFETR. *Fusion Engineering and Design*, 162:112078, 2021.

[72] B. Plaum, C. Lechte, W. Kasparek, S. Gaiser, A. Zeitler, V. Erckmann, M. Weißgerber, A. Bechtold, M. Busch, and B. Szcepaniak. Design of a remote steering antenna for ECRH heating in the stellarator Wendelstein 7-X. *Fusion Engineering and Design*, 96-97:568–572, 2015. Proceedings of the 28th Symposium On Fusion Technology (SOFT-28).

[73] R. A. Olstad, J. L. Doane, and C. P. Moeller. ECH MW-level CW transmission line components suitable for ITER. *Fusion Engineering and Design*, 74(1):331–335, 2005. Proceedings of the 23rd Symposium of Fusion Technology.

[74] W. Xu, H. Xu, D. Wu, Y. Yang, J. Zhang, X. Wang, J. Wang, Y. Hou, L. Zhang, and M. Li. Advances and Prospects of ECRH System on EAST. *IEEE Transactions on Plasma Science*, 52(10):5159–5172, 2024.

[75] Yunying Tang, Xiaojie Wang, Liyuan Zhang, Chao Zhang, Hanlin Wang, Wei Wei, Dajun Wu, Huaichuan Hu, and Fukun Liu. Design status of the ECRH system for CFETR. *Fusion Engineering and Design*, 182:113225, 2022.

[76] V. Erckmann and U. Gasparino. Electron cyclotron resonance heating and current drive in toroidal fusion plasmas. *Plasma Physics and Controlled Fusion*, 36(12):1869, dec 1994.

[77] V. Erckmann, P. Brand, H. Braune, G. Dammertz, G. Gantenbein, W. Kasparek, H. P. Laqua, H. Maassberg, N. B. Marushchenko, G. Michel, M., Y. Turkin, M. Weissgerber, A. Weller, , and and. Electron Cyclotron Heating for W7-X: Physics and Technology. *Fusion Science and Technology*, 52(2):291–312, 2007.

[78] A. Moro, A. Bruschi, F. Fanale, P. Fanelli, E. Gajetti, S. Garavaglia, G. Granucci, S. Meloni, A. Pepato, P. Platania, A. Romano, A. Salvitti, L. Savoldi, S. Schmuck, M. Scungio, A. Simonetto, M. Turcato, and E. Vassallo. Progress and challenges of the ECH transmission line design for DTT. *Fusion Engineering and Design*, 202:114391, 2024.

[79] E. Gajetti, G. Boccardo, L. Savoldi, and L. Marocco. Hydrodynamic characterization of Gyroid, Diamond and Split-P Triply Periodic Minimal Surfaces as porous medium. *International Journal of Heat and Mass Transfer*, 252:127439, 2025.

[80] L. Savoldi, A. Cammi, E. Gajetti, and L. Marocco. Investigating the Reynolds analogy for Triply Periodic Minimal Surfaces in low-Reynolds flow regime. *Conference paper: THMT-25 Turbulence, Heat and Mass Transfer 11, 21-25 July 2025, Tokyo, Japan*, 2025.

[81] R. B. Bird, W. E. Stewart, and E. N. Lightfoot. *Transport phenomena*. J. Wiley, 2002.

[82] H. Barokh, S. P. Zoiee, H. Najafi, M. Siavashi, and M. A. Sobati. A detailed comparison of heat transfer and fluid dynamics in Voronoi foam and triply periodic minimal surfaces (TPMS) via pore-scale investigation. *International Journal of Heat and Mass Transfer*, 245:127007, 2025.

[83] M. Matyka and Z. Koza. How to calculate tortuosity easily? *AIP Conference Proceedings*, 1453:17–22, 03 2012.

[84] K. Graczyk and M. Matyka. Predicting porosity, permeability, and tortuosity of porous media from images by deep learning. *Scientific Reports*, 10, 12 2020.

[85] J. Luo, L. Chen, T. Min, F. Shan, Q. Kang, and W. Tao. Macroscopic transport properties of gyroid structures based on pore-scale studies: Permeability, diffusivity and thermal conductivity. *International Journal of Heat and Mass Transfer*, 146:118837, 2020.

[86] H. Montazerian, M.G.A. Mohamed, M. Mohaghegh Montazeri, S. Kheiri, A.S. Milani, K. Kim, and M. Hoorfar. Permeability and mechanical properties of gradient porous PDMS scaffolds fabricated by 3D-printed sacrificial templates designed with minimal surfaces. *Acta Biomaterialia*, 96:149–160, 2019.

[87] J. W. Fisher, S. W. Miller, J. Bartolai, T. W. Simpson, and M. A. Yukish. Catalog of triply periodic minimal surfaces, equation-based lattice structures, and their homogenized property data. *Data in Brief*, 49:109311, 2023.

[88] F. Dolamore, B. Houlton, C. J. Fee, M. J. Watson, and D. J. Holland. A numerical investigation of the hydrodynamic dispersion in triply periodic chromatographic stationary phases. *Journal of Chromatography A*, 1685:463637, 2022.

[89] M. G. Gado, S. Ookawara, S. Nada, M. F. Elkady, and H. Hassan. Adsorbent beds packed in triply periodic minimal surface-derived structures and their performance in adsorption desalination/cooling systems. *International Communications in Heat and Mass Transfer*, 150:107205, 2024.

[90] B. D. Wood, X. He, and S. V. Apte. Modeling turbulent flows in porous media. *Annual Review of Fluid Mechanics*, 52(Volume 52, 2020):171–203, 2020.

[91] A. Banerjee, S. Pasupuleti, M. Singh, S. Dutta, and G N. P. Kumar. Modelling of flow through porous media over the complete flow regime. *Transport in Porous Media*, 08 2019.

[92] S. P. Burke and W. B. Plummer. Gas flow through packed columns1. *Industrial & Engineering Chemistry*, 20(11):1196–1200, 1928.

[93] H. K. Versteeg and W. Malalasekera. *An Introduction to Computational Fluid Dynamics, The Finite Volume Method*. Pearson Education, 2007.

[94] T. Pires, J. Santos, R. B. Ruben, B. P. Gouveia, A. P. G. Castro, and P. R. Fernandes. Numerical-experimental analysis of the permeability-porosity relationship in triply periodic minimal surfaces scaffolds. *Journal of Biomechanics*, 117:110263, 2021.

[95] ESI OpenCFD. simpleFoam. https://www.openfoam.com/documentation/guides/latest/doc/guide-applications-solvers-incompressible-simpleFoam.html.

[96] American Society of Mechanical Engineers. *Standard for Verification and Validation in Computational Fluid Dynamics and Heat Transfer: An American National Standard*. American Society of Mechanical Engineers, 2009.

[97] B. R. Munson, T. H. Okiishi, D. F. Young, and W. W. Huebsch. *Funcamentals of Fluid Mechanics - seventh edition*. John Wyley & sons, 2013.

[98] E. Crevacore, T. Tosco, R. Sethi, G. Boccardo, and D. L. Marchisio. Recirculation zones induce non-fickian transport in three-dimensional periodic porous media. *Physycal Review E*, 94:053118, Nov 2016.

[99] S. J. P. Callens, C. H. Arns, A. Kuliesh, and A. A. Zadpoor. Decoupling Minimal Surface Metamaterial Properties Through Multi-Material Hyperbolic Tilings. *Advanced Functional Materials*, 31(30):2101373, 2021.

[100] Z. Cheng, R. Xu, and P. Jiang. Morphology, flow and heat transfer in triply periodic minimal surface based porous structures. *International Journal of Heat and Mass Transfer*, 170:120902, 2021.

[101] P. Guo. Dependency of tortuosity and permeability of porous media on directional distribution of pore voids. *Transport in Porous Media*, 95, 11 2012.

[102] A. Koponen, M. Kataja, and J. Timonen. Permeability and effective porosity of porous media. *Physycal Review E*, 56, 09 1997.

[103] F. P. Incropera, D. P. Dewitt, T. L. Bergman and A. S. Lavine. *Fundamentals of Heat and Mass Transfer, sixth edition*. John Wyley & sons, 2007.

[104] ESI OpenCFD. scalarTransportFoam. https://www.openfoam.com/documentation/guides/latest/doc/guide-applications-solvers-basic-scalarTransportFoam.html.

[105] ESI OpenCFD. snappyHexMesh. https://www.openfoam.com/documentation/user-guide/4-mesh-generation-and-conversion/4.4-mesh-generation-with-the-snappyhexmesh-utility.

[106] A. Mortazavi, A.L. Ávila Marín, H. Ebadi, E. Gajetti, C. Piatti, L. Marocco, and L. Savoldi. Experimental investigation of Triply Periodic Minimal Surfaces for high-temperature solar receivers. *Case Studies in Thermal Engineering*, 60:104771, 2024-08.

[107] E. Gajetti, G. Boccardo, A. Buffo, V. Gentile, A. Lucchini, L. Marocco, C. Piatti, A. Quamori Tanzi, and L. Savoldi. Assessment of numerical tools and models for the simulation of flow through TPMS structures. *Presented at the 9th European Congress on Computational Methods in Applied Sciences and Engineering - ECCOMAS*, 2024.

[108] E. Gajetti, V. Gentile, A. Lucchini, L. Marocco, C. Piatti, A. Quamori Tanzi, and L. Savoldi. Experimental investigation of fluid flow through Triply Periodic Minimal Surfaces structures. *Presented at the 41st UIT International Heat Transfer Conference*, 2024.

[109] Dassault Systèmes. Solidworks.
urlhttps://www.solidworks.com/, 2021.

[110] nTop, Computational Design Software. https://www.ntop.com/.

[111] J. Li, J. Gonzalez-Aguilar, and M. Romero. Line-concentrating flux analysis of 42kwe high-flux solar simulator. *Energy Procedia*, 69:132–137, 05 2015.

[112] BIPM, IEC, IFCC, ILAC, ISO, IUPAC, IUPAP and OIML. Jcgm 100:2008. evaluation of measurement data-guide to the expression of uncertainty in measurement. Technical report, Joint Committee for Guides in Metrology, 2008.

[113] P. Wang, H. Guan, Z. Liu, G. Wang, F. Zhao, and H. Xiao. High temperature collecting performance of a new all-glass evacuated tubular solar air heater with U-shaped tube heat exchanger. *Energy Conversion and Management*, 77:315–323, 2014.

[114] M. Nemś and J. Kasperski. Experimental investigation of concentrated solar air-heater with internal multiple-fin array. *Renewable Energy*, 97:722–730, 2016.

[115] Afaq J. M. Thermal evaluation of a double-pass unglazed solar air heater with perforated plate and wire mesh layers. *Sustainability*, 12(9), 2020.

[116] G. Chouhan and B. Gunji. Additive manufacturing tpms lattice structures: Experimental study on airflow resistivity. *Results in Materials*, 20:100478, 2023.

[117] A. Zimmer, J. D. PachecoAraújo, K. A. Andreassen, and C. A. Grande. Effect of Manufacturing Techniques in Pressure Drop on Triple Periodical Minimal Surface Packings. *Chemie Ingenieur Technik*, 93(6):967–973, 2021.

[118] Siemens Digital Industries Software, "Simcenter STAR-CCM+, version 2310.001".

[119] Ansys Fluent. urlhttps://www.ansys.com/products/fluids/ansys-fluent.

[120] ESI OpenCFD. ESI OpenCFD Release OpenFOAM ®v2212. https://www.openfoam.com/news/main-news/openfoam-v2212.

[121] T. Shih, W. W. Liou, A. Shabbir, Z. Yang, and J. Zhu. A new $k-\varepsilon$ eddy viscosity model for high reynolds number turbulent flows. *Computers & Fluids*, 24(3):227–238, 1995.

[122] Paul A. Durbin. On the k-3 stagnation point anomaly. *International Journal of Heat and Fluid Flow*, 17:89–90, 1996.

[123] F. R. Menter. Two-equation eddy-viscosity turbulence models for engineering applications. *AIAA Journal*, 32(8):1598–1605, 1994.

[124] Siemens. Siemens Digital Industries Software STAR-CCM+ User Guide v2310.001, year = 2023.

[125] S. Lardeau and F. Billard. Development of an elliptic-blending lag model for industrial applications. *54th AIAA Aerospace Sciences Meeting*, 2016.

[126] R. Tunstall, S. Lardeau, D. Laurence, and R. Prosser. An elliptic blending lag model for flows in thermal-hydraulics systems. *ETMM11*, 2016.

[127] S. Lardeau and R. Manceau. Computations of complex flow configurations using a modified elliptic-blending Reynolds-Stress model. *10th International ERCOFTAC Symposium on Engineering Turbu lence Modelling and Measurements*, 2014.

[128] A. Revell, S. Benhamadouche, T. Craft, and D. Laurence. A Stress-Strain Lag Eddy Viscosity Model for Unsteady Mean Flow. *International Journal of Heat and Fluid Flow*, 27:821–830, 10 2006.

[129] R. Difonzo, E. Gajetti, L. Savoldi, and N. Fathi. Assessment of different RANS turbulence models in mini-channels for the cooling of MW-class gyrotron resonators. *International Journal of Heat and Mass Transfer*, 193:122922, 2022.

[130] N. Baobaid, M. I. Ali, K. A. Khan, and R. K. Abu Al-Rub. Fluid flow and heat transfer of porous tpms architected heat sinks in free convection environment. *Case Studies in Thermal Engineering*, 33:101944, 2022.

[131] M. Alteneiji, M. I. Hassan Ali, K. A. Khan, and R. K. Abu Al-Rub. Heat transfer effectiveness characteristics maps for additively manufactured tpms compact heat exchangers. *Energy Storage and Saving*, 1(3):153–161, 2022.

[132] C. Xu, Y. Rao, and K. Yeranee. Experiments and numerical analysis of turbulent flow heat transfer and pressure loss of a channel with triply periodic minimal surface structures. *International Journal of Thermal Sciences*, 220:110334, 2026.

[133] L. Dharmalingam, B. O'Malley, J. Tancabel, and V. Aute. Design, optimization, and validation of a triply periodic minimal surface based heat exchanger for extreme temperature applications. *International Journal of Heat and Mass Transfer*, 242:126797, 2025.

[134] Siemens Digital Industries Software. Simcenter STAR-CCM+ User Guide v. 2022.1.1, Siemens 2022.

[135] M. Wolfshtein. The velocity and temperature distribution in one-dimensional flow with turbulence augmentation and pressure gradient. *International Journal of Heat and Mass Transfer*, 12(3):301–318, 1969.

[136] E. Gajetti, M. Bonesso, A. Bruschi, F. Fanale, S. Garavaglia, G. Granucci, A. Moro, A. Pepato, A. Romano, and L. Savoldi. A New Efficient Mirror Cooling for the Transmission Line of Fusion Reactor ECH Systems Based on Triply Periodic Minimal Surfaces. *IEEE Transactions on Plasma Science*, pages 1–7, 2024.

[137] E. Gajetti, A. Bruschi, S. Garavaglia, F. Fanale, L. Marocco, A. Romano, and L. Savoldi. Development of a novel TPMS cooling structure for the launcher mirror M2 of the DTT ECH system. *Presented at the 33rd Symposium on Fusion Technology - SOFT*, 2024.

[138] E. Gajetti, A. Bruschi, F. Fanale, W. Ferretto, G. Granucci, A. Lucchini, L. Marocco, A. Romano, and L. Savoldi. Design, manufacturing and experimental characterization of a first-of-a-kind DTT ECH mirror equipped with TPMS. *Submitted to IEEE Transactions on Plasma Science*, 2025.

[139] A. Bruschi, M. Bonesso, D. Busi, C. Cesari, R. Chomicz, R. Dima, F. Fanale, P. Fanelli, G. Favero, E. Gajetti, S. Garavaglia, G. Granucci, A. Pagliaro, A. Pepato, P. Platania, N. Rispoli, a. Romano, A. Salvitti, L. Savoldi, A. Simonetto, M. Turcato and F. Zanon. Challenges of the DTT ECH Launchers

and options under study. *Submitted to IEEE Transactions on Plasma Science*, 2025.

[140] R. Ambrosino. DTT - Divertor Tokamak Test facility: A testbed for DEMO. *Fusion Engineering and Design*, 167:112330, 2021.

[141] R. Albanese, F. Crisanti, P. Martin, A. Pizzuto, G. Mazzitelli, A.A. Tuccillo, R. Ambrosino, A. Appi, G. Di Gironimo, A. Di Zenobio, A. Frattolillo, G. Granucci, P. Innocente, A. Lampasi, R. Martone, G.M. Polli, G. Ramogida, P. Rossi, S. Sandri, M. Valisa, R. Villari, and V. Vitale. Design review for the Italian Divertor Tokamak Test facility. *Fusion Engineering and Design*, 146:194–197, 2019. SI:SOFT-30.

[142] F. Romanelli et al. Divertor Tokamak Test facility project: status of design and implementation. *Nuclear Fusion*, 64(11):112015, sep 2024.

[143] R. Martone, R. Albanese, F. Crisanti, P. Martin, and A. Pizzuto. Divertor Tokamak Test facility Interim Design Report. Technical report, ENEA, Italian National Agency for New Technologies, Energy and Sustainable Economic Development, Via Enrico Fermi 45, 00044 Frascati (Roma), Italy, 04 2019.

[144] Z. C. Ioannidis, F. Albajar, S. Alberti, K. A. Avramidis, W. Bin, T. Bonicelli, A. Bruschi, J. Chelis, F. Fanale, G. Gantenbein, J. Genoud, J.-P. Hogge, V. Hermann, S. Illy, J. Jelonnek, J. Jin, W. Kasparek, G. P. Latsas, F. Legrand, C. Lechte, I. Gr. Pagonakis, T. Rzesnicki, F. Sánchez, C. Schlatter, M. Schmid, I. G. Tigelis, M. Thumm, M. Q. Tran, A. Zisis, and A. Zein. Recent experiments with the European 1MW, 170GHz industrial CW and short-pulse gyrotrons for ITER. *Fusion Engineering and Design*, 146:349–352, 2019. SI:SOFT-30.

[145] F. Braunmueller, T. P. Goodman, J. Genoud, F. Albajar, S. Alberti, K. A. Avramidis, R. Bertazzoni, W. Bin, D. Bonetti, A. Bruschi, A. Cammi, M. Cavinato, I. Chelis, D. Dall'Acqua, R. Difonzo, L. Feuerstein, E. Gajetti, G. Gantenbein, S. Garavaglia, J. Gontard, G. Granucci, J. Hogge, S. Illy, C. Introini, Z. Ioannidis, J. Jelonnek, J. Jin, A. Leggieri, F. Legrand, C. Lievin, R. Marchesin, I. M. Oumar, O. Picas, A. Romano, T. Rzesnicki, F. Sanchez, L. Savoldi, S. Stanculovic, I. Tigelis, E. Vallée, and M. Thumm. Results on the 1 MW CW 170 GHz gyrotron TH1509UA for ITER and DTT at the FALCON test stand. *EPJ Web Conf.*, 313:04005, 2024.

[146] A. Bruschi, A. Allio, F. Fanale, P. Fanelli, S. Garavaglia, F. Giorgetti, G. Granucci, A. Moro, P. Platania, A. Romano, A. Salvitti, L. Savoldi, S. Schmuck, and A. Simonetto. Conceptual design of the DTT ECRH quasi-optical transmission line. *Fusion Engineering and Design*, 194:113727, 2023.

[147] A. Allio, A. Bruschi, D. Busi, A. Bussolan, F. Fanale, P. Fanelli, S. Garavaglia, F. Giorgetti, A. Romano, A. Salvitti, and L. Savoldi. Assessment of the Performance of Different Cooling Configurations for the Launcher Mirrors of the ECRH System of the DTT Facility. *IEEE Transactions on Plasma Science*, 50(11):4054–4059, 2022.

[148] A. Pagliaro, F. Braghin, A. Bruschi, D. Busi, E. De Marchi, F. Fanale, G. Granucci, A. Romano, and F. Zanon. Variable-Depth Complementary Spiral cooling channel design for the steerable ECRH mirrors of DTT. *Fusion Engineering and Design*, 219:115276, 2025.

[149] P. F. Goldsmith. *Quasioptical Systems: Gaussian Beam Quasioptical Propogation and Applications*. Springer New York, NY, 01 1998.

[150] X. Wang, F. Liu, W. Wei, Y. Tang, B. Li, L. Zhang, H. Xu, D. Wu, J. Shan, H. Hu, J. Wang, Z. Wu, W. Ma, J. Zhang, M. Li, Y. Zhang, Y. Liu, and EAST team. Research activities and progress on the long pulse ECRH launcher for EAST. *EPJ Web Conf.*, 203:02012, 2019.

[151] Mi J., Minho W., Jongwon H., Sonjong W., Sunggug K., Sanghee H., Dongjea L., Jonggu K., and Robert E. Design of ECH launcher for KSTAR advanced Tokamak operation. *Fusion Engineering and Design*, 151:111395, 2020.

[152] P. Santos Silva, R. Chavan, T.P. Goodman, A. Mas Sanchez, and M. Vagnoni. Design concept and thermal-structural analysis of a high power reflective mm-wave optical mirror (M2) for the ITER ECH-UL. *Fusion Engineering and Design*, 146:618–621, 2019. SI:SOFT-30.

[153] D. Li, Y. Tang, C. Zhang, H. Wang, L. Zhang, X. Wang, and F. Liu. Preliminary design and thermo-mechanical analysis of the ECRH equatorial launcher focusing mirror (M1) towards the CFETR. *Fusion Engineering and Design*, 191:113723, 2023.

[154] H. Hailer, G. Dammertz, V. Erckmann, G. Gantenbein, F. Hollmann, W. Kasparek, W. Leonhardt, M. Schmid, P.G. Schüller, M. Thumm, and M. Weissgerber. Mirror development for the 140 GHz ECRH system of the stellarator W7-X. *Fusion Engineering and Design*, 66-68:639–644, 2003. 22nd Symposium on Fusion Technology.

[155] A. Mas Sanchez, T. Boutboul, R. Chavan, D. Dall'Acqua, T. P. Goodman, C. Marraco Borderas, H. Torreblanca Quiroz, and A. Xydou. Fluid-dynamic and thermo-mechanical analyses of the iter electron cyclotron miter bend mirror for the off-centered beam scenario. *Fusion Engineering and Design*, 192:113643, 2023.

[156] M. Vagnoni, R. Chavan, A. M. Sanchez, T. P. Goodman, and P. Santos Silva. Design Concept and Thermal–Mechanical Analysis of the Optical Mirror (M3) for the ITER ECH Upper Launcher. *IEEE Transactions on Plasma Science*, 48(6):1543–1548, 2020.

[157] L. Zhang, X. Wang, H. Xu, D. Wu, Y. Tang, J. Wang, W. Xu, and F. Liu. A new design of launcher mirror for EAST electron cyclotron resonance heating system. *Fusion Engineering and Design*, 173:112802, 2021.

[158] W. H. Carter. Electromagnetic field of a gaussian beam with an elliptical cross section. *J Opt Soc Am*, 62(10):1195 – 1201, 1972.

[159] A. Salvitti, A. Bruschi, D. Busi, F. Fanale, F. Giorgetti, G. Granucci, G. Calabrò, P. Fanelli, and M. Nobili. Preliminary design and thermal analyses of the steerable mirror cooling channel of the DTT ECRH. *Fusion Engineering and Design*, 161:111880, 2020.

[160] A. Salvitti, A. Bruschi, G. Calabrò, F. Fanale, P. Fanelli, S. Garavaglia, F. Giorgetti, G. Granucci, A. Moro, P. Platania, and A. Romano. Preliminary thermal and structural analyses on the parabolic mirror of the Multi-Beam Transmission Line of the DTT ECH system. *Fusion Engineering and Design*, 200:114106, 2024.

[161] Ansys Mechanical. https://www.ansys.com/products/structures/ansys-mechanical.

[162] J. W. Davis. ITER Material Properties Handbook. Technical report, Oak Ridge National Laboratory (ORNL), Oak Ridge, TN (United States), 09 1994.

[163] G. Yan, M. Sun, Y. Liang, S. Li, Z. Zhang, X. Zhang, Y. Song, Y. Liu, and J. Zhao. Simulation and experimental study on flow and heat transfer performance of sheet-network and solid-network disturbance structures based on triply periodic minimal surface. *International Journal of Heat and Mass Transfer*, 219:124905, 2024.

[164] Xiaoxin Z., Yingli Y., Sanqing Z., Jun Z., and Qingzhi Y. Microstructure stability, softening temperature and strengthening mechanism of pure copper, CuCrZr and Cu-Al2O3 up to 1000°C. *Nuclear Materials and Energy*, 30:101123, 2022.

[165] A. Quamori Tanzi, A. Cammi, L. Marocco, and L. Savoldi. Design of a 10 MW/m2-heat-flux removal system for a W7-X divertor tile using Triply Periodic Minimal Surfaces. *Case Studies in Thermal Engineering*, 63:105405, 2024.

[166] D. Busi, A. Bussolan, F. Braghin, A. Bruschi, F. Fanale, S. Garavaglia, G. Granucci, A. Romano, and F. Zanon. Study of magnetic effects on DTT ECRH front-steering mirror. *Fusion Engineering and Design*, 191:113550, 2023.

[167] S. Sanchez, P. Smith, Z. Xu, G. Gaspard, C. J. Hyde, W. W. Wits, I. A. Ashcroft, H. Chen, and A. T. Clare. Powder bed fusion of nickel-based superalloys: A review. *International Journal of Machine Tools and Manufacture*, 165:103729, 2021.

[168] National Institute of Standards and Technology, U.S: Department of Commerce.

[169] B. Zhou, P. Xu, W. Li, Y. Liang, and Y. Liang. Microstructure and Anisotropy of the Mechanical Properties of 316L Stainless Steel Fabricated by Selective Laser Melting. *Metals*, 11:775, 05 2021.

[170] C. A. Sumanariu, C. G. Amza, F. Baciu, M. I. Vasile, and A. I. Nicoara. Comparative Analysis of Mechanical Properties: Conventional vs. Additive Manufacturing for Stainless Steel 316L. *Materials*, 17(19), 2024.

[171] B. Jagadeesh and P. Kuppan. Experimental investigations on the material behaviour of SLM fabricated SS316L. *Materials Today: Proceedings*, 2023.

[172] I.A. Segura, J. Mireles, D. Bermudez, C.A. Terrazas, L.E. Murr, K. Li, V.S.Y. Injeti, R.D.K. Misra, and R.B. Wicker. Characterization and mechanical properties of cladded stainless steel 316L with nuclear applications fabricated using electron beam melting. *Journal of Nuclear Materials*, 507:164–176, 2018.

[173] S. Garavaglia et al. First RF operations of the gyrotron for the DTT ECRH System. *Submitted to Fusion Engineering and Design*, 2025.

[174] T. P. Goodman, M. Cavinato, R. Chavan, A. Más-Sanchez, P. Santos Silva, M. Vagnoni, T. Tersztyanszky, and S. Carre. High-Power Testing of Guided-Wave Components for the ITER ECH Upper Launcher at the FALCON Test Facility. *IEEE Transactions on Plasma Science*, 48(6):1537–1542, 2020.

[175] T. Dudziak, R. Buzolin, and E. Rzad. Effect of 316l stainless steel fabrication on oxidation resistance, surface morphology, and hot tensile behavior. *Journal of Material Engineering and Performance*, 32:10443–10454, 2023.

[176] F. Ternero, L. G. Rosa, P. Urban, J. M. Montes, and F. G. Cuevas. Influence of the total porosity on the properties of sintered materials—a review. *Metals*, 11(5), 2021.

[177] F. Davoodi, M. Taghian, G. Carbone, A. Saboori, and L. Iuliano. An Overview of the Latest Progress in Internal Surface Finishing of the Additively Manufactured Metallic Components. *Materials*, 16(10), 2023.

[178] K. Yan, H. Deng, Y. Xiao, J. Wang, and Y. Luo. Thermo-hydraulic performance evaluation through experiment and simulation of additive manufactured Gyroid-structured heat exchanger. *Applied Thermal Engineering*, 241:122402, 2024.

[179] K. Yan, H. Deng, Y. Xiao, J. Wang, Y. Luo, and J. Yan. Influence of polishing process on surface morphology and thermo-hydraulic performance of additively manufactured Gyroid-structured heat exchanger. *Applied Thermal Engineering*, 253:123828, 2024.

[180] F. Eichler, N. Balc, S. Bremen, and P. Nink. Investigation of laser powder bed fusion parameters with respect to their influence on the thermal conductivity of 316l samples. *Journal of Manufacturing and Materials Processing*, 8(4), 2024.

[181] J. C. Simmons, X. Chen, A. Azizi, M. A. Daeumer, P. Y. Zavalij, G. Zhou, and S. N. Schiffres. Influence of processing and microstructure on the local and bulk thermal conductivity of selective laser melted 316L stainless steel. *Additive Manufacturing*, 32:100996, 2020.

[182] S. Zhou, F. Zhang, J. Li, H. Gong, X. Gu, W. Xie, B. Li, and Z. Shao. Sub-millisecond response fiber-optic temperature sensor based on microfabricated silicon Fabry-Pérot interferometer. *Optical Fiber Technology*, 95:104401, 2025.

[183] W. E. Lorensen and H. E. Cline. Marching cubes: A high resolution 3D surface construction algorithm. *SIGGRAPH Comput. Graph.*, 21(4):163–169, August 1987.

[184] W. Schroeder, R. Maynard, and B. Geveci. Flying edges: A high-performance scalable isocontouring algorithm. In *2015 IEEE 5th Symposium on Large Data Analysis and Visualization (LDAV)*, pages 33–40, 2015.

[185] R. Sekerak. *Voxel*, pages 2662–2663. Springer New York, New York, NY, 2011.

[186] W. Schroeder and S. Tsalikis. Really Fast Isocontouring. https://www.kitware.com/really-fast-isocontouring/.

[187] MATLAB Mathworks. https://it.mathworks.com/help/medical-imaging/ref/extractisosurface.html.

[188] Inc. Kitware. Visualization toolkit. https://vtk.org/.

[189] O. Al-Ketan and R. K. Abu Al-Rub. MSLattice: A free software for generating uniform and graded lattices based on triply periodic minimal surfaces. *Material Design & Processing Communications*, 3(6):205, 2021.

[190] K. Marchais. Microgen. https://github.com/3MAH/microgen.

[191] F. Günther, S. Pilz, M. Wagner, Gebert A., and M. Zimmermann. MATLAB script for generating lattices based on triply periodic minimal surfaces (TPMS) in STL file format. https://doi.org/10.5281/zenodo.6973498, 2022.

[192] Siemens Digital Industries Software. NX Design - Design with a Purpose: Introduction into Lattice Structures. https://blogs.sw.siemens.com/nx-design/design-with-a-purpose-introduction-into-lattice-structures/.

[193] Autodesk. Fusion 360 - Create volumetric lattice. https://help.autodesk.com/view/fusion360/ENU/?guid=SLD-CREATE-VOLUMETRIC-LATTICE.

[194] E. Gajetti and U. Follo. TPMSproject. https://github.com/EGajetti/TPMSproject.

[195] ESI OpenCFD. Coupled conditions in OpenFOAM v2212. https://doc.openfoam.com/2212/tools/processing/boundary-conditions/rtm/derived/coupled/#.

[196] ESI OpenCFD. energyJump. https://www.openfoam.com/documentation/guides/latest/api/classFoam_1_1energyJumpFvPatchScalarField.html#details.

[197] M. Coe and D. Holland. A cyclic heat transfer solver for openfoam. *OpenFOAM® Journal*, 3:225–251, Dec. 2023.

[198] E. Gajetti. foamGyroid. https://github.com/EGajetti/foamGyroid.git.

[199] R. P. França, A. C. Borges Monteiro, R. A., and Y. Iano. Chapter 3 - an overview of deep learning in big data, image, and signal processing in the modern digital age. In *Trends in Deep Learning Methodologies*, Hybrid Computational Intelligence for Pattern Analysis, pages 63–87. Academic Press, 2021.

[200] A. Marcato, G. Boccardo, and D. Marchisio. A computational workflow to study particle transport and filtration in porous media: Coupling CFD and deep learning. *Chemical Engineering Journal*, 417:128936, 2021.

[201] What is a neural network? https://www.geeksforgeeks.org/machine-learning/neural-networks-a-beginners-guide/, 2025.

[202] Activation functions in neural networks. https://www.geeksforgeeks.org/machine-learning/activation-functions-neural-networks/, 2025.

[203] S. R. Dubey, S. K. Singh, and B. B. Chaudhuri. Activation functions in deep learning: A comprehensive survey and benchmark, 2022.

[204] D. Wlodzislaw and N. Jankowski. Survey of Neural Transfer Functions. *Neural Computing Surveys*, 2:163–212, 11 1999.

[205] D. Clevert, T. Unterthiner, and S. Hochreiter. Fast and Accurate Deep Network Learning by Exponential Linear Units (ELUs), 2016.

[206] Backpropagation in neural networks. https://www.geeksforgeeks.org/machine-learning/backpropagation-in-neural-network/, 2025.

[207] M. Nielsen. Neural Network and Deep Learning. http://neuralnetworksanddeeplearning.com/index.html, 2019.

[208] G. Orr and K. Müller. *Neural Networks: Tricks of the Trade*. Springer, 01 1998.

[209] A. Oppermann. How Loss Functions Work in Neural Networks and Deep Learning. https://builtin.com/machine-learning/loss-functions, 2022.

[210] PyTorch Loss Functions. https://www.geeksforgeeks.org/deep-learning/pytorch-loss-functions/, 2023.

[211] D. P. Kingma and J. Ba. Adam: A method for stochastic optimization. https://arxiv.org/abs/1412.6980, 2017.

[212] Optimization Rule in Deep Neural Networks. https://www.geeksforgeeks.org/deep-learning/optimization-rule-in-deep-neural-networks/, 2025.

[213] I. Belcic. What is learning rate in machine learning? https://www.ibm.com/think/topics/learning-rate, 2024.

[214] Batch Size in Neural Network. https://www.geeksforgeeks.org/deep-learning/batch-size-in-neural-network/, 2025.

[215] ESI OpenCFD. blockMesh. https://www.openfoam.com/documentation/user-guide/4-mesh-generation-and-conversion/4.3-mesh-generation-with-the-blockmesh-utility.

[216] Michael Dawson-Haggerty. trimesh. https://trimesh.org/, 2022.

[217] A. Paszke, S. Gross, F. Massa, J. Lerer, A.and Bradbury, G. Chanan, T. Killeen, Z. Lin, N. Gimelshein, L. Antiga, A. Desmaison, A. Kopf, E. Yang, Z. DeVito, M. Raison, A. Tejani, S. Chilamkurthy, B. Steiner, L. Fang, J. Bai, and S. Chintala. Pytorch: An imperative style, high-performance deep learning library. In *Advances in Neural Information Processing Systems 32*, pages 8024–8035. Curran Associates, Inc., 2019.

[218] Z-Score Normalization: Definition and Examples. https://www.geeksforgeeks.org/data-analysis/z-score-normalization-definition-and-examples/, 2024.

[219] L. Huang, J. Qin, Y. Zhou, F. Zhu, L. Liu, and L. Shao. Normalization Techniques in Training DNNs: Methodology, Analysis and Application. https://arxiv.org/abs/2009.12836, 2020.

Appendix A

An automatic algorithm for the generation of TPMS with arbitrary porosity

This appendix describes a code for creating custom TPMS geometries with a simple, efficient and open-source code.

TPMS can be analytically generated by considering their characteristic equations $f(x, y, z,) = c$ or $(f(x, y, z) = c) \cup (f(x, y, z) = -c)$. To create a discrete geometry that can be used in traditional numerical tools, such as CFD, a triangulation of the isosurface must be performed via isocontouring algorithm, as the *marching cubes* [183] or *flying edges* [184]. The Marching Cubes algorithm [183] is one of the best-known techniques for extracting isosurfaces from a three-dimensional scalar field. The method, proposed by Lorensen and Cline in 1987, works by analyzing the volume “cube by cube”; for each cube formed by eight adjacent voxels, the field values are compared with the isovalue. This allows each cube vertex to be assigned a bit (1 if above threshold, 0 otherwise), thus generating 256 possible configurations. The voxels are equivalent to pixels in 3D, i.e. voxel represents a defined volume and can be located by coordinates on a three-dimensional grid [185]. Each configuration corresponds - via a precomputed table - to one or more triangulation that locally represent the surface. The vertices of the triangles are positioned using linear interpolation on the voxel data, resulting in a mesh that approximates the surface of interest. The Flying Edges algorithm [184], introduced to improve isocontouring performance on large datasets, rearranges the volume traversal. Instead of processing cubes one by one, Flying Edges systematically traverses rows ("edge by edge") and operates in multiple steps, making the method easily parallelizable. The computation of intersections with the surface is separated on the various directions, allowing efficient overlapping of data and better prediction of memory requirements. In addition, Flying Edges reduces computational work compared to Marching Cubes, especially on modern hardware. This solution is particularly advantageous in the context of voluminous datasets and modern scientific visualization [186].

The Marching Cubes (or Flying Edges) algorithm is used in several programming languages for the isocontouring of scalar field, such as MATLAB with *extractIsosurface* [187]. The Visualiztion Toolkit (VTK) [188], an open-source library for data-visualization implemented both algorithms for numerous open-source programming languages, as for instance Python, C++, Fortran. In literature, many researchers wrote their own code to generate TPMS by usually exploiting MATLAB or VTK ready-to-use modules: MSLattice [189], Microgen [190], designTPMS [191]. The list could be extremely long. However, most of the code are written in MATLAB or Python to exploit the simplicity of the languages, but none to the author's knowledge in compiled languages such as C++, which could on the other hand be quite faster and, with respect to MATLAB, open-source. Other commercial softwares are available to generate TPMS geometries, as nTop [110] or Altair Inspire, often integrated with CAD programs as Siemens NX [192] or Fusion 360 [193]. While the numerous codes found online are mostly open-source, though in most cases complex to understand and modify and mainly lacking in performance, commercial programs are significantly faster but difficult to automate. Reason being, a code in C++ employing VTK was written, and named *TPMSproject*, to allow for automation of custom TPMS structures while still maintaining good performance. It is available on Github in [194].
The TPMSproject pipeline is based on four steps:

1. Mathematical definition of the TPMS topologies
2. Three-dimensional grid sampling. A 3D grid covering the domain of interest is defined and the TPMS function is evaluated at each point on this grid to generate a scalar field
3. Isosurface extraction corresponding to the desired isovalue

4. Visualisation/export. The created mesh can be visualized directly with VTK or exported in standard formats (e.g. STL)

The code structure is reported in Fig. A.1: the main file *mainTPMS* invokes functions from *TPMSsheetGenerator* and *TPMSsolidGenerator* to create the discrete TPMS geometry, from *TPMS.cpp* to handle the TPMS surfaces, such as the triangulation, rotation, transformation and cleaning, and from *Utils.cpp* to visualize the geometry, print the executing time and read the configuration file. The scope of the configuration file *configuration.txt*, present in the *build* directory, is to define the topology, type, size, isovalue, number of cells in the three dimensions and possible rotation of the TPMS.

```
TPMSproject/
├── build/
│   └── configuration.txt
├── TPMSsheetGenerator.cpp
├── TPMSsolidGenerator.cpp
├── TPMS.cpp
├── Utils.cpp
└── mainTPMS.cpp
```

Fig. A.1 Directory tree layout of the TPMSproject showing main folders and files.

The developed algorithm was also compared to a basic MATLAB code for TPMS construction [191] and the time performance shown in Fig. A.2, where the produced number of solid-Gyroid cells is plotted against the generation time. For each cell, 60 points were used in each direction to discretize the characteristic equation. It is evident how TPMSproject in C++ is extremely faster than MATLAB code in creating numerous cells. The test was performed on Windows 11, using a 12th Gen Intel(R) Core(TM) i7-1255U (1.70 GHz). The TPMSproject code was compiled using Visual Studio.

In figure A.3 shows a single Gyroid cell created with the two codes.

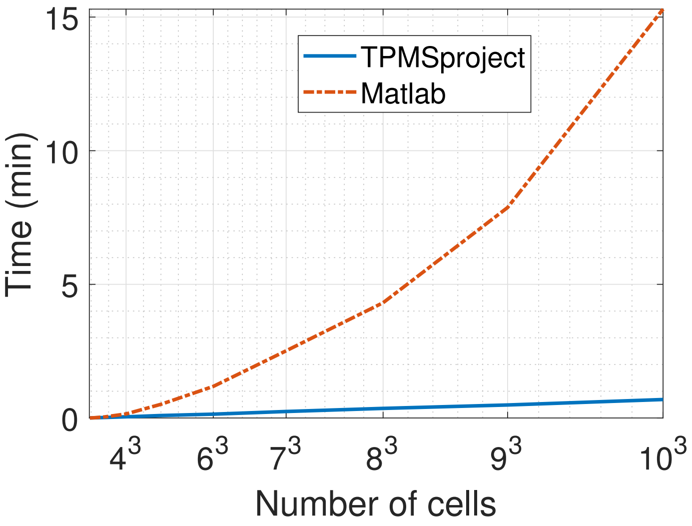

Fig. A.2 Comparison of time performance of the TPMSproject and MATLAB code of Gunther et al. [191], creating solid-Gyroid cells.

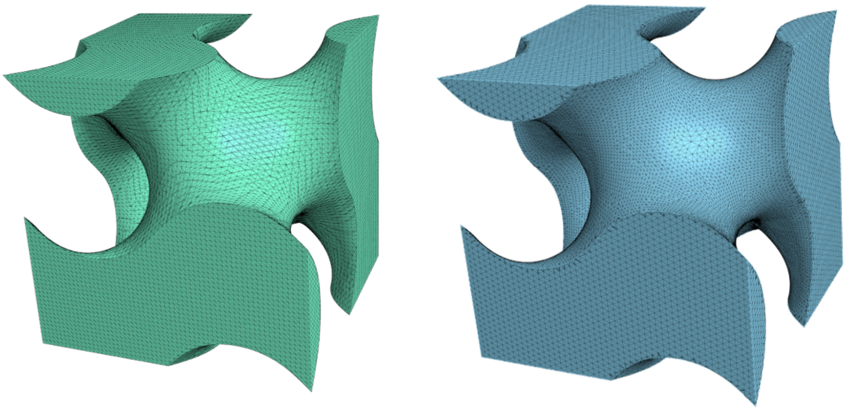

(a) (b)

Fig. A.3 Comparison of a Gyroid cell generated with (a) MATLAB code of Gunther et al. [191] and (b) TPMSproject.

Appendix B

Thermal periodic boundary condition implementation in OpenFOAM

This appendix aims at describing the implementation of a thermal periodic boundary condition in OpenFOAM to be used for cyclic boundaries.

In CFD, simulating a thermally periodic flow is less straightforward than modeling a purely hydraulic fully developed periodic flow. In OpenFOAM, any built-in periodic boundary conditions [195] are not present for the temperature, but for the internal energy, such as [196], and the most commonly employed approach is to use modified solvers for the energy field rather than temperature, as performed by Coe and Holland in 2023 [197].

In order to model the thermal behavior by solving the temperature transport equation without complex workarounds, a fully-developed periodic condition was implemented, following [103, 118], on the normalized temperature θ, defined in Chapter 2 in Eq. (2.51). T_b is the mass flow average temperature, as in Eq. (2.48) for a constant properties fluid. The fully-developed condition in a simple circular pipe implies that the relative shape of the temperature field (i.e. of the normalized temperature) does not change anymore with the flow coordinate [103], resulting in Eq. (B.1), where ξ is the radial coordinate. The same thermal periodic condition is implemented in STAR-CMM+ [134].

$$\frac{\partial}{\partial x}\left[\frac{T_w(x)-T(\xi,x)}{T_w(x)-T_b(x))}\right]=0 \tag{B.1}$$

In TPMS, where the passage area changes continuously, this condition can be applied between two surfaces that are separated by one period, and thus equivalent, so that $\theta_{inlet} = \theta_{outlet}$.. In the case of imposed constant wall temperature, the boundary condition can be utilized as it, considering T_w as a predefined value.
For this case, the developed code, presented below in listing B.1 for completeness, can be found on Github [198].

Listing B.1 Implementation of the thermal periodic boundary condition for $T_w = const.$

```
inlet
{
  type    codedFixedValue;
  value   uniform 300; // Placeholder
  name    periodicT;

  codeInclude #{include "fvCFD.H" #};
  codeOptions #{-I$(LIB_SRC)/finiteVolume/lnInclude #}; code #{

    // Access the mesh
    const fvMesh& fluidMesh = db().parent().objectRegistry::
        lookupObject<fvMesh>("region0");
    const IOdictionary& transportDict = db().lookupObject<
        IOdictionary>("transportProperties");

    // Extract Twall and Tb_in from the transportProperties
    const scalar Twall (transportDict.getScalar("Tw"));
    const scalar Tb_in (transportDict.getScalar("Tbin"));

    // Retrieve the outlet patch
    label patchID_outlet = fluidMesh.boundaryMesh().findPatchID
        ("outlet");
    const polyPatch& outletPatch = fluidMesh.boundaryMesh()[
        patchID_outlet];

    // Extract the outlet temperature and volume flux field
    scalarField outletT = fvc::interpolate(fluidMesh.
        lookupObject<volScalarField>("T")).ref().boundaryField()
        [patchID_outlet];
    scalarField outletPhi = fluidMesh.lookupObject<
        surfaceScalarField>("phi").boundaryField()[
        patchID_outlet];
```

```
    // Initialize the sum of dA*u*T and dA*u in each face of the outlet patch
    scalar sum_A_ui_Ti = 0.0;
    scalar sum_A_ui = 0.0;

    // Loop over all faces of the outlet patch to calculate Tb
    forAll(outletPatch, facei)
    {
      scalar phii = outletPhi[facei];    // Flux at face i
      scalar Ti = outletT[facei];        // Temperature at face i
      sum_A_ui_Ti += Ti * phii;
      sum_A_ui    += phii;
    }

    // Compute the boundary temperature value Tb_out
    scalar Tb_out = sum_A_ui_Ti / sum_A_ui;
    // Assign the new values to the inlet patch
    operator==(Twall - (Twall - outletT) / (Twall - Tb_out) * (Twall - Tb_in));
    #};
}
```

An example of the periodic θ field between inlet and outlet is shown in Fig. B.1.

In the case of constant imposed heat flux, it might be demonstrated that the periodic relevant temperature is not anymore θ, but a simpler condition $T_{in}(x,y) - T_{b,in}(x) = T_{out}(x,y) - T_{b,out}(x)$ can be enforced [103]. The code then simply changes its last line as in listing B.2.

Listing B.2 Implementation of the thermal periodic boundary condition for $q_w = const.$

```
    operator==(outletT - Tb_out + Tb_in);
```

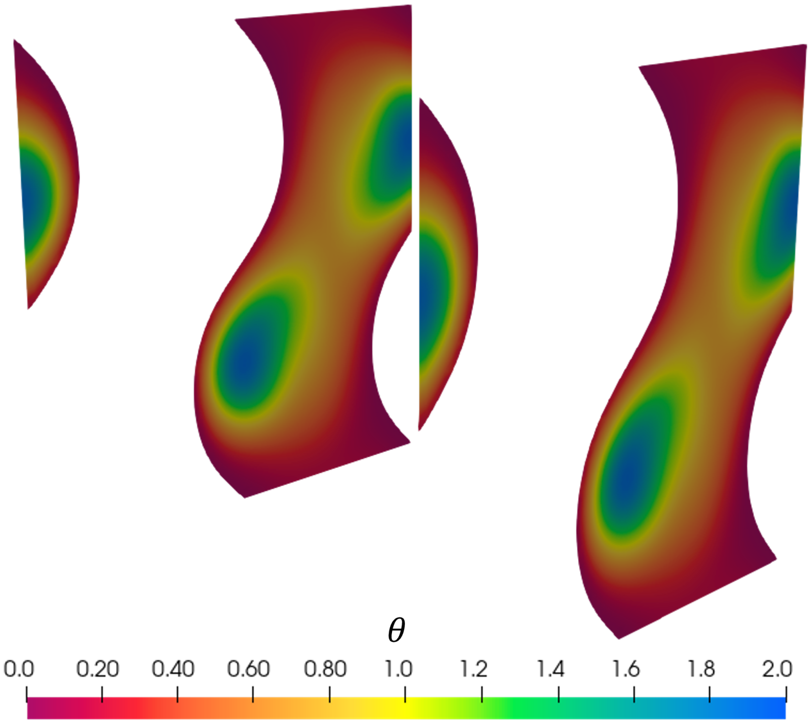

Fig. B.1 Example of θ at inlet and outlet computed on the Gyroid at 50% and Re_{D_h} = 50.

Appendix C

A machine learning algorithm as alternative surrogate model of TPMS

In this thesis, traditional correlations were developed for the thermal and hydraulic characterization of TPMS. However, the use of more innovative methodologies, such as machine learning (ML), could enable the development of surrogate models capable of capturing complex nonlinear relationships between the variables of interest, while also taking advantage of the larger number of degrees of freedom offered by these techniques. Thus, this appendix describes the use of a neural network (NN) as a surrogate model for CFD in thermal-hydraulic analysis. The use of a neural network offers the advantage of simplicity over other machine learning techniques, thanks to its relatively straightforward mathematical formulation, which also makes it well-suited for integration with possible gradient-based optimization methods.

First, a brief introduction on machine learning and neural networks is given in Section C.1, then the explanation of the completely open-source and automated workflow for creating the database in Section C.2, and finally the training and testing of the neural network on TPMS in Section C.3.

C.1 Neural network

Machine learning is a subset of artificial intelligence that allows computers to learn from data and improve their performance with experience, without being explicitly programmed for each task [199]. Machine learning algorithms identify patterns and correlations in large datasets to formulate decisions or predictions, and their effectiveness grows with access to ever larger and more varied data.

A neural network is a machine learning algorithm inspired by the functioning of the human brain, employed to recognize relationships in data. It consists of nodes (or artificial neurons) organized in layers: an input layer, one or more hidden layers and an output layer. Each neuron is linked to the neurons of the previous and following layers by weighted connections $w_{i,j}$. During the training, these weights are updated to improve the accuracy of the model [200, 201]. In particular, with reference to Eq. C.1, the value of each $j-th$ neuron $y_j^{(k)}$ of the $k-th$ layer is computed by a certain activation function f_{act}, taking as input the sum of the weighted values of the previous layer neurons $y_i^{(k-1)}$. b_{k-1} is called the bias of the previous layer, m_{k-1} is the number of neurons of the previous layer. The activation function inserts non-linearity in the model, without which the neural network would be as a simple linear regression function [202].

$$y_j^{(k)} = f_{act}\left(b_{k-1} + \sum_{i=1}^{m_{k-1}} w_{i,j}^{(k)} y_i^{(k-1)}\right) \tag{C.1}$$

An example of a simple neural network is drawn in Fig. C.1: an input and an output layers and a single hidden layer. From the two inputs i_1 and i_2 the hidden neuron h_1 is computed as $h_1 = f_{act}(b_1 + w_1 i_1 + w_2 i_2)$. Consequently, the output neuron is equal to $out = f_{act}(b_2 + w_3 f_{act}(b_1 + w_1 i_1 + w_2 i_2))$. Without the activation function, it would be simply $out = b_2 + w_3(b_1 + w_1 i_1 + w_2 i_2)$.

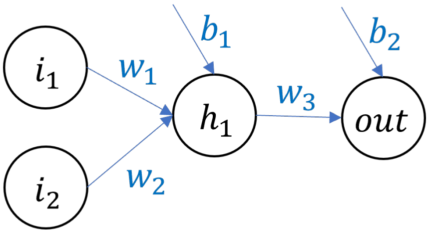

Fig. C.1 Sketch of a simple neural network with 2 input neurons, one neuron in a single hidden layer and single output.

Several activation functions exist [202–204] and may be grouped in three characteristic types:

- *Sigmoid/Tanh* Unit Based activation functions

- *Rectified Linear* Unit (ReLU) Based activation functions,
- *Exponential Linear* Unit (ELU) Based activation functions

The Sigmoid/Tanh are defined as $1/(1+e^{-x})$ or $(e^x - e^{-x})/(e^x + e^{-x})$ and were used in the early days of the NN development. They are mainly affected by the vanishing of the gradient for very large or small inputs. The Rectified Linear function is defined in Eq. (C.2), and it consists of the identity function for positive x and zero for negative x.

$$ReLU(x) = max(0,x) = \begin{cases} x, & \text{if } x \geq 0 \\ 0, & \text{otherwise} \end{cases} \tag{C.2}$$

Again, it suffers from the vanishing gradient for the negative inputs, which is partly solved by the Leaky ReLU (LReLU) as in Eq. (C.3). Different slope values can be used, depending on the problem.

$$LReLU(x) = \begin{cases} x, & x \geq 0 \\ 0.01x, & x < 0 \end{cases} \tag{C.3}$$

To cope with the vanishing gradient problem of Sigmoid/Tanh and ReLU functions, the Exponential Linear functions is defined in Eq. (C.4), where α is a learnable parameter. Compared to LReLU, it is differentiable, and its saturation at negative values adds some robustness to noise [205].

$$ELU(x) = \begin{cases} x, & x > 0 \\ \alpha(e^x - 1), & x \leq 0 \end{cases} \tag{C.4}$$

Besides these main cases listed above, many other activation functions have been studied over the years, modifying these major ones and adding adaptability and complexity, e.g. the use of learning parameters [203].

Developing a neural network model begins with a large dataset with certain inputs and outputs. The dataset must be divided into a training set, for the training of the NN, and a testing set, for the testing of the NN on data not used in the training. The weights and biases of Eq. (C.1) are modified during the training process of the neural network through the *back-propagation* algorithm [206–208], that aims at minimizing the errors of the predictions of the NN. Practically, a loss function to be minimized is defined. One of the most commonly utilized loss function is the *Mean Squared Error* (MSE) [209, 210] of Eq. (C.5).

$$MSE = \frac{1}{n}\sum_{i=1}^{n}(y_i - \hat{y}_i)^2 \tag{C.5}$$

The minimization of the loss function is implemented through an optimizer. Again, several types of optimizers can be employed in NN training, but the most common and efficient one is the *Adam* optimizer [211, 212], which provides very fast convergence, at the expense of computation resources.

At each step of the training, the dataset is divided into smaller group, processed independently before the model parameters are adjusted based on the *learning rate* [208, 213]. The *batch* size refers to the number of samples used in each of these smaller group during training [214]. A larger learning rate could provide faster convergence at the expense of stability. A complete passage over all the batches of the dataset is defined as an *epoch*, which is essentially equivalent to an iteration of neural network optimization. The optimizer, batch size and learning rate are called *hyperparameters* of the model, because they are decided a priori and remain unchanged at the end of the training process.

C.2 Dataset creation

Training a neural network requires the availability of very large datasets, which are complex to manually produce by treating each case individually. Therefore, an automatic working process was developed that, starting from N pre-chosen input parameters, generates the desired geometries via the in-house code (Appendix A), and then simulates them hydraulically and thermally on OpenFOAM [120], following the flow-chart of Fig. C.2.

Consistently with Chapter 2, a single periodic unit cell was used for simulations.

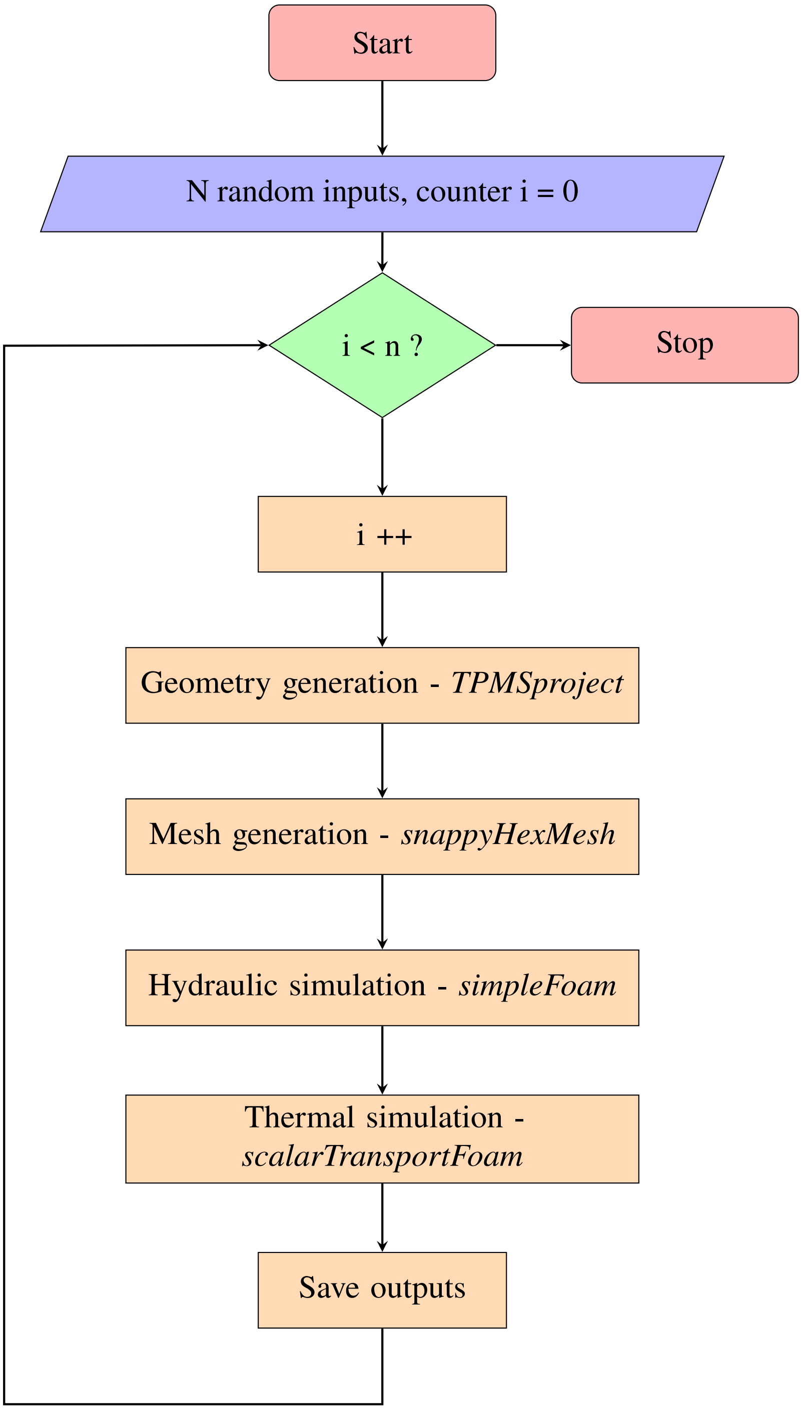

Fig. C.2 Automatic workflow for dataset creation

C.2.1 Dataset inputs

The relevant inputs to study the performance of a TPMS are the geometrical parameters, such as the porosity and topology, the hydraulic and the thermal conditions. Practically, the topology could be unequivocally defined by the combination of the hydraulic diameter and porosity (i.e. each topology has its own D_h vs φ curve, non-intersecting with the other topologies curves, see Fig. 2.2c), the hydraulic conditions by the Re_{D_h} and the thermal conditions by the heat flux (or temperature) applied to the wall. The range of porosities and Reynolds numbers used in this work is the same of Chapter 2.4, i.e. φ between 30% and 70% and Re_{D_h} between 20 and 100. Three solid-TPMS topologies were studied: Gyroid, Diamond and SplitP1. SplitP2 was not included in the investigation due to the difficulty in distinguishing it from SplitP1 with geometric parameters such as hydraulic diameter. In the simulations, the wall fixed temperature was used as thermal driver and ranged between $350\,K$ and $450\,K$. Since simulations need an input velocity, it was computed from the Reynolds numbers considering the different hydraulic diameters of the three topologies. Constant properties were used. For more details on the numerical methodology, refer to Chapter 2.4.

C.2.2 TPMS geometry and meshing

The in-house code of Chapter A was coupled with the meshing tool of OpenFOAM, snappyHexMesh [105]. snappyHexMesh (SHM) is an open-source code that creates a hexahedral-dominant grid starting from surface geometries (such as stl or obj files). SHM requires in input, in addition to the geometry file, a background mesh created by the blockMesh utility [215] and an instruction to the volume to be meshed, internally or externally to the provided geometry. To compensate for the fact that the geometry is constantly changing during the automatic workflow, an algorithm was written for identifying a point within the geometry, using the python module *trimesh* [216]. Moreover, the snappyHexMesh dictionary, where all the meshing instructions are given, needs different input in the case in which the domain has one or more non-contiguous regions, as in some cases of TPMS at large porosity. An example of two non contiguous parts of the same unit cell is shown in Fig. C.3. The code for the meshing process of TPMS is available on Github [198].

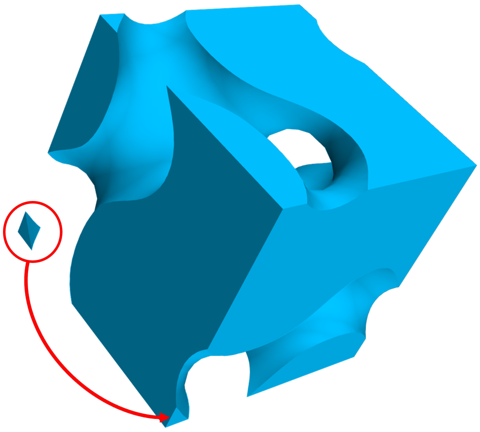

Fig. C.3 Example of non contiguous regions belonging to the same unit cell. Gyroid at 70% porosity.

C.2.3 Thermal-hydraulic simulations

As in Chapter 2, the single TPMS unit cell was simulated, using *simpleFoam* (employing the simple algorithm to solve the Navier-Stokes equations) in laminar mode. All the boundaries of the cube were set as cyclic two-by-two, and along the inlet-outlet direction a momentum source was imposed, as in Fig. 2.21a.

The hydraulic and thermal simulations were performed uncoupled, first computing the velocity field with *simpleFoam* [95] and then, frozing the simple solver and using the velocity field as input, solving the thermal transport via *scalarTransportFoam* [104]. The full simulation setup is available on Github [198].
From the thermal and hydraulic simulations, the friction factor and Nusselt numbers were extracted, as defined in Chapter 2, and used for the training of the neural network.

C.3 Neural network training and testing

300 simulations were performed for each TPMS topology, resulting in a final dataset of 900 points. Using PyTorch [217], a neural network model was developed to predict hydraulic and thermal results (in terms of friction factor and Nusselt number) based on the Reynolds number and porosity for a single topology, and Reynolds number, porosity and hydraulic diameter for the three topologies together. The dataset of the

three topology is shown in Fig. C.4. As shown in Chapter 2, the Nusselt number and friction factor are linked by a relationship that depends on the Reynolds number and the porosity, which justifies the use of a single neural network, i.e. a single model, with two inputs (or three when adding the hydraulic diameter for the three topologies together) and two outputs.

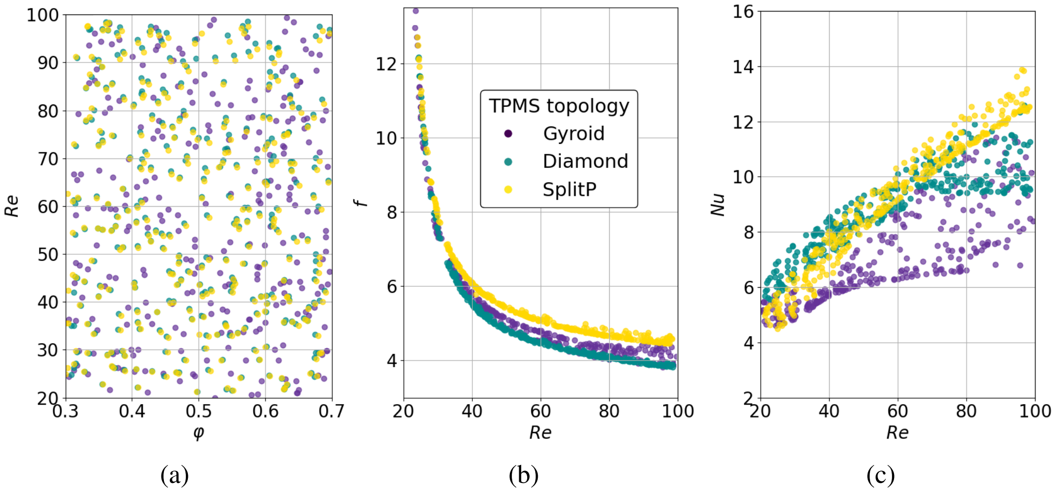

(a) (b) (c)

Fig. C.4 TPMS dataset. (a) Reynolds number vs porosity, (b) friction factor versus Reynolds number and (c) Nusselt number vs Reynolds number.

C.3.1 Hyperparameters tuning

A study on the single Gyroid dataset was performed to select the hyperparameters, by training the neural network present in Fig. C.5. The Nusselt number and friction factor data were normalized using the Z-score normalization technique [218] as in Eq. (C.6), also called standardization, to improve convergence speed and balance the impact of data on the learning process [219]. In Eq. (C.6) X are the data, X_{norm} the normalized data, $\overline{X}$ and $stdev$ the mean and standard deviation of the dataset.

$$X_{norm} = \frac{X - \overline{X}}{stdev} \tag{C.6}$$

First, different subsets of the total dataset were used, i.e. 100, 200 or 300 points, to investigate the convergence of the training process, as presented in Fig. C.6, using two hidden layers with 32 and 64 neurons, a learning rate of 0.001 and batch size of 30, using the ELU activation function.

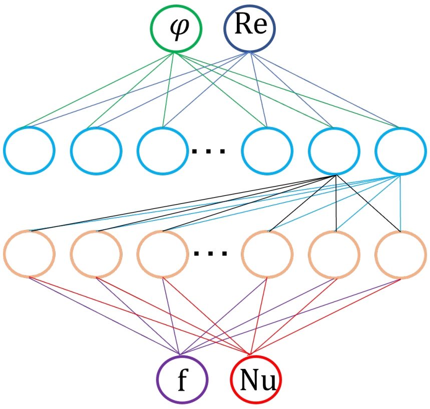

Fig. C.5 Neural network sketch. φ and Re as input neurons, f and Nu as output.

After 500 epochs/iterations, the NN trained on 300 points had a testing loss lower than 1%, while the 200 points-trained NN had around 2% loss.

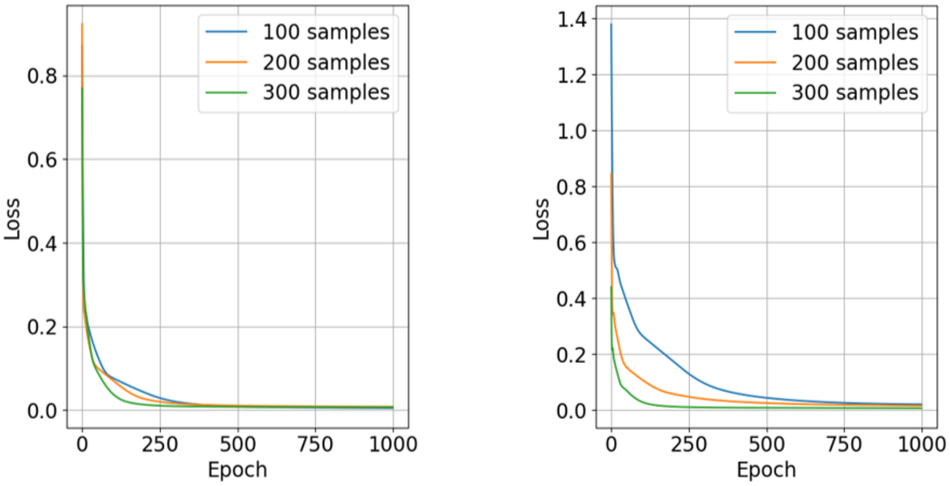

(a)

(b)

Fig. C.6 Loss function evaluation during the training process. (a) Losses computed on the training dataset and (b) losses computed on the testing dataset.

In a second moment, the tuning of the batch size, learning rate and number of layers and neurons was performed, and reported in Fig. C.7 through the mean relative difference between predictions and testing set. Each point, with a certain learning rate, network architecture and batch size was repeated five times, and the the average values are shown in Fig. C.7. The NN with a single hidden layer is the most stable, even at larger learning rate, while the multiple hidden layers NN showed divergence of the model at learning rate of 10^{-1}. The multiple layers NN had similar behavior for low learning rates. In particular, the two layers with 32 and 64 neurons network was chosen because of its simpler architecture compared to the others and equivalent performance at a learning rate of 10^{-3}. The ELU activation function was compared to the LReLU and found faster, thus selected.

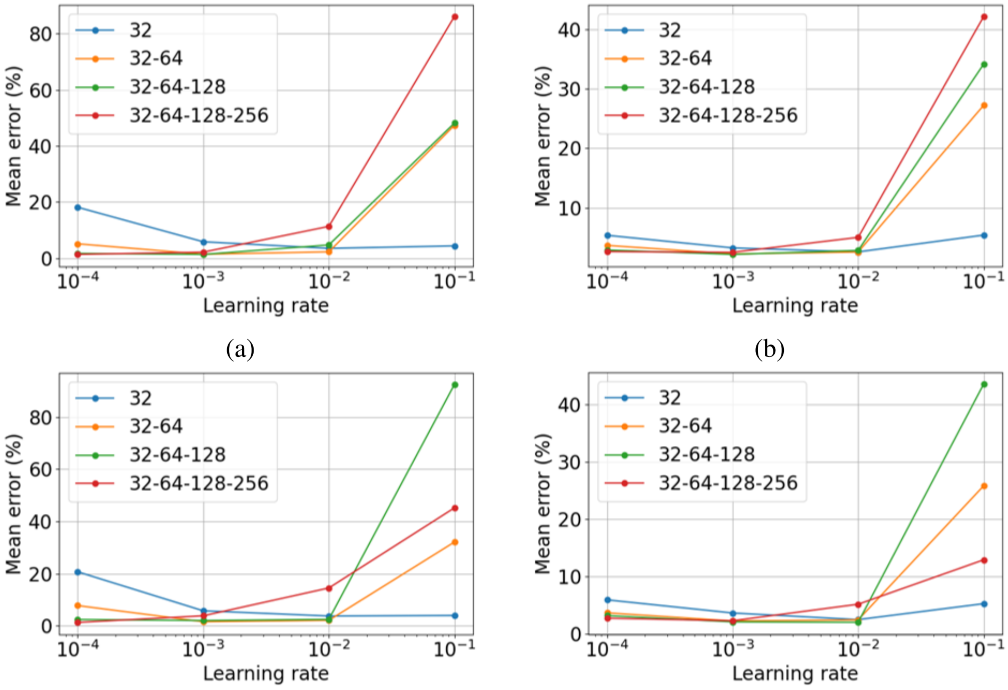

(a) (b)

(c) (d)

Fig. C.7 Hyperparameters investigation: (a) and (c) mean error on f prediction, (b) and (d) mean error on Nu prediction. (a) and (b) batch size = 30, (c) and (d) batch size = 40.

C.3.2 Predictive ability of the NN

The hyperparameters chosen in Section C.3.1 were used to develop a neural network trained on the Gyroid data in a first moment, and then trained on the three TPMS data together. The predictive ability of the Gyroid-trained and TPMS-trained NN are shown in Fig. C.8 and Fig. C.9, respectively. In both cases, the NN was able to predict the friction factor and Nusselt number with a good degree of accuracy. For the Gyroid-trained NN, the mean percentage error on the testing data after 1000 epochs was 1.4% and 2.1% for f and Nu, while in the TPMS-trained NN after 1000 epochs was 6.3% and 1.6%. The NN based only on Gyroid data was trained in 40 s, while the NN based on the three topologies together was trained in 75 s, with a larger batch size of 50. These results are encouraging because the maximum mean errors of the friction factors on the testing data are approximately of the same order of magnitude of the errors computed in Section 2.3.2, with the correlations for the permeability and drag inertial coefficient. On the other hand, the maximum computed mean error on the Nusselt number are lower than the errors computed in Section 2.4.3 on the correlations for the Stanton number. Moreover, employing a neural network to simultaneously model multiple topologies without compromising

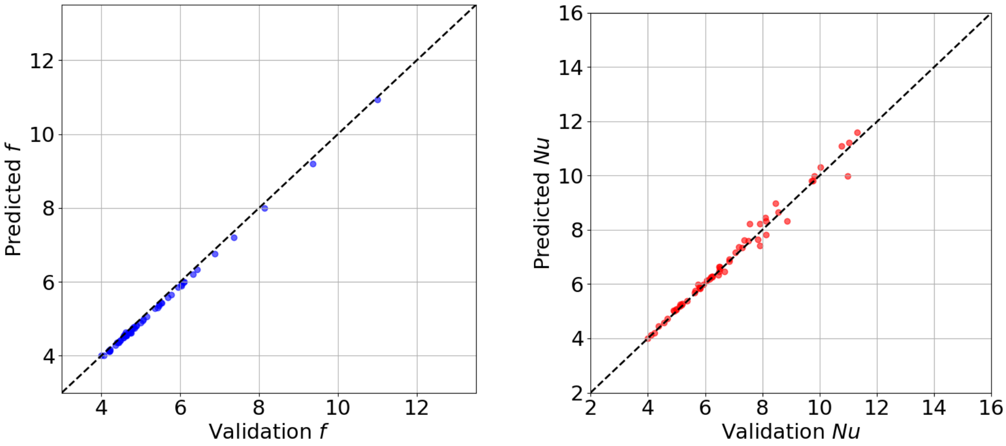

(a) (b)

Fig. C.8 Predictive ability of the neural network trained and tested on the sole Gyroid data.

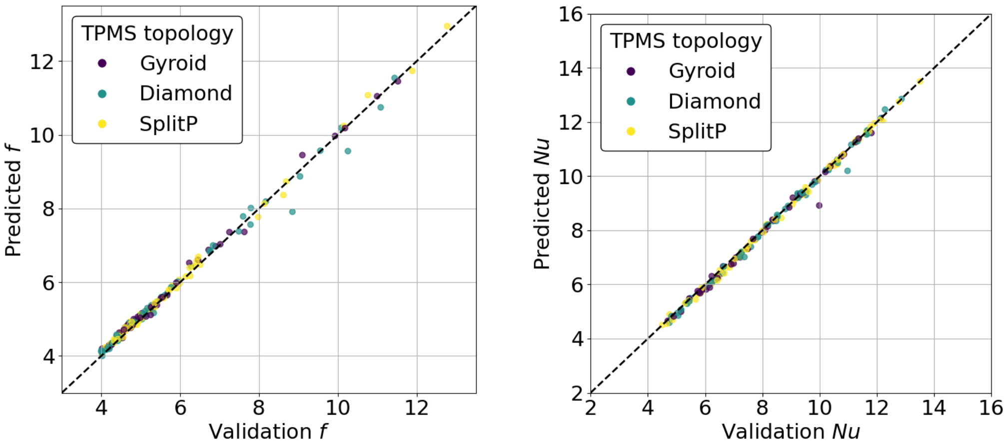

(a) (b)

Fig. C.9 Predictive ability of the neural network trained and tested on the dataset containing the three TPMS topologies. (a) Prediction of f and (b) prediction of Nu.

accuracy is particularly promising, as it may pave the way for their broader adoption by integrating different topologies within a unified framework.

Appendix D

A correlation between “solid” and “sheet” structures

In this appendix, geometric considerations are applied to the TPMS sheet and solid to derive correlations between the hydraulic parameters that characterize them. Considering a certain sheet-Gyroid, defined as $(fun(x, y, z) = c) \cup (fun(x, y, z) = -c)$, the two subvolumes of the sheet geometry are identical to the two subvolumes that are considered solid-Gyroid, as reported in Fig. D.1. Moreover, Fig. D.1b and Fig. D.1c are antisymmetric, so they are topologically equivalent. Moreover, the two channels of the sheet-Gyroid are two parallel channels, which are thus subject to equal pressure drop along them, and, being equivalent, they have the same flow rate flowing through them. If we consider only one subvolume of the solid type, if it is subject to the same pressure drop of a sheet geometry (Eq. (D.1)), it will experience a flow rate which is double than the sheet flow rate (Eq. (D.2)).

$$\left(\frac{\Delta p}{L}\right)_{sheet} = \left(\frac{\Delta p}{L}\right)_{solid} \tag{D.1}$$

$$\dot{V}_{sheet} = 2\dot{V}_{solid} \tag{D.2}$$

Therefore, the superficial velocity of the sheet type is two times the solid one, as in Eq. (D.3).

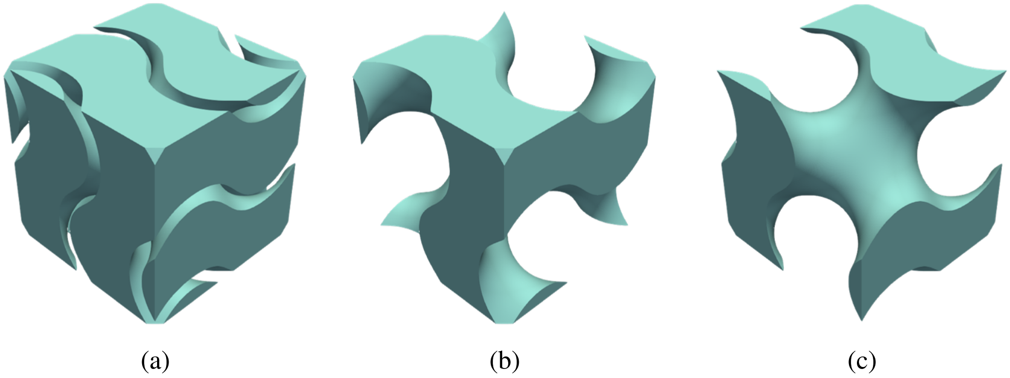

Fig. D.1 Comparison sheet-solid Gyroid: (a) the two subvolumes of the sheet type, (b) and (c) the two solid subvolumes.

$$U_{s,sheet} = 2U_{s,solid} \tag{D.3}$$

Considering that the sheet geometries have two subvolumes, and the solid only one, $A_{w,sheet} = 2A_{w,solid}$ and $\varphi_{sheet} = 2\varphi_{solid}$. Thus, the hydraulic diameter of the sheet geometry is equal to the solid hydraulic diameter.

$$D_{h,sheet} = D_{h,solid} \tag{D.4}$$

D.1 Viscous regime

In the viscous regime, where the pressure losses in a porous medium depend linearly on the superficial velocity, based on Eq. (2.19), Eq.(D.1) might be written as in Eq. (D.5), which then results in Eq. (D.6) by using Eq. (D.3).

$$\frac{\mu}{K_{sheet}} U_{s,sheet} = \frac{\mu}{K_{solid}} U_{s,solid} \tag{D.5}$$

$$\frac{2U_{s,solid}}{K_{sheet}} = \frac{U_{s,solid}}{K_{solid}} \tag{D.6}$$

Eq. (D.6) can be further simplified in Eq. (D.7), thus the permeability of the solid geometry - having half the porosity of the sheet geometry - is half the permeability of the sheet type.

$$K_{sheet} = 2K_{solid} \tag{D.7}$$

These considerations are valid also for the TPMS in which the isosurface divides the volume into two subvolumes with non-identical topology, as the SplitP, for which anyway the permeability is equal (as discussed in Section 2.3.2).

D.2 Inertial regime

In the inertial regime, the Forchheimer term must be accounted, too, as in Eq. (2.20), thus Eq. (D.5) becomes Eq. (D.8).

$$\frac{\mu}{K_{sheet}}U_{s,sheet} + \rho\frac{C_{F,sheet}}{\sqrt{K_{sheet}}}U^2_{s,sheet} = \frac{\mu}{K_{solid}}U_{s,solid} + \rho\frac{C_{F,solid}}{\sqrt{K_{solid}}}U^2_{s,solid} \tag{D.8}$$

Similarly to the previous reasoning, considering that $U_{s,sheet} = 2U_{s,solid}$ and $K_{s,sheet} = 2K_{s,solid}$, Eq. (D.8) becomes Eq. (D.9) and then Eq. (D.11), through the simplifications of Eq. (D.10).

$$\frac{\mu}{2K_{solid}}2U_{s,solid} + \rho\frac{C_{F,sheet}}{\sqrt{2K_{solid}}}4U^2_{s,solid} = \frac{\mu}{K_{solid}}U_{s,solid} + \rho\frac{C_{F,solid}}{\sqrt{K_{solid}}}U^2_{s,solid} \tag{D.9}$$

$$\frac{\mu}{\cancel{2K_{solid}}}\cancel{2U_{s,solid}} + \cancel{\rho}\frac{C_{F,sheet}}{\sqrt{2\cancel{K_{solid}}}}4\cancel{U^2_{s,solid}} = \frac{\mu}{\cancel{K_{solid}}}\cancel{U_{s,solid}} + \cancel{\rho}\frac{C_{F,solid}}{\sqrt{\cancel{K_{solid}}}}\cancel{U^2_{s,solid}} \tag{D.10}$$

$$C_{F,sheet} = \frac{\sqrt{2}}{4}C_{F,solid} \tag{D.11}$$

Thus, the inertial drag coefficient has a more complex relation between solid and sheet structures than the permeability. On the other hand, also the friction factor can be investigated, such that, remembering that $\Delta p/L$ is equal in the sheet and solid geometries:

$$\frac{\frac{1}{2}\,\rho\, f_{sheet}\, U^2_{s,sheet}}{D_{h,sheet}\,\varphi^2_{sheet}} = \frac{\frac{1}{2}\,\rho\, f_{solid}\, U^2_{s,solid}}{D_{h,solid}\,\varphi^2_{solid}} \tag{D.12}$$

Again, by considering that $U_{s,sheet} = 2U_{s,solid}$, $D_{h,sheet} = D_{h,solid}$ and $\varphi_{sheet} = 2\varphi_{solid}$, Eq. (D.12) becomes Eq. (D.13), so that the resulting sheet friction factor is equal to the solid friction factor.

$$f_{sheet}\frac{4U^2_{s,solid}}{4\varphi^2_{solid}} = f_{solid}\frac{U^2_{s,solid}}{\varphi^2_{solid}} \tag{D.13}$$

The above considerations are valid for all the TPMS that are exactly divided in two equivalent and topologically identical subvolumes by the zero isovalue, such as Gyroid, Diamond, Primitive. This consideration not being valid for the SplitP, for example, for which the zero isovalue divides the structure into two equivalent but not topologically equal subvolumes, a further step must be taken to correlate the behavior of the two solid-SplitP with the sheet-SplitP. In Fig. D.2, the example of the two SplitP subvolumes, clearly geometrically diverse.

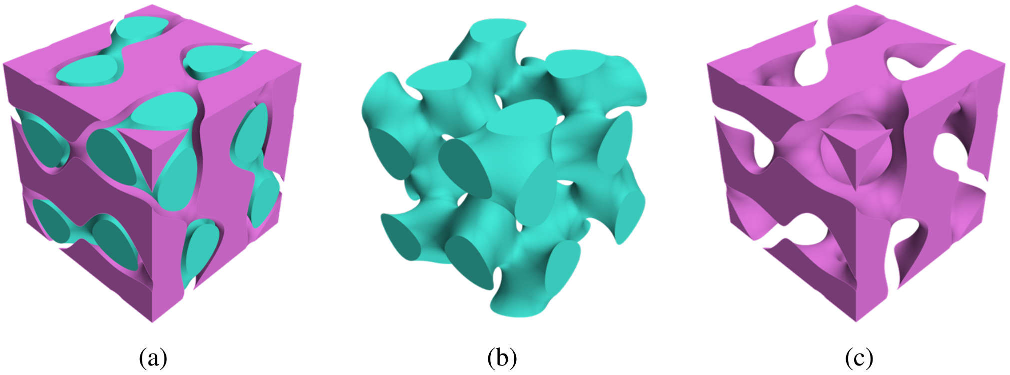

(a) (b) (c)

Fig. D.2 Comparison sheet-solid SplitP: (a) the two subvolumes of the sheet type, (b) SplitP1 and (c) SplitP2 solid subvolumes.

When offsetting equally the isosurface in both normal directions, the two subvolumes in which the SplitP isosurface divides the space have the same volume and same wet area, thus same porosity. As before, they can be considered as parallel channels, thus with the same pressure losses (as in Eq. (D.14)). However, having different geometries, different flow rates must be accounted for.

$$\Delta p_{solid1} = \Delta p_{solid2} = \Delta p_{sheet} \tag{D.14}$$

As described in Chapter 2.3, the two solid-SplitP have the same permeability, $K_{solid1} = K_{solid2}$, thus Eq. (D.14) can be developed into Eq. (D.15), considering Eq. D.7 and that $K_{sheet} = 2K_{solid1} = 2K_{solid2} = 2K_{solid}$.

$$\begin{aligned} \Delta p_{solid1} &= \frac{\mu}{K_{solid}} U_{s,solid1} + \rho \frac{C_{F,solid1}}{\sqrt{K_{solid}}} U^2_{s,solid1} = \\ \Delta p_{solid2} &= \frac{\mu}{K_{solid}} U_{s,solid2} + \rho \frac{C_{F,solid2}}{\sqrt{K_{solid}}} U^2_{s,solid2} = \\ \Delta p_{sheet} &= \frac{\mu}{2K_{solid}} U_{s,sheet} + \rho \frac{C_{F,sheet}}{\sqrt{2K_{solid}}} U^2_{s,sheet} \end{aligned} \tag{D.15}$$

With regard to the above equation, if we sum the pressure losses in the two solid subvolumes, the result will be equal to twice the pressure loss in the sheet-SplitP, $\Delta p_{solid1} + \Delta p_{solid2} = 2\Delta p_{sheet}$, thus:

$$\begin{aligned} &\frac{\mu}{K_{solid}} (U_{s,solid1} + U_{s,solid2}) + \frac{\rho}{\sqrt{K_{solid}}} (C_{F,solid1} U^2_{s,solid1} + C_{F,solid21} U^2_{s,solid2}) = \\ &= \frac{\mu}{K_{solid}} U_{s,sheet} + \frac{2}{\sqrt{2}} \frac{\rho}{\sqrt{K_{solid}}} C_{F,sheet} U^2_{s,sheet} \end{aligned} \tag{D.16}$$

In Eq. (D.16), it is clear that the first term of the left hand side is equal to the first term of the right hand side, as well as the second. For the first terms, the trivial result $U_{s,sheet} = U_{s,solid1} + U_{s,solid2}$ was already known from Eq. (D.3), while equating the second terms results in Eq. (D.17).

$$\begin{aligned} \frac{2}{\sqrt{2}} C_{F,sheet} U^2_{s,sheet} &= (C_{F,solid1} U^2_{s,solid1} + C_{F,solid21} U^2_{s,solid2}) \\ C_{F,sheet} &= \frac{\sqrt{2}}{2} \frac{C_{F,Solid1} U^2_{s,solid1} + C_{F,Solid2} U^2_{s,solid2}}{(U_{s,solid1} + U_{s,solid2})^2} \end{aligned} \tag{D.17}$$

Considering the generic Darcy-Fochheimer law for both subvolumes, by knowing the pressure drop Δp, the superficial velocity can be obtained from the formula of a second-degree polynomial, resulting in Eq. (D.18).

$$
\begin{aligned}
U_{s,solid1} &= \frac{-\frac{\mu}{K_{solid}} + \sqrt{\left(\frac{\mu}{K_{solid}}\right)^2 + 4\frac{\Delta p}{L}\rho\frac{C_{F,solid1}}{\sqrt{K_{solid}}}}}{2\rho\frac{C_{F,solid1}}{\sqrt{K_{solid}}}} \\
U_{s,solid2} &= \frac{-\frac{\mu}{K_{solid}} + \sqrt{\left(\frac{\mu}{K_{solid}}\right)^2 + 4\frac{\Delta p}{L}\rho\frac{C_{F,solid2}}{\sqrt{K_{solid}}}}}{2\rho\frac{C_{F,solid2}}{\sqrt{K_{solid}}}}
\end{aligned}
\tag{D.18}
$$

By substituting Eq. (D.18) within Eq. (D.17), the correlation between the sheet inertial drag coefficient and the two solid inertial drag coefficients might be found.

Everything here was developed considering that $\dot{V}_{sheet} = 2\dot{V}_{solid}$ at the same porosity. If, on the other hand, $\dot{V}_{sheet} = \dot{V}_{solid}$, then $(\Delta p/L)_{sheet} < (\Delta p/L)_{solid}$ and in particular considering the quadratic dependence of the linear pressure drop on the superficial velocity, $(\Delta p/L)_{sheet} \sim (\Delta p/L)_{solid}/4$. However, in many works in literature the solid and sheet-types are compared at the same porosity. In this case, the $(\Delta p/L)_{solid}$ is considerably lower and it is not straightforward to predict a priori which structure has larger flow impedance.

These geometric considerations to develop analytical correlations between the sheet and solid structures can be very useful since in literature very often solid and sheet structures are treated separately, while they should be considered as the same type of structures.